

Review

Design Principles and Engineering Strategies for Stabilizing Ni-Rich Layered Oxides in Lithium-Ion Batteries

Alain Mauger * and Christian M. Julien 

Institut de Minéralogie, de Physique des Matériaux et de Cosmologie (IMPMC), Sorbonne Université, UMR-CNRS 7590, 4 Place Jussieu, 75752 Paris Cedex 05, France; christianjulien@sorbonne-universite.fr

* Correspondence: alain.mauger@sorbonne-universite.fr

Abstract

Nickel-rich layered oxides such as $\text{LiNi}_x\text{Mn}_y\text{Co}_z\text{O}_2$ (NMC), $\text{LiNi}_x\text{Co}_y\text{Al}_z\text{O}_2$ (NCA), and $\text{LiNi}_x\text{Mn}_y\text{Co}_z\text{Al}_{(1-x-y-z)}\text{O}_2$ (NMCA), where $x \geq 0.6$, have emerged as key cathode materials in lithium-ion batteries due to their high operating voltage and superior energy density. These materials, characterized by low cobalt content, offer a promising path toward sustainable and cost-effective energy storage solutions. However, their electrochemical performance remains below theoretical expectations, primarily due to challenges related to structural instability, limited thermal safety, and suboptimal cycle life. Intensive research efforts have been devoted to addressing these issues, resulting in substantial performance improvements and enabling the development of next-generation lithium-ion batteries with higher nickel content and reduced cobalt dependency. In this review, we present recent advances in material design and engineering strategies to overcome the problems limiting their electrochemical performance (cation mixing, phase stability, oxygen release, microcracks during cycling). These strategies include synthesis methods to optimize the morphology (size of the particles, core–shell and gradient structures), surface modifications of the Ni-rich particles, and doping. A detailed comparison between these strategies and the synergistic effects of their combination is presented. We also highlight the synergistic role of compatible lithium salts and electrolytes in achieving state-of-the-art nickel-rich lithium-ion batteries.



Academic Editor: Claudio Gerbaldi

Received: 22 May 2025

Revised: 24 June 2025

Accepted: 1 July 2025

Published: 4 July 2025

Citation: Mauger, A.; Julien, C.M.

Design Principles and Engineering Strategies for Stabilizing Ni-Rich Layered Oxides in Lithium-Ion Batteries. *Batteries* **2025**, *11*, 254. <https://doi.org/10.3390/batteries11070254>

Copyright: © 2025 by the authors. Licensee MDPI, Basel, Switzerland. This article is an open access article distributed under the terms and conditions of the Creative Commons Attribution (CC BY) license (<https://creativecommons.org/licenses/by/4.0/>).

Keywords: nickel-rich cathodes materials for lithium-ion batteries; doping; coating; morphology control; interface engineering; lithium salts; electrolytes

1. Introduction

Lithium-ion batteries (LIBs) have been a major advance in the energy storage, and in the development of many devices, from portable phones and laptops to electric vehicles (EVs). For the latter application, LIBs fall short of meeting the demand for ever-increasing EV mileage, requiring LIBs with ever-increasing energy density. This energy density is determined by the cathode active material. The more redox potential of this material vs. Li^+/Li , the more energy density; thus, a lot of attention has been devoted to the study of cathode materials with a redox potential > 4 V.

The initial commercial success of $\text{LiNi}_{1/3}\text{Mn}_{1/3}\text{Co}_{1/3}\text{O}_2$ (NMC333) has been the motivation for continuous research on NMC-based cathodes. In these materials, Ni is the active element, as it can cycle between $\text{Ni}^{2+}/\text{Ni}^{3+}$ and $\text{Ni}^{3+}/\text{Ni}^{4+}$ redox couples. Mn and Co stabilize the layered structure. Therefore, research has been focused on ways to increase the Ni concentration at the expense of Mn and Co without compromising the layered structure

needed to the electrochemical performance. In this context, Ni-rich $\text{LiNi}_{1-x-y}\text{Co}_x\text{M}_y\text{O}_2$ (NMC, $1 - x - y \geq 0.5$, M = Mn or Al) are a promising choice for high-capacity and low-cost cathode materials [1,2]. They are already utilized in many electric vehicles [3], and many efforts are being made to improve their performance [4–8]. Another family of Ni-rich cathode elements is $\text{LiNi}_x\text{Co}_y\text{Al}_z\text{O}_2$ with $x \geq 0.8$ (NCA). NCA and NMC have related structures, very similar electrochemical behavior, and show similar performance. Both cells of the same size 21700 with NMC and NCA cathodes are available at a capacity of 5 Ah. The current commercial high-Ni cathode materials are $\text{LiNi}_{0.8}\text{Mn}_{0.1}\text{Co}_{0.1}\text{O}_2$ (NMC811) and $\text{LiNi}_{0.8}\text{Co}_{0.15}\text{Al}_{0.05}\text{O}_2$, i.e., materials with Ni concentration $x = 0.8$. However, compared to NCA, NMC811 possesses the advantages of lower capital and production cost (simple co-precipitation method without extra heat treatment process), higher energy density, and better thermal stability; thus, it has been the subject of particular attention [9,10].

Super Ni-rich cathode materials with higher Ni contents ($x \geq 0.85$) are currently under study [11]. Higher Ni concentrations, however, mean aggravated electrode–electrolyte interphase deterioration [12], microcrack formation [13], and surface rock-salt phase (NiO) formation, which is already a problem when $x = 0.8$ [14,15].

The increase in Ni concentration did increase the capacity, but the correlated decrease in the stability of the structure associated with the decrease in Co and Mn concentrations resulted in a large increase in the capacity fading and growth of impedance [16,17]. In general, NMC-based cathodes with more Mn content tend to possess better cycling stability [18,19], whereas NMC-based cathodes with more Ni content are incapable of reaching high cutoff voltages due to the lack of Mn^{4+} as a structure stabilizer [20].

The investigation of the thermal runaways of 18650 lithium-ion batteries shows that the safety issues of Ni-rich NMC and NCA are similar [21]. More precisely, NCA cells react faster than NMC cells above $1\text{ }^{\circ}\text{C min}^{-1}$ and, thus, reach thermal runaway a little earlier, but react slower than NMC cells below $1\text{ }^{\circ}\text{C min}^{-1}$ [22]. The high redox potential of Ni-rich cathode materials is also the cause for their poor thermal and structural stability. Ten years ago, Huggins already warned the community that the partial pressure of oxygen at equilibrium increases with voltage, which accelerates exothermic reactions and causes instability with oxygen release [23]. Therefore, the utilization of Ni-rich cathode elements is possible only if the material is modified to avoid oxygen release and improve safety, following processes that have been the subject of intensive research since then.

Many efforts have been made to find remedies to this drawback, which were reviewed [18,24–28], including cationic doping and coating of the particles [29–31], gradient layers and core–shell structuration [32], and electrolyte additives [33]. The studies have revealed that parasitic reactions [16], cation mixing (leading to restructured surface regions) [34], oxygen release to maintain the valence equilibrium upon surface transitioning from the layered to the spinel and finally the rock-salt structure of the surface layer [34–40], active material dissolution [41], the evolution of surface layers, and surface chemistries during cycling [29,42] are the primary factors responsible for cathode degradation. Higher energy density with Ni-rich cathodes issues from the higher operating voltage of the lithium battery. The gaseous oxygen released from the cathode will migrate to the anode side, where it will undertake exothermic reactions, eventually enhanced by thermal abuse, resulting in thermal runaway [43]. The main cause of thermal runaway is the chemical interactions between the cathode and both the anode and the liquid electrolyte [44]; thus, it is crucial to protect the surface of Ni-rich cathode elements, and/or utilize solid electrolytes. In addition, intergranular cracking can weaken connections between primary particles [18,45,46], and accelerate transition-metal (TM) ion dissolution and migration [47]. Moreover, the surface chemistry and bulk microstructure engage in a complex interplay closely linked to the electrochemical properties [48]. Over the years, different reviews

have reported the advances in the research on Ni-rich batteries. They include a discussion on the mitigation strategies and trade-offs, such as the selection of dopants or coating materials [49], and the design [50]. An analysis of surface modification techniques, analysis of the manufacturing process, and cost of the surface modification methods has been published few years ago [51].

In the present work, attention is focused on the progress that had been made recently to obtain batteries with Li-rich cathode materials with improved energy density and rate capability, without compromising safety, at the laboratory scale. For a report and discussion to bridge the technological gap between basic research on materials and industrial-scale fabrication, while controlling the cost-effectiveness in the process, we guide the reader to a recent review on the advances in multi-scale design and fabrications processes [52].

2. Goals and Issues

2.1. Why Decrease the Co Concentration?

The first motivation to reduce the use of cobalt is its scarcity, and thus its high cost [53]. The Democratic Republic of the Congo (DRC) accounts for 69% of global cobalt production. Russia ranks number two, but its production is ten times smaller than that of DRC [54,55], and the DRC has the world's largest reserves of cobalt ore. Refined cobalt products are centralized mainly in China, accounting for 67% of the world's refined battery-grade cobalt sulfate (CoSO_4) capacity in 2020. Other than China, only Finland has significant refining capacity for cobalt materials, accounting for only 10% of total supply in 2020 [56]. This concentration in a single country, both in production (DRC) and in refining (China), poses a political problem of energy independence to other countries. The United States has taken steps to increase domestic cobalt supplies with the announcement in 2022 of a USD 3 billion investment toward increasing domestic supplies of refined battery metals [57,58].

Another motivation to decrease the consumption of cobalt comes from its toxicity. Impacts of cobalt-bearing LIB chemistries on the environment are well-documented [59–64] and are greater than cobalt-free chemistries [65]. The results show that the refining process is the major contributor to global warming potential, freshwater ecotoxicity, and carcinogenic and noncarcinogenic emissions. This stems from the diesel fuel used in refining processes that also contributes to ozone depletion [53]. Moreover, mining contributes significant levels of particulate matter formation.

Due to the high cost and supply difficulties of cobalt, efforts have been made to reduce the concentration of cobalt in Ni-rich cathode materials [66,67]. Nevertheless, cobalt plays a critical role to ensure thermodynamic stability, so the continued use of cobalt in nickel-based EV batteries is predicted [68,69], even though continuous progress has been made to decrease its concentration [70–74]. Liu et al. demonstrated that the chemical and structural stability of the deep delithiated NMC cathodes are significantly dominated by Co rather than the widely reported Mn [75]. *Operando* synchrotron X-ray characterization coupled with *in situ* mass spectrometry reveals that the Co^{4+} reduces prior to the reduction of Ni^{4+} , which postpones the oxygen release and thermal failure. The results of these authors highlight the difficulty to guarantee the safe operation of Ni-rich/Co-free layered oxide cathode materials, even though Mn^{4+} can enhance the thermal/crystal stability in NMCs [76]. The role of Mn in the crystal stability, however, is controversial. Song et al. have recently revealed that the real origin of the stability of Co-free Ni-rich cathodes is Li/Ni intermixing rather than the traditional Mn stabilization mechanism [77].

The Ni-rich materials crystallize in the $R\bar{3}m$ structure. In this structure, Li/Ni intermixing, a problem we will discuss in the next section, is favored by the strong 180° interplane super-exchange interaction [70,78–81]. The introduction of the non-magnetic ion Co^{3+} in the TM layer reduces this super-exchange interaction, so that Co can efficiently

reduce the Li/Ni exchange [82]. For example, Co is still needed in NCA, where it not only reduces the Li/Ni mixing, but also increases the energy density; Co-free $\text{LiNi}_{0.95}\text{Al}_{0.05}\text{O}_2$ has an improved rate capability, but a smaller cycling ability [83], the reason for the doping with Al [84]. LiNiO_2 suffers from instability issues that plague the material. Some Co-free ultrahigh-Ni NMC cathodes including $\text{LiNi}_{0.90}\text{Mn}_{0.10}\text{O}_2$ [85], $\text{LiNi}_{0.90}\text{Mn}_{0.05}\text{Al}_{0.05}\text{O}_2$ [86], and $\text{LiNi}_{0.96}\text{Mg}_{0.02}\text{Mn}_{0.02}\text{O}_2$ [87], exhibit an improved cycle ability compared to the current commercial cathodes, but a lower capacity because the cutoff voltage is lowered. Due to the dissolution tendency of Mn, efforts are being made to obtain not only Co-free, but also Mn-free ultrahigh-Ni NMC cathodes, namely $\text{LiNi}_x\text{Fe}_y\text{Al}_z\text{O}_2$, [88] $\text{LiNi}_{0.96}\text{Mg}_{0.02}\text{Ti}_{0.02}\text{O}_2$ [89,90], $\text{LiNi}_{0.95}\text{Al}_{0.05}\text{O}_2$, and $\text{LiNi}_{0.95}\text{Mg}_{0.05}\text{O}_2$ [91]. All of them, however, suffer from a capacity penalty. On the other hand, Cui et al. have synthesized a $\text{LiNi}_{0.93}\text{Al}_{0.05}\text{Ti}_{0.01}\text{Mg}_{0.01}\text{O}_2$ (NATM) cathode that delivered a capacity of 221 mAh g^{-1} with a capacity retention of 82% after 800 deep cycles in pouch full cells [92]. This cathode exhibits superior electrochemical performance and improved thermal stability with respect to the Co-containing cathode $\text{LiNi}_{0.94}\text{Co}_{0.06}\text{O}_2$ and the NMC $\text{LiNi}_{0.90}\text{Mn}_{0.05}\text{Co}_{0.05}\text{O}_2$ cathode. Noteworthy, despite the absence of Co, this NATM shows a negligible degree of Ni/Li mixing.

The strategies that have been implemented to overcome these difficulties with Co-free cathode materials, and open questions that remain to be addressed were reviewed by Bianchini et al. [93], and more recently by Ge et al. [71].

2.2. Problems Limiting the Electrochemical Performance

2.2.1. Cation Mixing

The radii of Ni^{2+} (0.69 \AA) and Li^+ (0.76 \AA) are similar, so that Li^+ and Ni^{2+} can exchange positions in a delithiated state through Ni^{2+} diffusion to the octahedral sites of Li^+ . This antisite defect can lower spacing between atomic layers in the lattice of the NMC-based cathodes, hinder Li^+ movement, and reduce the amount of active Ni and Li. This antisite defect and its negative effect on the electrochemical performance have been extensively studied a long time ago for NMC333, and the problem is the same in the Ni-rich NMCs. In this later case, Cui et al. have shown that this defect is predominantly observed at the surface of the particles [94], where it creates a Li^+ diffusion bottleneck [95]. As a result, the rate capability is reduced. The antisite defect also presumably plays a role in the irreversibility in the first cycle, which is related to the irreversibility of the Ni charge state [96] and irreversible O₃/H1-3 phase transition [97]. In Ni-rich NMC, Mn⁴⁺ can partially be replaced by Ni, which increases the valence of Ni and therefore lowers the possibility of Ni atoms migrating to 3a sites [17]. Nevertheless, Ni²⁺ migration still occurs. The origin and the migration of Ni is well-known and well-documented [98]. The gradual growth of Li vacancies with increasing state of charge leads to easier migration. Moreover, in the high charge voltage, oxygen vacancies are generated, favoring a large Ni migration. Therefore, the tendency of Li/Ni mixing is more severe and frequent with increasing charge state and operating voltage. Using operando neutron diffraction measurements, Wu et al. showed that Li–O–Li configurations resulting from the Li–Ni antisite defect can increase anionic redox activity and promote Ni migrations, particularly at high voltages [99]. Nevertheless, the degradation of electrochemical performance of Ni-rich cathode materials under overcharging conditions primarily originates from the collapse of the cathode material, the precipitation of oxygen, which mainly occurs on the surface of the primary particles, and the formation of voids in the grain boundary region [100].

2.2.2. Phase Stability

Cation mixing can also induce a transition to disordered spinel structure (*Fd3m*) when LIBs are charged to high voltages (4.8 V) [101–104]. Spinel phases can also be formed

on charged cathodes stored at 90 °C for a week [105]. Investigations on NMC revealed that long term cycling can result in phase changes to an *Fm3m* structure (cubic rock-salt phase) consisting of Ni²⁺, Mn²⁺, and Co²⁺ [102,106], an effect also observed with NCA cathodes [107]. This phase transition is accompanied with a release of O₂ into the cell, which can react with electrolytes to generate CO₂ and increase the interfacial resistance of the cell [108]. NMC811 cathodes pretreated with ramping to 4.5 V limited the growth of the rock-salt layer in subsequent cycles by isolating the surface of NMC particles [109].

2.2.3. Oxygen Release

Oxygen release is a significant cause of degradation of the Ni-rich cathodes [110,111]. The mechanisms of the oxygen release of the Ni-rich materials are well-documented [112]. This release essentially results from the change of the TM-O bond from ionic to more covalent character induced by Li⁺ extraction, due to the removal of electrons to maintain charge neutrality. In particular, this effect has been clearly evidenced in NCA [113]. This oxygen release results in a destabilization of the layered structure, which is aggravated in highly delithiated states, and increases with Ni concentration [114]. Therefore, in practice, the voltage of the batteries with pristine NMC811 is limited at 4.2 V [34]. Moreover, the oxygen release results in a thermal instability and safety concern [115]. In addition, the thermal stability is impacted by chemical reactions with the electrolyte. This is illustrated in Figure 1 for the case of NMC84 (LiNi_{0.84}Co_{0.11}Mn_{0.05}O₂) charged at 4.3 V in the commonly used carbonate electrolyte with LiPF₆ salt (LB301).

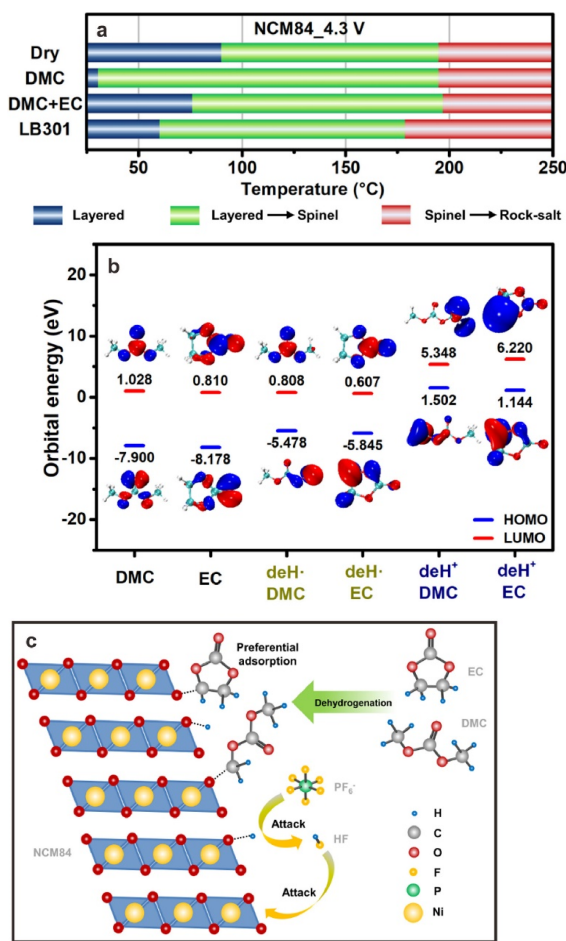


Figure 1. Temperature regions of different thermal decomposition stages of NCM84_4.3 V samples in different electrolyte components (a). Molecular orbital energy levels of carbonate molecules and their dehydrogenation products (b). Schematic diagram of near-surface structural thermal stability modulated by electrolyte components (c). Reproduced from ref. [114]. Copyright 2022 Elsevier.

The onset temperature of thermal decomposition is already reduced by the carbonates, in particular dimethyl carbonate (DMC), and further reduced by the introduction of LiPF₆. Furthermore, the outward migration of oxygen is accompanied with an outward migration of Ni. This process of Ni and O co-migration along (003) planes was observed, for example, in NMC811 [116]. This continuous advance of the surface degradation layer toward the particle interior results in an increase of the thickness of the surface inactive rock-salt phase layer, leading to a rapid degradation of the electrochemical properties [15]. In addition, during the delithiation process, the outward diffusion of Li⁺ generates a concentration gradient and vacancies in the layered structure [117]. The smaller variation of the lattice in the Li-rich (vacancy-poor) domains along the *c*-axis direction than in Li-poor (vacancy-rich) domains results in an anisotropic lattice contraction that may induce microcrack formation at grain boundaries [9,118].

2.2.4. Modifications During Cycling

NMC oxide possesses a *R̄3m* structure (rhombohedral symmetry) with a Li-layer on the 3a site, an NMC layer on the 3b site and an oxygen layer on the 6c site [16]. X-ray measurements and infrared spectroscopy reveal the deformation of the lattice during cycling [16,119,120]. The *c*-axis parameter expands during charging, due to the repulsive force generated from MO₆ slabs, which are positively charged, whereas the *a*-parameter is reduced because the radii of the transition metal ions are reduced by the loss of electrons [121] and the increase of their valences [122]. The *a*-axis of the Ni-rich cathode material remains constant at potentials exceeding 4.3 V, and the steep drop of the *c*-axis occurs at potentials exceeding 4.2 V, becoming steeper as the Ni content increases [16,120,123,124]. This drop is due to the fact that the repulsion between O²⁻ layers decreases with more covalent M–O bonding at higher delithiated states [125,126]. Two processes are involved in the delithiation of Ni-rich NMC-based cathodes. Until a certain degree of delithiation, Li can exit through oxygen dumbbell hopping, while at higher degree of delithiation, Li can exit through tetrahedral site hopping [127,128].

During cycling, Ni²⁺/Ni⁴⁺ mainly reacts in the low-voltage region and Co³⁺/Co⁴⁺ mainly reacts in the high-voltage region. As Li⁺ is removed from the Li slab during charging, the Ni-rich cathode undergoes the successive phase transitions H1-M-H2-H3, due to change in the repulsive force in O-Li-O caused by local structural distortion [129]. The H2–H3 phase transition is the most problematic for the electrochemical performance, because it is accompanied with an evolution of oxygen in the lattice and large volume changes. These changes can cause microcracks in the cathode active material, an additional exposure of the cathode active material surface to the electrolyte [130]. Both effects result in reduced cycle ability [131], and rate capability [132] (see Figure 2). This problem is particularly important in Ni-rich cathode materials as the onset potential corresponding to the H2–H3 phase transition decreases when the Ni concentration decreases, from 4.6 V vs. Li⁺/Li in NMC111, to 4.2 V in NMC811. While we have explained in a previous section (Section 2.1) the current efforts to reduce the cobalt concentration, it should also be mentioned that cobalt has also adverse effects. The addition of Co to Ni-rich layered structure can cause a more serious H2–H3 phase transition when charging and discharging between 2.8 and 4.5 V [72,133]. Moreover, the structural instability of the Ni-rich cathode materials is strongly correlated with the cell gas release in a charged state. That is why, even though adequate strategy (coating, doping) reviewed hereunder is efficient to reduce the instability, the practical voltage for charging is limited to 4.5 V [134], inasmuch as at such a high potential, the formation of Ni/Li antisite is unavoidable. The main attention on the Ni-rich cathodes these recent years has thus been focused on the study of these degradation mechanics and the solutions to avoid them [135–138]. Otherwise, *operando* X-ray diffraction

(XRD) and scanning electron microscopy (SEM) results indicated that particle fracture from increased structural distortions at >4.3 V was a contributor to capacity fade [139].

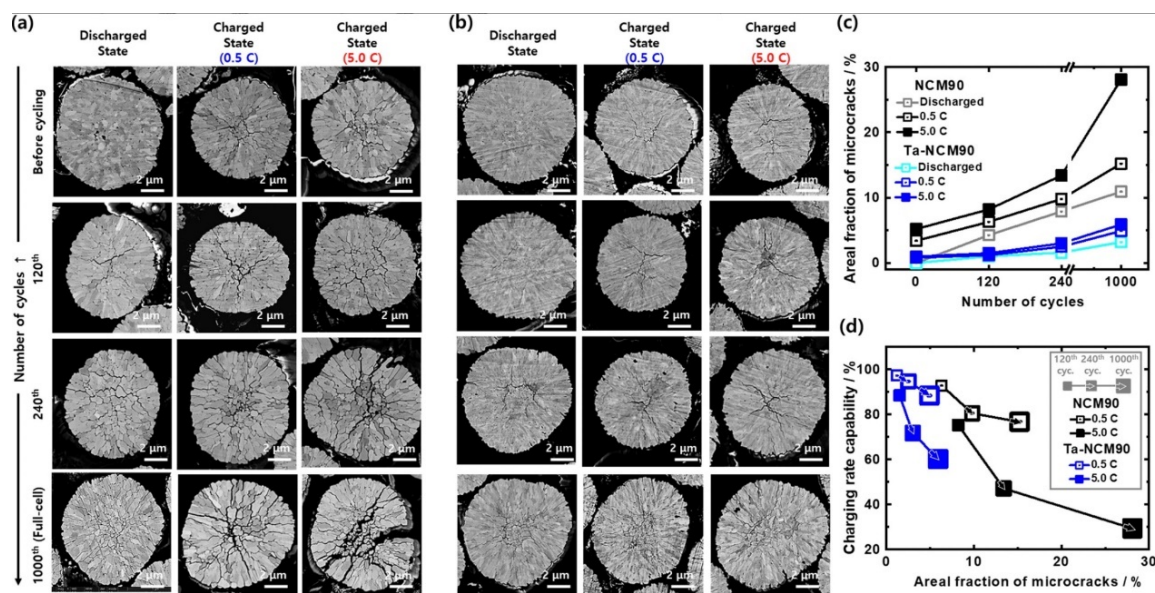


Figure 2. Cross-sectional SEM images of the (a) NCM90 and (b) Ta-doped NCM90 cathodes at fully discharged (2.7 V) or charged state (4.3 V, at 0.5 or 5.0 C) depending on number of cycles. (c) Areal fraction of microcracks in cathodes plotted against number of cycles. (d) Charging rate capability of cathodes with respect to areal fraction of microcracks at 120th, 240th, and 1000th cycles. Reproduced from ref. [132]. Copyright 2024 Wiley.

2.2.5. Microcracks

The capacity degradation of Ni-rich NMC is not only due to surface chemical instability, but also to mechanical destruction in the form of microcracks [15,140–143]. The H2 → H3 transition is not the only source of microcracks. As a matter of fact, different sources of cracking may affect Ni-rich cathode materials: intragranular cracking may occur under the effect of cation mixing [15], while the H2–H3 phase transition is mainly responsible for intergranular cracking. In addition, the antisite defect can also be formed during cycling, and cause a structural transition from rom the layered phase to the spinel-like phase [144], so that both the rate capability and the cycle ability are reduced. In addition, the cracking exposes fresh surfaces to the electrolyte, and thus reduces the efficacy of protective surface. It is thus crucial to avoid the cracking of the particles, which has been the subject of intensive research.

The cracking process is initiated by the anisotropic volume change in primary particles and lattice strain, which provokes the mechanical destruction of secondary particles [145–147]. Differences in the lattice volume of domains with different Li⁺ concentrations inside a primary particle induce the localization of stress between the domains, which is likely to create intraparticle microcracks along (003) planes [148–151]. These effects explain that microcracks are generated by the inhomogeneous distribution of Li, so that their formation depends on the state of charge of the cathode [152]. Note that we consider here electrochemical crack formation that occurs mainly at high state-of-charge (SOC) levels. Another mechanism of chemical crack formation has been recently evidenced at low SOC levels, driven by chemical corrosion [153], but this phenomenon is observed at high temperature (~60 °C). The inhomogeneity of the lithium distribution during cycling has been observed in NMCs by operando optical microscopy [154]. The evolution of the stress associated with the anisotropic Li distribution has been studied as a function of the state of charge in different works [155–157]. Combined with lattice strain, the anisotropic

volume change results in both intergranular and intragranular cracking [158–162]. When the Ni concentration is ≤ 0.6 , only one phase transition $H1 \leftrightarrow M$ phase is observed upon cycling [34,163]. Unfortunately, the cracking effects are more important in Ni-rich NMC at Ni concentration $x \geq 0.8$, since the structural phase transitions are more severe [164]. During the first charge–discharge cycle, a series of phase transition processes increase interlayer spacing, including $H1-M$ and $M-H2$ transitions, followed by a shrinking of the interlayer spacing during the $H2-H3$ phase transition process, which is most damageable to the integrity of the particles [129,164–166]. The local stress distribution associated with the anisotropic lattice contraction responsible for the structural instability caused by the $H2-H3$ transition in the deeply charged state can be overcome by the synthesis of single-crystal Ni-rich cathode elements [167,168]. Consequently, monocrystalline NMCs demonstrate a significantly better cycling ability than polycrystalline NMCs [169]. Even the morphology of the precursors matters. Liang et al. demonstrated that the spheroidization of the precursor can enhance uniformity in structural evolution during solid-phase lithiation [170] (see Figure 3). The resulting $LiNi_{0.92}Co_{0.04}Mn_{0.04}O_2$ cathode material delivered a capacity of 234.2 mAh g^{-1} , in the range of $2.7\text{--}4.3\text{ V}$, with capacity retention of 89.3% after 200 cycles at 0.5 C . Ni-rich cathode materials with different morphology structures obtained by adjusting the ratio of solvent and water in the solvothermal process [4]. This work illustrates the impact of different morphologies on the electrochemical properties. Coating is also a pertinent strategy, because the surface of Ni-rich materials free from electrolyte attack undergo limited structural degradation [171]. Morphologies of the primary particles of Co-containing $Li[Ni_xCo_y(Al\text{ or }Mn)_{1-x-y}]O_2$ cathodes can be engineered to optimize the electrochemical properties [172,173]. For example, ultrafine-grained structures in the $Li[Ni_{0.95}Co_{0.04}Mo_{0.01}]O_2$ cathode provided paths deterring the propagation of intergranular cracks, allowing for high-capacity retention and fast-charging capability [173].

Wang et al. introduced a coherent perovskite phase into the layered structure functioning as a ‘rivet’, which significantly mitigates the pernicious structural evolutions by a pinning effect. The resulting enhanced mechanochemical stability was attributed to the presence of significant energy barriers for phase transitions within the rivet phase, similar to a pinning effect [174]. The gas release pattern and stress distribution of NCM particles can be governed by the microstructure engineering [175]. In particular, the strain between the grains in the NMC811 secondary particle can be dissipated by radially aligned grains near the particle surface. However, the mismatched strain between disoriented primary grains in the interior of the particle leads to the development of microcracks in the central region of the NMC811 secondary particle [147]. The electrolyte penetrates in the interior of the particles via these microcracks, resulting in the formation of LiO rock-salt phase that reduces the Li^+ interfacial resistance [176]. On the other hand, the electrolyte infiltration shortens the Li^+ diffusion distance [177]. As a result of the balance between these two effects, the Li^+ diffusion kinetics has been found accelerated in polycrystalline cathodes with respect to single-crystal cathodes without grain boundaries [178]. In addition, typical structural defects of primary particles such as twin boundaries [179], dislocations [180], or even Li^+/Ni^{2+} anti-site defects [181] serve as preferred sites for the nucleation and propagation of intragranular microcracks. In single-crystallized particles, the tensile stress triggers gliding along the (003) plane. This effect has been observed by through aberration-corrected scanning transmission electron microscopy (STEM) and analyzes by theoretical calculations [182]. These planar gliding processes corresponds to the in-plane migration of Ni ions, the barrier energy of which is reduced in presence of oxygen vacancies [183]. Since these processes are not entirely reversible, they also lead to microcracking along the (003) plane in single-crystallized particles. However, Sun et al. showed that the destructive volume change and $H3$ phase formation presented in polycrystals are effectively suppressed

in single-crystals when cycling at a high cut-off voltage of 4.6 V [184]. This feature clarifies the origin of high-voltage stability in single-crystal cathode, but also the improved cycle ability with respect to polycrystals.

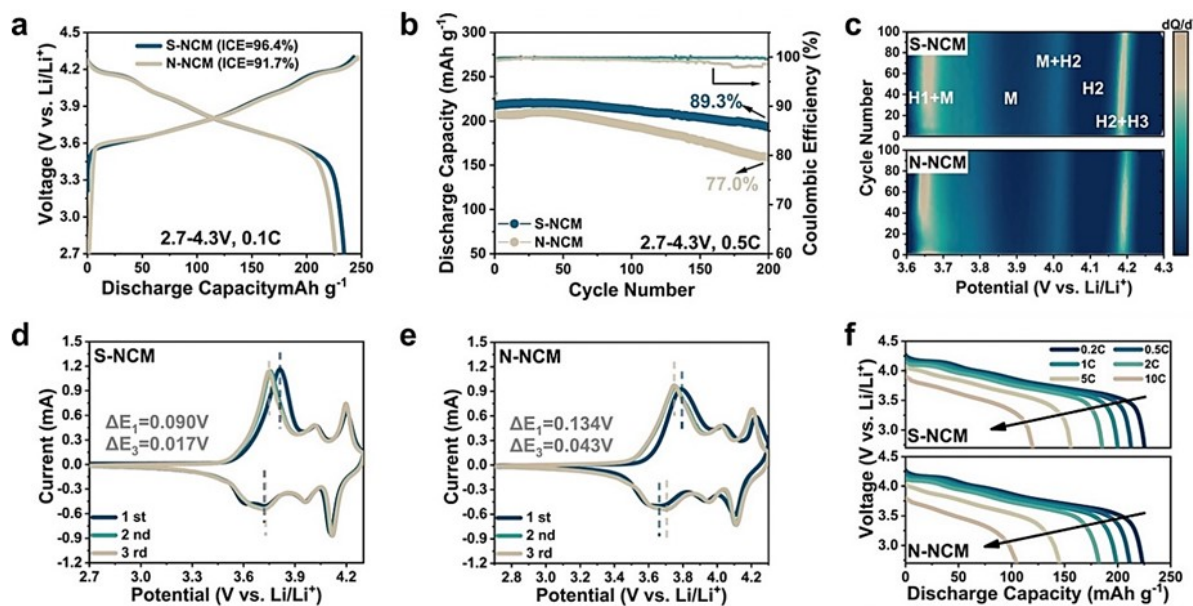


Figure 3. Electrochemical characterization of coin-cells at 25 °C with $\text{LiNi}_{0.92}\text{Co}_{0.04}\text{Mn}_{0.04}\text{O}_2$ cathode materials derived from spherical precursors (S-NCM) and non-spherical precursors (N-NCM). (a) Initial charge–discharge voltage profiles of S-NCM and N-NCM. (b) Cycling stability of half-cells for S-NCM and N-NCM versus Li^+/Li between 2.7 and 4.3 V at 0.5 C. (c) dQ/dV curves of S-NCM and N-NCM at charge process determined from every five cycles. CV profiles of the S-NCM (d) and the N-NCM (e) at the 1st, 2nd, and 3rd cycles. (f) Discharge profiles of S-NCM and N-NCM at different rates. Reproduced from ref. [170]. Copyright 2024 Wiley.

3. Synthesis Methods

A review on the synthesis process has been recently published [185]. Different synthesis routes give good results, including hydrothermal process [186–188], sol–gel process [189,190], and solid-state process [190,191]. The sol–gel method offers some advantages. In particular, Zheng et al. successfully synthesized single-crystal Ni-rich cathode materials via a two-step solid-state method [192], but the preparation and refinement of raw ingredients required is still difficult. That is why the co-precipitated method is widely used for the current commercial synthesis of NMC Ni-rich materials by stirring and mixing the stoichiometric ratio of transition metal salt solutions to form homogeneous precursors [193]. Among various synthetic methods for NMC materials mentioned above, the co-precipitation method is the recognized as one of the most effective processes for preparing Ni-rich cathode materials with the best electrochemical performance [194,195]. This method, however, is difficult to use for NCA because Al^{3+} ions have a propensity to form double hydroxides in solution. Therefore, alternative solutions have been adopted for NCA, namely the hydrothermal method, which is complicated and not cheap, or the solid-state method, which has been reviewed by Wang et al. [196]. However, a recent comparison of the electrochemical properties of $\text{LiNi}_{0.8}\text{Mn}_{0.15}\text{Al}_{0.05}\text{O}_2$ prepared by coprecipitation and sol–gel methods highlights the superior crystallinity, particle uniformity, and compositional accuracy of coprecipitation, making it more effective for enhancing electrochemical stability and efficiency, despite the presence of Al [197]. The common and commercialized method is to prepare precursors via co-precipitation first, and then subject it to high temperature calcination with lithium salt together. Efforts have been made to

optimize the synthesis parameters [198], including the calcination temperature [199,200], lithium source type [201,202], and calcination atmosphere [203].

The influence of the precursors on the electrochemical performances of Ni-rich layered oxides has been discussed by several workers. Cui et al. [94] investigated the effect of cationic uniformity in the precursors on Li/Ni mixing of Ni-rich layered cathodes. The cationic uniformity in precursors is regulated by the sol-gel and solvothermal method. All cations in the precursors obtained by the sol-gel method mix uniformly at a molecular scale, while the solvothermal method with a post-addition of Li salts causes a heterogeneous mixture between Li and transition-metal ions. Therefore, advanced Ni-rich layered cathodes should simultaneously possess low Li/Ni mixing and reversible H₂-H₃ transition.

The conventional precursor for the synthesis of NMC materials is $\text{Ni}_{1-x-y}\text{Co}_x\text{M}_y(\text{OH})_2$ particles, prepared by co-precipitation in a mechanically stirred tank reactor, under conditions that lead to a homogeneous elemental distribution [204–208]. This is considered as the most viable option for large-scale production [209–212]. The effects of the β -($\text{Ni}_{0.6}\text{Mn}_{0.2}\text{Co}_{0.2}$)(OH)₂ content in hydroxide precursor on the structure and electrochemical performance of NCM622 cathode materials were investigated by Xu et al. [210]. The cathode material sintered from the mixed phase of α -($\text{Ni}_{0.6}\text{Mn}_{0.2}\text{Co}_{0.2}$)(OH)₂ and β -($\text{Ni}_{0.6}\text{Mn}_{0.2}\text{Co}_{0.2}$)(OH)₂ shows the highest discharge capacity of 192 mAh g⁻¹ and best rate performance.

The microstructures of $\text{Ni}_{1-x-y}\text{Co}_x\text{M}_y(\text{OH})_2$ particles are crucial to obtain Ni-rich cathodes with the best electrochemical properties, and many works have been devoted to optimize them, reviewed in [195]. These microstructures depend on various factors, including the pH value [213–215], ammonia concentration [216,217] (see Figure 4), reaction temperature [218], reaction time [219], and stirring rate [220]. Depending on these different parameters, different morphologies of the precursor particles are obtained, including microspheres [160,221,222], rods [223–225], and hollow spheres [189]. Among them, the spherical $\text{Ni}_{1-x-y}\text{Co}_x\text{M}_y(\text{OH})_2$ particles form spherical $\text{LiNi}_{1-x-y}\text{Co}_x\text{M}_y\text{O}_2$ after lithiation, a shape that forms a more tightly packed structure during battery manufacturing. As a result, the volume energy density is increased, and the Li^+ ion migration is facilitated [226,227].

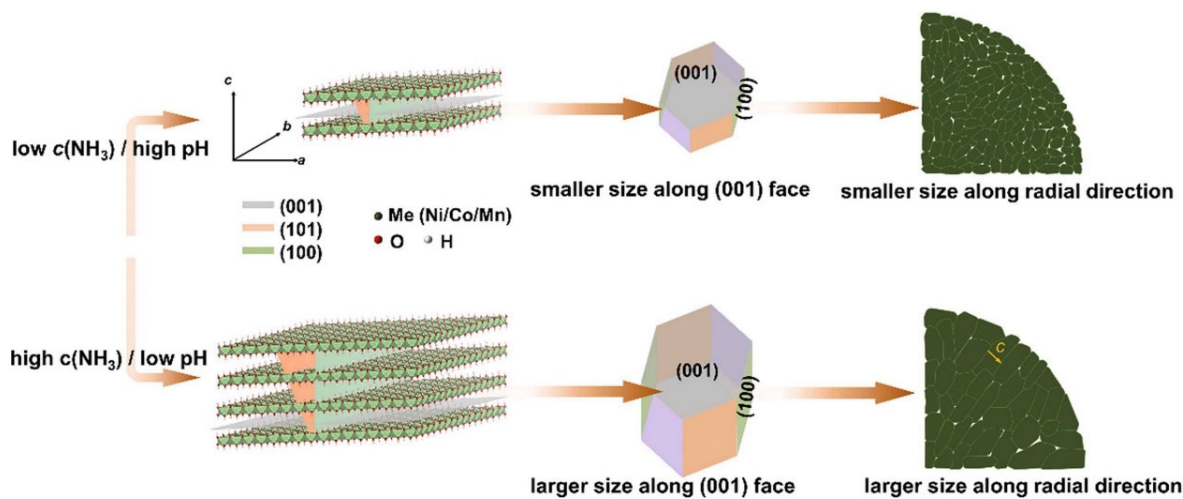


Figure 4. Schematic illustration of growth of grains synthesized at different pH at different ammonia concentration in precipitation process. High ammonia concentration induces crystal growth along the direction perpendicular to [001] and the direction parallel to [001]. With the maximized face along the (001) crystal face and proper size along the (100) crystal face, a precursor with radially ordered structure is easily formed. Reproduced from ref. [224]. Copyright 2024 Elsevier.

These examples illustrate that the morphology of the particles is important. In particular, the role of ammonia concentration in determining the particle shape and size of

Ni-rich cathode materials during co-precipitation has been recently deciphered by Zhang et al. Moreover, they showed that ammonia concentration affects the thickness-to-length ratio of the precursor's primary particles, which in turn influences the morphology of the $\text{LiNi}_{0.95}\text{Al}_{0.05}\text{O}_2$ cathode materials during lithiation [228]. Lower NH_4OH /metal ratios produce more porous precursors, which enhance Li-source diffusion and promote uniform sintering [229]. Pristine NMC811 nano-cubic microstructure is successfully synthesized via a rapid precipitation assisted with hydrothermal treatment, which maintains a high capacity ($188.2 \text{ mAh}\cdot\text{g}^{-1}$) with a retention of 87.2% at 1 C after 200 cycles, a remarkable result that shows how important the synthesis of nano-sized and single crystallized particles is [230]. We will return to morphology aspects later in this review, when they are monitored by doping, for example.

The lithiation process consists in the calcination of $\text{Ni}_{1-x-y}\text{Co}_x\text{M}_y(\text{OH})_2$ with a lithium source (Li_2CO_3 or LiOH) at high temperature and in an oxygen atmosphere [95,231–234]. New synthesis processes have recently emerged, such as the synthesis of Ni-rich gradient material by Taylor–Couette cylindrical reactor [235], and the synthesis of single-crystallized samples by microfluidic co-precipitation [236]. The lithium salt used as a precursor is usually Li_2CO_3 or $\text{LiOH}\cdot\text{H}_2\text{O}$. Li_2CO_3 has lower corrosion, and it is suitable for NCM523 and NCM622. Unlike these, preparation of NMC811 should be calcined under the oxygen atmosphere and lower temperature, so the more reactive $\text{LiOH}\cdot\text{H}_2\text{O}$ is the best option. Oxygen partial pressure during the calcination process is also an important parameter [50,237].

The sintering temperature is a crucial parameter. A too-small sintering temperature fails to provide enough energy for the decomposition of the precursors. The high sintering temperature is needed to obtain a good crystallinity, which is essential to the electrochemical performance of the cathode material. However, the high sintering temperature has two negative effects. First, as Li is volatile, some Li evaporates. This problem can be solved by the addition of excess Li during the high-temperature calcination process, which must be adjusted to obtain a stoichiometric final product [238,239]. The consequence is an excess of lithium at the surface. However, a dry cobalt hydroxide coating effectively removes the residual lithium, as shown by Kim et al. in the particular case of NMC91 [240]. The second drawback is more challenging; this high temperature makes almost inevitable the cation mixing between Ni and Li [241], which is detrimental to the electrochemical performance. In practice, above 780°C , the cationic mixed degree increases [242]. Therefore, 750°C is the best calcination temperature for NMC811 [243]. However, the synthesis temperature of single-crystal structures is usually about 100°C higher than that of polycrystals [244], implying more severe Li/Ni cationic disorder in single-crystal structures than in polycrystalline structures [245,246]. Post-process (i.e., heat-treatment after washing) is commonly used, as it improves the cycle life of Ni-rich materials [247].

To minimize Ni^{2+} migration, researchers also reported that mitigation methods can be used to modify cathodes [243]. Luo et al. have recently reported an ion-exchange method to prepare Ni-rich layered oxide materials, consisting in the choice of sodium-based layered oxides as precursors, for ion exchange with Li^+ ion in lithium molten salts [36]. The reaction temperature in this process is reduced to 300°C . However, additional heat treatment at 700°C was essential for obtaining well-ordered layered structure. Nevertheless, Ni-rich cathodes synthesized by sodium-to-lithium-ion exchange are devoid of $\text{Ni}\cdot\text{Li}$ antisite defects [248]. In a different approach, Wang et al. reported that the Li/Ni disorder can be facilely tuned through post-synthesis annealing [249]. Recently, Mo et al. adopted a certain amount of H_2O_2 to treat the precursor of spherical $\text{Ni}_{0.8}\text{Co}_{0.1}\text{Mn}_{0.1}(\text{OH})_2$. The H_2O_2 pre-oxidation reduced $\text{Li}^+/\text{Ni}^{2+}$ mixing to below 0.34%, extending the capacity retention of NMC811 to 98.5% over 100 cycles [250]. However, this does not exempt us from using

the usual means to reinforce the structural and thermal stability of these materials, such as doping or coating.

These results illustrate the major influence of the precursors on the electrochemical properties. The shape, size distribution, and primary/secondary particle structure of the hydroxide precursors directly translate to the final cathode material, strongly affecting Li-ion diffusion and electrode kinetics. Co-precipitation parameters (pH, temperature, stirring, ammonia feed rate) are crucial—altering them changes nucleation and growth, which in turn impacts particle uniformity and tap density. Solid vs. polycrystalline vs. single-crystal morphologies in precursors yields cathodes with starkly different cycling stability and crack resistance. The precursor's crystallinity and defect landscape steer the final oxide's structural integrity. Poor crystallinity can promote lithium–nickel mixing, which undermines capacity and cycle life. As we shall see in the next section, incorporating dopants or surface modifiers during precursor formation—like tungsten (W), Al, or rare-earth ions—can significantly enhance cycle life, mitigate microcracking, and stabilize surface layers.

3.1. Single Crystals Versus Polycrystals

Many works demonstrated that polycrystals have a significantly weaker structural stability than single crystallized Ni-rich particles [178,192,251]. This explains that many efforts have been made to synthesize single-crystallized Ni-rich particles, reviewed in [252]. In particular, Liu et al. reported that heavily cycled commercial-grade pouch cells with NMC811 cathodes showed very little microcracking when single particles are employed [253]. Through comparative experiments, Kong et al. found that single-crystal NMC811 particles have better storage performance than their polycrystalline counterparts [254]. They also demonstrated that the concentration of impurities generated on single-crystal materials is also significantly less, and the electrochemical performance can be better maintained. Lüther et al. studied the electrochemical properties of single- and poly-crystallized NMC811 synthesized with comparable bulk and surface characteristics from identical self-synthesized precursors. This study also demonstrated the superiority of single-crystallized particles [255]. Qian et al. showed that single-crystal NMC622 particles exhibited remarkable cycling stability, and retained ~94% of the initial capacity after 300 cycles at 1 C rate (from 161 to 151 mAh g⁻¹), significantly higher than that of the polycrystalline NMC622 under the same condition (~52%, from 155 to 82 mAh g⁻¹). This result was attributed to the limitation of the Li-ion transport across neighboring primary grains in poly-crystallized particles, as these grains are not perfectly aligned, while there is no such misalignment effect in single-crystal particles [256]. Fan et al. also reported that single-crystallization of LiNi_{0.83}Co_{0.11}Mn_{0.06}O₂ particles mitigate undesired side interactions and significantly prevent the generation of intergranular cracks, to achieve a capacity retention of 84.8% at 45 °C after 600 cycles at a current rate of 1 C [257]. For the same reason, in full cells between 3.00 V and 4.35 V, LiNi_{0.83}Co_{0.10}Mn_{0.07}O₂ delivers a reversible capacity of 167.0 mAh g⁻¹ with capacity retention of 84.8% after 400 cycles at 0.5 C/25 °C, far larger than 107.7 mAh g⁻¹ and 54.1% of conventional polycrystalline LiNi_{0.83}Co_{0.10}Mn_{0.07}O₂ [258]. Still, these results can be improved by appropriate interfacial modification. Examples with single-crystal NMC811 are the *in situ* planting of an electrolyte film-forming additive on a single-crystal NMC811 surface by consuming the residual lithium to develop a functional Al(Li)BOB nano-layer [259], and surface spinel-phase modification [260]. On the other hand, Ge et al. reported sluggish kinetics in single-crystals governed by ionic transport at low state of charge, which, however, can be alleviated through synergistic interaction with polycrystals integrated into a same electrode [261].

Therefore, the single crystallization is an important path to avoid cracking and ensure that high-nickel cathode materials have both high energy density and long cycling stability [262–264]. This is clearly evidenced, for instance, in the work of Zhao et al. [265] on NMC622. Within *operando* X-ray imaging, spectroscopic technologies, and diffraction methods, Zhang et al. observed that phase transitions from homogeneity to heterogeneity during cycling induce particle crack formations at the surface, and play a dominant role in the structural robustness of single crystals. They also demonstrated that using a lithium source to replenish lattice sites during re-calcination under oxygen flow and high-temperatures (denoted as t-NCM) can induce homogeneous phase distribution, enhancing the capacity retention [266]. In addition, Hu et al. found that at high potentials, the amount of oxygen gas released in single-crystalline Ni-rich cathode materials is significantly lower than in polycrystalline cathode materials [267]. With NMC cathodes, single crystallization avoids cracking during cycling, but only when the Ni content does not exceed 90% [150]. Also, the study of cobalt-free polycrystalline (PC) and single-crystalline (SC) $\text{LiNi}_{0.9}\text{Mn}_{0.1}\text{O}_2$ showed that the PC material has lower $\text{Li}^+/\text{Ni}^{2+}$ mixing and a faster Li ion diffusion rate. As a consequence, intergranular cracking, surface pulverization, disorder phase transition, and interfacial side reactions were suppressed in the PC material but not in the SC material [167]. These two last results show that a Ni content greater than 90% is a bottleneck in improving the energy density and cycling performance of high-nickel single-crystal materials [78,268]. On the other hand, the study of single-crystallized and poly-crystallized $\text{LiNi}_{0.76}\text{Mn}_{0.14}\text{Co}_{0.1}\text{O}_2$ cathode materials evidenced that the gas evolution of single crystals is much lower than that of polycrystals even at high voltage potentials [267]. Therefore, the single crystallization of Ni-rich cathode materials is also important to solve the safety issues of these batteries. Single-crystal NMC811 demonstrated 98% capacity retention with no cracking after 1100 cycles [253]. Huang et al. [269] prepared single-crystal $\text{Li}(\text{Ni}_{0.9}\text{Co}_{0.05}\text{Mn}_{0.05})\text{O}_2$, in which an extra pulse high-temperature sintering at 1040 °C for 1 min is added in the traditional calcination process at 750 °C, which increased the tap density by 1/3 to 2.76 g cm^{-3} and suppressed the microcracks, improving both the cycling performance and thermal stability. High-temperature sintering is the most effective synthesis strategy for single-crystal materials, but a sintering temperature exceeding 830 °C can lead to undesirable outcomes, such as Li/Ni mixing and surface reconstruction of the cathode particles. The work of Huang et al. shows that this drawback can be avoided by reducing to the pulse-level the time during which higher sintering temperature is applied. In addition, high tap densities are obtained with small particles, more prone to failure during the cycling process. The work of Huang et al. also demonstrates a way to balance the tap density of the material with the selective failure of smaller particles, without the need of incorporating a mixture of polycrystalline and monocrystalline particles proposed by Li et al. [270]. In addition, the orientation of the crystals matters. For example, CeO_2 with well-oriented (011) facets have a shorter linear Li^+ migration path and higher electron conductivity, so that they perform better when coated on NMC811 than the (124) and (311) orientations [271]. Single-crystalline-based electrodes show significantly improved cycling ability because the smaller size of the particles result in a more uniform current distribution in the cathode, whereas in the case of polycrystalline electrodes, inert dead zones are caused by large microcracks [272]. The single-crystal architecture can effectively retard the layered to spinel and rock-salt phase transition and mitigate the crack formation [273]. The comparison of polycrystalline and single-crystal cathodes has been reviewed [274–276], and demonstrates that the single-crystallization is one of the most prospective routes for the modification of Ni-rich layered cathodes, in particular when the synthesis parameters are chosen to obtain particles with optimum micro-size [277]. The main drawback is the lower redox kinetics of the single-crystal cathodes. The Ni^{3+} oxidizes

to Ni⁴⁺ all over the course of delithiation in polycrystals, but only at the end of delithiation in single crystals [261]. The sluggish redox kinetics at low state of charge leads to an abrupt reduction in Li⁺ diffusivity, responsible for responsible for the low Coulombic efficiency and poor rate capability of single-crystal cathodes [9,150]. On the other hand, the single-crystal cathodes are more resistant to mechanical damage during calendar aging [278]. Since the oxygen release occurs mainly near the surface, the small surface area of single crystals significantly limits the activation of oxygen vacancies, which not only improves the electrochemical properties, but also enhances thermal stability. This has been evidenced in NMC811 [279,280]. Single crystals give bigger particles than polycrystals, which tends to give cathodes delivering a capacity slightly smaller than their polycrystalline counterparts, but this drawback can be easily overcome by doping [281].

3.2. Synthesis of Single Crystals

Single crystals have a clear advantage to improve the electrochemical properties, but their synthesis is complex and expensive [282]. Recently, the difficulty has been circumvented by using a facile ball-milling method to transform pristine micron-sized polycrystalline NCM particles into submicron pseudo-single-crystal particles [283]. The co-precipitation method is widely used to prepare the precursors for both the polycrystals and the single crystals. In addition, the spray-drying method is of interest for the synthesis of the precursors for single crystals, because the porous precursor caused by solvent volatilization is conducive to the fusion and growth of grains, allowing for the synthesis of single crystals at a lower operating temperature (e.g., 750 °C) [284]. In addition, pores inside Ni-rich cathode materials can effectively reduce stress accumulation caused by anisotropic lattice expansion and shrinkage, and decrease the generation of microcracks [285]. Indeed, the synergetic effects of porosity and radial structure significantly improve the electrochemical performance of Ni-rich cathode materials [286]. Precursors with larger specific surface area exhibit smaller pore size, ensuring the better wettability and enhanced capillarity for homogeneous lithiation reaction [287]. The generation of meso- and macropores can be alleviated by controlling the homogeneity of the synthetic reaction [288]. At present, the sintering processes for single-crystal cathode materials include continuous high-temperature sintering, pulse high-temperature sintering, and molten-salt sintering [289–291] (see Figure 5). For high-temperature synthesis, higher calcinating temperature is required, bringing aggravated particle agglomeration and Li/Ni mixing. On the other hand, the low synthesis temperature used in the synthesis of polycrystals is damageable to the mechanical properties. As a consequence, the particles on the upper layer of the electrode may be damaged by the pressure applied during the manufacturing [292]. This destruction of the polycrystalline particles during the calendaring process in the manufacturing of the cathode was also observed by Raman spectroscopy measurements [278]. As an example of the performance achieved with the high-temperature synthesis, single-crystal LiNi_{0.83}Co_{0.10}Mn_{0.07}O₂ in full cells between 3.00 and 4.35 V delivers reversible capacity of 167 mAh g⁻¹ and capacity retention of 84.8% after 400 cycles at 0.5 C [258]. With a low-temperature synthesis (sintered at 750 °C with 50% Li-excess), NMC811 exhibits a discharge capacity of 178.1 mAh g⁻¹ with the capacity retention of 95.1% after 100 cycles at 1 C [293]. As for molten-salt synthesis, modifications on the conventional tunnel furnace to prevent an explosive spillover of hot liquid, additional salts as assisted solvent, and water-washing process to remove the salt residues are explored. However, the water-washing process itself may degrade the electrochemical properties, so additional treatments such as heating and coating are undertaken [294,295]. However, Hu et al. have shown that washing NCA with ammonium dihydrogen phosphate (NH₄H₂PO₄) solution simultaneously enhances electrochemical performance and air stability, due to an in situ generated Li₃PO₄ coating

layer [296]. Therefore, a lot of attention is devoted to the fabrication of single-crystallized Li-rich cathode elements [290]. The molten-salt-assisted method using low-melting-point carbonates was used to synthesize single-crystalline NMC622 delivering 174 mAh g^{-1} at 0.1 C , $3.0\text{--}4.3 \text{ V}$, with capacity retention of 87.5% after 300 cycles at 1 C [297]. In addition, this molten-salt-assisted method exhibits its effectiveness in directly regenerating NMC622 from the spent material. Single-crystal NMC811 prepared by molten-salt process still delivered a capacity of 80.7 mAh g^{-1} after 300 cycles at the high rate of 5 C , which corresponds to a capacity retention of 62.0% [298]. The infusion of molten salts to protect grain boundaries of $\text{LiNi}_{0.5}\text{Mn}_{1.5}\text{O}_4$ increase the capacity of this cathode element from 89.5 to 133 mAh g^{-1} at 2 C , 50°C [299]. Wu et al. have recently reported the important relationship between the precursors, lithium salts, sintering atmospheres, sintering temperature, and sintering procedure to be used to obtain such materials [300], including LiNiO_2 [301]. Insight on calcination and sintering of these materials can be found in [301,302]. The aspects of precursor orientational growth, crystal morphology optimization, and composite structure design can be found in [8].

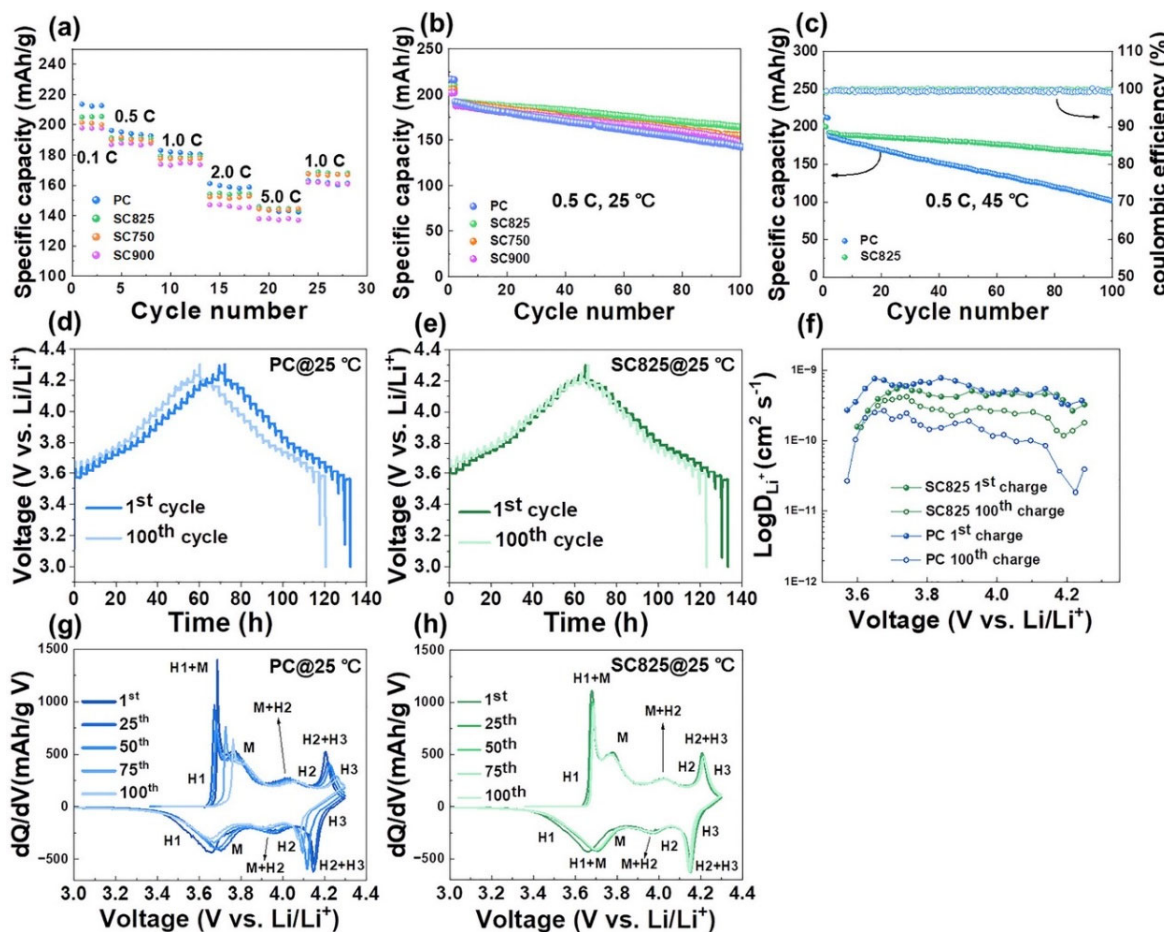


Figure 5. Electrochemical properties of polycrystalline (PC), and single-crystal (SC) $\text{LiNi}_{0.92}\text{Co}_{0.04}\text{Mn}_{0.04}\text{O}_2$ synthesized via LiCl-NaCl molten-salt method at different temperatures (750 , 825 , and 900°C). (a) Rate capabilities of PC, SC750, SC825, and SC900 cathodes (RT). (b) Cycling performance of PC, SC750, SC825, and SC900 cathodes at 0.5 C (RT). (c) Cycling performance of PC and SC825 at 0.5 C (45°C). (d,e) GITT curves of PC and SC825 cathodes during charge/discharge process and (f) corresponding diffusion coefficient. (g,h) dQ/dV curves of PC and SC825 cathodes, respectively. Reproduced from ref. [291]. Copyright 2024 under Creative Commons CC BY license.

4. Coating

To improve the thermal stability and structural stability, surface modifications of the Ni-rich materials is a predominant strategy [303]. Surface coating is a common process to avoid the presence of residual alkalis, such as LiOH and Li₂CO₃ at the surface of the particles. These residual alkalis are one of the dominant reasons for the phase change and electrochemical degradation [304]. In addition, the coating also protects them against side-reactions with the electrolyte. It is difficult to compare the results obtained with different coating materials, because the efficiency of the coating depends not only on its chemical formula, but also on the synthesis method. Han et al. demonstrated this effect by comparing two different synthesis approaches, wet chemical (WC) coating and atomic layer deposition (ALD), for alumina coatings on LiNi_{0.5}Mn_{0.3}Co_{0.2}O₂ [305]. They showed that the ALD method leads to a better initial quality of the coating layers and is less influenced by the post-coating annealing process, while for WC method the high-temperature treatment is highly needed. Cheng et al. utilized ALD coating and annealing protocol to demonstrate the individual and coupling effects of surface coating and grain boundary engineering on cycling stability of NMC811. This engineering allowed them to achieve superior cycle stability even upon high voltage cycling (91% retention after 200 cycles at 2.7–4.7 V at C/3 rate) [306]. Moreover, the electrochemical performance of the materials depends on the synthesis process and synthesis parameters described above, and also on the morphology. That is why we prefer, when possible, to evaluate the performance by comparing the results reported for coated and uncoated samples in the same work, since the coating is the only parameter that makes a different in this case.

4.1. Li-Free Surface Layers

Carbon coating is commonly used for all kinds of active particles for cathodes of lithium batteries, and it has been also applied to Ni-rich cathode materials with success [307–309]. Different forms of conductive carbon have been utilized, including composites such as graphene nanosheets with NMC811 [310], carbon nanotubes with NMC532 [311,312], and interwoven carbon fibers with NMC622 [313]. Density functional theory calculations (DFT) play a crucial role in screening dopants (e.g., Al, Mg, Zr) that can stabilize the Ni-rich structure and reduce cation disordering. It also models interactions with protective coatings such as LiNbO₃ and Al₂O₃, helping design surface modifications that enhance stability and minimize electrolyte decomposition. Ning et al. prepared uniform reduced graphene oxide (rGO)-wrapped NMC811 with the help of a semi-conductive perylene-3,4,9,10-tetracarboxylic dianhydride (PTCDA) layer, ensuring the adhesion of graphene on the particle surface [314]. Poursalehi et al. employed the scalable electrophoretic deposition (EPD) procedure to make instantly a binder-free Li-ion battery cathode, consisting of LiNi_{0.8}Mn_{0.1}Co_{0.1}O₂ (NMC811), sulfonated reduced graphene oxide (SRGO) sheets, and carbon black (CB) particles [315]. The EPD process caused a squeezing force, which not only wrapped the SRGO sheets around the NMC811 nanoparticles, but also inserted the CB particles into the composite. The volume expansion of the active particles was mitigated during cycling due to wrapping graphene sheets, and the restacking of graphene sheets was inhibited by sulfonated groups and CB spacers. At the current density of 0.2 C, the half-cell with this electrode and 1M LiPF₆ in ethylene carbonate (EC) and dimethyl carbonate (DMC) (1:1, v/v) electrolyte delivered discharge capacities of 170.3 and 143.7 mAh g⁻¹ at the 1st and 200th cycle, respectively. The rate capability was also enhanced (42.3 mAh g⁻¹ at 10 C). The method is also scalable, because it takes only 10 min of ultrasonication and EPD when mass-produced SRGO and commercial NMC811 and CB particles are used as the starting materials. Graphitic carbon nitride (g-C₃N₄)-coating can also improve the electrochemical properties of NMC811, provided that the thickness of the coat

is thin enough (20 nm) to avoid the hindering of the lithium diffusion [316]. Park et al. used a dispersion of electrochemically exfoliated graphite nanosheets that are functionalized with an amphiphilic surfactant acting as glue for graphite coating on the surface of Ni-rich oxides [317]. As a result, the cathode (99 wt.% NCA; electrode density (ρ) \sim 4.3 g cm $^{-3}$) exhibited a 38% increase of the areal capacity and 34% increase of the volumetric capacity at current rate of 0.2 C with respect to the bare commercial NCA cathodes. We shall return on the coating devoted to the protection of the particles against side reactions with the electrolyte in a section devoted to the formation of the cathode–electrolyte interface.

Li-free coatings have been extensively investigated, including metal oxides such as SiO₂ [318,319], ZrO₂ [320–322], TiO₂ [323–325], CeO₂ [326], and Al₂O₃. In particular, Al₂O₃ coating of LiNi_{0.6}Co_{0.2}Mn_{0.2}O₂ improves coulombic efficiency, reduces impedance, and improves capacity retention [327]. Even better electrochemical properties for this material were found with uniform C-Al₂O₃ coating obtained by the pyrolysis of molecular layer deposited alucone in argon, due to the synergistic effect between the amorphous Al₂O₃ and conductive carbon composite coating [328]. For Ni-richer NMC811, the positive effect of Al₂O₃ coating is evidenced by the increase of the capacity retention from 500 cycles to 1100 cycles at 1 C rate [329]. In a comparison between LiAlO₂ and Al₂O₃ coatings of NMC622, Liu et al. showed that LiAlO₂ coating is superior to Al₂O₃ and significantly improves the capacity retention and rate capability [330]. Note, however, that the efficiency of the coating depends on the properties of the coat, so that direct comparison may be misleading. In particular, microporous Al₂O₃ coating [331] and ultrathin Al₂O₃ coating [332] gives remarkable electrochemical properties. Therefore, Al₂O₃ coating is still widely used today, inasmuch as it is now possible to control not only the uniformity but also the thickness of the Al₂O₃ coating, allowing for its optimization [333]. Other metal oxide coatings include ZnO [334], MgO [335], Mg-Al layered double oxide [336], and Ta₂O₅ [337]. A Ta₂O₅ protective layer on the surface of NCA with Ta⁵⁺ entering the lattice gifts the cathode had a capacity retention of 94.46% at 1 C after 200 cycles (60.97% for the pristine NCA) [338]. B₂O₃ coating treatment is an effective approach to reinforce the air storage stability and cyclic stability of Ni-rich cathode materials. Even exposing to ambient air for 8 weeks, B₂O₃-coated NMC811 cathode still delivers a high initial capacity of 161 mAh g $^{-1}$ and a satisfactory capacity retention of 75.6% after 200 cycles at 0.5 C [339]. B₂O₃-coated LiNi_{0.87}Co_{0.10}Al_{0.03}O₂ with 2.0 wt.% B₂O₃ delivered a capacity of 184 mAh g $^{-1}$ with a capacity retention of 86% after 100 cycles at 0.2 C [340].

Among metal oxides, Al₂O₃ coating has been most investigated, because of its efficiency. In particular, it introduces new energy levels that prevent the reduction of Ni ions by O²⁻ [341–343] (see Figure 6). It can also suppress the Li-Ni cation mixing. It also maintains stabler cathode–electrolyte interface [344]. Wang et al. reported a surface-targeted healing (TH) strategy through atomic layer deposition of Al₂O₃ [345]. The modified NMC811 cathodes exhibited 78.6% capacity retention after 400 cycles at 1 C and 55 °C compared to 70.6% after 200 cycles for the pristine material. Cheng et al. coated polycrystals of LiNi_{0.83}Mn_{0.05}Co_{0.12}O₂ with Al₂O₃ by ALD and a subsequent annealing method according to which the sample was placed at a high temperature of 750 °C and annealed for 2 h. With this process, the primary grains remain intact, and the Al is enriched at the grain boundaries only. After 300 cycles at 4.3 V and at rate C/3, this cathode maintained 143.8 mAh g $^{-1}$ with 84.7% capacity retention, compared to 118.6 mAh g $^{-1}$ in case of gradual heating annealing [346]. This improvement was attributed to the rapid heating process, which minimizes Li/O loss and prevents the formation of a disordered phase. It is worth noting that a rapid heating process (by microwave techniques in this case) has recently been used to synthesize a Ni-rich Co-free LiNi_{0.9}Fe_{0.05}Al_{0.05}O₂ with also improved electrochemical properties with respect to gradual heating annealing [347].

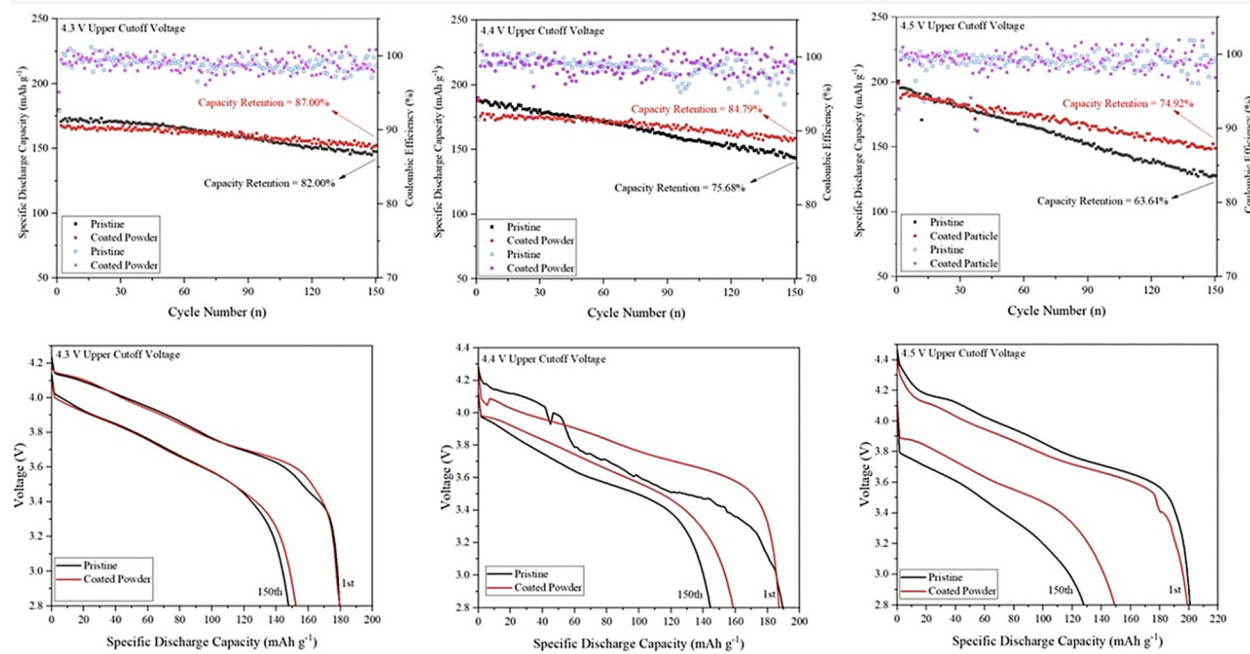


Figure 6. Electrochemical properties of bare and Al_2O_3 -coated NMC811 over 150 cycles (1 C) at 4.3, 4.4, and 4.5 upper cutoff voltages. Upper figures compare cycling stability of samples, while lower figures illustrate voltage fading after 150 cycles. Reproduced from ref. [343]. Copyright 2024 under the Creative Commons CC BY license.

The crystallization of amorphous TiO_2 applied on NMC811 surfaces can result in Li_2TiO_3 -coated NMC811, which can further inhibit phase transformation from H2 to H3 [348]. The capacity retention of Li_2TiO_3 -coated NMC811 was raised at 90% (174.6 mAh g^{-1}) after 200 cycles at 1 C with the voltage 2.70–4.55 V, owing to the additional gradient Ti-doping below the surface layer [349]. Sulfated ZrO_2 coatings can incorporate sulfate groups forming $-\text{SO}_3^-$ to stabilize the interface of NMC particles with the electrolyte [350]. The synergistic effect of the ZrO_2 coating in combination with a zirconium doping enhanced the cycling stability of NMC811 [351]. Defect-rich strontium titanate (SrTiO_{3-x}) coating of NCA cathode exhibited a capacity of 170 mAh g^{-1} after 200 cycles under 1 C with capacity retention of 81.1% [352]. $\text{Al}_2(\text{WO}_3)_4$ is a negative thermal expansion (NTE) material, having the unique properties of abnormal thermal expansion, and has been utilized to significantly suppress heat release and deformation of NMC811 [353]. When cycled at 1 C, NMC811 material modified with 7 wt.% $\text{Al}_2(\text{WO}_3)_4$ retained 162.0 and 171.5 mAh g^{-1} after 100 cycles at 25 and 60°C , respectively, about 13.8 and 25.4% higher than those of the pristine NMC811. Not only did $\text{Al}_2(\text{WO}_4)_3$ reduce the side reactions between the cathode and electrolyte, but it also enhanced the thermal stability of the pristine NMC811.

A drawback of these oxide-based materials utilized to coat the Ni-rich cathode materials their small ionic conductivity. It is thus desirable to investigate more conductive coatings [354,355]. In particular, MoO_3 is attractive, because its ionic conductivity is orders of magnitude larger, compared to Al_2O_3 or MgO . MoO_3 -coated NMCs demonstrated the superior capacity retention of 79.8% under the high 5 C [356]. Benefiting from a high ionic and electronic conductivity of NiFe_2O_4 , a NiFe_2O_4 -coated NMC622 cathode achieved a capacity retention of 81.72% after 100 cycles (at 60°C @ 1 C) and an excellent rate capability ($109.86 \text{ vs. } 49.52 \text{ mAh g}^{-1}$ for the pristine material at 10 C) [357]. This coating was recently extended to NMC811 [358] (see Figure 7). The NiFe_2O_4 -coated NMC811 exhibited a superior rate capability of $112.7 \text{ mA h g}^{-1}$ at 10 C, and high-temperature stability of 130 mA h g^{-1} after 100 cycles at 60°C . Li_2SiO_3 is also employed, as it is a fast ionic conductor [359]. TiNb_2O_7

coating was found beneficial to the electrochemical performance of $\text{LiNi}_{0.88}\text{Co}_{0.06}\text{Mn}_{0.06}\text{O}_2$, by significantly improving the capacity retention of modified material after 200 cycles at 1 C from 59.8% of the pristine material to 87.2% [360]. A 0.3% Nb_2O_5 -coated NMC811 cathode exhibits superior rate capability (146.4 mAh g⁻¹@400 mA g⁻¹) and remarkable rate cyclic stability (188.5 mA h g⁻¹ after 100 cycles with capacity retention of 94.8% [361].

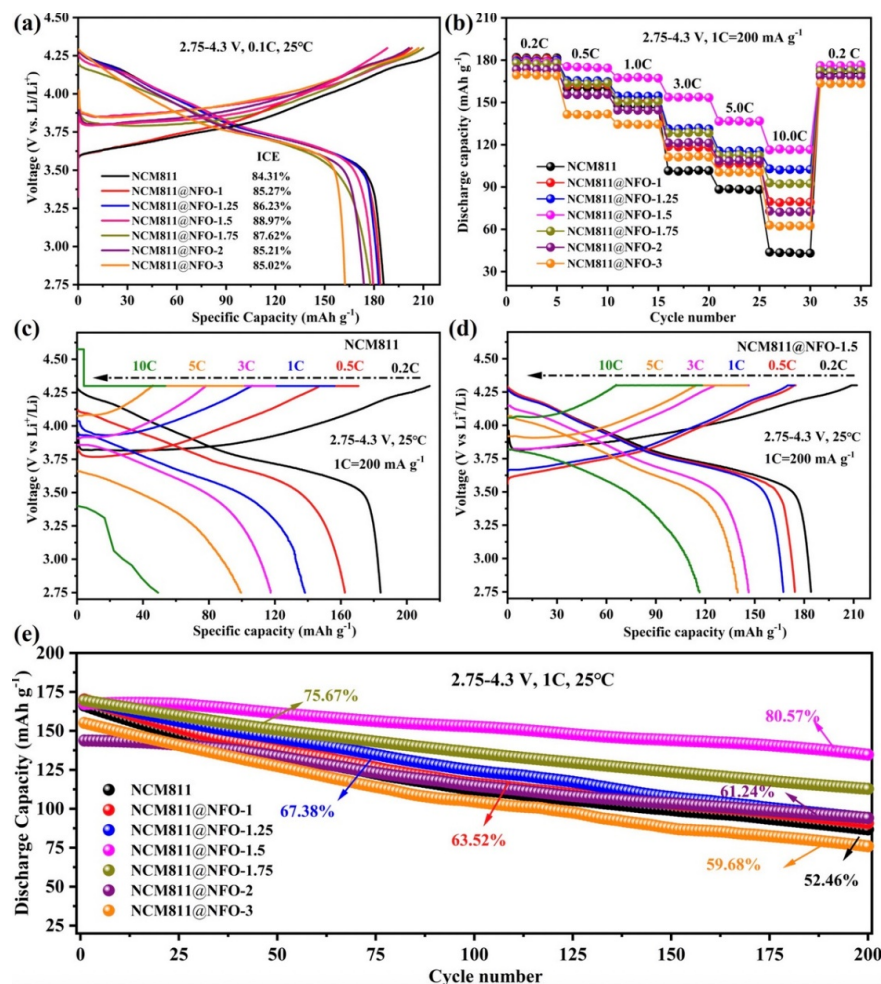


Figure 7. Electrochemical properties of NMC811 uncoated and coated with different NiFe_2O_4 (NFO) weights (in wt.%). (a) Initial charge/discharge profiles of different cathodes at 0.1 C, (b) rate capability, (c,d) capacity–voltage curves at various current densities, and (e) long-term cycling performance at 1 C of prepared cathodes (within 2.75–4.3 V at 25 °C). Reproduced from ref. [358]. Copyright 2024 American Chemical Society.

Coatings of TiO_x (TO) and $\text{Li}_x\text{Ti}_y\text{O}_z$ (LTO) deposited over NMC622 proved to be efficient to protect significantly the particles and suppress the crack formation during cycling [362]. The surficial Ti^{4+} doping induces the reduction of Ni^{3+} to Ni^{2+} at surface region, and the latter tends to migrate into Li-slabs, preforming a 5 nm-thick cation-mixing layer. This less-ordered layer makes the H2–H3 transition reversible [129]. This surficial Ti^{4+} substitution in $\text{LiNi}_{0.9}\text{Co}_{0.1}\text{O}_2$ cathode material for the optimized Ti-concentration of 5 mol% enhanced the capacity retention from 69.7% to 97.9%. Coating with metal phosphates is also of interest because they are thermodynamically stable at the operation window of Ni-rich cathode materials [363]. Moreover, the strong covalent bonds between PO_4^{3-} and the metal ions hinder the reactions of the Ni-rich material with the electrolyte. Examples include coating of NCA with $\text{Ni}_3(\text{PO}_4)_2$ [364] and NMC811 with $\text{Co}_3(\text{PO}_4)_2$ [365], FePO_4 [366,367], AlPO_4 [368], LaPO_4 [369], Li_3PO_4 [370–373], and MnPO_4 [374]. $\text{LiNi}_{0.83}\text{Co}_{0.12}\text{Mn}_{0.05}\text{O}_2$ was coated with CeP_2O_7 through a polyethylene

glycol (PEG)-assisted water deposition method and obtained a cathode exhibiting a retention rate of 92.38% after 100 cycles under the conditions of 2 C and 4.3 V upper cut-off voltage [375]. In a study of the efficiency of 16 metal phosphate coatings on $\text{LiNi}_{0.91}\text{Co}_{0.06}\text{Mn}_{0.03}\text{O}_2$, Min et al. determined that Mn-, Co-, and Fe-phosphate materials improve the electrochemical properties; only TiPO_4 failed [376]. Peng et al. constructed $\text{LiNiO}_2/\text{Na}_{1-x}\text{Ni}_{1-y}\text{PO}_4$ surface hybrid coating layer and Na bulk doping of NMC811 simultaneously [377]. DFT calculations showed that the improvement of the electrochemical properties was attributable to the removal of surface oxygen vacancy and residual lithium. Zeng et al. coated NMC811 with dihexadecyl phosphate (DHP). The outer long-chain alkyl layer inhibited the adverse chemical reaction with $\text{H}_2\text{O}/\text{CO}_2$ in ambient air and improved the structural stability, while the phosphate-based inner coating accelerates Li^+ transport [378].

Huang et al. used alkyl phosphoric material with hydrophobic groups to coat $\text{LiNi}_{0.83}\text{Mn}_{0.11}\text{Co}_{0.06}\text{O}_2$ (N83) [379]. This coat effectively suppressed the surface residual lithium due to H^+/Li^+ ion exchange and enhanced the chemical stability of the cathode–air interface. In the case of LaPO_4 , the $\text{LiNi}_{0.87}\text{Co}_{0.09}\text{Al}_{0.04}\text{O}_2$ sample modified with the optimum 2 wt.% LaPO_4 exhibited capacity retention rates of 96.0% and 85.1% after 100 cycles at 25 and 60 °C, respectively, against 87.1% and 74.2%, respectively, for the uncoated material. NMC622 was coated with $\text{Mn}_3(\text{PO}_4)_2$ [380]. In the case of LaPO_4 , the $\text{LiNi}_{0.87}\text{Co}_{0.09}\text{Al}_{0.04}\text{O}_2$ sample modified with the optimum 2 wt.% LaPO_4 exhibited capacity retention rates of 96.0% and 85.1% after 100 cycles at 25 and 60 °C, respectively, against 87.1% and 74.2%, respectively for the uncoated material.

4.2. Li-Based Surface Layers

These coatings with metal oxides or phosphides are efficient to reduce the side reactions with the electrolyte. However, as they do not contain Li in their composition, they increase the charge transfer resistance. To remedy this problem, the Ni-rich particles were also coated with Li-containing layers, such as NMC333 [381], Li_2ZrO_3 [382–384], LiAlO_2 [385], Li_2SiO_3 [386], Li_2MnO_3 [387,388], LiNbO_3 [389–392], Li_2ZrO_3 [105], LiAlF_4 [393], Li_2SO_4 [394], LiBO [395], $\text{Li}_{0.5}\text{La}_{2}\text{Al}_{0.5}\text{O}_4$ [396], $\text{Li}_x\text{W}_y\text{O}_z$ [397] including Li_xWO_3 [398], Li_2MoO_4 [399], and LiTaO_3 [81,400]. Sun et al. reported on a 2.5 nm-thick Li_2ZrO_3 layer coated onto $\text{LiNi}_{0.90}\text{Co}_{0.04}\text{Mn}_{0.03}\text{Al}_{0.03}\text{O}_2$ and demonstrated that the coating layer lowers activation energy and polarization potential, thereby facilitating the Li^+ motion. At 1 C, the capacity retention rate of the cathode material coated with 1 wt.% of the layer after 100 cycles was 90.2%, while it was only 74.6% for the bare material [383]. The comparison of coated NMCs shows the following trend for coatings to increase in rate performance: $\text{TiO}_2 < \text{Al}_2\text{O}_3 < \text{Li}_4\text{Zr}_3\text{O}_8 < \text{LiAlO}_2 < \text{Li}_4\text{Ti}_5\text{O}_{12} < \text{ZrO}_2$ [401]. The difference in the ranking between $\text{Li}_4\text{Zr}_3\text{O}_8$ and ZrO_2 comes from the reduced porosity of the $\text{Li}_4\text{Zr}_3\text{O}_8$ coating, and high porosity is required to obtain a high-rate capability. On the other hand, a high coverage of the surface enhances long-term cycling stability and decrease the crack generation, which is best obtained with Al-containing coats. That is why long-term cycling stability with high capacity has been obtained for the NMC coated with LiAlO_2 [401]. Tang et al. reported an effective etching-induced coating strategy to shield $\text{LiNi}_{0.8}\text{Co}_{0.1}\text{Mn}_{0.1}\text{O}_2$ electrode materials by LiAlO_2 [402]. The 2.2 wt.% LiAlO_2 -coated NMC811 cathode delivers a high-rate capacity of 135.2 mAh g^{-1} at 10 C and capacity retention of 85.8% after 200 cycles at 0.5 C. With an optimized LiAlO_2 coating amount of 3 wt.%, the capacity retention of $\text{Ni}_{0.9}\text{Co}_{0.07}\text{Mn}_{0.01}\text{Al}_{0.02}\text{O}_2$ increased from 70.7% to 88.3% after 100 cycles at 1 C. It also delivered a capacity of 162 mAh g^{-1} at 5 C, while that of an uncoated sample is only 144 mAh g^{-1} [385]. This result illustrates the efficiency of LiAlO_2 coating to improve the structural stability of Ni-rich cathode elements. Nevertheless, this

coat is not sufficient to protect the electrode materials from HF etching, in contrast with fluoride coatings [403]. To circumvent this drawback, Wang et al. constructed a hybrid LiAlO₂/LiF-AlF₃ coating layer, combining the advantages of LiAlO₂ and fluorinated LiF-AlF₃. The hybrid layer modified NMC611 exhibited a discharge capacity of 166.8 mAh g⁻¹ with capacity retention of 74.5% at 5 C after 300 cycles [404]. Zhang et al. benchmarked Al₂O₃, ZrO₂, and LBO (Li₂O-2B₂O₃) coatings on NMC811, and found that LBO is the best to improve charge–discharge specific capacity, Coulomb efficiency, water absorption stability, cycle characteristics, and resistance stability of the NMC811 cathode material [405]. Jamil et al. coated NCA with Li₂O-BPO₄ and obtained a cathode exhibiting a capacity retention of 92.3% at 1 C in 2.7–4.3 V and 76.2% at high voltage in 2.7–4.7 V [406]. Wu et al. coated LiNi_{0.82}Co_{0.15}Mn_{0.03}O₂ (Ni82) with the fast-ion conductor Li_{6.4}La₃Zr_{1.4}Ta_{0.6}O₁₂ (LLZTO). This modified cathode delivered a discharge capacity from 168.3 to 121.2 mAh g⁻¹ with the retention rate of 72% after 80 charge/discharge cycle at the very high voltage of 4.7 V [407].

Lithium boron oxide (LiBO) coating of NCA increases the capacity retention to 93.59% after 100 cycles at 2 C [408]. Dot-like Nb₁₂WO₃₃ plus uniform LiBO coating of Li(Ni_{0.90}Co_{0.06}Mn_{0.04})_{0.995}Al_{0.005}O₂ Nb₁₂WO₃₃ provided a rapid Li transmission channel, improving the rate capability with respect to the L-B-O coating alone, with a discharge capacity of 179.1 mAh g⁻¹ at 5 C [409]. The LiBO-coated LiNi_{0.90}Co_{0.06}Mn_{0.04}O₂ material showed a discharge capacity of 222.0 mAh g⁻¹ with 88.1% of capacity retention after 100 cycles at 1 C [395]. Qiao et al. synthesized Li₂SiO₃-coated NMC811 (NCM@LSO) by the precoating and solid-state lithiation methods. The capacity retention reached 97% after 500 cycles at 0.5 C, while that of bare NCM was limited to 79% after 450 cycles [386]. Xiao et al. synthesized LiNi_{0.8}Co_{0.15}Al_{0.05}O₂ using CoAl-layered double hydroxide (CoAl-LDH) nanosheet-coated Ni(OH)₂ as the precursor, improving significantly the properties of NCA, compared with NCA synthesized from nickel–cobalt–aluminum hydroxide and Al(OH)₃-coated nickel–cobalt hydroxide precursors. The improvement was attributed to the formation of a Li_{1-x}(Co_{0.75}Al_{0.25})_{1+x}O₂ mesophase as the buffer layer, reducing the Li⁺/Ni²⁺ cation mixing. In addition, the presence of Co on the surface promoted the diffusion of Al during the lithiation–calcination process, thus avoiding the formation of undesired Al-related phases. This cathode delivered a discharge capacity of 194.5 mAh·g⁻¹ at 0.1 C and a capacity retention of 90.9% after 100 cycles at 0.2 C [410].

Lithium phosphates have also been utilized as coating materials, including LiFePO₄ to take advantage of the remarkable stability of this cathode element [411,412], Li₃PO₄ [413–416] (see Figure 8), LiH₂PO₄ [417], LiZr₂(PO₄)₃ [418], and Li_{1.3}Al_{0.3}Ti_{1.7}(PO₄)₃ [419]. Infusing Li₃PO₄ (LPO) in the grain boundaries of secondary particles to coat NMC particles is very promising, because it reinforces the microstructure by shielding off liquid electrolytes within secondary particles [413]. Due to the synergistic effects of Mg-doping and LiFePO₄ coating NMC811, Zhang et al. obtained a cathode that delivered an initial capacity of 181.5 mAh g⁻¹, with 90.8% capacity retention after 100 cycles at 0.2 C, demonstrating the increase of the structural stability due to the coating. The rate capability was also significantly increased, with a capacity still at 120.7 mAh g⁻¹ at 5 C [412]. A still higher capacity at 5 C was obtained with LiH₂PO₄-coated NCA (147.8 mAh g⁻¹). At 0.5 C, this LiH₂PO₄-coated NCA delivered a capacity of 180.2 mAh g⁻¹, decreasing to 172.6 mAh g⁻¹ after 100 cycles, which corresponds to a capacity retention of 95.8% [417].

Coating fluorides on Ni-rich cathode materials can reduce charge transfer resistance and thus improve rate capability, but also increase the cycle life. Directly coating LiF on the surface of Li_{1.2}Ni_{0.2}Mn_{0.6}O₂ stabilized the cathode over 280 cycles and maintained a capacity of 110 mAh g⁻¹ at 1 C [420]. Metal fluoride materials have better resistance to HF attack than metal oxides, and can thus be utilized to coat Ni-rich cathodes. In particular, AlF₃ is known for its beneficial effects in Li-ion batteries [421]. In NMC-based

cells, however, AlF_3 coating has been used mainly in NMC333 [422]. On the other hand, NMC811 was coated with PrF_3 [422]. This cathode exhibited a capacity retention of 86.3% after 100 cycles at 1 C.

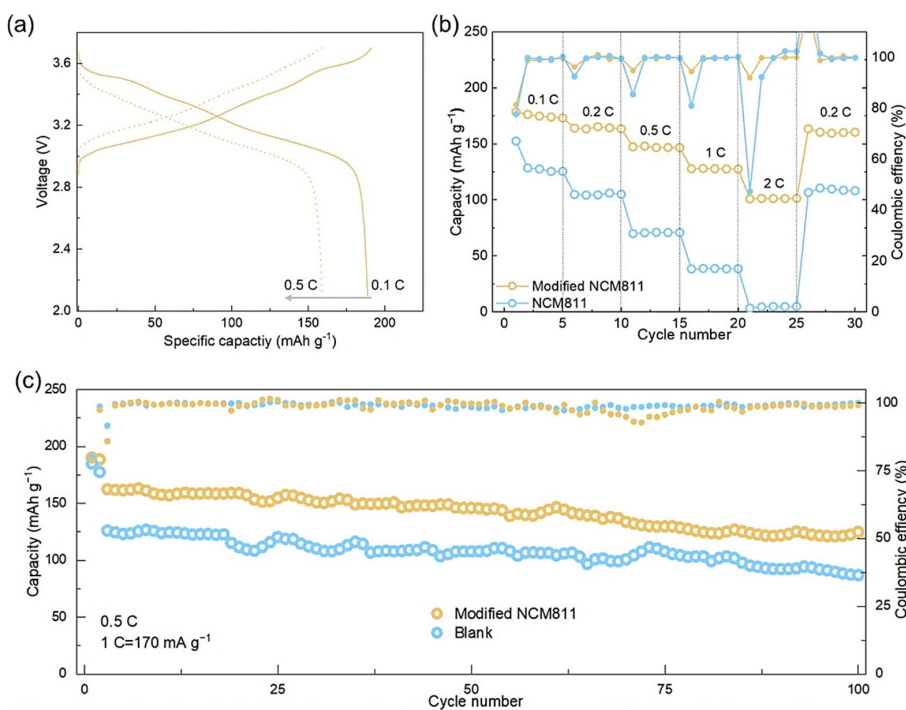


Figure 8. Electrochemical performance of all-solid-state Li-ion cells with an Li-In anode, sulfide solid electrolyte, and NMC811 cathodes at 25 °C. (a) Charge/discharge curves under 0.1 and 0.5 C; (b) rate capabilities and (c) cycling performance of cells with two kinds of NMC811 cathodes: pristine, and modified by Li_3PO_4 coating. Reproduced from ref. [416]. Copyright 2025 Elsevier.

The primary purpose of the coating is to prevent cathode surfaces containing highly reactive Ni^{4+} from contacting the electrolyte and therefore to reduce side reactions. But the coating can also avoid excessive Li on cathode surfaces from causing gas evolution due to its possible transformation into lithium carbonate and hydroxide as well as further side reactions with electrolytes [423]. In particular, metal oxides can allow for excessive Li on the surface of NMC particles to transform into $\text{Li}_x\text{M}_y\text{O}_z$ coatings at certain temperatures. V_2O_5 coating is a good example. Ti-doped V_2O_5 ($\text{Ti}_{0.05}\text{V}_{1.96}\text{O}_5$) on NMC811 effectively enhanced both the rate capability and the cycling stability [424]. DFT calculations demonstrated that the introduction of Ti into V_2O_5 introduced excessive free electrons, while reducing the energy barrier for Li^+ diffusion. Li et al. proposed a hybrid coating strategy incorporating lithium ions conductor Li_xAlO_2 with superconductor $\text{Li}_x\text{Ti}_2\text{O}_4$ to resolve the issue of excessive Li [425]. With this coating, NMC811 exhibited an initial discharge capacity of 227 mAh g^{-1} at 4.4 V cutoff voltage with Coulombic efficiency of 87.3%, and reversible capacity of 200 mAh g^{-1} with 98% capacity retention after 100 cycles at a current density of 0.5 C. Let us recall that the investigation of oxygen release in NMC cathodes has evidenced that stable cycling of NMC is possible up to 4.5 V only for Ni compositions ≤ 0.6 , and is possible only up to 4.0 V for pristine NMC811, because of the phase transition $\text{H}2 \rightarrow \text{H}3$ [34]. Therefore, the result of Li et al. suggests that the coating utilized in this work prevents or at least softens this transition.

Recently, Qu et al. developed a lithium boron carbon oxide ($\text{Li}_x\text{B}_y\text{C}_{1-y}\text{O}_z$) coating using the sol–gel method to recover the air-exposed NMC811 from degradation [426]. The authors demonstrated that this coating is a promising approach to recovering the degraded surface structure and electrochemical performance of NMC cathodes.

4.3. Organic Layers

Organic compounds have also been considered as promising coating materials. Conductive polymers can also be utilized successfully. In particular, Hwang et al. [427] synthesized a lithium-containing “BTJ-L” hybrid oligomer obtained through polymerization of bismaleimide by using a bismaleimide with a polyether monoamine, thiocyanic acid (TCA), and LiOH. NMC811 coated with this polymer demonstrated an improved capacity retention (86.1% vs. 72.9%) after 100 cycles at 1 C, attributed to the excellent wettability toward the electrolyte and the extra Li^+ ions contributed by the hybrid BTJ-L oligomer additive. Coating with polypyrrole (PPy), another conductive polymer, is efficient to stabilize the Ni-rich particles [428] (see Figure 9). Dry-coating PPy on NCA nanofibers increased the capacity retention from 73.7% to 83.1% after 50 cycles at 0.5 C [429]. Another polymer, polymethyl methacrylate (PMMA) was also successfully coated on NMC8111 [430]. The electron transfer from the interfacial Ni^{2+} to the ester group of PMMA anchors the Ni cations and reduced interfacial side reactions. The NMC811 with the PMMA nanolayer the electrode exhibited a discharge capacity of 181.1 mAh g^{-1} at 1 C rate, with capacity retention of 91.2% after 100 cycles. Gan et al. used polyvinylpyrrolidone (PVP) as an inductive agent to controllably coat a uniform conductive polyaniline (PANI) layer on NMC811 (NMC811@PANI-PVP) [431]. PANI-coated $\text{LiNi}_{0.9}\text{Co}_{0.085}\text{Mn}_{0.015}\text{O}_2$ also exhibited improved electrochemical properties compared to the pristine material [432]. He et al. coated $\text{LiNi}_{0.95}\text{Mn}_{0.05}\text{O}_2$ (NM95) with polyaniline–polyethylene glycol (PANI-PEG) to obtain a cathode maintaining capacity retention of 94.7% (1 C, 100th cycle) and 79.0% (5 C, 200th cycle) under cut-off voltage of 4.3 V [433]. Huang et al. adopted an effective Mo/PANI co-modification strategy on a $\text{LiNi}_{0.96}\text{Co}_{0.02}\text{Mn}_{0.02}\text{O}_2$ cathode material [434]. This cathode delivered a capacity of 209.3 mAh g^{-1} with an upper cut-off voltage of 4.4 V at 1 C, and its capacity retention reached 95.7% after 100 cycles. Benefiting of the high conductivity of PANI, the rate capability was also significantly improved, with a capacity of 167.1 mAh g^{-1} at 10 C. Not only does PANI have a good electronic conductivity, but it also prohibits direct contact of the electrode with the electrolyte, so that the NMC811@PANI-PVP cathode exhibited good cycle ability (88.7% after 100 cycles at 200 mA g^{-1}) and rate performance (152 mAh g^{-1} at 1000 mA g^{-1}). Polyacrylonitrile (PAN) was employed by Huang et al. as a proof-of-concept organic coating with better electro-negativity on NMC81, because The $\text{C}\equiv\text{N}$ functional groups in the PAN coating can adsorb $\text{O}^{\alpha-}$ ($\alpha < 2$) and provide it with electrons for its reduction to stable O^{2-} , thus inhibiting oxygen release. This modified NMC811 displayed a high-capacity retention of 86.3% after 200 cycles at 1 C, 75.1% after 350 cycles at 5 C, and 83.1% after 100 cycles at 1 C and 55°C [435]. Li et al. coated NMC622 with a cross-linked epoxy natural rubber (CENR). The viscoelastic properties of CENR alleviated mechanical stresses during cycling. Moreover, the strong adhesion to the surface of Ni-rich cathodes suppressed detrimental interfacial reactions [436]. This coated NMC622 cathode material retained 95.9% of its capacity after 300 cycles at 0.5 C and 82.8% after 500 cycles at 1 C. $\text{LiNi}_{0.83}\text{Co}_{0.11}\text{Mn}_{0.06}\text{O}_2$ was coated with 7 nm-thick polysiloxane via in situ hydrolysis-polycondensation of tetraethyl orthosilicate. The corresponding cathode exhibited a capacity retention of 81.8% after 150 cycles at 1 C [437]. Lin et al. Coated NMC811 with poly (pyrrole-co-citral nitrile) (PPC). The discharge capacity of NMC811@PPC after 200 cycles at 1 C in the voltage range $3.0\text{--}4.5 \text{ V}$ was 173.6 mAh g^{-1} , which is even higher than the initial discharge capacity (102.66%). This little rebound was ascribed to the opening and broadening of the lithium ion channels [438].

Yoon and Shin utilized a cyclopropenium cationic covalent organic framework (C-COF) as a coating material of NCM with 94% Ni content. In the C-COF skeleton, cation moieties attract PF_6^- anions in the Li salts of the electrolyte, suppressing the solvation between Li^+ and PF_6^- . This coating increased the diffusion coefficient of the lithium by a

factor 3, and increased the capacity retention from 60.17 to 71.31% after 200 cycles at 1 C (see Figure 10) [439]. A summary of the effect of different coatings on the cycle ability of Ni-rich cathodes is reported in Table 1.

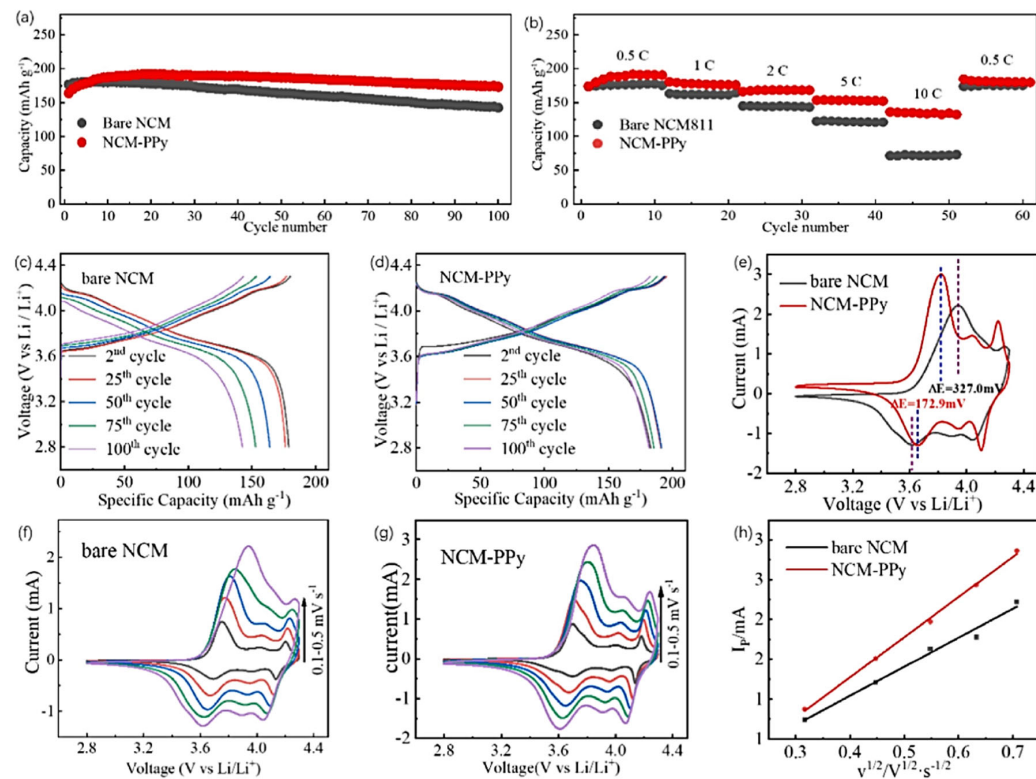


Figure 9. NMC811 coated with PPy (a) Cycling performance at 2 C and (b) rate capability. (c,d) GCD curves at different cycles of NMC811@PPy and bare NMC811. (e) CV comparation between NMC811 and NMC811@PPy with rates of 0.5 mV s^{-1} . CV curves of (f) NMC811 and (g) NMC811@PPy with scan rates increased from 0.1 to 0.5 mV s^{-1} . (h) Plots of peak current density as a function of the square root of the scan rate. Reproduced from ref. [428]. Copyright 2023 Elsevier.

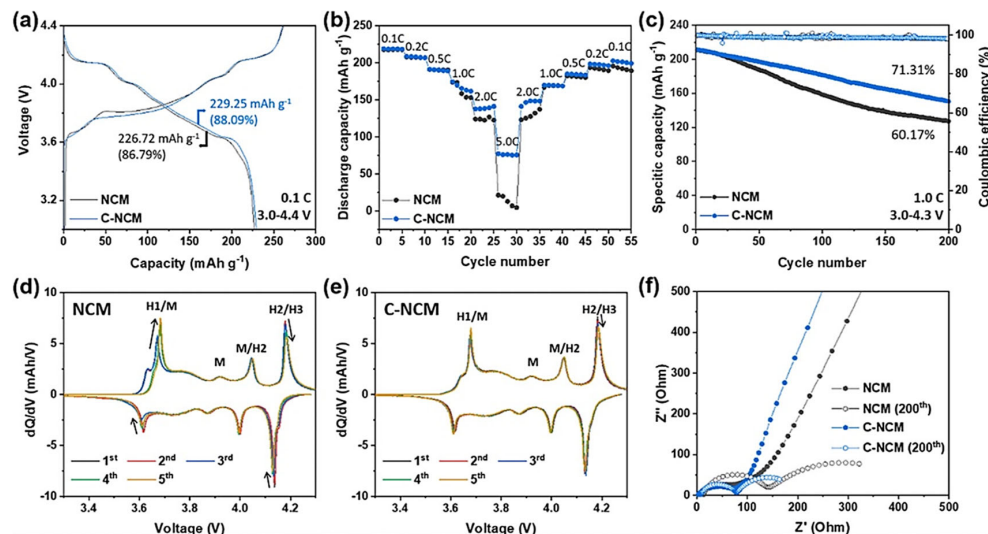


Figure 10. Effect of COF-coating on $\text{LiNi}_{0.948}\text{Co}_{0.046}\text{Mn}_{0.006}\text{O}_2$ (C-NMC). (a) Initial charge–discharge performance of cells with NMC and C-NMC electrodes at a C-rate of 0.1 C . (b) Rate performance with various current densities from 0.1 to 5.0 C . (c) Long-term cycling performance during 200 cycles at 1.0 C . Differential capacity vs. voltage plots of (d) NCM and (e) C-NCM during initial five cycles. (f) Impedance spectra of EIS measurement. Reproduced from ref. [439]. Copyright 2024 American Chemical Society.

Table 1. Effects of coating on cycling ability of Ni-rich cathode elements. Capacity densities are expressed in mAh g^{-1} . Upper cut-off in cycles is 4.5 V for materials, followed by the symbol *. Otherwise, cut-off is 4.3 V. DHP = dihexadecyl phosphate; AP = alkyl phosphoric material (two hydrophobic coats intended to protect the Ni-rich element against moisture). BTJ-L = hybrid oligomer, obtained through polymerization of bismaleimide with a polyether monoamine (i.e., Jeffamine-M1000, JA), trithiocyanuric acid (TCA), and LiOH. CENR = cross-linked epoxy natural rubber.

Cathode Element	Coating	Cycles @C Rate	Pristine		Coated		Ref.
			Capacity (mAh g^{-1})	Retention (%)	Capacity (mAh g^{-1})	Retention (%)	
NMC811	$\text{g-C}_3\text{N}_4$	225@1 C	170	76.4	170	82.3	[316]
Sb-NCMA93	LiF	1000@1 C 4000@1 C	195	89.6	195	93.7 79.2	[318]
Zr-modified $[\text{Ni}_{0.8}\text{Co}_{0.1}\text{Mn}_{0.1}]\text{CO}_3$ *	Zr-rich	100@2 C	198	85.8	195.2	92.2	[320]
NMC622 *	ZrO_2	100@0.5 C	190	52.4	187.6	82.5	[321]
$\text{LiNi}_{0.85}\text{Co}_{0.10}\text{Mn}_{0.05}\text{O}_2$	ZrO_2	200@0.5 C	165	67.9	170	77.6	[322]
NMC532	ZrO_2	-	155	61.6	160	77.4	[382]
NMC622 *	TiO_2	50@1 C	175.1	78.1	178	88.7	[323]
$\text{LiNi}_{0.9}\text{Co}_{0.08}\text{Al}_{0.02}\text{O}_2$	TiO_2	100@2 C	178	63.3	181	77.0	[324]
$\text{LiNi}_{0.83}\text{Co}_{0.11}\text{Mn}_{0.06}\text{O}_2$ *	CeO_2	200@1 C	190	64.2	185	77.0	[326]
NMC811	Al_2O_3	200@1 C	180.7	82.7	170	95.42	[333]
NMC811 (at 50 °C)	ZnO	100@1 C	175	51.72	182	77.47	[334]
NMC811	Mg-Al oxides	100@0.5 C	200	65.3	176	83.3	[336]
NMC811	B_2O_3	200@0.5 C	147	58.4	121.7	75.6	[339]
$\text{LiNi}_{0.87}\text{Co}_{0.10}\text{Al}_{0.03}\text{O}_2$	B_2O_3	100@0.2 C	190	45	184	86	[340]
$\text{LiNi}_{0.70}\text{Co}_{0.15}\text{Mn}_{0.15}\text{O}_2$	Al_2O_3	130@C/2	152	60	155	90	[343]
NMC811	Al_2O_3	400@1 C	800 (mAh)	failed	780 (mAh)	78.6	[345]
$\text{LiNi}_{0.83}\text{Mn}_{0.05}\text{Co}_{0.12}\text{O}_2$	Al_2O_3	300@C/3	193	61.5	170	84.7%	[346]
NMC811	Ti-based	200@1 C	189	44	189	90.0	[349]
$\text{LiNi}_{0.8}\text{Co}_{0.15}\text{Al}_{0.05}\text{O}_2$	SrTiO_{3-x}	200@1 C	205	72.1	210	81.1	[352]
NMC811	$\text{Al}_2(\text{WO}_3)_4$	100@1 C	190.0	73.0	186.5	86.8	[353]
NMC811	MoO_3	100 100	182.5	85.8	186.1 160	92.5 79.8	[356]
NMC622	NiFe_2O_4	200@C/2	152	67.8	145	81.25	[357]
NMC811	NiFe_2O_4	200@1 C	162	52.4	162	80.57	[358]
NMC622	Li_2SiO_3	100@1 C	199	76.4	196	85.5	[359]
NMC811	Li_2SiO_3	450	170	79	166	98.0	[386]
$\text{Li}_{1.06}(\text{Ni}_{0.88}\text{Co}_{0.06}\text{Mn}_{0.06})_{0.94}\text{O}_2$	TiNb_2O_7	200@1 C	187	59.8	184	87.9	[360]
NMC811	$\text{Co}_3(\text{PO}_4)_2$	100@1 C	145	81.3	165	89.5	[365]
NMC811 *	FePO_4	400@C/5	195	63	197	86.0	[367]
NMC811 *	Li_3PO_4	100@1 C	196	75.4	192	88.4	[370]
$\text{LiNi}_{0.83}\text{Co}_{0.12}\text{Mn}_{0.05}\text{O}_2$	CeP_2O_7	100@1 C	179.2	82.8	176.6	92.3	[375]
NMC811	DHP	300@2 C	172	40.7	188	64	[378]
$\text{LiNi}_{0.83}\text{Mn}_{0.11}\text{Co}_{0.06}\text{O}_2$	AP	300	190	57.2	190	92.6	[379]
NMC622	Li_3PO_4	200@1 C	189.3	89.6	189.8	80.9	[380]
NMC622	$\text{LiZr}_2(\text{PO}_4)_3$	100@C/5	125.6	65.9	136.2	86.2	[383]
$\text{LiNi}_{0.90}\text{Co}_{0.04}\text{Mn}_{0.03}\text{Al}_{0.03}\text{O}_2$	Li_2ZrO_3	100@1 C	178.4	74.6	181.7	90.2	[384]
$\text{LiNi}_{0.9}\text{Co}_{0.07}\text{Mn}_{0.01}\text{Al}_{0.02}\text{O}_2$	LiAlO_2	100@1 C	190	70.7	190	88.3	[385]
NMC811	Li_2MnO_3	500@1 C	177	63.1	177	80.4	[387]
NMC532	LiNbO_3	100@1 C	174.6	73	190	92	[390]
NMC811	LiNbO_3	500@1 C	186	19	191	70	[391]

Table 1. Cont.

Cathode Element	Coating	Cycles @C Rate	Pristine		Coated		Ref.
			Capacity (mAh g ⁻¹)	Retention (%)	Capacity (mAh g ⁻¹)	Retention (%)	
LiNi _{0.90} Co _{0.05} Mn _{0.05} O ₂ *	LiNbO ₃	200@1 C	199.45	63.0	193.27	75.6	[392]
LiNi _{0.85} Co _{0.10} Mn _{0.05} O ₂	Li ₂ SO ₄	200@1 C	190	73.3	189	81.5	[394]
NMC811 (4.6 V)	Li _x W _y O _z	100@1 C	183	80	183	85	[397]
NMC811	Li _x WO ₃	100@C/2	180	48	182	93	[398]
NMC811	Li ₂ MoO ₄	100@1 C	177.7	64.6	177.7	90.5	[399]
LiNi _{0.82} Co _{0.12} Mn _{0.06} O ₂	LiTaO ₃	100@C/2	175	55.2	180	92.3	[400]
LiNi _{0.7} Mn _{0.15} Co _{0.15} O ₂	LiAlO ₂	100@C/2	170	85	180	88	[401]
LiNi _{0.6} Co _{0.2} Mn _{0.2} O ₂	LiAlO ₂ /LiF-AlF ₃	300@5 C	160	4.6	166.8	74.5	[404]
LiNi _{0.87} Co _{0.1} Al _{0.03} O ₂	Li ₂ O-BPO ₄	100@1 C	200	75.7	200	92.3	[406]
LiNi _{0.8} Co _{0.15} Al _{0.05} O ₂	Li-B-O	100@2 C	170.7	72	159.7	94.9	[408]
Li(Ni _{0.90} Co _{0.06} Mn _{0.04}) _{0.995} Al _{0.005} O ₂ (at 60 °C)	Nb ₁₂ WO ₃₃ (dots) + Li-B-O	100@3C	217	76.91	227	84.7	[409]
LiNi _{0.8} Co _{0.15} Al _{0.05} O ₂ *	LiFePO ₄	100@C/2	204	82.5	210	95	[411]
LiNi _{0.76} Mn _{0.14} Co _{0.10} O ₂ *	Li ₃ PO ₄	200@C/3	170	79	180	91.6	[413]
NMC811	Li ₃ PO ₄	200@C/2	200	59.3	200	84.6	[414]
LiNi _{0.91} Co _{0.06} Mn _{0.03} O ₂	Li ₃ PO ₄	60@1 C	192.3	60	180	81.8	[415]
NMC811	Li ₃ PO ₄	100@C/2	125	60	162	77	[416]
LiNi _{0.8} Co _{0.15} Al _{0.05} O ₂	LiH ₂ PO ₄	200@2 C	160.1	73.1	166.4	90.1	[417]
LiNi _{0.83} Co _{0.06} Mn _{0.06} Al _{0.05} O ₂	LATP	300@1 C	163.1	83.3	189.6	91.5	[419]
NMC811	PrF ₃	100@1 C	197.4	73.8	186	86.3	[422]
NMC811	Ti _{0.05} V _{1.96} O ₅	100@1 C	165.3	66.8	170.4	78.7	[424]
NMC811	BTJ-L	100@1 C	171	72.9	173	86.1	[427]
NMC811	PPy	100@1 C	175	84.5	175.3	90.7	[428]
NMC811	PMMA	200@1 C	177	80.1	181.1	91.2	[430]
NMC811	PAN	200@1 C	190	57.5	210	86.3	[435]
NMC811	PANI	100@1 C	198	80.1	200	88.7	[431]
LiNi _{0.95} Mn _{0.05} O ₂	PANI-PEG	100@1 C	203.7	33.3	219.4	94.7	[433]
NMC622	CENR	500@1 C	150	40.9	150	82.8	[436]
LiNi _{0.83} Co _{0.11} Mn _{0.06} O ₂	polysiloxane	150@1 C	170	75.8	180	85.4	[437]
LiNi _{0.948} Co _{0.046} Mn _{0.006} O ₂	COF	200	210	60.1	210	71.3	[439]

4.4. Dual Coating

Dual-coating can also be performed to obtain a synergistic effect. For example, Zhao et al. coated NMC with Al₂O₃ and AlPO₄ [440], using a dry coating strategy based on the interaction between NMC811 and Al(OH)₃ nanoparticles to obtain a dual LiAlO₂ and chemical-inert Al₂O₃ coating. They obtained the optimal electrochemical performance when the coating strikes a balance of ion-conducting LiAlO₂ and chemical-inert Al₂O₃ phases [441]. Bai et al. constructed a uniform LiAlO₂+Li₃PO₄ protective layer with gradient Al doping (LAP modification) of single-crystalline LiNi_{0.90}Co_{0.05}Mn_{0.04}Al_{0.01}O₂. This cathode exhibited a capacity retention of 74.4% at a high voltage of 4.5 V after 200 cycles at 1 C, while the capacity retention without this modification was only 63% after 100 cycles [442]. Similarly, Liu et al. combined La₂Li_{0.5}Al_{0.5}O₄ with gradient Al doping of NMC811 and obtained a cathode exhibiting a capacity retention of 90.9%, after 200 cycles at 1 C [443]. Mohsen et al. improved the structural stability and the rate capability of NCA by coating the particles with graphene and Y₂O₃ [444]. Poly (dimethyl diallyl ammonium chlo-

ride)/graphene oxide (PDDA/GO) dual-layer coating on the surface of single-crystal NMC811 exhibited a 77% capacity retention after 500 cycles at the current density of 50 mA g^{-1} , against 28% for pristine NMC811 [445].

Liu et al. reported $\text{LiNbO}_3 + \text{Li}_3\text{BO}_3$ dual-coating of single-crystal $\text{Li}[\text{Ni}_{0.92}\text{Co}_{0.06}\text{Mn}_{0.02}]\text{O}_2$ (SC-Ni0.92). The all-solid-state battery with this cathode $\text{Li}_6\text{PS}_5\text{Cl}$ solid electrolyte and Li-In anode exhibited a capacity retention rate of 88.4% for 100 cycles at a current density of 1.5 mA cm^{-2} (1 C) and a discharge capacity of 150.1 mAh g^{-1} at a high current density of 7.49 mA cm^{-2} (5 C) [446]. This performance was attributed to the melting of Li_3BO_3 during hot sintering, which diffused into the crystalline LiNbO_3 coating to form a dense coating. Yang et al. reported $\text{LiF} + \text{Li}_3\text{BO}_3$ dual-coating of NMC811. This cathode achieved a capacity of 205.4 mAh g^{-1} within a voltage window of 2.8–4.5 V at 1 C. with a capacity retention of 70.6% after 500 cycles [447].

Yang et al. prepared $\text{Li}_{0.5}\text{La}_2\text{Al}_{0.5}\text{O}_4$ (LLAO)-coated $\text{LiNi}_{0.82}\text{Co}_{0.14}\text{Al}_{0.04}\text{O}_2$ [396]. In situ coating LLAO is formed from the reaction among La_2O_3 , Li_2O , and Al_2O_3 at 800°C . This reaction, however, will consume some Al atoms in the superficial phase of secondary particles. Therefore, stoichiometric Mn atoms are doped into the Al-deficient layer to form the $\text{LiNi}_{0.82}\text{Co}_{0.14}\text{Al}_{0.04-x}\text{Mn}_x\text{O}_2$ (LNCAM), which becomes a transition layer suppressing the lattice mismatch on the interface. As a result, the prepared material includes three layers which are the amorphous $\text{Li}_{0.5}\text{La}_2\text{Al}_{0.5}\text{O}_4$ in situ coating layer, the LNCAM transition layer, and the pristine $\text{LiNi}_{0.82}\text{Co}_{0.14}\text{Al}_{0.04}\text{O}_2$ (LNCA) phase from the surface to the inside, respectively. This cathode exhibited a capacity retention of 96.2% after 100 cycles in the voltage range of 3.0–4.4 V at 1 C (13% higher than that of the pristine material), and 80.8% at 1 C after 300 cycles. This performance is due to the synergistic effect of the Mn-doping, which suppressed internal strain, and improved the structural stability of NCA, while the coating effectively restrained cracking of the secondary particles. In addition, LLAO is a good ionic conductor, which enhanced the lithium mobility.

5. Doping

Doping is another strategy to minimize side reactions on Ni-rich NMC particle surfaces. Cation doping is of interest if the ionic radius of the dopant is large, increasing distances between atomic layers in the lattice structure for easier lithiation/delithiation. This expansion not only increases the lithium diffusion, but it also improves the structural stability. Moreover, the higher ionic radii enable dopants to reside on cathode particles, preserving the particle surface and refining particle morphology to suppress crack formation [448]. Doping with metal elements M are employed to expand pathways for Li^+ diffusion, but also to oxidize Ni^{2+} to Ni^{3+} when doped into the material owing to its strong oxidation performance, thus reducing $\text{Li}^+/\text{Ni}^{2+}$ mixing. In addition, the strong M–O bonds can maintain the layered structure at high delithiation state.

5.1. Experimental Results

In situ operando analyses now give a comprehensive understanding of elemental doping of Ni-rich materials [449,450]. Fe^{3+} and Sn^{4+} with ionic radii larger than substituted Co^{3+} expand Ni-rich NMC crystal lattices horizontally [451], while Ca^{2+} (with a radius larger than Ni^{2+}) can expand lattices horizontally [452]. An extensive review on the results published on 46 dopant elements in NMCs through the years has been published by Ko et al. [453]. Hereunder, we focus attention on the best results obtained in recent years. Such doping elements include Mo^{6+} [454–457], W^{6+} [134,454–463], Te^{6+} [464], Ta^{5+} [465–472], Nb^{5+} [473–477], Ce^{4+} [478], Zr^{4+} [479–482], Ti^{4+} [483–490], Ge^{4+} [491], Hf^{4+} [492], Sn^{4+} [493], Ce^{4+} [494], Gd^{3+} [495], and Al^{3+} [2,86]. Al-doping alleviates anisotropic lattice changes and volume changes during cycling. It also main-

tains a wider LiO_6 inter-slab thickness without collapse at highly charged states, allowing Li-ions to be deintercalated/intercalated reversibly [496]. As a result, Al-doped $\text{LiNi}_{0.7}\text{Co}_{0.1}\text{Mn}_{0.2}\text{O}_2$ at a high cut-off voltage (4.4 V) delivered a capacity of $144.69 \text{ mAh g}^{-1}$, with a capacity retention of 80.26% after 90 cycles at 1 C [497]. Due to the Al-doping, $\text{LiNi}_{0.92}\text{Co}_{0.03}\text{Mn}_{0.03}\text{Al}_{0.02}\text{O}_2$ demonstrates a capacity retention of 92% after 100 cycles at 0.5 C rate, against 69% with undoped $\text{LiNi}_{0.94}\text{Co}_{0.03}\text{Mn}_{0.03}\text{O}_2$ [498]. An important parameter is the concentration of Al, 2% in this case, while the optimized concentration is 3% after Kim et al. [499]. They reported that $\text{Li}[\text{Ni}_{0.89}\text{Co}_{0.041}\text{Mn}_{0.034}\text{Al}_{0.031}]\text{O}_2$ cathode demonstrates excellent long-term cycling stability, retaining >90% of its initial capacity after 500 cycles, while the $\text{Li}[\text{Ni}_{0.91}\text{Co}_{0.04}\text{Mn}_{0.04}\text{Al}_{0.01}]\text{O}_2$ cathode loses 38.3% of its initial capacity after 500 cycles [499]. Positive effects of Al-doping have also been observed with cobalt-free cathodes, such as $\text{LiNi}_{0.90}\text{Mn}_{0.06}\text{Al}_{0.04}\text{O}_2$ [500], $\text{LiNi}_{0.8}\text{Mn}_{0.16}\text{Al}_{0.04}\text{O}_2$ [501], LiNiO_2 [502], Al-doped NCM [503], and $\text{LiNi}_x\text{Mn}_{1-x}\text{O}_2$ [504], although the electrochemical performance remains below that of Co-containing Ni-rich cathodes, even with single crystallized particles [505]. Other doping elements of Ni-rich elements include Gd^{3+} [505], Cr^{3+} [506,507], Sc^{3+} [508], Y^{3+} dopant of both NMC [509] and NCA [510], La^{3+} [511], Mg^{2+} [191,512–517], Ca^{2+} [518], Sr^{2+} [519,520], Zn^{2+} [13,521], Ag^+ [522], and Na^+ [523–525].

All the transition metal doping elements we have mentioned form stronger bonds with oxygen and reduced energy loss, promote lithium migration, and reduce the Ni/Li mixing of NMCs. Nevertheless, among V, Nb, and Zr doping, V-doping is the most advantageous to improve the electrochemical properties of NMC811 by reducing significantly the lithium divacancy barrier [526]. This may not be true, however, for NCA cathodes, because this effect in NMC comes from the suppression of the lattice distortion, due to the radius of V^{5+} being close to the radius of Mn^{4+} . Actually, 0.3 wt.% Nb-doped $\text{LiNi}_{0.94}\text{Co}_{0.02}\text{Al}_{0.04}\text{O}_2$ delivers 172 mAh g^{-1} after 300 charge–discharge (voltage window: 2.8–4.3 V) cycles at 2 C (see Figure 11) [527]. Recently, Li et al. investigated the relationship between the diffusion depth and distribution behavior of foreign elements within the cathode material and the composition of the Li-rich cathode material. They determined the diffusion coefficients between Zr^{4+} and transition metal elements TM^{n+} ($\text{TM} = \text{Ni, Co, Mn}; n = 3, 4$) [528]. As a result, these coefficients follow the trend: $\text{Zr}^{4+}/\text{Mn}^{4+} > \text{Zr}^{4+}/\text{Mn}^{3+} > \text{Zr}^{4+}/\text{Co}^{3+} > \text{Zr}^{4+}/\text{Ni}^{3+}$, the $\text{Zr}^{4+}/\text{Mn}^{4+}$ diffusion couple having the smallest diffusion activation energy of only 0.43 eV. In particular, this work explains the reason for the formation of a Li_2ZrO_3 secondary phase coating layer on the surface of Ni-rich cathode material particles.

Al-doped LNO ($\text{LiNi}_{1-x}\text{Al}_x\text{O}_2$) with $x = 0.02$ exhibits a very good cycle ability, with a capacity of 145 mAh g^{-1} after 400 cycles at 0.5 C [529]. The 1 mol% Cr-doped NMC622 exhibits a capacity of 100.6 mAh g^{-1} after 200 cycles at 10 C, corresponding to a retention of 93.1%, in the potential range of 2.7–4.3 V. Extending the potential range to 2.7–4.5 V, the cathode still delivered 166.8 mAh g^{-1} and keeps 75.0% of the initial value at the 200th cycle at 3 C and 50 °C [507]. At 5 C, the Cu-doped NCM622 exhibits a high discharge capacity of 140.8 mAh g^{-1} with an increased capacity retention of 77% as compared to that of the bare NCM622 (62%) after 350 cycles [530]. At 1 C, the capacity retention of Ta-doped $\text{LiNi}_{0.88}\text{Co}_{0.09}\text{Al}_{0.03}\text{O}_2$ is 93% (171 mAh g^{-1}) after 100 cycles at 1 C, compared to 68.6% for the pristine material [465]. Park et al. conducted the study of the effects of Co^{3+} , Al^{3+} , Ti^{4+} , Nb^{5+} , Ta^{5+} , W^{6+} , and Mo^{6+} doping on the properties of $\text{LiNi}_{0.9}\text{Mn}_{0.1}\text{O}_2$ [456] and concluded that Mo-doping give the best results.

Non-metallic dopant elements include B^{3+} [531–534]. The introduction of high-bond-energy B-O covalent bonds can inhibit the change of 2p orbitals of oxygen atoms and the formation of particle microcracks during cycling. Sun et al. [531] studied the effect of B doping on the microstructure of NCA. The study found that B-doping can reduce the surface energy of the (003) crystal plane, promote the preferential growth of the (003) crystal

plane, and change the microstructure. $\text{LiNi}_{0.878}\text{Co}_{0.097}\text{Al}_{0.015}\text{B}_{0.01}\text{O}_2$ cathode material can maintain 83% of its capacity retention after 1000 cycles at a discharge depth of 100%, while the normal undoped $\text{LiNi}_{0.885}\text{Co}_{0.1}\text{Al}_{0.015}\text{O}_2$ showed a capacity retention rate of 49%. $\text{LiNi}_{0.83}\text{Co}_{0.05}\text{Mn}_{0.12}\text{O}_2$ doped with 0.6 mol% B showed enhanced rate capability and excellent cycling stability. The retention after 500 cycles in the soft-pack full cell can reach 91.35%, and the capacity decay per cycle was only 0.0173% [533].

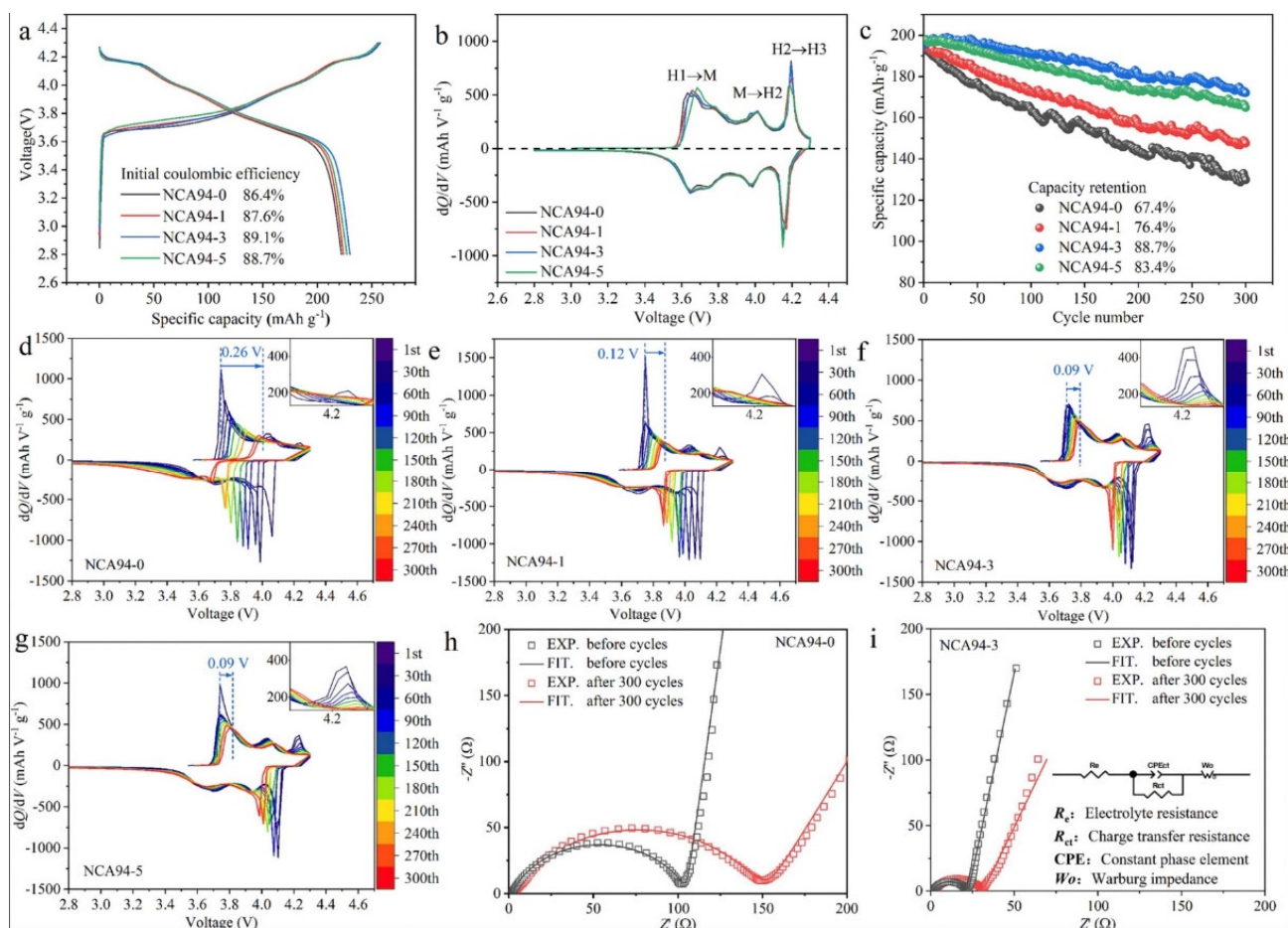


Figure 11. Galvanostatic charge–discharge measurements and EIS results. (a) Initial charge–discharge curves at 0.1 C. (b) Differential capacity plots derived from 0.1 C charge–discharge curves. (c) Cycling performances at 2 C. (d–g) Differential capacity plots derived from 2 C charge–discharge curves at different cycles. (h,i) Nyquist plots of pristine $\text{LiNi}_{0.94}\text{Co}_{0.02}\text{Al}_{0.04}\text{O}_2$ (NCA94-0) and NCA94 doped with 3 wt.% Nb (NCA-3) after 300 cycles at 2 C. Reproduced from ref. [527]. Copyright 2023 Elsevier.

Among Li-site dopants (Na, K, Rb, Ca), Na gives the best results. The substitution of Na^+ for Li^+ at 3a sites enlarges the distance between layers, benefitting from the larger radius of Na^+ . Additionally, Na doping suppresses the cation mixing [535] and weakens Li–O bonds, thus enhancing the potential capacity. A Na-doped NCM622 cathode shows an initial discharge specific capacity of 175 mAh g^{-1} and a high-capacity retention of 90.8% after 100 cycles at 0.2 C, compared to an initial capacity of 160 mAh g^{-1} and retention of 67.5% for the pristine material [525]. Na^+ -doped $\text{Li}_{0.98}\text{Na}_{0.02}\text{Ni}_{0.6}\text{Co}_{0.05}\text{Mn}_{0.35}\text{O}_2$ exhibited a higher capacity retention rate (93.3% vs. 83.2%) after 100 cycles and a superior rate capacity (121 mAh g^{-1} vs. 93 mAh g^{-1}) at 3 C current density compared to the pristine NMC under 4.5 V voltage [536]. On a general basis, Li-site doping ions with suitable ionic radii are beneficial to improve Li^+ diffusion in the positive electrode materials, and thus improve the electrochemical properties. Nevertheless, the dopant must have an ionic radius

that is not too big; otherwise, it can generate blocking effects and lattice distortion that are damageable to the cycle life. For example, among alkali metal elements, Na-doped NMC811 has significantly higher capacity and capacity retention than Rb- and K-doped NMC811 [537]. For the same reason, Na-doping has also positive effects in Li-rich, Mn-rich NMC [538].

The bore is a O-dopant. It raises the capacity retention of $\text{LiNi}_{0.95}\text{Co}_{0.04}\text{Al}_{0.01}\text{O}_2$ to 88% after 100 cycles at 0.5 C [539]. Anion doping is mostly conducted using halogens, such as F^- [540–543]. Other halogens doping elements include Br and Cl, which increased the capacity retention of NMC811 by 10%, due to the low-melting eutectic salt and the increase of the electrochemically active surface area [544].

Positive effects of Sn-doping have been demonstrated both in NMC622 [545,546] and more recently in NMC811 [547,548]. In particular, the capacity for the optimized 2% Sn-doping of NMC811 remains at 183.9 mAh g^{-1} after 270 cycles at 0.5 C, corresponding to 93.7% of the initial discharge capacity. Sn-doped $\text{Li}[\text{Ni}_{0.90}\text{Co}_{0.05}\text{Mn}_{0.05}]\text{O}_2$ ($\text{Li}[\text{Ni}_{0.897}\text{Co}_{0.05}\text{Mn}_{0.05}\text{Sn}_{0.003}]\text{O}_2$) delivers a discharge capacity of 224.3 mAh g^{-1} and exhibits a capacity retention of 92.9% after 100 cycles at 4.3 V and 82.9% at 4.4 V [451]. Like doping with other elements, Sn-doping stabilizes the structure, but in addition, it modifies the structure, as Sn-doped material has radially oriented thin primary particles, which is not the case for the undoped material, and this radial orientation is known to increase the electrochemical properties [204,451].

Mg^{2+} acts differently. It possesses a similar radius to Li^+ and will enter the Li-layer rather than the transition metal layer on the surface region of Li-rich NMC particles [549]. The larger valence with respect to Li^+ is responsible for a repulsion of Mg^{2+} to transition metal ions, allowing for the suppression of cation mixing, and delaying the surface transformation to a spinel structure. As for anionic doping, fluorine is most popular. Not only does it expand both lattice parameters by reducing transition metal ions (mainly Ni and Mn), but it also increases mean charging voltages due to increased bond energy of Li–F as compared with Li–O. In particular, 0.5% Mg-doping of $\text{LiNi}_{0.9}\text{Co}_{0.05}\text{Mn}_{0.05}\text{O}_2$ reduces the capacity loss at 1 C rate from 3.5% to 1.7% after 100 cycles [99].

Kim et al. compared the electrochemical performance of $\text{Li}[\text{Ni}_{0.92-x}\text{Co}_{0.04}\text{Mn}_{0.04}\text{Al}_x]\text{O}_2$ cathodes for different Al concentrations x . Primary particle elongation and radial alignment increase with increasing x , which dissipates strain resulting from the abrupt contraction of unit cells during the $\text{H}_2 \rightarrow \text{H}_3$ transition. The best results were obtained for an Al content of 3 mol%. The $\text{Li}[\text{Ni}_{0.894}\text{Co}_{0.041}\text{Mn}_{0.034}\text{Al}_{0.031}]\text{O}_2$ cathode demonstrated a capacity retention above 90% after 500 cycles, and an energy density of 740 Wh kg^{-1} [499]. For NCA, the optimum Al concentration is 5.6%. At C/3 rate, the capacity retention of $\text{LiNi}_{0.85}\text{Co}_{0.094}\text{Al}_{0.056}\text{O}_2$ is almost 100% after 100 cycles, [550].

The cathode obtained by incorporating 2 mol% Zn^{2+} into $\text{LiNi}_{0.94}\text{Co}_{0.06}\text{O}_2$ delivers an initial discharge capacity of 200 mA h g^{-1} at a C/2 rate, and retains 74% of the initial capacity after 500 cycles in a full cell assembled with a graphite anode (against 62% before Zn doping) [13]. Yi et al. synthesized a LiNiO_2 co-doped with 1 mol% Mg and 2 mol% B [551]. This cathode in pouch full cell configurations with graphite anode exhibited a high initial 1 C discharge capacity of 210 mAh g^{-1} with a 20% capacity retention improvement over 500 cycles when benchmarked against pristine LiNiO_2 . The result was attributed to the stabilization of the CEI reducing TM dissolution.

All the dopants serve as pillars for enhancing the structural stability. In addition, high-valence dopants Nb^{5+} , Ta^{5+} , Sb^{5+} , Mo^{6+} , and W^{6+} modify the microstructure through lowering the energy of the (003) surface, which dramatically dissipates the strain arising from $\text{H}_2 \rightarrow \text{H}_3$ phase transition [459,552]. The change in morphology, crystal structure, and electrochemical properties associated with such doping is illustrated in Figure 12 for

the particular case of LiNiO_2 . They are thus the subject of increasing interest, and their application as modifiers in Ni-rich cathodes [553]. W-doping showed remarkable results. At 1 C, the 1.0-mol% W-doped $\text{Li}[\text{Ni}_{0.90}\text{Co}_{0.05}\text{Mn}_{0.05}]_{\text{O}_2}$ cathode in a pouch-type full cell using a graphite anode retained 89% of its initial capacity after 500 cycles [134]. Kim et al. constructed a W-doped $\text{Li}[\text{Ni}_{0.8}\text{Co}_{0.15}\text{Mn}_{0.05}]_{\text{O}_2}$ cathode that showed nearly no drop in specific capacity even after 1000 cycles at full depth of discharge at 1 C [554]. Kim et al. obtained W-doped $\text{Li}[\text{Ni}_{0.95}\text{Co}_{0.04}\text{Al}_{0.01}]_{\text{O}_2}$ cathode with columnar grains by introducing WS_2 . [460]. The study of W-doped $\text{LiNi}_{0.88}\text{Co}_{0.09}\text{Mn}_{0.03}\text{O}_2$ also demonstrated that the primary particles of the cathode become finer with the increase of W-doping amount [555]. As a result, at a high rate of 10 C, this W-modified cathode exhibited capacity retentions of 94.68% and 89.63% at 25 and 45 °C after 100 cycles, respectively. At full depth of discharge, $\text{Li}[\text{Ni}_{0.90}\text{Co}_{0.09}\text{Ta}_{0.01}]_{\text{O}_2}$ exhibits 90% capacity retention after 2000 cycles, when $\text{Li}[\text{Ni}_{0.90}\text{Co}_{0.09}\text{Al}_{0.01}]_{\text{O}_2}$ cathode loses ~40% of its initial capacity within 500 cycles [466]. Another example of high-valence doping is provided by Nb-doped Ni-rich cathode that consists of the elongated and radially aligned primary particles with increased oxygen stable (003) planes [556]. In this work, Nb-doped $\text{LiNi}_{0.9}\text{Co}_{0.1}\text{O}_2$ cathodes in a pouch-type full cell exhibited a capacity retention of 91.9% at 1 C after 500 cycles and 80.5% at 5 C after 2000 cycles within 3.0–4.2 V. The Nb-doping is efficient to stabilize the structure, but coating may be desirable to increase the conductivity at the surface of the particles. For example, a dual-modification strategy of Nb doping and Li_4SiO_4 coating combined the two effects to obtain a NCA cathode exhibiting a specific capacity of $199.2 \text{ mA h g}^{-1}$ at 1 C with a capacity retention of 93.3% after 100 cycles due to the doping, but it also delivered a high capacity of 160.0 mAh g^{-1} at 10 C, much higher than the pristine NCA (138.2 mAh g^{-1}), due to the coating [557]. Note, however, that a simple dual-site Nb-doped NMC811 cathode delivered 202.8 mAh g^{-1} with a capacity retention of 81% after 200 cycles at 2 C, and delivered a capacity of 176 mAh g^{-1} at 10 C rate [558]. This result demonstrates that Nb doping is capable of effectively stabilizing the structure at a high voltage, suppressing the Li/Ni disordering, and improving the electrochemical performance of the NCM cathode. Zhang et al. demonstrated recently that the introduction of Co at a doping level (1.5%) into $\text{LiNi}_{0.9}\text{Mn}_{0.1}\text{O}_2$ is sufficient to obtain a cathode exhibiting a discharge specific capacity of 167.1 mAh g^{-1} after 100 cycles at 1 C and 121.2 mAh g^{-1} after 200 cycles at 5 C, respectively [559].

Machine learning techniques can be applied to efficiently and accurately screen appropriate dopants [560]. Recently, Kim et al. developed a machine-learning-based model for Ni-rich cathodes. They implemented 33 elements as potential dopants, which led to the identification of 101 Co-free compounds demonstrating their superior performance. Among them, the top ten $\text{Li}_{0.85}\text{D}'_x\text{D}''_{(0.15-x)}\text{O}_2$ compounds are obtained. Only one of them contains Mn: $\text{LiNi}_{0.85}\text{Ti}_{0.05}\text{Mn}_{0.1}\text{O}_2$, and one of them has only one dopant: $\text{LiNi}_{0.85}\text{B}_{0.15}\text{O}_2$. The other ones are co-doped, with B, Cu, Al, Cr, Ti, and V as D' and D'' dopants. Their calculated energy density is in the range $1160\text{--}1204 \text{ mWh g}^{-1}$, calculated capacity in the range $277\text{--}287 \text{ mAh g}^{-1}$, with a calculated volume change during cycling $\leq 2.6\%$ [561]. For comparison with cathodes that are currently investigated, NMC811 has a theoretical capacity of 200 mAh g^{-1} [562], average voltage 3.5 V when doped with Fe [563], and volume change of $7.8\% \pm 1.5\%$ [564]; NCA80 ($\text{LiNi}_{0.80}\text{Co}_x\text{Al}_y\text{O}_2$) has a theoretical capacity of 279 mAh g^{-1} , average voltage 3.9 V at $x = 0.15$ and $y = 0.05$ [565], and volume change of 4.2% at $x = 0.16$ and $y = 0.04$ [566]. This result illustrates how useful artificial intelligence (AI) is for helping to determine next-generation cathode candidates. A comparative study of the effects of doping on the cycling ability of Ni-rich cathode materials is summarized in Table 2.

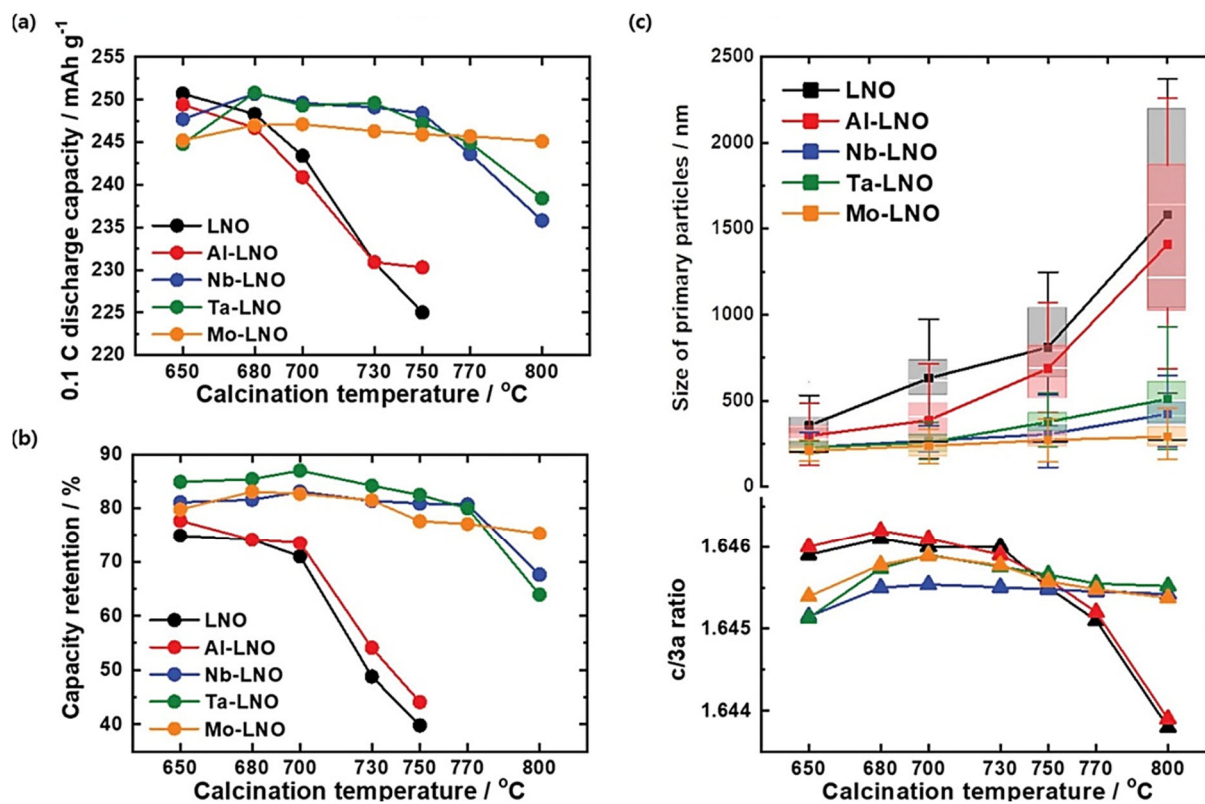


Figure 12. Effect of doping on electrochemical performance of LiNiO_2 (LNO) with high-valence elements. (a) Discharge capacity (at 0.1 C) and (b) capacity retention after 100 cycles (at 0.5 C in half cells) of LNO, Al-LNO, Nb-LNO, Ta-LNO, and Mo-LNO cathodes as a function of calcination temperature. (c) Fundamental physical properties (average particle size and $c/3a$ ratio) of cathodes as a function of calcination temperature. Reproduced from ref. [552]. Copyright 2023 Wiley.

Table 2. Effects of single doping on cycling ability of Ni-rich cathode elements. Capacity densities are expressed in mAh g^{-1} . Asterisk symbol after cathode element indicates that upper voltage cut-off for cycles is 4.5 V. Otherwise, unless specified, cut-off is 4.3 V.

Cathode	Dopant	Cycles at C Rate	Pristine		Doped		Ref.
			Capacity (mAh g^{-1})	Retention (%)	Capacity (mAh g^{-1})	Retention (%)	
NMC811	Mo	100@C/3	150	78	180	81.6	[454]
$\text{LiNi}_{0.84}\text{Co}_{0.11}\text{Mn}_{0.05}\text{O}_2$	Mo	80@C/10	195	46.5	205	-	[455]
		80@C/2	191	-	191	87.2	
NCMA94	Mo	100@C/2	238.3	87	236.8	93.1	[457]
LiNiO_2	W	100@C/2	230	83.7	228	90.3	[458]
NCA95	W	100@C/2	220	81	230	90.3	[460]
$\text{LiNi}_{0.83}\text{Co}_{0.11}\text{Mn}_{0.06}\text{O}_2$	W	500@2 C	140	53.5	165	69.9	[461]
NMC811	W	200@1 C	170	81.3	170	92.3	[463]
$\text{LiNi}_{0.88}\text{Co}_{0.09}\text{Mn}_{0.03}\text{O}_2$	W	100@1 C	192	62.21	188	93.51	[555]
$\text{LiNi}_{0.9}\text{Mn}_{0.1}\text{O}_2$	W	200@1 C	170	77.1	170	95.3	[463]
$\text{LiNi}_{0.88}\text{Co}_{0.09}\text{Al}_{0.03}\text{O}_2$	Ta	100@1 C	208	68	198	93	[465]
NMC622 *	Ta	100@1 C	143.4	80.1	148.1	83.6	[467]
$\text{Li}[\text{Ni}_{0.91}\text{Co}_{0.09}]\text{O}_2$	Ti	100@C/2	227–230	78.8	227–230	94	[468]
	Ta					97	
	Mo					94.9	
$\text{LiNi}_{0.865}\text{Co}_{0.095}\text{Al}_{0.04}\text{O}_2$	Ta	200@1 C	180	97.87	188	79	[469]
$\text{LiNi}_{0.83}\text{Co}_{0.11}\text{Mn}_{0.06}\text{O}_2$	Ta	200@1 C	91.4	50	160.3	97.5	[472]

Table 2. Cont.

Cathode	Dopant	Cycles at C Rate	Pristine		Doped		Ref.
			Capacity (mAh g ⁻¹)	Retention (%)	Capacity (mAh g ⁻¹)	Retention (%)	
NMC8111	Nb	300@1 C	184.9	79.8	180.2	96.9	[473]
NMC8111	Nb	100@1 C	181.5	67.6	181.6	94.55	[474]
LiNi _{0.83} Co _{0.11} Mn _{0.06} O ₂	Nb	200@1 C	181	61.2	181	86.6	[477]
LiNi _{0.94} Co _{0.02} Al _{0.04} O ₂	Nb	300@2 C	192	67.4	194	88.7	[527]
NMC811 *	Ce	100@5 C	129.6	70.7	161	86.9	[478]
LiNi _{0.90} Co _{0.07} Al _{0.03} O ₂ *	Zr	100@C/2	205.9	62.02	191.7	84.86	[480]
LiNi _{0.9} Al _{0.1} O ₂	Zr	100@1 C	105	81.04	177.5	92.45	[481]
LiNi _{0.83} Co _{0.12} Mn _{0.05} O ₂	Zr	100@5 C	178	86.5	180	97.6	[482]
NMC811	Ti	50@C/2	180	91.1	180	96.7	[484]
NMC811	Ti	100@C/10	116.5	64.1	180.6	96.9	[486]
LiNi _{0.83} Co _{0.11} Mn _{0.06} O ₂	Ti	100@2 C	168.5	76.3	164	95.4	[488]
LiNi _{0.88} Co _{0.06} Mn _{0.06} O ₂	Ti	100@1 C	181.5	78.9	193.8	93.6	[489]
LiNi _{0.90} Co _{0.05} Mn _{0.05} O ₂	Ti	150@1 C	195	72.6	170	94.4	[490]
LiNi _{0.9} Co _{0.08} Al _{0.02} O ₂	Hf	100@1 C	200	82.0	200	95.3	[492]
NMC622 *	Ce	100@1 C	167.2	63.63	188.7	74.66	[494]
LiNi _{0.88} Co _{0.09} Al _{0.03} O ₂	Gd	100@1 C	151	77	176	89.3	[495]
NMC90	Sn	100@C/2	230	87.1	230	92.9	[451]
NMC811	Sn	270@C/2	192	61.6	190.3	96.6	[547]
LiNi _{0.90} Co _{0.04} Mn _{0.03} Al _{0.03} O ₂	Sn	200@1 C	185	67	185	83	[493]
LiNi _{0.80} Co _{0.15} Mn _{0.05} O ₂	Al	100@C/10	214.1	92.4	208.1	97.2	[496]
NMC811 (4.4 V)	Al	90@1 C	180	70	180	80	[497]
LiNi _{0.92} Co _{0.03} Mn _{0.03} Al _{0.02} O ₂	Al	100@C/2	210	69	190	92	[498]
Li[Ni _{0.92} Co _{0.04} Mn _{0.04}]O ₂ (4.2 V)	Al	1000@1 C	193	53.4	186	88.3	[499]
LiNi _{0.90} Mn _{0.06} Al _{0.04} O ₂ LiNi _{0.90} Mn _{0.06} Co _{0.04} O ₂	Al	200@1 C 200@1 C	- 170	- 78.3	165 -	82.9% -	[500]
LiNi _{0.8} Mn _{0.16} Al _{0.04} O ₂	Al	200@1 C	161	69.4	178	82.2	[501]
LiNi _{0.6} Mn _{0.4} O ₂ *	Al	100@1 C	136.8	70.4	179	87.6	[504]
LiNiO ₂	Al	600@C/2	187	66.8	175	81.7	[529]
LiNi _{0.6} Co _{0.2} Mn _{0.2} O ₂	Cr	200@1 C	137.2	84.9	149.8	91.0	[507]
NMC811	Sc	150@1 C	185	77.9	185	81.7	[508]
LiNi _{0.925} Co _{0.03} Mn _{0.045} O ₂	Y	150@1 C	197.7	65.39	196	82.7	[509]
LiNi _{0.88} Co _{0.09} Al _{0.03} O ₂	Y	100@1 C	190.8	60.1	192.7	88.9	[510]
LiNi _{0.9} Co _{0.1} O ₂	La	300@C/2	205	62.2	209	75.2	[511]
LiNi _{0.88} Co _{0.05} Mn _{0.07} O ₂	Sr	100@1 C	191.4	88.48	189.1	96.61	[520]
LiNi _{0.83} Co _{0.12} Mn _{0.05} O ₂ *	Mg	200@1 C	201.8	74.0	199.7	87.2	[512]
LiNi _{0.6} Co _{0.2} Mn _{0.2} O ₂	Mg	100@1 C	162.6	79.33	180	90.02	[549]
LiNi _{0.9} Co _{0.05} Mn _{0.05} O ₂	Zn	80@C/2	190	69.8	190	91.7	[521]
NMC622	Na	100@C/5	160	67.5	175	90.8	[525]
LiNi _{0.6} Co _{0.05} Mn _{0.35} O ₂ (4.45 V)	Na	150@C/2	160	80.23	160	84.4	[536]
NMC811	B	100@C/2	178	93	180	97	[532]
LiNi _{0.83} Co _{0.05} Mn _{0.12} O ₂	B	500@C/2	1.73 Ah	66.95	1.78 Ah	91.35	[533]
NMC811	B	120@C/2	170	53	170	87	[534]
NMC811	F	100@C/2	170	58	175	93	[540]
LiNi _{0.9} Co _{0.05} Mn _{0.05} O ₂	F	100@2 C	176.7	85.3	181.1	95.5	[541]

Table 2. Cont.

Cathode	Dopant	Cycles at C Rate	Pristine		Doped		Ref.
			Capacity (mAh g ⁻¹)	Retention (%)	Capacity (mAh g ⁻¹)	Retention (%)	
LiNi _{0.8} Co _{0.15} Al _{0.05} O ₂	F	100@2 C	183	77.6	157.8	98.3	[542]
LiNi _{0.82} Mn _{0.18} O ₂ *	F	100@C/2	170	47	180	70	[543]
NMC811 *	Cl	100@C/2	197	81.8	202	96.1	[544]
	Br	100@C/2	197	81.8	197	95.3	

5.2. Theoretical Calculations

Density functional theory calculations provide critical insights into Ni-rich cathode materials at the atomic and electronic levels, aiding in their optimization and performance enhancement. They enable the prediction of phase transitions and structural changes during battery operation. By analyzing lattice parameters and atomic interactions, DFT helps identify factors contributing to phase segregation and degradation, such as the migration of Ni ions into the Li layer. DFT is used to calculate the band structure and density of states (DOS), revealing how Ni concentration affects charge transport. Additionally, Li-ion diffusion barriers can be computed to optimize ionic conductivity and rate capability. These insights help fine-tune material compositions for better conductivity and fast-charging capabilities. By evaluating lithium chemical potential, DFT aids in understanding the stability of Ni-rich cathodes and their decomposition tendencies. This information is vital for designing materials with higher capacity retention and minimal voltage fade. DFT calculations allow for the investigation of oxygen evolution. By understanding these degradation pathways, researchers can develop strategies to mitigate these effects and enhance cathode longevity. DFT calculations determine vacancy formation energies and their impact on charge compensation mechanisms. By analyzing these defects, researchers can fine-tune material stoichiometry to achieve optimal electrochemical properties. That is why DFT calculations are very often included in the publications to support the experimental results and their interpretation. Another example of the contribution of DFT is the calculation on LiNi_{0.9}Co_{0.1}O₂ providing insights into the performance-limiting factors of this cathode element, emphasizing the need for a higher concentration of cobalt doping to effectively stabilize the Ni-rich cathode [567].

In the context of doping and coating strategies, DFT plays a crucial role in screening dopants that can stabilize the Ni-rich structure and reduce cation disordering. It also models interactions with protective coatings, helping design surface modifications that enhance stability and minimize electrolyte decomposition. For example, DFT calculations demonstrate that Mg²⁺ doping not only inhibits the H2–H3 phase, but also improves the number of free electrons near the fermi level from 15.66 for the pristine LiNi_{0.80}Co_{0.05}Mn_{0.15}O₂ (FNCM) to 17.30 for Mg-doped FNCM [568]. Bader atomic charge calculation found that Ga-doping brings an additional charge of 0.1864 to the oxygen atom in LiNiO₂ [569]. DFT calculations also gave insight on the effects of oxidized dopants with more electrons near the fermi level, which reduces charge transfer resistance and improves electron conductivity [570–572] (see Figure 13). DFT is also useful in determining the chemical stability of the coatings. For example, it shows that the coating with phosphates LiMPO₄ (*M* = Ni, Co, Mg) has improved stability compared with sulfates, which is confirmed by experiments [573]. The calculation of binding energy between the Li-rich material and the coating layer also gives insight into the structural stability and improvement of the lithium diffusion [574–577]. Finally, DFT calculations facilitate the exploration and parameter optimization of new materials, and the coupling with machine learning will be of great value in selecting the

most appropriate coating materials and dopants for Ni-rich cathodes [578]. A first example of this coupling has been recently reported [579].

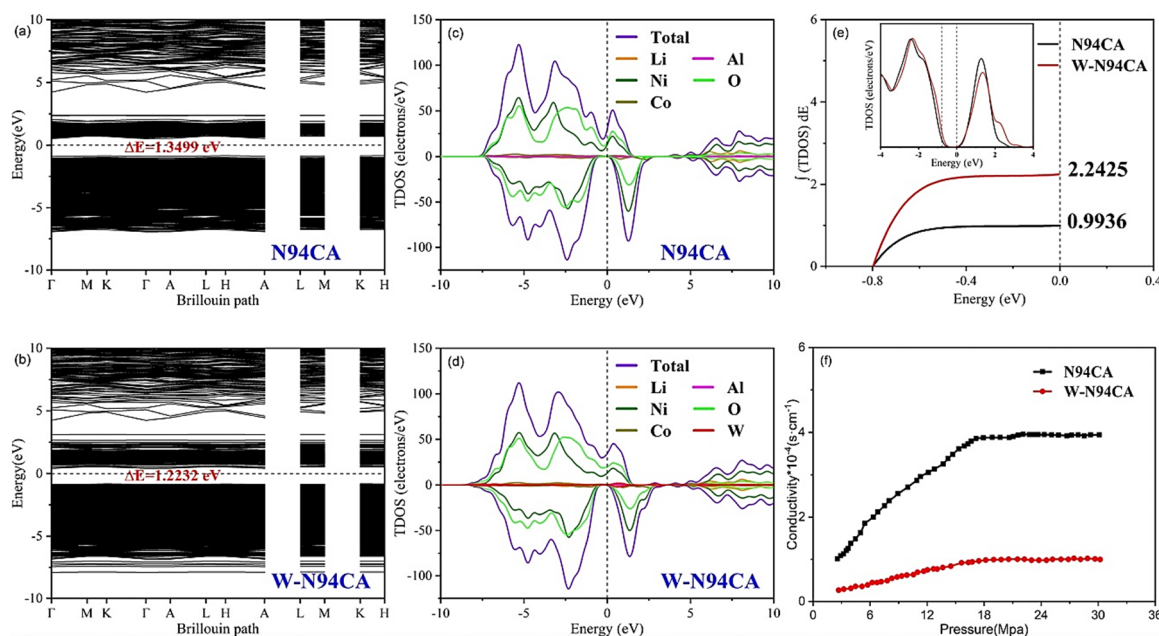


Figure 13. Results of DFT calculations: the band structures of (a) $\text{LiNi}_{0.94}\text{Co}_{0.04}\text{Al}_{0.02}\text{O}_2$ (N94CA) and (b) W-doped N94CA; density of states of (c) N94CA and (d) W-N94CA; (e) integration of DOS from (c,d). DFT calculations show that W-doping results in an increase of Fermi level toward conduction band and an increase of total density of states (TDOS), as shown in the insets. Results are in agreement with the increase of electronic conductivity of powder samples in (f). Reproduced from ref. [571]. Copyright 2023 Elsevier.

5.3. Morphology Aspects

Doping has beneficial effects on the morphology of the particles. For example, we have already mentioned that Nb^{5+} doping significantly improves the electrochemical properties of Ni-rich materials. In addition, Nb^{5+} doping of $\text{LiNi}_{0.88}\text{Co}_{0.05}\text{Mn}_{0.07}\text{O}_2$ modifies the particle morphology, yielding radially distributed, elongated, rod-like structures. This cathode delivered an initial capacity of 200.3 mAh g^{-1} at 1 C, within a voltage range of 2.7–4.5 V, with a capacity retention of 92.9% after 100 cycles [580]. This rod-like morphology effectively mitigates the anisotropic volume changes during cycling and thus increases the cycle ability. Li et al. have shown that the one-dimensional morphology of the primary particles provides shorter electron/ion diffusion distances and high tolerance to corresponding stress changes, significantly improving the electrochemical properties [223]. Other dopants preserve the rod-like structure. In particular, excess Al dopant effectively preserves the needle-like morphology of compositionally partitioned precursors during lithiation [581], and segregates at grain boundaries, inhibiting the growth of primary particles [582]. This segregation of high-oxidation-state dopants at grain boundaries is commonly observed because their ionic radii limit their solubility [583]. The amount of dopant also modifies the size and morphology of primary particles. B-dopant is an example. It lowers the surface energy of the (003) planes, thereby producing a strong crystallographic texture in B-doped cathodes [531]. In addition, as the bore dopant concentration increases, the primary particles elongate along the radial direction [584]. All these results show that the orientation of primary particles has been extensively controlled using high-valence dopants during calcination. Concentration gradients also favor the rod-like structure, as will be seen in the section devoted to them. Ta-doping increases the number of small primary particles and increases the degree of heterogeneity of particle orientation. This effectively

mitigates the local strain accumulation during cycling due to the random orientation of primary particles [472].

In addition, the role of the hydroxide precursor is also critical in synthesizing radially aligned Ni-rich cathodes. Through stepwise control of ammonia concentration and pH during precipitation, elongated primary particles with appropriate size along [001] are promoted, facilitating the formation of radially aligned particles in the precursor. This approach enabled Wang et al. to synthesize $\text{LiNi}_{0.94}\text{Co}_{0.02}\text{Mn}_{0.04}\text{O}_2$ cathodes with exceptional radially aligned microstructure [585]. This cathode material delivered a capacity of 230 mAh g^{-1} at 0.05 C and 186 mAh g^{-1} at 5 C , with capacity retention of 95.6% after 100 cycles at 1 C and 25°C in half cell and 93.2% after 1000 cycles at 1 C and 30°C in full cell. This is an illustration of the morphological relationship of cathode materials to their electrochemical performance, which has been reviewed by Meng et al. [586].

Other morphologies are also of interest. Wu et al. successfully synthesized NMC811 cathode material, arranging the hexagonal nanosheets with exposed {104} facets by a co-precipitation process and a high-temperature lithiation reaction. The tightly adhered nanosheets on the (001) surface help to alleviate stress changes caused by the anisotropic structure and inhibit the fragmentation of secondary particles [587]. This cathode exhibited a discharge capacity of 203.8 mAh g^{-1} at 0.1 C and stable cycling performance (89.3% capacity retention after 100 cycles at 1 C , 55.3% after 300 cycles at 5 C , and 59.6% after 300 cycles at 10 C).

5.4. Synergetic Effects of Co-Doping and/or Multiple Coating

Synergetic effects can be obtained by combining multiple dopants and/or multiple coatings [588,589].

5.4.1. Dual Doping

For example, as the Mg-doping is beneficial for stabilizing the structure, while Zr-doping improves the kinetics, the electrochemical properties of NMC811 are enhanced by Mg+Zr co-doping with the discharge capacity 199.7 mAh g^{-1} at cut-off potential of 4.7 V , along with a capacity retention of 74.4% after 100 cycles [590]. W+Mg co-doping improves the electrochemical performance, because of the reduced particle size induced by the W^{6+} and increased free electron induced by the Mg^{2+} [591] (see Figure 14). This co-doping of $\text{LiNi}_{0.9}\text{Co}_{0.06}\text{Mn}_{0.04}\text{O}_2$ single-crystal raised the capacity retention to 86.7% after 150 cycles at 2 C current density. K+F co-doping of single-crystalline $\text{LiNi}_{0.85}\text{Co}_{0.05}\text{Mn}_{0.10}\text{O}_2$ (NCM85) endowed this cathode with a very high reversible capacity of 222.3 mAh g^{-1} .

A superior capacity retention of 91.3% was obtained after 500 times at 1 C in pouch-type full cells, and a prediction value of 75.3% is given after cycling for 5000 h [592]. K+Ti-co-doped NMC811 delivered a capacity of $160.42 \text{ mAh g}^{-1}$ and 91.19% capacity retention at 1 C after 200 cycles between 2.75 and 4.35 V due to the synergistic effect of K doping and Li_2TiO_3 coating associated with the introduction of Ti [593].

K doping enlarges the interlayer space to accelerate Li^+ transport, while Ti doping can strengthen Ni–O bonds to improve the structure stability. The Li_2TiO_3 coating protected the surface of the particles against side reactions with the electrolyte. Al+Fe co-doping into NMC622 combines the polarization effects of Fe with the lower chemical potential attributed to Al [545]. However, the performance was not as good as in NMC doped with Sn, studied in the same work. He et al. synthesized single-crystal $\text{LiNi}_{0.92}\text{Co}_{0.04}\text{Mn}_{0.04}\text{O}_2$ with cation Mo^{6+} and anion F^- elements co-doped in the near-surface region. For this purpose, nano- MoO_3 was additionally added at the stage of mixing precursor of the NMC synthesis. Then, NMC powder was blended with NH_4F via ball-milling [594]. Al+Na co-doping combines Al-doping that forms strong Al-O bonds and reduces the $\text{Li}^+/\text{Ni}^{2+}$

mixing, and Na-doping that widens the ion diffusion channels. As a result, the full concentration gradient $\text{Li}_{1-y}\text{Na}_y\text{Ni}_{0.80}\text{Co}_{0.05}\text{Mn}_{0.15-x}\text{Al}_x\text{O}_2$ co-doped with 0.1 mol% Al and 1 mol% Na exhibited a capacity retention of 93% after 200 cycles at a rate of 1 C [595]. Mo^{6+} and F^- constructed an appropriate $\text{Li}^+/\text{Ni}^{2+}$ antisite defects structure at the particle surface, boosting the interfacial stability and reducing the lattice mismatch. In addition, this surface modification maintained the low-defect Li^+ layered channel inside the bulk simultaneously. The corresponding cathode delivered a high capacity of 204 mAh g^{-1} at 1 C. A full cell constructed with this cathode element exhibited a capacity retention of 91.9% after 400 cycles in 2.8–4.4 V, against 76.9% for the pristine cathode. Na+F co-doping of NMC622 also significantly improved the electrochemical properties [596]. Nb+B co-doping of NMC811 exhibits strong radial orientation and exposes a large number of active (003) lattice plane on the particle surface. As a cathode, this modified NMC811 maintained a capacity retention of 86.71% after 200 cycles at 1 C [597]. Li et al. synthesized a Ce+Gd dopant-concentrated layer single-crystal $\text{LiNi}_{0.83}\text{Co}_{0.07}\text{Mn}_{0.10}\text{O}_2$, including a Gd doped LiCeO_2 (LCGO) shell and Ce/Gd dopant-concentrated layer [598]. The corresponding cathode capacity retention of 90.2% after 100 cycles at 1.0 C. In a different approach, Park and Kim introduced B and Ca in the cathode–electrolyte interface, where the B-functional group decreases the residual Li^+ species, while Ca suppresses the microcracks [599]. With this CEI, the capacity retention after 100 cycles at 0.5 C was improved from 44.3% to 72.4%. Recently, Usman et al. synthesized V+Zn-co-doped LiNiO_2 and found that $\text{LiNi}_{0.52}\text{Zn}_{0.16}\text{V}_{0.32}\text{O}_2$ has a discharge capacity of 48–246 mAh g^{-1} with an intercalation voltage of 5.77–3.35 V [600]. The Ti+Al co-substituted $\text{LiNi}_{0.92}\text{Co}_{0.08}\text{O}_2$ cycled in a voltage range of 2.75–4.3 V at a rate of 0.2 C, delivered an initial capacity of 197.7 mAh g^{-1} with a capacity retention of 82.6% after 100 cycles [601]. Ti+F-co-doped NMC811 delivered a discharge capacity of $202.2 \text{ mA h g}^{-1}$ at 1 C and 45 °C, with a capacity retention of 88.1% after 200 cycles (only 45.2% for the pristine NMC811). This performance was attributed not only to the bulk doping effect, but also the fact that Ti^{4+} and F^- co-dopants induce the formation of an ultra-thin rock-salt phase on the cathode surface, which provides a protective layer [602]. Such a surface rock-salt nanolayer was also successfully developed on the $\text{LiNi}_{0.9}\text{Co}_{0.1}\text{O}_2$ subsurface via heteroatom anchoring utilizing high-valence element molybdenum modification [603]. With this modification, the cathode exhibited a capacity of 245.4 mAh g^{-1} at 0.1 C, remarkable rate performance of 169.3 mAh g^{-1} at 10 C at 4.5 V, and a high capacity retention of 70.5% after 1000 cycles in full cells at a high cut-off voltage of 4.4 V. Fe+F-co-doped Ni-rich, Li-rich cathode elements have improved electrochemical properties, because the Fe dopant increases both the electronic and ionic conduction, while the F dopant can improve the cycling stability remarkably by lowering the O_{2p} band top to suppress the lattice oxygen escape [604]. In addition, F doping within the oxygen sites with a larger ionic radius increases the distance between the (003) planes, and thus increases the lithium diffusivity. Moreover, the bonding energy between transition metals (TMs) and F (TM-F) is larger than that of TM-O, so that F can fix Ni^{2+} at the Ni site, thereby reducing the cation mixing [543]. In+Sn-co-doped $\text{LiNi}_{0.85}\text{Mn}_{0.09}\text{Al}_{0.06}\text{O}_2$ exhibited a capacity retention of ~100% and ~90% within the voltage range of 2.7–4.5 V at 30 °C and 45 °C, respectively, after 100 cycles at 0.4 C [605]. This result is due not only to the bulk doping, but also to in situ formed coating of LiInO_2 effectively protecting the cathode. Na^+ inserted into the Li site expands the Li slab, due to its large ionic radius, while Al^{3+} stabilizes the structure through a high Al-O bonding energy. Combing these two advantages, Na+Al-co-doped $\text{LiNi}_{0.88}\text{Co}_{0.08}\text{Mn}_{0.04}\text{O}_2$ cathode material exhibited a capacity retention of 84% after 50 cycles at 1 C [606], higher compared with the pristine material doped with only Al or only Na. Peng et al. synthesized NMC811 modified by Mg+Ti not only in the bulk, but also by the formation of an Mg_2TiO_4 and $\text{Mg}_{0.5-x}\text{Ti}_{2-y}(\text{PO}_4)_3$ outer layer with Mg and Ti vacancies [607]. The corresponding

cathode cycled in the voltage range 2.7–4.5 V at 1 C rate exhibited a capacity retention of 89.3% after 200 cycles. Zhang et al. evaluated concentration-gradient Mg+Al-co-doped $\text{LiNi}_{0.95}\text{Co}_{0.03}\text{Al}_{0.01}\text{Mg}_{0.01}\text{O}_2$. As a cathode, this material exhibited a high-rate capacity (172.9 mAh g^{-1} at 10 C rate), enhanced cyclability (95.6%, 100 cycles at 1 C) and less microcrack formation [608]. Ba+Al co-doping of $\text{LiNi}_{0.85}\text{Co}_{0.05}\text{Mn}_{0.10}\text{O}_2$ (NCM85) single-crystalline cathode increased the capacity up to 87.5% after 500 cycles at 1 C in a pouch-type full cell [609]. The strong Zr-O bond facilitates the lithium diffusion, while Ga doping can promote cation order and strengthen the TM-O bond energy, diminishing the oxygen loss. As a result, Zr+Ga-co-doped $\text{LiNi}_{0.94}\text{Co}_{0.03}\text{Mn}_{0.03}\text{O}_2$ exhibited a capacity retention of 91.9% at 0.5 C after 100 cycles, compared to 72.64% for the pristine material [610]. The optimal amount (0.5 mol.%) of each Na^+ and Y^{3+} dopants increased the capacity retention of NCA to 92.34% of its capacity after 100 charge and discharge cycles at a rate of 0.5 C, compared to 67.11% for the pristine NCA [611]. In this case, the calculated Bader charge of oxygen in pristine and modified materials increased from -1.18 to -1.38 e in the fully lithiated structures, confirming the significant impact of doping on reducing the oxygen release rate.

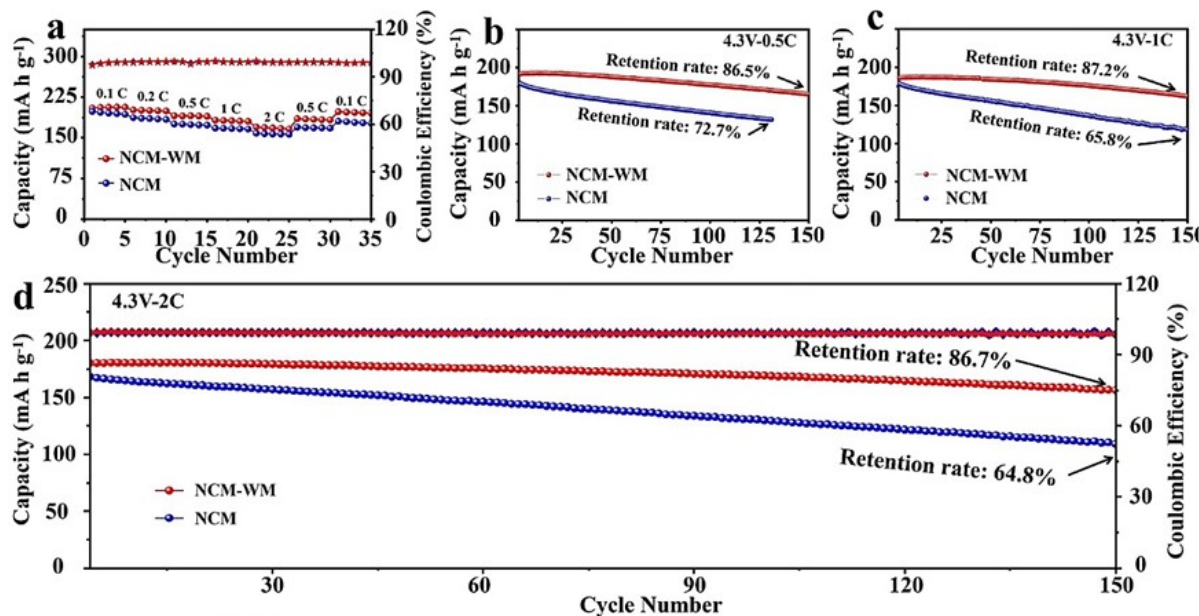


Figure 14. Electrochemical performance comparison of pristine $\text{LiNi}_{0.9}\text{Co}_{0.06}\text{Mn}_{0.04}\text{O}_2$ (NCM) and NCM co-doped with W and Mg (NCM-WM). (a) Rate capability of NCM-WM in 3.0–4.3 V. Cycling performance of NCM and NCM-WM at 25 °C between 3.0 and 4.3 V at (b) 0.5 C, (c) 1 C, and (d) 2 C. Reproduced from ref. [591]. Copyright 2025 Elsevier.

Co-doping with high-valence dopants is also efficient. Li-ion pouch cells with Ta^{5+} - and Mo^{6+} -doped $\text{Li}[\text{Ni}_{0.91}\text{Co}_{0.09}]\text{O}_2$ cathodes retain about 81.5% of their initial specific capacity after 3000 cycles at 200 mA g^{-1} [468]. Y^{3+} and W^{6+} co-doping of the single-crystal cobalt-free $\text{LiNi}_{0.9}\text{Mn}_{0.1}\text{O}_2$ cathode exhibited a capacity retention of 82.1% at 1.0 C after 100 cycles (compared to 71.9% for the undoped cathode), and at 3 C the co-doped sample displayed a high specific capacity of 152.0 mAh g^{-1} , while the value for the pristine is only 139.8 mAh g^{-1} [612]. More recently, Zhang et al. co-doped $\text{LiNi}_{0.9}\text{Mn}_{0.1}\text{O}_2$ with Zr^{4+} and Mo^{6+} substituting transition metal element and Mg^{2+} replacing Li^+ to obtain a cathode exhibiting 87.5% capacity retention after 210 cycles at 1 C and 85.5% after 150 cycles at 2 C [613] (see Figure 15).

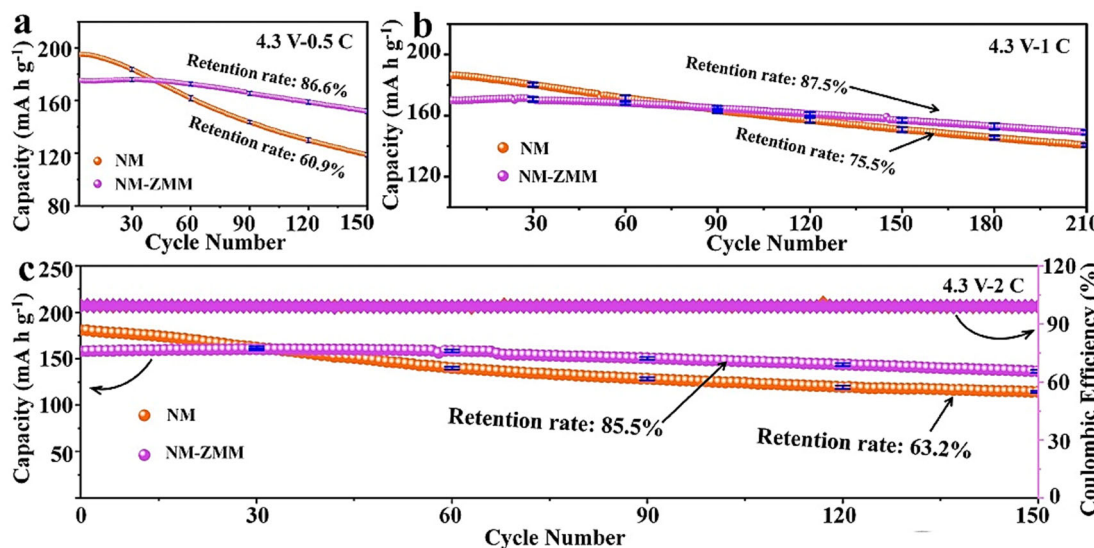


Figure 15. Electrochemical performance comparison of pristine $\text{LiNi}_{0.9}\text{Mn}_{0.1}\text{O}_2$ (NM) and NM doped with Zr^{4+} , Mo^{6+} substituting transition metal element and Mg^{2+} replacing Li^+ (NM-ZMM). Cycling performance of pristine NM and NM-ZMM electrode materials between 3.0 and 4.3 V at (a) 0.5 C, (b) 1 C, and (c) 2 C. Reproduced from ref. [613]. Copyright 2025 Elsevier.

The high-valence dopant W^{6+} and low-valence Na^+ co-doping is also a good strategy, since the high-valence doping element improves the structural stability by forming strong metal–oxygen binding forces, while the low-valence doping element eliminates high cation mixing. A single-crystal Ni-rich $\text{LiNi}_{0.83}\text{Co}_{0.12}\text{Mn}_{0.05}\text{O}_2$ cathode material with this-co-doping exhibited a capacity retention of 87% after 1000 cycles (vs. graphite/ Li^+) in pouch-type full cells at a high temperature of 55 °C [614].

Other co-doping improving the electrochemical and structural stability of NMC materials includes $\text{Na}+\text{F}$ [538,615], $\text{Na}+\text{Al}$ [616], $\text{Al}+\text{Nb}$ [617–619], $\text{Ga}+\text{B}$ [620], $\text{Al}+\text{Y}$ [621], $\text{Zr}+\text{B}$ [622,623], $\text{Zr}+\text{Mg}$ [590], $\text{Zr}+\text{Al}$ [624], $\text{Zr}+\text{La}$ [625], $\text{Ti}+\text{Ta}$ [626], $\text{Mo}+\text{F}$ [627], $\text{Mo}+\text{Ti}$ [628], $\text{Ti}+\text{Al}$ [601,629], $\text{Cu}+\text{Ti}$ [630], $\text{B}+\text{Ti}$ [631], $\text{Mg}+\text{Ti}$ [632,633], $\text{Mg}+\text{F}$ [634], $\text{Na}+\text{Y}$ [611], and $\text{Co}+\text{Ti}$ [635]. Xiao et al. gave evidence of the important role of Co+Al doping in inhibiting cation disorder to increase the lithium-ion diffusion rate in $\text{LiNi}_{0.84}\text{Mn}_{0.10}\text{Co}_{0.03}\text{Al}_{0.03}\text{O}_2$ [636]. Shi et al. selected Co+La co-coating. The single-crystal NMC811 prepared by Shi et al. with 2 wt.% $\text{La}_2\text{Li}_{0.5}\text{Co}_{0.5}\text{O}_4$ coating exhibited a capacity retention of 81.15% after 200 cycles at 1 C [637]. This is a 18% improvement with respect to the pristine NMC811 prepared by Shi et al., but smaller than that of the pristine nano-sized and single crystallized NMC811 particles of Lao et al. [230], which emphasizes the important role of the morphology to optimize the electrochemical properties. Yoon et al. reported a room-temperature synthesis route to achieve a full surface coverage of secondary particles and facile infusion into grain boundaries, and thus offered a complete Co+B ‘coating-plus-infusion’ strategy, by applying cobalt boride metallic glass to NMC811 [638]. The effect of B+Al doping of LiNiO_2 was investigated by Kim et al. [639]. They found that the low solubility of B into the host structure leads to a surface-confined distribution of B, inhibiting the growth of primary particles, whereas the highly soluble Al facilitates primary particle growth. As a consequence of this difference, boron-doping was found the most effective dopant strategy for microstructural engineering of the primary particles. The B-doped LiNiO_2 cathode exhibited a capacity retention of 81% in full cells, after 300 cycles, significantly better compared with Al-doped LiNiO_2 . While B accumulates close to the surface, Ti is uniformly distributed in NMCs, so that the formation of strong Ti-O bond effectively alleviates the bulk phase structure degradation. As a result, Ti+B-modified NMC exhibited a capacity retention of 95.4% after 150 cycles between 2.7–4.3 V at 1 C and excellent rate performance of 137.7 mAh g^{-1} at

5 C [640]. Kuo et al. investigated the effect of B^{3+} and Ru^{5+} on the structure and electrochemical performance of NMC811 [641]. They demonstrated that B-doping leads to the formation of a boron oxide-containing surface coating, mainly on the outer surface of secondary particles, thus improving the cycle ability. On the other hand, Ru preferentially occupies incoherent grain boundary sites, resulting in smaller primary particle size. DFT calculations confirm that B-doping forms an enriched surface, and also find that Al-doping results in Al-rich bulk [642].

Zhang et al. [483] synthesized high-voltage single-crystal cathode material $LiNi_{0.6}Co_{0.1}Mn_{0.3}O_2$ with in situ doping of Zr^{4+} and Ti^{4+} by precursor co-precipitation. The synergistic effect of Zr/Ti co-doping on the transition metal (TM) sites in the SC-NCM material not only effectively improved the diffusion migration rate of Li^+ but also reduced the stress concentration and cation disorder inside particles. The capacity retention rate of its soft-packed full battery was 80.6% after 4000 cycles.

Al+Zr-co-doped single-crystalline $LiNi_{0.88}Co_{0.09}Mn_{0.03}O_2$ delivered a discharge capacity of 121.2 mAh g^{-1} at 5.0 C (1000 mA g^{-1}) with a cut-off voltage of 4.6 V after 350 cycles, while the pristine material falls to nearly zero after 200 cycles under the same conditions [643]. The authors attributed the effect of the Al/Zr doping to the reduction of the Li^+ ion energy barrier from 500 meV in the pristine material to 70–130 meV, and the increase of the Ni atomic transfer barrier from the initial 2.07 eV to 2.37–2.68 eV, indicating that Ni can exist in a stable state. The Al^{3+} and PO_4^{3-} co-doping of NMC811 inhibited the mixing of lithium and nickel, and maintained the good lamellar structure of the cathode material [644]. As a result, the capacity retention rate of the cathode with this modified NMC811 was 14.1% higher than that of the raw material after 100 cycles at 1 C. The rate capability was also increased, with a capacity of 155.8 mAh g^{-1} at 5 C. In the particular case of NCA, Al+Mn, Mg+Mn, Fe+Al, Ti+MgAl+Ti+Mg co-doping also proved useful to improve the electrochemical properties and structural stability, as reviewed in [71]. A comparative study of the dual-doping effect on Ni-rich cathodes is reported in Table 3.

Table 3. Effects of dual-doping on cycling ability of Ni-rich cathode elements. Capacity densities are expressed in mAh g^{-1} . Asterisk symbol after cathode element indicates that upper voltage cut-off for cycles is 4.5 V. Otherwise, unless specified, cut-off is 4.3 V.

Cathode Element	Dual Doping	Cycle at C-Rate	Pristine		Doped		Ref.
			Capacity (mAh g^{-1})	Retention (%)	Capacity (mAh g^{-1})	Retention (%)	
NMC811 (cut-off at 4.8 V)	Mg+Zr	100@C/10	201.8	66	232.2	70.5	[590]
$LiNi_{0.90}Co_{0.06}Mn_{0.04}O_2$	Mg+W	150@2 C	170	64.8	180	86.7	[591]
$LiNi_{0.85}Co_{0.05}Mn_{0.10}O_2$ *	K+F	500@1 C	185	75	190	91.5	[592]
NMC811	K+Ti	200@1 C	182	59.4	175	91.2	[593]
$LiNi_{0.92}Co_{0.04}Mn_{0.04}O_2$ *	Mo+F	200@1 C	200	0	204	87.1	[594]
$LiNi_{0.80}Co_{0.05}Mn_{0.15}O_2$ *	Al+Na	200@1 C	196	70	205	84	[595]
NMC811	B+Nb	200@1 C	175	76.1	175	86.7	[597]
$LiNi_{0.83}Co_{0.07}Mn_{0.10}O_2$	Ce+Gd	100@1 C	192.6	82.5	194.6	90.2	[598]
$LiNi_{0.83}Co_{0.11}Mn_{0.06}O_2$	B+Ca	100@C/2	190	44.3	190	72.4	[599]
$LiNi_{0.92}Co_{0.08}O_2$	Ti+Al	100@C/5	208.7	76.5	197.7	93.8	[601]
$LiNi_{0.85}Mn_{0.09}Al_{0.06}O_2$	In+Sn	100@C/2	160	86.6	162	100	[605]
$LiNi_{0.88}Co_{0.08}Mn_{0.04}O_2$	Na+Al	50@1 C	183.91	78.6	192.49	83.7	[606]
$LiNi_{0.95}Co_{0.03}Al_{0.01}Mg_{0.01}O_2$	Mg+Al	100@1 C	190	60.8	200	95.6	[608]
$LiNi_{0.8}Co_{0.15}Al_{0.05}O_2$	Na+Y	100@C/2	172	67.1	175	92.3	[611]
$LiNi_{0.9}Mn_{0.1}O_2$	W+Y	100@1 C	178	71.9	180	82.1	[612]

Table 3. Cont.

Cathode Element	Dual Doping	Cycle at C-Rate	Pristine		Doped		Ref.
			Capacity (mAh g ⁻¹)	Retention (%)	Capacity (mAh g ⁻¹)	Retention (%)	
LiNi _{0.9} Mn _{0.1} O ₂	Zr+Mo+Mg	150@2 C	180	63.2	160	85.5	[613]
LiNi _{0.83} Co _{0.12} Mn _{0.05} O ₂ at 55 °C	Na+W	1000@1 C 500@1 C	185 80	0 80	197.5	87	[614]
NMC811	Na+Al	80@1 C	175	84.5	175	93	[616]
LiNi _{0.96} Co _{0.04} O ₂ (cut-off 4.4 V)	Al+Nb	300	200	48.5	200	77.8	[617]
Li[Ni _{0.92} Co _{0.04} Mn _{0.04}]O ₂	Al+Nb	500@1 C	195	0	183	75.6	[618]
LiNi _{0.83} Co _{0.12} Mn _{0.05} O ₂	Al+Nb	100@1 C	172	75	172	95.1	[619]
LiNi _{0.94} Co _{0.06} O ₂	Al+Y	500@1 C	200	54.6	200	80.2	[621]
Li[Ni _{0.885} Co _{0.100} Al _{0.015}]O ₂	Zr+B	1000@1 C	190	48	178	95	[623]
LiNi _{0.83} Co _{0.12} Mn _{0.05} O ₂	Zr+Al	300@5 C	150	26.1	157	80.5	[624]
LiNi _{0.83} Co _{0.11} Mn _{0.06} O ₂ *	Zr+La	200@1 C	200.9	66.2	189.0	86.1	[625]
NMC811	Ti+Ta	250@1 C	155.4	59.8	161.1	87.1	[626]
NMC811	Mo+F	500@1 C	182	67.3	181	87.1	[627]
Ni _{0.9} Co _{0.05} Mn _{0.05} O ₂	Mo+Ti	100@C/2	96.09	53	98.85	69	[628]
Li(Ni _{0.83} Co _{0.12} Mn _{0.05})O ₂ *	Ti+Al	500@1 C	170	35.1	180	71.8	[629]
NMC811	Ti+B	100@1 C	186.8	71.1	173.4	94.7%	[631]
Li[Ni _{0.90} Co _{0.05} Mn _{0.05}]O ₂	Ti+Mg	100@1 C	157	86.6	158	98.9	[632]
LiNi _{0.89} Co _{0.11} O ₂	Ti+Mg	200@1 C	195	74.3	190	86.5	[633]
LiNi _{0.8} Co _{0.15} Al _{0.015} O ₂	Mg+F	200@1 C	175	55.7	175	82.6	[634]
NMC811	Co+Ti	400@1 C	175	89.9	170	97.1	[635]

5.4.2. Doping Plus Coating

Doping is often concomitant with surface coating to benefit from the synergistic effect [645]. When cycled at a discharge rate of 3 C for 500 cycles within 2.75–4.3 V, the cell with Ge-doped ((Ni+Mn):Ge = 100:0.5 in molar ratio) LiNi_{0.9}Mn_{0.1}O₂ cathode and graphite anode exhibited a discharge capacity retention of 80.5%, whereas that of the cell without Ge is only 52.9% [491]. Note that the improvement does not come only from the Ge⁴⁺-doping, but also from the fact that the doping is accompanied with the coating with a Li₄GeO₄ layer. The doping stabilizes the ordered layered structure and limits the Ni-Li substitution, which increases the rate capability, while the coat performs as a barrier to reduce the parasitic reactions, which increases the cycle life. Park et al. have advanced in microstructure engineering by the formation of F-rich species on the surfaces of internal grains, combined with 2 mol% F⁻ doping inside Li[Ni_{0.900}Co_{0.047}Mn_{0.048}Mo_{0.005}]O₂ [646]. The full cell with this cathode material and graphite anode delivered a capacity of 177.2 mAh g⁻¹ (90.4% of its initial capacity) after 800 cycles at 1 C and 45 °C. Synergetic effects are obtained by combining doping and coating. We have already mentioned the capacity retention of 93.7% obtained for 2% Sn-doped NMC811, after 270 cycles at 0.5 C. This capacity retention rises to 96.6% when the Sn-doped particles are also Li₂SnO₃-coated [547]. The positive effect of Sn-doping is mainly due to higher structural stability and reduction of the Li/Ni mixing, and lower polarization than those of the bare NMC811. The Li₂SnO₃-coating improves the interfacial stability. The same Li₂SnO₃-coating plus Sn⁴⁺ doping strategy has been recently utilized to modify LiNi_{0.8}Mn_{0.2}O₂ [647] (see Figure 16). This Co-free cathode with the optimized amount (2 wt.%) Li₂SnO₃ delivered an initial capacity of 173.20 mA h g⁻¹ and a capacity retention of 90.54% after 300 cycles at 0.2 C, outperforming the results with pristine LiNi_{0.8}Mn_{0.2}O₂ cathode.

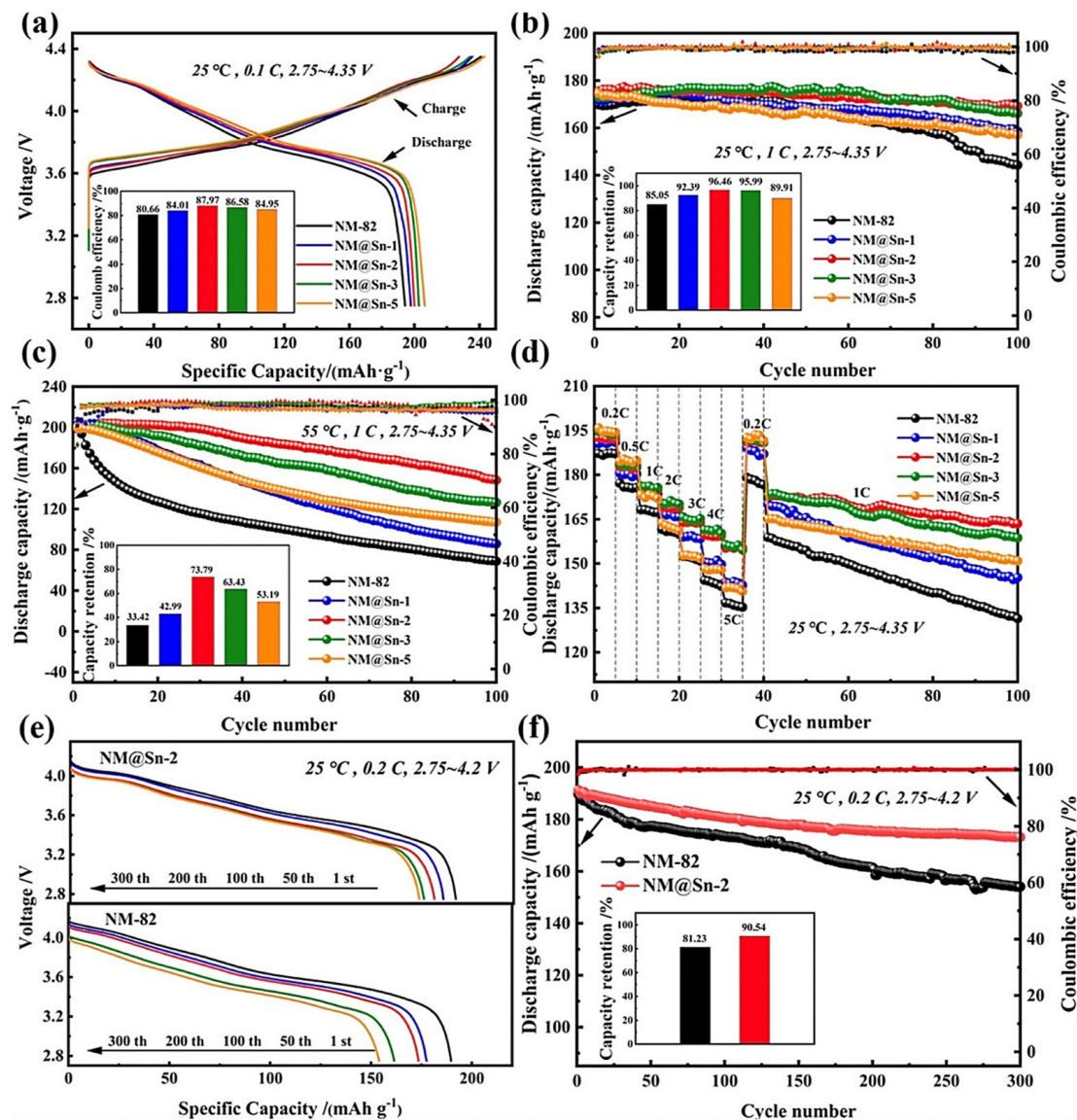


Figure 16. Electrochemical performance of different Sn-doped $\text{LiNi}_{0.8}\text{Mn}_{0.2}\text{O}_2$ materials coated with Li_2SnO_3 ($\text{NM}@\text{Sn}-n$) materials, where n is nominal mass fraction of SnO_2 in wt.%. Half-cell tests: (a) Charge/discharge profiles for an initial cycle at 0.1 C, (b) cycle performance at 1.0 C at 25 °C, (c) cycle performance at 1.0 C at 55 °C, and (d) rate capability at 25 °C. Full-cell tests: (e) Charge/discharge profiles and (f) cycle performance of the NM-82 and NM@Sn-2 cathodes. Reproduced from ref. [647]. Copyright 2023 American Chemical Society.

The same strategy consisting in combining coating and doping was applied, choosing boron instead of the tin element. Lithium tetraborate $\text{Li}_2\text{B}_4\text{O}_7$ coating and boron doping applied to the Co-less Ni-rich $\text{LiNi}_{0.925}\text{Co}_{0.03}\text{Mn}_{0.045}\text{O}_2$ cathode increased the capacity retention at 0.2 C from 59.65% for the pristine material to 72.86% after 100 cycles at 55 °C. At room temperature, the capacity retention of this B-modified cathode was raised to 76.29% after 150 cycles at 1 C [648]. Li et al. synthesized B-doped and $\text{La}_4\text{NiLiO}_8$ -coated $\text{LiNi}_{0.825}\text{Co}_{0.115}\text{Mn}_{0.06}\text{O}_2$. This cathode demonstrated a capacity retention of 93.49% after 500 cycles at 1 C. [649]. This outstanding performance is due to the combination of the protecting role played by the $\text{La}_4\text{NiLiO}_8$ coat, and the boron doping that not only stabilized the structure by restraining the H2–H3 transition, but also adjusted the orientation of primary particles to a radial alignment, which is obstructive to the arise of microcracks. This result outperforms a previous study of the NMC811 with the same coating but Ti-

doped instead of B-doped, which exhibited a capacity of 158.3 mAh g^{-1} after 200 cycles at 1 C, corresponding to a capacity retention of 90.6% [650]. Kim et al. synthesized a fast ionic conductor Li_3BO_3 coating and B^{3+} -doped co-modified $\text{LiNi}_{0.91}\text{Co}_{0.06}\text{Mn}_{0.03}\text{O}_2$ [651]. This significantly improved the rate capability, with a discharge capacity of 88.6 mAh g^{-1} at 5 C while pristine delivered only 45.8 mAh g^{-1} . It also improved the cycle ability, with the capacity retention of 79.4% as compared to 67.3% for the pristine material after 100 cycles 2 C. The same synergistic effect of Li_3BO_3 coating was used to modify single-crystal Zr-doped $\text{LiNi}_{0.83}\text{Co}_{0.11}\text{Mn}_{0.06}\text{O}_2$ (Zr-NCM83@B) [652]. The Zr-NCM83@B//graphite pouch-type full cell displayed excellent capacity retention of 83.5% over 1400 cycles at 1 C with high voltage range of 2.8–4.4 V.

Cao et al. produced a dual-modified coating of B_2O_3 and LiBO_2 to the high-nickel material $\text{LiNi}_{0.89}\text{Co}_{0.08}\text{Mn}_{0.03}\text{O}_2$ [653]. With this protection, the cathode delivered a high capacity of 180.4 mAh g^{-1} along with an excellent capacity retention of 90% after 100 cycles at 1 C in 2.75–4.35 V (59% for the pristine material). The same dual-modified coating was applied to NMC811 with the same success [654]. Li_3BO_3 -coating was also associated with La-doping. When applied to NMC811, the capacity was raised to 230.6 mAh g^{-1} at 0.5 C under a high cutoff voltage of 4.8 V, with a 73.8% capacity retention after 100 cycles [655].

NASICON is an acronym for sodium (Na) super ionic conductor, which usually refers to a family of solids with the chemical formula $\text{Na}_{1+x}\text{Zr}_2\text{Si}_x\text{P}_{3-x}\text{O}_{12}$, $0 < x < 3$. We use this term in the following in a broader sense, for similar compounds where Na, Zr and/or Si are replaced by isovalent elements. Tang et al. constructed a protective NASICON-type $\text{Li}_{1.3}\text{Y}_{0.3}\text{Zr}_{1.7}(\text{PO}_4)_3$ (LYZP) coating with Zr gradient doping on the surface/subsurface of single-crystalline $\text{LiNi}_{0.83}\text{Co}_{0.11}\text{Mn}_{0.06}\text{O}_2$ (SC-NCM83) [656]. The full-cell LYZP-modified SC-NCM83//graphite demonstrated a capacity retention of 83.7% after 500 cycles at 0.5 C, a performance that highlights its potential for commercial applications. Another NASICON-type $\text{LiZr}_2(\text{PO}_4)_3$ coating of NCA enhanced the capacity to 182 mAh g^{-1} at 1 C in 2.7–4.3 V, with the capacity retention of 84.6% after 100 cycles [657].

The Li-free Nb oxide treatment removed surface impurities forming a $\text{LiNbO}_3/\text{Li}_3\text{NbO}_4$ coating of Ni-rich cathode materials, to reduce the first capacity loss and to improve the rate performance. Nb substitution stabilized the structure, increasing the capacity retention to 93.2% after 250 cycles at C/3 rate in the voltage range 2.8–4.4 V [658]. Xin et al. performed Li-Nb-O coating and Nb substitution on NMC811, enhancing both the rate (158 vs. 135 mAh g^{-1} at 2 C) and capacity retention (89.6 vs. 81.6% after 60 cycles) performance [659]. Zhang et al. proposed dual-modification strategy, in which Sm was both doped into and coated on NMC811 [660]. With the optimum Sm content (0.5%), this modified NMC811 demonstrated a discharge specific capacity of 184.2 mAh g^{-1} at 1 C rate, a capacity retention of 94.19% after 100 cycles at 1 C, and a good rate performance (152.2 mAh g^{-1} at 5 C).

A thermochemical investigation shows that Zr preferentially form secondary phases rather than becoming doped in the NMC crystal; therefore, the equilibrium doping concentration of Zr in the NMC is very low and the material is a mixture of almost undoped NMC with a Li_2ZrO_3 secondary phase [661]. In the case of $\text{LiNi}_{0.96}\text{Mn}_{0.04}\text{O}_2$, the introduction of Zr resulted in the Li_2ZrO_3 coating of the particles [662]. On the other hand, Zheng et al. successively processed NCA carbonate oxalate precursors with $(\text{NH}_4)_2\text{HPO}_4$ and ZrOCl_2 solutions to obtain an ultrathin Zr-contained gradient layer at the surface of NCA. Experimental characterization together with DFT calculations revealed that Zr at lithium site strengthens the adjacent (Ni,Co)-O bonds, inhibiting the oxygen evolution and stabilizing the surface. As a result, the cathode delivered a high capacity of $219.7 \text{ mA h} \cdot \text{g}^{-1}$, 23% higher than NCA at 0.1 C, and exhibits superior rate capability ($128.2 \text{ mA h} \cdot \text{g}^{-1}$ capacity at 16 C) and cycling stability (capacity of 110.5 mAh g^{-1} after 300 cycles at 1 C) [574]. Dai et al.

synthesized a highly-antioxidative BaZrO₃ thermal barrier engineered LiNi_{0.8}Co_{0.1}Mn_{0.1}O₂ cathode. Analyses showed that the Zr element was penetrated uniformly into the interior region, so that the material benefited of the rigid Zr–O bonds, which improve the structural stability. On the other hand, the Ba element was only concentrated in the exterior region of secondary particles, impeding the fast heat exchange between electrode and electrolyte [663]. This cathode in a pouch cell delivered a specific energy density of 690 Wh kg⁻¹ at active material level with an excellent capacity retention of 92.5% after 1400 cycles under 1 C at 25 °C. At high temperature of 55 °C, the pouch cell exhibited 88.7% in capacity retention after 1200 cycles. Here, Zr was effectively incorporated in the structure to form Zr–O bonds ensuring stability of lattice O upon cycling. As a result, the cell with this cathode and graphite anode exhibited a superior capacity retention of 92.5% after 1400 cycles at 25 °C, and a resultant 174.1 mAh g⁻¹ with 88.7% in capacity retention after 1200 cycles at 55 °C. In situ Zr-doping achieved a gradient distribution of Zr inside the particles of full-concentration-gradient LiNi_{0.80}Co_{0.05}Mn_{0.15}O₂. The corresponding cathode delivered an initial discharge specific capacity of 181.7 mAh g⁻¹ with 91.9% capacity retention at room temperature and 85.2% at 50 °C, after 200 cycles (1 C, 2.7–4.3 V) [664]. Instead of Zr, yttrium can be utilized [665]. Luo et al. utilized synergetic effects of Y³⁺ doping and Y₂O₃ coating of NMC to prolong the lifetime of Ni-rich Co-less material exposed to air [666]. The same synergetic effect has been observed in ultrahigh-Ni NMC cathodes, such as in situ synthesized Y-doped and yttrium orthophosphate (YPO₄)-modified LiNi_{0.88}Co_{0.09}Al_{0.03}O₂ [510]. The enrichment of these functional elements Ti [92], Zr, or Y at the particle surface is easily obtained in situ due to the slow kinetics of their diffusion.

Ti-doped and TiO₂-coated NMC811 full cells cycled for 200 cycles between 2.8 and 4.4 V at C/3 improves from 86.1% for the pristine NMC811 to 89.4% and 91.5%, respectively [667]. TiO₂ coating improves the cycling stability of NMC811 by minimizing contact between the active material and the electrolyte [668] and reduces the air and moisture sensitivity of NMC622 [669]. Due to the synergistic effects of the Li₃PO₄ coating and Ti-doping, the dual-modified LiNi_{0.9}Co_{0.09}Mo_{0.01}O₂ exhibited a discharge capacity of 218.7 mAh g⁻¹ at 0.1 C (1 C = 220 mA g⁻¹) and a capacity retention of 93.7% at 0.5 C after 100 cycles [670]. Al₂O₃-coated/Al³⁺ and Zr⁴⁺ co-doped NMC811 delivered an initial capacity of 196 mAh g⁻¹ and arrived at a high discharge capacity of 120 mAh g⁻¹ after 200 cycles at 0.5 C, corresponding to a capacity retention of 98%, compared to 70.4% for the pristine material [671].

Recently, Chen et al. modified LiNi_{0.84}Co_{0.11}Mn_{0.05}O₂ with Al³⁺ doped bulk lattice, W⁶⁺ doped subsurface region and hetero-epitaxially grown Li₂WO₄. The modified LiNi_{0.84}Co_{0.11}Mn_{0.05}O₂ showed a capacity retention rate of 88.98% after 200 cycles at 1 C rate in the potential range of 2.7–4.3 V and 82.41% after 200 cycles at 1 C with a high cut-off voltage of 4.5 V at 30 °C [672]. With Zr⁴⁺ doping plus Li₆Zr₂O₇ coating LiNi_{0.83}Co_{0.12}Mn_{0.05}O₂ cycled at 1 C delivered a capacity of 183.7 mAh g⁻¹ with a capacity retention of 94.6% after 200 cycles, compared to 129.9 mAh g⁻¹ and 68.6%, respectively, for the pristine material [479]. W⁶⁺ doping plus WO₃ coating improved the capacity retention of NMC above 90.2% after 200 cycles at 1 C [673]. Li et al. have recently evidenced the fastest inter-diffusivity of W⁶⁺/Mnⁿ⁺ (*n* = 3 and 4) couple in Ni-rich cathodes. As a result, when Mn proportion is decreased to 10%, Li₆WO₆ coating of grain boundaries and bulk W-doping have been achieved in LiNi_{0.9}Mn_{0.1}O₂ and LiNi_{0.8}Co_{0.1}Mn_{0.1}O₂ cathodes, so cyclic stabilities of W-modified LiNi_{0.9}Mn_{0.1}O₂ have been prominently improved [463]. Recently, Li(Ni_{0.80}Mn_{0.18}Al_{0.02})_{1-x}W_xO₂ with the optimized value *x* = 0.02 as a cathode delivered an initial discharge specific capacity of 212.9 mAh g⁻¹ at 0.1 C in 2.7–4.5 V and the capacity retention reached 91.91% after 100 cycles at 1 C [674], also emphasizing the effect of tungsten, which promotes Li⁺ migration and suppresses surface side reactions. WO₃-coated

and Mg²⁺-doped NMC811 exhibited a capacity retention of 73.5% after 100 cycles at 1 C rate against 53.6% for the pristine material [675].

Xiao et al. coated K-doped LiNi_{0.83}Co_{0.11}Mn_{0.06}O₂ with Li₃PO₄. This cathode delivered a discharge specific capacity of 148.9 mAh·g⁻¹ with a capacity retention of 84.1% after 200 cycles at 1.0 C [676]. PO₄³⁻-doping and Li₃PO₄-coating of dual modification of LiNiO₂ significantly improved the structural stability, and thus the cycle ability of this electrode which exhibited a capacity retention of 81.6% (from 180.8 to 147.6 mAh g⁻¹) after 200 cycles at 0.5 C, when cycled in the range 3–4.3V, and 51.0% capacity retention after 1000 cycles at 1 C [677]. The good cycle ability is due to the coating, while the improved rate capability (a capacity of 130.2 mAh g⁻¹ at 5 C) is attributable to the enlargement in *c*-axis of the material crystal structure upon the PO₄³⁻ doping. Li₃PO₄ coating was also associated with Nb⁵⁺ doping of LiNi_{0.83}Co_{0.11}Mn_{0.06}O₂ (NCM83) cathode powders [678]. The corresponding half-cell cell delivered an initial discharge specific capacity of 173.5 mAh g⁻¹ at 1.0 C and 25 °C with a capacity retention ratio of 88.8% after 200 cycles. Li₃PO₄ coating was also associated with Mg²⁺ doping to modify LiNi_{0.95}Mn_{0.05}O₂ to obtain a cathode with increased rate capability (130.6 mAh·g⁻¹ at 10 C, 1 C = 189.6 mA·h·g⁻¹) [679].

Tang et al. introduced C₆H₉O₆Sb with the precursors before calcination to synthesize LiNi_{0.92}Co_{0.04}Mn_{0.04}O₂ which was not only coated with Li₃Ni₂SbO₆, but also doped with Sb³⁺ which has an ionic radius close to that of Ni²⁺ [680]. This Sb-modified NMC demonstrated a capacity at 5 C equal to 88.5% at 0.1 C and a capacity retention of 82.9% at 5 C after 125 cycles. Combining in situ Na⁺ doping with carbon coating single-crystal NMC811, Sun et al. obtained a cathode delivering a capacity of 140 mAh g⁻¹ after 500 cycles at 5 C, which corresponds of a capacity retention of 83.1% [681]. In the case of Li₃PO₄ coating, the Ni-rich particles were not only coated, but also doped with Mg²⁺ [380,517]. In particular, Li₃PO₄-coated and Mg²⁺-doped single-crystal LiNi_{0.925}Co_{0.03}Mn_{0.045}O₂ cathode exhibited a retention of 89.36% after 100 cycles at 1 C (79.78% with the pristine NMC cathode) [380].

Yu et al. combined in one-step Ta doping and CeO₂ coating of NMC811 [682] (see Figure 17). The strong Ta–O bond helped forming the elongated primary particles for inhibiting microcrack generation, and the CeO₂ coating layer could effectively capture the remaining escaped oxygen. As a result, this cathode retained 90.9% of its initial capacity after 1000 cycles at 2.7–4.5 V and 1 C rate in a pouch-type full cell. LiNi_{0.92}Co_{0.04}Mn_{0.04}O₂ (NCM92) coated with a nano-level CeO₂ buffer layer and simultaneously doped with Ce showed the discharge specific capacity of 141.4 mAh g⁻¹ after 80 cycles at 0.2 C with 79.32% capacity retention at 60 °C [683]. Liu et al. prepared Mg/Ti/Sb-co-doped and CeO₂-coated LiNi_{0.9}Al_{0.1}O₂ cathode material. At a high voltage of 2.8–4.5 V and 1 C, the capacity retention of this cathode after 100 cycles reached 90.2% (from 200 mAh g⁻¹ to 181 mAh g⁻¹) [684].

Recently, Li₄TeO₅ surface coating along with bulk Te-gradient doping of single-crystalline Ni-rich LiNi_{0.90}Co_{0.05}Mn_{0.05}O₂ showed improved Li⁺ diffusion kinetics and thermodynamic stability, as well as an improved capacity retention of 95.83% and 82.12% after 200 cycles at the cut-off voltage of 4.3 and 4.5 V [685]. This illustrates the best performance that can be achieved when combining the synergetic effects of coating, doping, and single-crystal morphology. Wang et al. introduced an advanced surface reconstruction strategy combining a LiScF₄ coating, Sc+F surface co-doping, and a cation-mixing layer, which improved the thermal stability, structural integrity, and electrochemical performance of Ni-rich cathodes [686]. A comparison between different results obtained on doped plus coated Ni-rich cathodes is reported in Table 4.

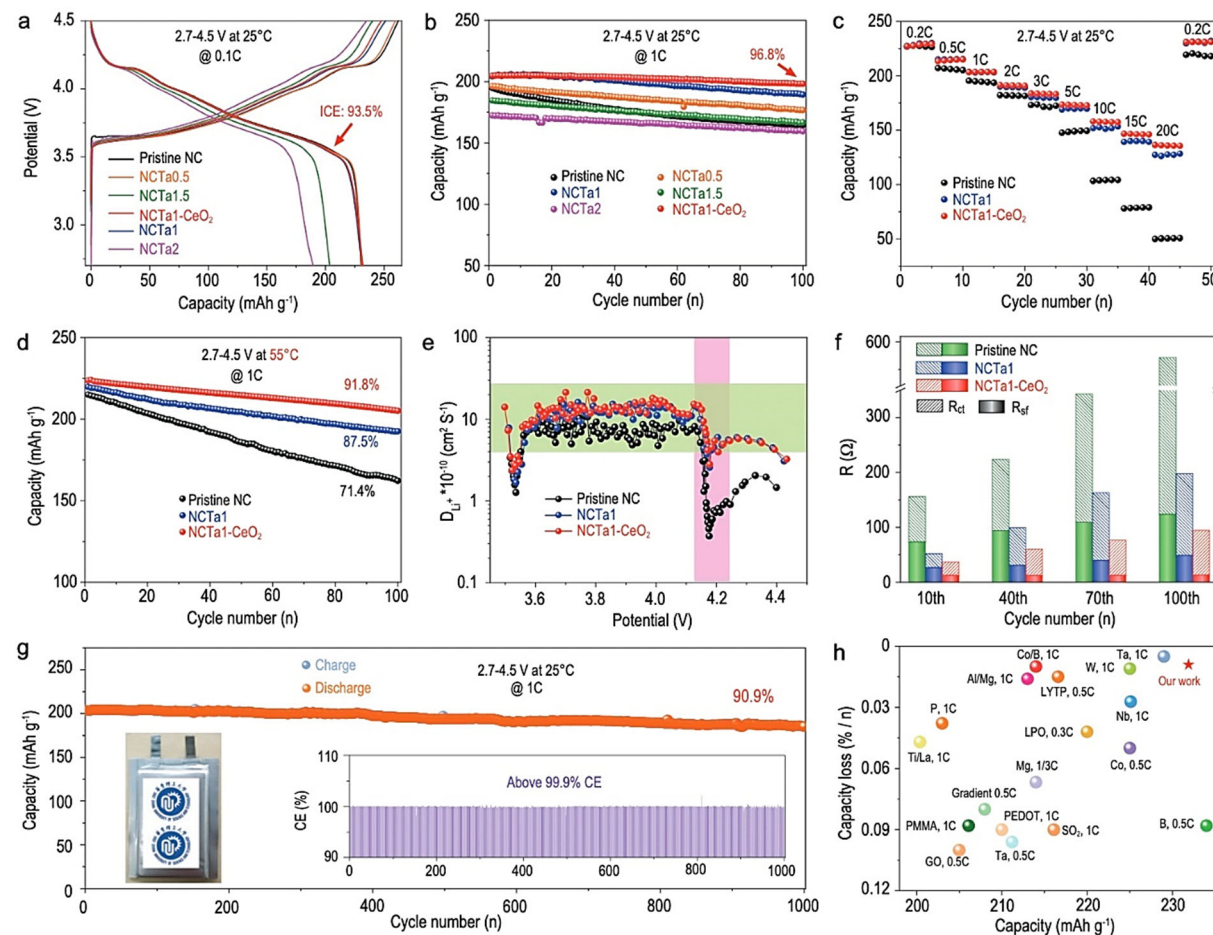


Figure 17. Superior electrochemical performance and cycling stability in half cell and full cell with Ta-doped and CeO₂ coated LiNi_{0.9}Co_{0.1}O₂ (NCTa1–CeO₂) cathodes with respect to pristine NCTa1. (a) Initial charge–discharge curves at 0.1 C and (b) cycle performance at 1 C within 2.7–4.5 V for all samples. (c) Specific capacities at 0.2–20 C, (d) cycle performance at 55 °C, (e) Li-ion diffusion coefficient based on GITT data and (f) comparison of R_{sf} and R_{ct} at different cycles within 2.7–4.5 V for pristine NC, NCTa1, and NCTa1–CeO₂. (g) Cycle stability at 1 C of NCTa1–CeO₂ // graphite full cells within 2.7–4.5 V. (h) Comparisons of 0.1 C discharge capacity and capacity loss per cycle with reported Ni-rich cathodes. Reproduced from ref. [682].

Table 4. Effects of doping plus coating on the cycling ability of Ni-rich cathode elements. Capacity densities are expressed in mAh g⁻¹. Unless specified, cut-off voltage is 4.3 V.

Cathode Element	Dopant + Coating	Cycles at C-Rate	Pristine		Coated		Ref.
			Capacity (mAh g ⁻¹)	Retention (%)	Capacity (mAh g ⁻¹)	Retention (%)	
NMC811	Mg + LiFePO ₄	100	183.48	81.7	181.5	90.8	[412]
LiNi _{0.8} Co _{0.15} Al _{0.05} O ₂	Ta + Ta ₂ O ₅	200@1 C	168	60.97	180	94.46	[338]
LiNi _{0.90} Co _{0.05} Mn _{0.05} O ₂	Ta + Li ₂ MnO ₃	300@1 C	201.9	85.8	204.2	91.6	[388]
LiNi _{0.82} Co _{0.14} Al _{0.04} O ₂	Mn + Li _{0.5} La ₂ Al _{0.5} O ₄	100@1 C	181	83.2	182	96.2	[396]
	Zr + WO ₃ /Li ₂ WO ₄	@C/3	173	85	180	93	[645]
NMC811	Na + LiNiO ₂ + Na _{1-x} Ni _{1-y} PO ₄	200@1 C	200	59	202	88	[377]
NMC811	Sn + Li ₂ SnO ₃	280@C/2	192	61.6	190.3	96.6	[547]
LiNi _{0.8} Mn _{0.2} O ₂	Sn + Li ₂ SnO ₃	300@C/5	189.70	81.23	191.3	90.54	[647]
LiNi _{0.925} Co _{0.03} Mn _{0.045} O ₂ At 55 °C	B + Li ₂ B ₄ O ₇	100	210	59.65	210	72.86	[648]

Table 4. Cont.

Cathode Element	Dopant + Coating	Cycles at C-Rate	Pristine		Coated		Ref.
			Capacity (mAh g ⁻¹)	Retention (%)	Capacity (mAh g ⁻¹)	Retention (%)	
LiNi _{0.825} Co _{0.115} Mn _{0.06} O ₂	B + La ₄ NiLiO ₈	500@1 C	165	73	165	93.49	[649]
LiNi _{0.91} Co _{0.06} Mn _{0.03} O ₂	B + Li ₃ BO ₃	100@2 C	170	67.3	175	79.4	[651]
LiNi _{0.89} Co _{0.08} Mn _{0.03} O ₂	B + B ₂ O ₃ & LiBO ₂	100@1 C	195	59	195	90	[653]
LiNi _{0.83} Co _{0.11} Mn _{0.06} O ₂ (cut-off 4.4 V)	Zr + Li ₃ BO ₃	1400@1 C	700 Wh/kg	71.4	700 Wh/kg	83.5	[652]
NMC811	B + LiBO ₂ /B ₂ O ₃	140@1 C	170	91	170	>99	[654]
NMC811 cut-off 4.6 V	La + Li ₃ BO ₃	300@C/2	176.9	27.0	201.4	63.7	[655]
LiNi _{0.83} Co _{0.11} Mn _{0.06} O ₂ (full cell)	Zr + Li _{1.3} Y _{0.3} Zr _{1.7} (PO ₄) ₃	500@C/2	19.87 mAh	70.6	23.48 mAh	83.7	[656]
NMC811	Sm dopant + coat	100@1 C	184	57.6	184.2	94.2	[660]
LiNi _{0.96} Mn _{0.04} O ₂	Al+Zr+ Li ₂ ZrO ₃	100@1 C	187	75	195	81.2	[662]
NMC811	Zr + BaZrO ₃	1400@1 C	190	92.3	190	92.5	[663]
NMC811 (cut-off 4.4 V)	Ti + TiO ₂	200@C/3	193	86.1	192	90.2	[667]
NMC811 (cut-off 4.3 V)	Ti + TiO ₂	1000@1 C	175	24.3	160	63.4	[668]
LiNi _{0.9} Co _{0.09} Mo _{0.01} O ₂	Ti + Li ₃ PO ₄	100@1 C	156.1	75.1	189.8	92.1	[670]
NMC811	Zr + Al ₂ O ₃	100@C/5	180	82.7	186	92	[671]
LiNi _{0.84} Co _{0.11} Mn _{0.05} O ₂	Al + Li ₂ WO ₄	200@1 C	172	72.9	178	88.9	[672]
NMC811	W + WO ₃	200@1 C	170.21	74.5	184.21	90.2	[673]
LiNiO ₂	PO ₄ ³⁻ + Li ₃ PO ₄	1000@1 C	200	23.3	175	51.0	[677]
LiNi _{0.83} Co _{0.11} Mn _{0.06} O ₂	Nb + Li ₃ PO ₄	200@1 C	178	59.5	173.5	88.8	[678]
LiNi _{0.92} Co _{0.04} Mn _{0.04} O ₂	Sb + Li ₃ Ni ₂ SbO ₆	200@5 C	185.7	39.2	149.4	75.7	[680]
NMC811	Na + carbon	500@5 C	125	41.1	165	83.1	[681]
LiNiO ₂ (cut-off 4.5 V)	Ta + CeO ₂	100@1 C	195	85	205	96.8	[682]
NMC92 at 60 °C	Ce + CeO ₂	80@C/5	91.8	49.25%	141.5	79.32%	[683]
LiNi _{0.9} Al _{0.1} O ₂ (4.5 V)	Mg/Ti/Sb + CeO ₂	100@1 C	192	60.1%	200	90.2%	[684]
LiNi _{0.90} Co _{0.05} Mn _{0.05} O ₂	Te + Li ₄ TeO ₅	200@1 C	198	82.05%	198	95.83%	[685]

5.4.3. Multiple Coatings

Multiple coatings were achieved with PPy. In particular, dual-conductive layers composed of Li₃PO₄ and PPy were utilized to improve the performance of NMC811, due to the conversion of excessive Li into Li₃PO₄ [687]. Another dual-conductive coating utilized to coat NMC811 is PPy-LiAlO₂. With the optimal amount of PPy coating (2 wt.%), the PPy-LiAlO₂ coated NMC811 delivered a capacity of 118 mAh g⁻¹ at 10 C. The capacity retention was 90.9% after 100 loops at 1 C [688]. NMC811 was also enwrapped by a functional reduced graphene oxide (RGO)-KH560 polymer composite layer which consists of an inner high-flexibility epoxy-functionalized silane (KH560) layer and an outer RGO layer [689]. Here, the KH560 layer was especially critical in connecting the layer of outer RGO and the inner surface of the active material, while uniform coating with RGO alone is almost impossible, due to the 2D nature of RGO or graphite. The NMC811 cathode with RGO (0.5%)–KH560 (0.5%) coating exhibited a capacity retention of 95.2 after 150 cycles at 1 C.

Recently, Tan et al. designed a single-crystal LiNi_{0.9}Co_{0.05}Mn_{0.05}O₂ in which coherently grown MgO₆ octahedra and BO₄ tetrahedra were incorporated into the lattice, and a stabilizing Mg₃(BO₃)₂ layer was concurrently formed on the particle surface [690]. These modifications reduced planar gliding and delamination cracking, even during prolonged

cycling. A pouch-type full cell with this cathode and a graphite anode sustained a specific discharge capacity of 177 mAh g^{-1} after 500 cycles, with 90% capacity retention.

Cheng et al. coated NCA with a triple composite Li-ion conductor coating layer ($\text{Y}(\text{PO}_3)_3\text{-Li}_3\text{PO}_4\text{-YPO}_4$) [691]. The metal phosphite $\text{Y}(\text{PO}_3)_3$ was here to optimize the surface residual alkaline lithium salt of NCA to expel H_2O and CO_2 in advance, which effectively reduced the electrolyte's hydrolysis and gas generation. The electrode modified with 2 mol% $\text{Y}(\text{PO}_3)_3$ showed excellent rate performance ($156.3 \text{ mAh}\cdot\text{g}^{-1}$ at 5 C) with a capacity retention of 88.3% after 200 cycles.

6. Core–Shell and Gradient Structures

6.1. Core–Shell Structures

The design of core–shell structures is a strategy commonly used to improve the electrochemical properties of Ni-rich cathode materials [692–697]. In such structures, the core is a Ni-rich material, and the shell is a Mn-rich component, which is structurally stronger and has thus the ability to protect the inner part from contact with the electrolyte. For example, Li et al. [692] prepared a core–shell structure with the inner core composed of NMC811, while the outer layer named Li–Mn–O contains Mn^{4+} , with higher concentration than that of the core. The corresponding cathode delivered the same capacity (118 mAh g^{-1}) as that of pristine NMC811 at the rate of 10 C in the voltage range of 3.0–4.3 V, but the capacity decay was limited to 18.4% after 200 cycles compared to 27% decay with the pristine material. Cathode materials with the overall composition of NMC811 in which the nickel-rich composition ($\text{LiNi}_{0.9}\text{Mn}_{0.05}\text{Co}_{0.05}\text{O}_2$) is the core and the manganese-rich composition ($\text{LiNi}_{0.33}\text{Mn}_{0.33}\text{Co}_{0.33}\text{O}_2$) is the shell improved capacity retention of 76.6% compared to the commercial homogeneous NMC811 [695]. Bae et al. synthesized $\text{LiNi}_{0.8}\text{Co}_{0.1}\text{Mn}_{0.1}\text{Al}_x\text{O}_2$ with an inner porous layer. This structure was obtained by the intermittent addition of Al salt during hydroxide precursor co-precipitation, exhibiting the spherical morphology with the structure of core (active material particle) and shell (the inner porous layer). This modified cathode material demonstrated a capacity retention of 98.2% after 100 cycles at 1 C and a cut-off voltage of 4.5 V [698]. In addition, this synthesis is scalable to commercial production due to its simple and facile procedure. Shi et al. redesigned $\text{Li}[\text{Ni}_{0.7}\text{Co}_{0.1}\text{Mn}_{0.2}]\text{O}_2$ into a core–shell structure with the core of $\text{Li}[\text{Ni}_{0.8}\text{Co}_{0.1}\text{Mn}_{0.1}]\text{O}_2$ delivering a high capacity and the shell of $\text{Li}[\text{Ni}_{0.45}\text{Co}_{0.1}\text{Mn}_{0.45}]\text{O}_2$ providing structurally stability [699]. The core–shell electrodes displayed enhanced cycling stability and thermal stability compared with the non-core–shell electrodes. Xia et al. proposed core–shell-structured Ni-rich cathodes composed of $\text{LiNi}_{0.6}\text{Co}_{0.2}\text{Mn}_{0.2}\text{O}_2$ (NCM622) shell and $\text{LiNi}_{0.9}\text{Co}_{0.05}\text{Mn}_{0.05}\text{O}_2$ (NCM9055) core. In addition, the NCM622 shell had radially oriented primary particles to reduce the surface side reaction with electrolyte and alleviate internal stress. The 40 wt.% NCM622 coating NCM9055 cathode exhibited a discharge capacity of 160.5 mAh g^{-1} with a capacity retention of 85.0% after 200 cycles at 0.5 C [700]. Ryu et al. synthesized a hybrid structure in which $\text{Li}[\text{Ni}_{0.92}\text{Co}_{0.04}\text{Mn}_{0.03}\text{Al}_{0.01}]\text{O}_2$ in the interior of the particle is encapsulated by $\text{Li}[\text{Ni}_{0.845}\text{Co}_{0.067}\text{Mn}_{0.078}\text{Al}_{0.01}]\text{O}_2$ that acts as a buffer against microstrain [693]. This hybrid cathode structure suppresses the formation of microcracks by creating a non-uniform spatial distribution of the microstrain within the cathode particle. As a result, this hybrid cathode material retained 84.7% of its initial capacity after 1500 cycles at 1 C, which is a 50% increase with respect to the retention obtained with the pristine $\text{Li}[\text{Ni}_{0.9}\text{Co}_{0.045}\text{Mn}_{0.045}\text{Al}_{0.01}]$ bulk material. The presence of $\text{Li}_x\text{W}_y\text{O}_z$ secondary phases in the grain boundaries eliminated the interdiffusion of Mn and Al from the shell to the core in these Ni-rich core–shell materials. Park et al. [696] constructed a core–shell structure with the core consisting mainly of $\text{Li}[\text{Ni}_{0.957}\text{Mn}_{0.043}]\text{O}_2$, while in the 3 μm -thick shell. the Ni concentration decreases to 83% and the Mn concentration increases to 17% at the secondary particle surface, resulting in

the surface composition of $\text{Li}[\text{Ni}_{0.834}\text{Mn}_{0.166}]\text{O}_2$. Therefore, the cathode material had the composition of Co-free $\text{Li}[\text{Ni}_{0.9}\text{Mn}_{0.1}]\text{O}_2$. This cathode retains 78.5% of its initial capacity after 2000 cycles at 1 C charge and 0.8 C discharge rates, and retains 79.5% capacity after 1000 cycles under fast-charging conditions (3 C charge and 1 C discharge), demonstrating the effective dissipation of internal strain and chemical protection provided by the Mn-rich shell. This recent result outperforms the electrochemical properties of prior Co-free cathodes [86,91], and proves that both cycle life and rate capability can be reached even with Co-free Ni-rich cathodes. So far, such a performance was obtained only with presence of cobalt, because Co^{3+} alleviates magnetic frustration during cycling, thus reducing the disordered cation mixing of Li^+ and Ni^{2+} [701], and increases electronic conductivity through CoO_6 octahedra with delocalized electronic states. The success of the cathode in [696] also comes from the fact that Mn-based shells are less prone to interdiffusion, compared to Mg- and Al-based shells, while interdiffusion has been identified as a major challenge to overcome for the preservation of core–shell structure. Han et al. proposed a new approach that fully utilizes Co by forming a Co nanoshell on a Ni-rich $[\text{Ni}_{0.90}\text{Co}_{0.05}\text{Mn}_{0.05}](\text{OH})_2$ precursor via a single coprecipitation process [702]. The Co nanoshell acts as a sintering inhibitor during calcination, thereby generating columnar structures that are not observed in the baseline $[\text{Ni}_{0.90}\text{Co}_{0.05}\text{Mn}_{0.05}]\text{O}_2$ cathode material. The Co nanoshell markedly improved the Li^+ kinetics and cycling stabilities of Ni-rich cathode materials.

Xue et al. introduced a proton-rich (ammonium bicarbonate) shell on $\text{LiNi}_{0.92}\text{Co}_{0.06}\text{Mn}_{0.02}\text{O}_2$ single crystals [703]. Once released during the first charge, the proton is immediately captured by LiPF_6 , in situ electrochemically converting to LiF and Li_3PO_4 sub-nano particle dense maskant. This surface modification enables 95% capacity retention after 100 cycles at a high voltage of 4.5 V in the half cell, and 83% capacity retention after 800 cycles in the full cell with graphite anode.

Tungsten oxide (WO_3) coating on the surface of precursors leads to the formation of $\text{Li}_x\text{W}_y\text{O}_z$ secondary phases during the heat treatment with $\text{LiOH}\cdot\text{H}_2\text{O}$. These $\text{Li}_x\text{W}_y\text{O}_z$ phases infuse into the grain boundaries and prevent interdiffusion between the core and shell phases [704]. This process was proposed by Rathore et al. who constructed a cobalt-free core–shell cathode material composed of inner core $\text{Ni}(\text{OH})_2$ and outer shell $\text{Ni}_x\text{M}_y(\text{OH})_2$ [697], enhancing the mechanical strength and electrochemical performance. This behavior is probably not unique to W, and it is expected that elements like Mo, Zr and Nb, which are also found in the grain boundaries, can be used to prevent the interdiffusion between shell and core, so that Co-free Ni-rich cathodes are very promising for the next generation of lithium batteries. Recently, Liu et al. used synergistic effects of Li_2WO_4 coating and W⁶ doping to obtain a modified single-crystal $\text{LiNi}_{0.9}\text{Co}_{0.05}\text{Mn}_{0.05}\text{O}_2$ (Ni90) cathode exhibiting 89.8% capacity retention after 300 cycles at 0.5 C [705]. Chu et al. coated single-crystal $\text{LiNi}_{0.92}\text{Co}_{0.04}\text{Mn}_{0.04}\text{O}_2$ with a layer composed of Li–B–O species and Li_2WO_4 . The cycling stability of such a cathode at a high cut-off voltage of 4.5 V was improved from 71.8% to 87.1% at 1 C after 100 cycles [706]. Du et al. introduced W into $\text{LiNi}_{0.9}\text{Co}_{0.05}\text{Mn}_{0.05}\text{O}_2$ and discovered that, during high-temperature solid-state reactions, a Li_4NiWO_6 defect phase is formed. This phase, combined with the amorphous $\text{Li}_x\text{W}_y\text{O}_z$ coating layer improved the electrochemical properties of this cathode, which exhibited a capacity retention of 97.31% (200.5 mAh g⁻¹ to 195.1 mAh g⁻¹) after 200 cycles in the voltage range 3–4.3 V at 0.5 C and 30 °C [707].

The hollow multi-shell structure (HoMS) allows Ni-rich cathode materials to have sufficient pore space to buffer the structural instability caused by volume expansion in the cyclic process. In particular, Ding et al. chose micro- and nanostructured Co_3O_4 as a template of the HoMS because the annealed Co_3O_4 template has a unique HoMS

layer structure, to prepare a NMC622cathode material that demonstrated a capacity of 148.5 mAh g^{-1} after 100 cycles at 0.5 C, corresponding to a capacity retention of 90.4% [708].

6.2. Gradient Layers

Concentration gradient cathodes are a good strategy to concentrate high Ni-concentrations in the core region, and smaller Ni concentrations near the surface to improve the structural stability. The concentration gradient design originates from a simple core–shell structure in which the core is Ni-rich NMC while the shell has other NMC compositions (lower Ni content and higher Mn content) to stabilize the layer structure at the surface. Concentration gradients are an alternative to core–shell structure to confine the Ni-rich part of the particles in the core. Actually, the two procedures are related when some interdiffusion occurs between the shell and the core. However, concentration gradient concept has an advantage, as it can effectively solve the problem of the reduced Li diffusion caused by the contraction of the crystal cell volume between the high-nickel core and the gradient shell [582,709–711]. Moreover, the core–shell design is responsible for voids generated during cycling between the shell and the core during long-term cycling and mismatches of different lattice parameters. Gradient layers avoid this problem, and have been used constantly for a decade to synthesize Ni-rich cathode materials [712].

The improved electrochemical properties of a gradient material with a high-nickel NMC811 as the core and a low-nickel $\text{LiNi}_{0.46}\text{Co}_{0.23}\text{Mn}_{0.31}\text{O}_2$ as the shell illustrate the benefit of the reduction of surface microcracks, and the rod-shaped morphology of the primary particles with radial growth orientation [713]. As a result, the capacity retention of 70% after 1000 cycles at a high temperature of 55 °C. The same morphology and same benefit were experienced with a material of average composition $\text{LiNi}_{0.75}\text{Co}_{0.10}\text{Mn}_{0.15}\text{O}_2$ with gradual composition with the inner core composed of high-nickel low-Mn $\text{LiNi}_{0.86}\text{Co}_{0.10}\text{Mn}_{0.04}\text{O}_2$, and the outer layer composed of low-nickel high-Mn $\text{LiNi}_{0.70}\text{Co}_{0.10}\text{Mn}_{0.10}\text{O}_2$ [709]. More recently, Wu et al. synthesized a Ni concentration gradient $\text{LiNi}_{0.8}\text{Co}_{0.15}\text{Al}_{0.05}\text{O}_2$ (NCG-NCA) cathode material using the characteristic reaction of Ni^{2+} and dimethylglyoxime [710]. Owing to the high nickel content in the core, and high cobalt content on the surface stabilizing the surface of the particles, the capacity retention was increased at 75% after 200 cycles at a current density of 10 C ($1 \text{ C} = 160 \text{ mA g}^{-1}$) under a high cut-off voltage of 4.5 V, compared with 50% for the homogeneous NCA material. Park et al. synthesized a core–shell with concentration gradient $\text{Li}[\text{Ni}_{0.90}\text{Co}_{0.045}\text{Mn}_{0.045}\text{Al}_{0.01}]\text{O}_2$ (CSG-NCMA90) consisting of fine, elongated primary particles that are radially aligned from the center of a spherical secondary particle [582]. This microstructure effectively suppressed the formation of cracks in the charged state, in agreement with the general trend that a spherical secondary cathode particle shape with uniform morphology can reduce the production of microcracks by effectively dispersing structural strain during cycling [714]. Moreover, these elongated particles largely featured (001) facets on their lateral sides, and were tolerant of electrolyte attack, thus suppressing surface degradation, enabling the CSG-NCMA90 cathode to retain 90.7% of its initial capacity after 1000 cycles at 100% depth of discharge (in the voltage range 3.0–4.2 V) at 1 C rate. The oriented growth of primary grains along (001) and parallel stacking of nanosheets can be achieved by optimizing the stable adsorption structures of metal-ammonia complexes on the precursor crystal facets under aqueous ammonia conditions [715,716]. Ryu et al. constructed a hybrid-structured $\text{Li}[\text{Ni}_{0.9}\text{Co}_{0.045}\text{Mn}_{0.045}\text{Al}_{0.01}]$ (HS-NCMA90) cathode, in which $\text{Li}[\text{Ni}_{0.92}\text{Co}_{0.04}\text{Mn}_{0.03}\text{Al}_{0.01}]\text{O}_2$ forms the interior of the cathode particle enclosed in a buffer layer of $\text{Li}[\text{Ni}_{0.845}\text{Co}_{0.067}\text{Mn}_{0.078}\text{Al}_{0.01}]\text{O}_2$. This structure develops radially aligned primary particles, enabling the primary particles to contract uniformly, thereby effectively suppressing the propagation of microcracks toward the outer surface [693]. The pouch cell with this cathode and a graphite anode retained retaining

90.0% of its initial capacity after 1000 cycles at 1 C in the voltage range 3.0–4.2 V. Another example of the effectiveness of the nanorod configuration is provided by Liu et al. who designed a unique bayberry-like $\text{Li}_{1.2}\text{Mn}_{0.54}\text{Co}_{0.13}\text{Ni}_{0.13}\text{O}_2$ cathode material, composed of a spherical core and the shell self-assembled by radially oriented nanorods [717] (see Figure 18). The radial texturing of the nanorods in shell layer formed a natural protective interface constituted by thermodynamically stable (003) planes, so this cathode delivered remarkable high-rate long-term cycling stability with capacity retentions of 91.2% after 500 cycles at 1 C and of 81.3% after 1000 cycles at 5 C. Guo et al. constructed a concentration-gradient $\text{LiNi}_{0.753}\text{Mn}_{0.247}\text{O}_2$ cathode that consists of the elongated and radially aligned primary particles through Mo+Ti+Mg doping [718]. With the synergetic effect of gradient concentrations and multi-doping, this Co-free Ni-rich cathode exhibited a capacity retention of 81.1% after 1000 cycles in a pouch full cell (commercial graphite anode) at 1 C within 2.7–4.5 V.

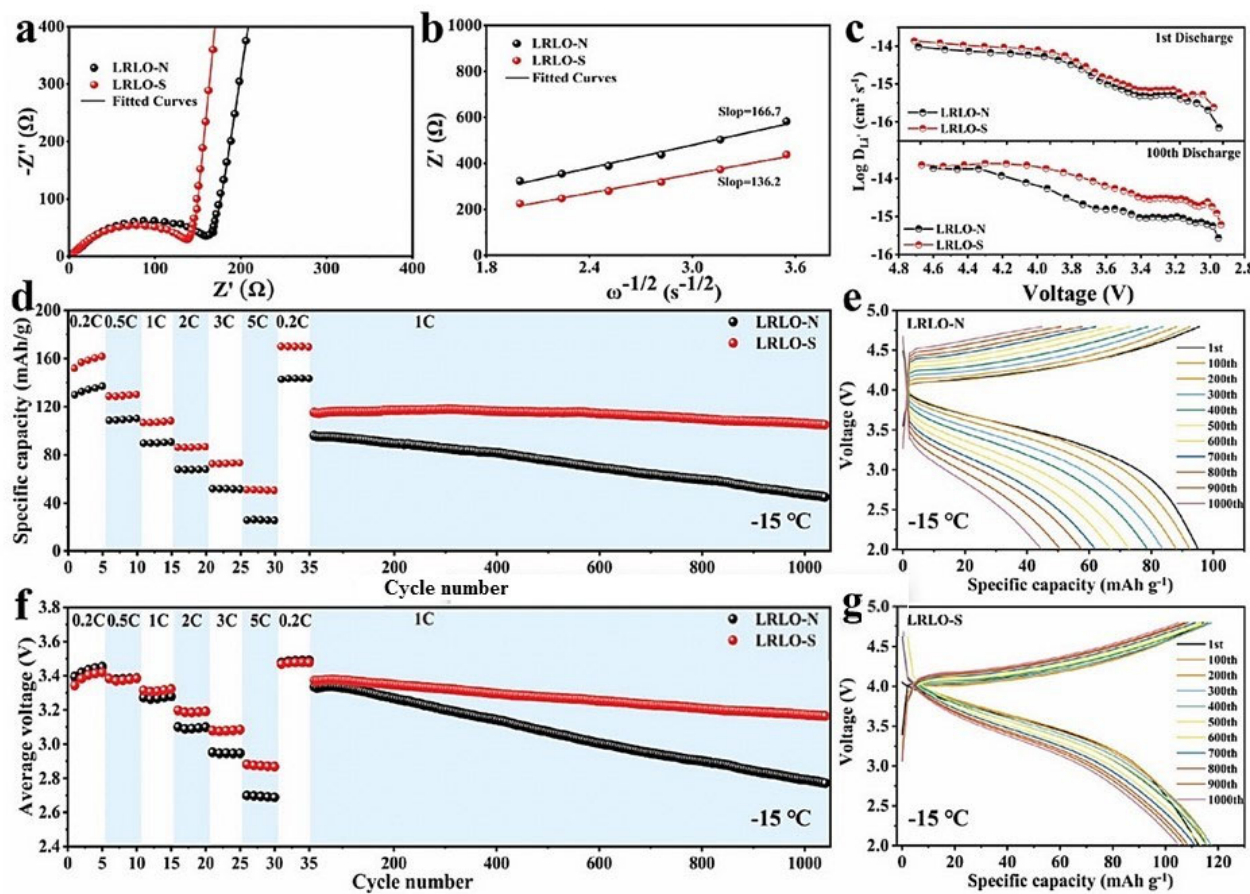


Figure 18. Properties of bayberry-like $\text{Li}_{1.2}\text{Mn}_{0.54}\text{Co}_{0.13}\text{Ni}_{0.13}\text{O}_2$ (LRLO-S) cathode material, composed of a spherical core and the shell self-assembled by radially oriented nanorods, in comparison with the same material with a different microstructure (LRLO-N). (a) Nyquist plots and (b) corresponding profiles of Z' versus $\omega^{-1/2}$ of LRLO-N and LRLO-S in half-cells. (c) Calculated Li^+ diffusion coefficients of LRLO-N and LRLO-S during discharging process after 1st and 100th cycles at 1 C. (d) Rate performance and subsequent long-term cycling performance at $-15\text{ }^\circ\text{C}$ and (f) corresponding average voltage and low-temperature charge/discharge curves at 1 C for (e) LRLO-N and (g) LRLO-S. Reproduced from ref. [717]. Copyright 2024 Wiley.

These results illustrate that concentration gradient layers can reshape primary particles into a rod-like or even needle-shaped structure, which can promote Li^+ movement by minimizing diffusion pathways [719]. Such cathode materials are usually prepared by calcining hydroxide precursors with Li salts at an optimum temperature,

high enough to obtain a good crystallization, but small enough to keep the rod-like morphology of the precursors. Jeyakumar et al. synthesized a double concentration-gradient $\text{Li}[\text{Ni}_{0.90}\text{Co}_{0.04}\text{Mn}_{0.03}\text{Al}_{0.03}]\text{O}_2$ with a Ni-rich-core, an Mn-rich shell, and Al on top surface [235]. This cathode exhibited a capacity retention of 91.5% after 100 cycles and 70.3% after 500 cycles at 1 C (against 83.4% and 47.6% for the material with uniform composition). While the concentration gradient concerns usually the concentration of nickel, Liu et al. synthesized a $0.5(\text{LiNi}_{0.8}\text{Mn}_{0.2}\text{O}_2)_{\text{bulk}}0.5(\text{LiNi}_{0.8}\text{Co}_{0.2}\text{O}_2)_{\text{surface}}$ sample (denoted as NM-NC82), where the Ni concentration is constant ($x = 0.8$) with a composition design where the central component is Ni/Mn/Co (8:2:0, molar ratio), then gradually changes to Ni/Mn/Co (8:0:2, molar ratio) toward the surface of the particle [133]. Benefiting from lower stiffness in Co-enriched surfaces, this cathode material showed negligible morphology damage, due to an improved stability of the H₂-H₃ phase transition. Maximizing the advantages of coating, doping, and concentration gradient, Park et al. constructed a core–shell structure in which the shell with Ni fraction of $\approx 84\%$ uniformly surrounded the core part of Ta-doped NMC particles of composition $\text{Li}[\text{Ni}_{0.935}\text{Co}_{0.040}\text{Mn}_{0.020}\text{Ta}_{0.005}]\text{O}_2$ with Ni fraction of $\approx 97\%$ [720]. When cycled in pouch-type full cells using graphite anodes in the voltage range of 3.0–4.2 V, this cathode demonstrated a capacity retention of 92.6% after 1000 cycles when charged at 2 C (discharge current 1 C).

Wu et al. identified recently the effectiveness of using such an anionic surfactant (β -styryl phosphonic acid) to assist the preparation of $\text{Ni}_{0.8}\text{Co}_{0.1}\text{Mn}_{0.1}(\text{OH})_2$ precursors in the coprecipitation [721]. With this configuration, the NMC811 exhibited capacity retention rates could reach 93% (164.5 mAh g⁻¹) after 100 cycles and 84.3% (149.0 mAh g⁻¹) after 300 cycles. Shang et al. synthesized NMC811 with dual Ni gradients on both primary and secondary particles by applying Ni-MOF-74 during the coprecipitation of precursors [711]. This cathode delivered a capacity of 203.5 mAh g⁻¹ at 0.1 C. At C/3, and the capacity retention was 88.5% after 300 cycles with a coulombic efficiency larger than 99.86%. At 1 C, the capacity retention was 84.1% after 500 cycles.

Gradient NMC cathode materials with high stability and excellent performance can be synthesized by capitalizing on the unique reactivity of the NMC precursor with ammonia and KMnO₄ [722]. According to this method, surficial Ni is dissolved from the NMC precursor through ammoniacal leaching and subsequently MnO₂ is deposited on the surface by reducing KMnO₄. This process allows for precise adjustment with reduced surficial Ni and enriched Mn. A 1.2 Ah pouch cell configurated with this modified NMC cathode and graphite anode demonstrates a lifespan of over 500 cycles with only 8% capacity loss.

NMC811 with a surface gradient layer and lithium phosphorus oxynitride (LIPON) coating showed improved capacity retention [723]. The formation of highly electronegative PO₄³⁻ polyanions in the layered material after P-doping enables the expansion of the layer spacing and stabilization of the lattice structure. Liu et al. synthesized P-doped NMC811 by a co-precipitation process, to obtain a cathode that exhibited a capacity retention of 83.53% after 100 cycles at 1 C [724]. Choi et al. coated 1 wt.% lithium and cobalt acetate precursor on the inner and outer surfaces of commercial polycrystalline NMC811, which improved electrochemical properties in cells with liquid electrolytes. On the other hand, when the coating was mainly on the outer surface of the material, the performance was improved in cells with solid-state electrolytes, as the contact between the electrolyte and the active material is only at the surface of the polycrystalline NMC811 [725].

Gradient layers can be extended into full concentration gradient (FCG) layers or multiple gradient layers with different slopes, to maximize the Ni content at the core as compared with single-sloped gradient layers. For instance, full-concentration-gradient $\text{Li}[\text{Ni}_{0.78}\text{Co}_{0.10}\text{Mn}_{0.12}]\text{O}_2$ obtained with the optimized calcination temperature of 790 °C

exhibited remarkable cycling stability, retaining 86.3% of its initial capacity after 4000 cycles, and superior rate capability [726]. Wu et al. studied a series of full concentration gradient-tailored Li-rich layered oxides, and found that the gradient-tailored materials with medium-slope show the best electrochemical performance (capacity retention of 88.4% within 200 cycles at 200 mA g⁻¹) [727]. Zhang et al. combined the full concentration strategy of Ni-rich material (overall composition: LiNi_{0.75}Co_{0.15}Mn_{0.1}O₂) with Ti pillar and Li₂ZrO₃ (LZO) coating modification [728]. The corresponding cathode exhibited 92.3% capacity retention at 1 C, and delivered a capacity of 137.9 mAh g⁻¹ at 10 C rate. Radially oriented rod-shaped primary particles in a cathode, resulting from the concentration grading (or compositional partitioning) of the cathode, also showed markedly improved electrochemical and thermal properties. [581,693,729]. In particular, a cathode with full-concentration-gradient Li[Ni_{0.78}Co_{0.10}Mn_{0.12}]O₂ active element retained 86.3% of its initial discharge capacity after 4000 cycles at 1 C in a full cell [726]. NMC811 with radially orientated primary particles resulting from Mn composition grading delivered ≈180.1 mAh g⁻¹ at 1 C and retained 96.2% of its initial discharge capacity after 100 cycles [730]. This is also the capacity retention obtained by designing a concentration gradient core–shell structure of Li(Ni_{0.794}Co_{0.11}Mn_{0.096})O₂ consisting of a nickel-rich core with a Ni:Co:Mn mole ratio of 9:0.5:0.5, two interlayers with increasing Mn content gradient, and a high-manganese thin shell [731]. Ni_{0.95}Mn_{0.025}Co_{0.025}O₂ with a Ni/Co gradient and radially oriented particles demonstrated greatly improved cycling stability (capacity fade per cycle of 0.04 ± 0.01% over 300 cycles at 1 C) [732]. Guo et al. reported the design and synthesis of a full concentration gradient LiNi_{0.75}Mn_{0.20}Co_{0.05}O₂ cathode with a Mn-rich Ni-poor surface, which has been realized by in situ forming a PO₄³⁻ gradient distribution after Li_{0.1}B_{0.967}PO₄ coating [733]. This cathode delivered a capacity of 212.6 mAh g⁻¹ at 2.7–4.5 V with an energy density of >800 Wh kg⁻¹_{cathode}. In commercial-grade full cells with commercial graphite anodes, a superior cycle life of 80.5% capacity retention is achieved at 1 C within 2.7–4.5 V after 1700 cycles. This performance is comparable to the state-of-the-art cathodes with Ni content of 90% at 2.7–4.3 V, but is safer as the exothermic peak is at higher temperature (261.4 °C). The concentration gradient design is thus particularly effective in the fabrication of high-density lithium batteries.

Gradient structure refers usually to a Ni concentration gradient, but concentration-gradient doping element is also a good strategy to improve the electrochemical properties [734,735]. Mu et al. developed a gradient Zr element doping, the orientations of which were achieved via coprecipitation in a positive or negative correlation between the concentrations of Zr and Ni. They found that the material behaves better when the Zr content is abundant in the core. The gradient Zr-doped LiNi_{0.65}Co_{0.20}Mn_{0.15}O₂ delivered a higher capacity retention of 85.6% after 300 cycles at 1 C (70.7%, 121.4 mAh g⁻¹ for the pristine sample) and an outstanding rate performance of 122.5 mAh g⁻¹ at 20 C [736]. Zhang et al. improved the performance of LiNiO₂ via concentration-gradient yttrium modification with LiYO₂-Y₂O₃ coating layer [737]. Other doping elements with gradient concentrations also led to better electrochemical properties. In particular, concentration-gradient niobium-doping strategy was applied to modify single-crystal LiNi_{0.83}Co_{0.12}Mn_{0.05}O₂, with Nb concentration decreasing linearly from the surface to the core of the particle [738].

7. Cells with Ni-Rich Cathodes

The general progress on the engineering of electrolytes for lithium batteries is out of the scope of the present work and have been reviewed elsewhere (for a recent review, see [739]). We only report in the following recent results obtained concerning batteries based on Ni-rich cathodes with Ni content > 0.5 of interest in the present work. The reason why we specify this point comes from the fact that electrolytes working for Ni

concentrations ≤ 0.5 do not necessarily work at higher concentrations. For instance, for various additives, which can greatly enhance the performance of Li-ion batteries with $\text{LiNi}_x\text{Co}_y\text{Mn}_{1-x-y}\text{O}_2$ ($x < 0.6$) cathodes, there is no obvious improvement for Ni-richer cathode materials [740].

7.1. Solid Electrolytes

All-solid-state lithium batteries (ASSLBs) with Ni-rich cathodes are the most promising solution to improve the safety and thermal stability limited by the conventional organic liquid electrolytes. In particular, sulfide-based solid electrolytes have been considered [741]. However, the interfacial resistance caused by poorly conductive side products, the contact loss, and the space charge layer effect have limited the application of Ni-rich oxide cathodes in sulfide-based ASSBs [742]. Again, coating has also been considered as a solution to overcome these difficulties. Payandeh et al. studied the effect of $\text{Li}_2\text{CO}_3/\text{LiNbO}_3$ coating on the cycling performance of NCM-851005 (85% Ni content) in pellet-stack solid-state-battery with $\text{Li}_6\text{PS}_5\text{Cl}$ as solid electrolyte and $\text{Li}_4\text{Ti}_5\text{O}_{12}$ anode and found that 80% of the initial specific discharge capacity is retained after 200 cycles ($\sim 160 \text{ mAh}\cdot\text{g}^{-1}$, $\sim 1.7 \text{ mAh}\cdot\text{cm}^{-2}$) at C/5 and 45 °C [743]. Walther et al. showed that the $\text{Li}_2\text{CO}_3/\text{LiNbO}_3$ coating suppresses the interfacial reaction at the cathode active material/ $\text{Li}_6\text{PS}_5\text{Cl}$ interface, in particular, the formation of oxygenated phosphorous and sulfur compounds [744]. An ASSB with LiNbO_3 -coated NMC811, an electrolyte consisted of a polar poly(vinylidene fluoride-co-trifluoroethylene) (P(VDF-TrFE)) framework and $\text{Li}_6\text{PS}_5\text{Cl}$ via an electrospinning-permeation-heating-pressing way $\text{Li}_6\text{PS}_5\text{Cl}$ electrolyte, and Li-In anode showed 71% capacity retention after 2000 cycles at current density of 0.1 mA cm^{-2} [745]. Li_3PO_4 coating also fulfill the purpose, because this phosphate contains the same anion (O^{2-}) and cation (P^{5+}) species as those present in the cathode and sulfide electrolyte, respectively, preventing the exchange of S^{2-} and O^{2-} in $\text{Li}_6\text{PS}_5\text{Cl}$ and NMC [746]. Atomic layer deposition of $\text{LiAl}(\text{PO}_3)_4$ onto $\text{LiNi}_{0.88}\text{Co}_{0.09}\text{Mn}_{0.03}\text{O}_2$ (NCM88) accelerated the charge transfer and mitigated the interfacial deterioration. The ASSB with this modified cathode, $\text{Li}_6\text{PS}_5\text{Cl}$ electrolyte, and Li-In anode, with a high loading of 20.1 mg cm^{-2} exhibited a reversible capacity of 4.25 mAh/cm^2 and a capacity retention of 98.3% after 440 cycles at 0.5 C [747] (see Figure 19). Lin et al. constructed a $\text{LiNi}_{0.83}\text{Co}_{0.12}\text{Mn}_{0.05}\text{O}_2$ (NCM83125) cathode modified by Zr+F co-doping, plus cyclized polyacrylonitrile (cPAN) coating. This polymer was chosen because the pyridine-based structure with delocalized π bonds via thermal cyclization of PAN units endows cPAN with satisfactory electronic conductivity. ASSLBs utilizing this modified NCM83125 as a cathode, $\text{Li}_6\text{PS}_5\text{Cl}$ electrolyte, and Li-In anode, exhibited a higher initial capacity (175 mAh g^{-1}) and Coulombic efficiency (82.7%), a capacity retention of 95% after 300 cycles at a rate of 0.2 C, and an enhanced rate performance (109 mAh g^{-1} at 3 C) [748]. Via atomic layer deposition of Li_3PO_4 and subsequent in situ formation of a gradient $\text{Li}_3\text{P}_{1+x}\text{O}_4\text{S}_{4x}$ coating, Liang et al. obtained a conformal covering for NMC811 particles [371]. Tested in combination with an indium metal negative electrode and a $\text{Li}_{10}\text{GeP}_2\text{S}_{12}$ solid electrolyte, this modified NMC811 enabled the delivery of a specific discharge capacity of 128 mAh g^{-1} after almost 250 cycles at 0.178 mA cm^{-2} and 25 °C. using advanced molecular layer deposition (MLD) technique, Su et al. coated single-crystal NMC811 with an elastic and sticky alucone/glycol layer [749]. This coat enabled NMC to be in close contact with the sulfide electrolyte, so that the ASSB with a mass loading of 20.4 mg cm^{-2} at 60 °C exhibited the capacity retention of 80.0% after 1000 cycles at 1 C.

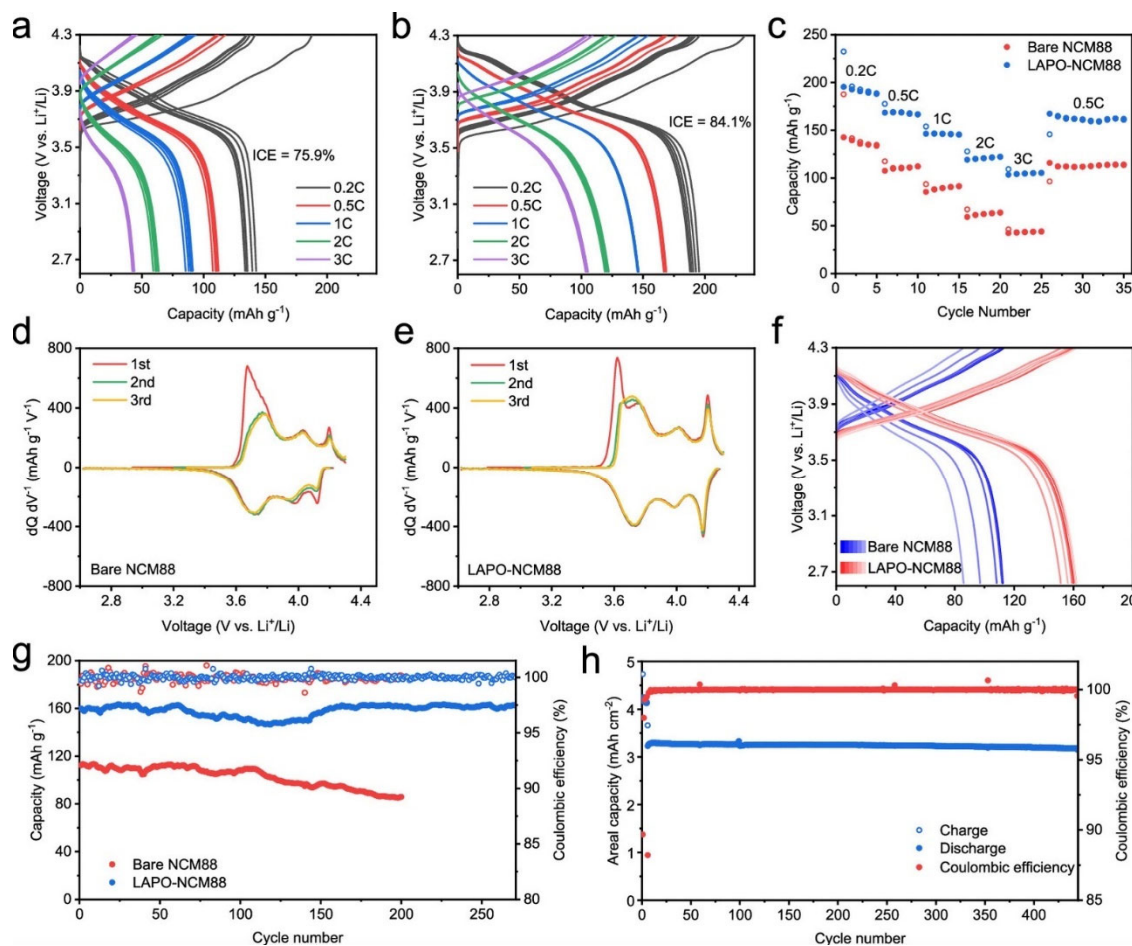


Figure 19. Electrochemical tests of bare $\text{LiNi}_{0.88}\text{Co}_{0.09}\text{Mn}_{0.03}\text{O}_2$ (NCM88) and $\text{LiAl}(\text{PO}_3)_4$ -coated NCM88 (LAPO-NCM88) between 2.62 and 4.3 V at 30 °C. Galvanostatic charge–discharge voltage profiles of ASSLBs based on (a) bare NCM88 and (b) LAPO-NCM88 at different rates. (c) Rate capability comparison between bare NCM88 and LAPO-NCM88-based ASSLBs. Mass-normalized dQ/dV curves of ASSLBs based on (d) bare NCM88 and (e) LAPO-NCM88 at 0.2 C. (f) Galvanostatic charge–discharge voltage profiles of bare NCM88 and LAPO-NCM88-based ASSLBs at 1st, 20th, 50th, 100th, 150th, and 200th cycle at 0.5 C. (g) Cycling stability and Coulombic efficiency of bare NCM88 and LAPO-NCM88-based ASSLBs at 0.5 C. (h) Cycling stability and Coulombic efficiency of LAPO-NCM88-based ASSLB at a LAPO-NCM88 areal loading of 20.1 mg cm^{-2} . Reproduced from ref. [747]. Copyright 2024 American Chemical Society.

To overcome the limitation of the performance due to the low conductivity of metal oxides used as coating layers, Kim et al. coated $\text{Li}[\text{Ni}_{0.88}\text{Co}_{0.11}\text{Al}_{0.01}]\text{O}_2$ with Li_3YCl_6 , the conductivity of which is 0.40 mS cm^{-1} . The solid-state battery with this Li_3YCl_6 -coated NCA, $\text{Li}_6\text{PS}_5\text{Cl}$ as solid electrolyte, and Li-In anode exhibited a capacity of 134 mA h g^{-1} at 2 C (vs. 53 with the pristine NCA) [750]. $\text{Li}_{6.25}\text{La}_3\text{Zr}_2\text{Al}_{0.25}\text{O}_{12}$ -coated Zr doped NMC811 exhibited a capacity retention of 70.1% after 1000 cycles at 1 C in a full ASSB cell with Li-In anode and $\text{Li}_6\text{PS}_5\text{Cl}$ electrolyte, demonstrating that this coating layer enhanced the stability between the Ni-rich cathode material and the sulfide electrolyte [751]. Wang et al. proposed a new process, where $\text{LiNi}_{0.88}\text{Co}_{0.09}\text{Mn}_{0.03}\text{O}_2$ (NCM88) cathode is sulfidized via a time-/cost-efficient strategy in a mixed N_2 and CS_2 gas atmosphere, improving the interfacial compatibility with $\text{Li}_6\text{PS}_5\text{Cl}$. The corresponding ASSB with $\text{Li}_6\text{PS}_5\text{Cl}$ electrolyte and $\text{Li}_{4}\text{Ti}_5\text{O}_{12}$ anode delivered a capacity of 200.7 mAh g^{-1} , 87% capacity retention after 500 cycles, and satisfactory rate capability (158.3 mAh g^{-1} at 1 C) [752]. Kitsche et al. prepared HfO_2 -coated $\text{LiNi}_{0.85}\text{Co}_{0.10}\text{Mn}_{0.05}\text{O}_2$ (NCM-851005) via atomic layer deposition

(ALD) of tetrakis(ethylmethylamido)hafnium(IV) with O_3 as the oxidant [753]. The test in a cell with this modified cathode, Li_6PS_5Cl electrolyte and $Li_4Ti_5O_{12}$ anode exhibited a capacity retention of 82% after 60 cycles at 0.5 C and 45 °C. A drawback with the use of thiophosphate-based electrolytes is their limited stability toward the oxidizing potentials of Ni-rich cathodes, which limits the cycle ability of the ASSBs. Therefore, efforts are made to choose different solid electrolytes, such as chloride-based SEs, principally Li_3InCl_6 . However, Li_3InCl_6 is unstable when in contact with the Li anode, so that Gao et al. introduced a layer of Li_3InCl_6 adjacent to the $LiNi_{0.83}Mn_{0.06}Co_{0.11}O_2$ cathode, and a Li_6PS_5Cl layer placed between this and the Li-In alloy acting as the anode [754]. Therefore, Li_6PS_5Cl could not be entirely suppressed. Nevertheless, the cell made of NMC, solid electrolyte, and carbon nanofiber mass ratios of 65, 30, and 5 wt.%, respectively, showed significantly improved electrochemical properties. When cycled at 1 $mA\ cm^{-2}$ and 80 °C under 2 MPa stack pressure at a cutoff voltage of 4.2 V, the cell delivered a capacity of 118 $mA\ h\ g^{-1}$ total, with capacity retention of 94% ± 1.2% after 50 cycles. Note the stack pressure was needed to obtain this result by limiting the volume change of the cathode material to approximately 2.5% during cycling.

The coating of the particles proved useful to suppress the cracking of the particles and protect them from side reactions with the electrolyte. However, the process increases the cost of fabrication of the cathodes. Recently, solid-state electrolytes (SSE) were employed to prevent the cracking of the Ni-rich particles without the need of coating, provided that intimate contact between the cathode material and the solid electrolyte is maintained. For this purpose, sulfide solid electrolytes should be avoided with unprotected Ni-rich materials, because they decompose at a cathode voltage as low as 2.6 V [755]. Note, however, that Kim et al. constructed an all-solid-state battery utilizing the argyrodite-type sulfide electrolyte, Li_6PS_5Cl (LPSCl), as the solid electrolyte, with an NMC811 cathode material coated with lithium lanthanum titanate (LLTO). The authors employed a rapid technique known as flash-light sintering (FLS) to fabricate a uniform and pure perovskite protective layer without inducing cation mixing in NMC [756]. The Li-In/LPSCl-modified NMC811 cell cycled in the voltage range 2.5–4.25 V exhibited an initial capacity at 1 C of approximatively 100 $mA\ h\ g^{-1}$ lower than that of bare NMC811 (167.96 $mA\ h\ g^{-1}$), and a better cycle ability, with a capacity retention of 95%, but over 40 cycles only. Zhao et al. coated quasi single-crystalline $LiNi_{0.83}Co_{0.12}Mn_{0.05}O_2$ (SC83) particles to protect the cathode material from Li_6PS_5Cl solid electrolyte. The all-solid-state cell exhibited a capacity retention of 88% after 1000 cycles at the 1 C rate, compared to only 71% for the uncoated counterpart [757] (see Figure 20).

On the other hand, the employment of >4 V-class cathode materials is enabled without any protective coating with lithium metal halide solid-state electrolytes, due to their high electrochemical oxidation stability [758–761]. An all-solid-state Li battery with $LiNi_{0.85}Co_{0.1}Mn_{0.05}O_2$ cathode and $Li_2In_xSc_{0.666-x}Cl_4$ ($0 \leq x \leq 0.666$) electrolyte exhibits a long life of >3000 cycles with 80% capacity retention at room temperature. High cathode loadings are also demonstrated in ASSBs with stable capacity retention of >4 $mA\ h\ cm^{-2}$ (~190 $mA\ h\ g^{-1}$) [762]. A remarkable performance was achieved in an all-solid-state cell composed of a single crystallized uncoated NMC811 as a cathode, a Li_3YCl_6 electrolyte, and a Li-In alloy anode: this ASSB delivered a discharge capacity of 170 $mA\ h\ g^{-1}$ at C/5 and an impressive capacity retention of nearly 90% after 1000 cycles [763]. Liu et al. reported the development of free-standing-type composite cathodes containing NCM (Ni stoichiometries ≥ 0.83) active materials and Li_3InCl_6 (LIC) solid electrolyte. The strong interface was realized via a novel in situ recrystallization process of LIC. The resulting free-standing composite cathode containing $LiNi_{0.88}Co_{0.06}Mn_{0.05}Al_{0.01}O_2$ (NCM88) and LIC sustained 1500 charge–discharge cycles under a low operating stacking pressure ~2 MPa [764].

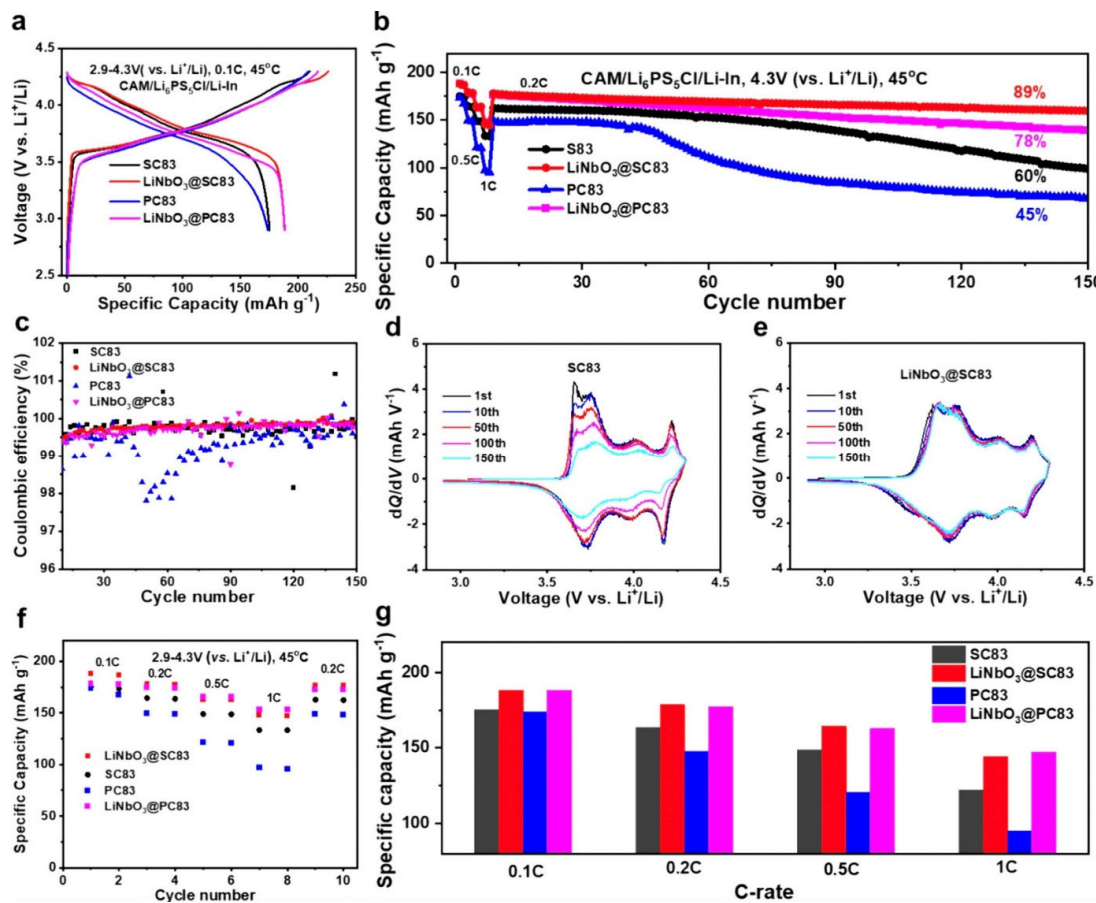


Figure 20. Cathode performance of all-solid-state batteries using quasi single-crystalline $\text{LiNi}_{0.83}\text{Co}_{0.12}\text{Mn}_{0.05}\text{O}_2$ (SC83) and SC83 coated with LiNbO_3 cathode materials, and $\text{Li}_6\text{PS}_5\text{Cl}$ electrolyte. **(a)** First-cycle voltage profiles at 0.1 C and 45 °C, **(b)** long-term cycling stabilities at 0.2 C, and **(c)** corresponding Coulomb efficiencies. Differential capacity curves of 1st, 10th, 50th, 100th, and 150th cycles for **(d)** SC83 and **(e)** $\text{LiNbO}_3@\text{SC83}$. **(f)** Rate capabilities and **(g)** corresponding specific capacities at C-rates ranging from 0.1 to 1 C. Reproduced from ref. [757]. Copyright 2025 American Chemical Society.

7.2. Liquid Electrolytes

With liquid electrolytes, the residual Li species present on the surfaces of Ni-rich particles promote the decomposition of electrolytes to produce corrosive HF. This enhances the dissolution of the TM ions in the electrolyte [765], and it reduces the Li^+ diffusion coefficient [766]. The migration of these TM ions to the anode side hinders the insertion of lithium inside the anode, which implies a loss of capacity and the deterioration of the battery [767]. Note that there is a difference between NMC and NCA materials concerning the dissolution of TM ions. The disproportionation of Mn ions ($\text{Mn}^{3+} \rightarrow \text{Mn}^{4+} + \text{Mn}^{2+}$) may lead to more severe dissolution of Mn than Ni and Co ions [768]. This is consistent with the fact that the capacity loss of batteries is closely related to the concentration of Mn ions in the cathode. Actually, a Ni-rich pristine NCA cathode exhibits much less dissolution of TM (where TM = Ni) than a Ni-rich pristine NMC (where TM = Ni + Mn), due to the stabilized effect of Al^{3+} [769].

Highly delithiated (highly charged) states generate large amounts of Ni^{4+} that can react with electrolytes. This results in a thickening of the cathode–electrolyte interface (CEI), reducing the number of available Li^+ and generating a resistive surface layer [18]. The high Ni^{4+} concentration also leads to a decay in the electrochemical reaction activity [9]. It will also result in a decrease of the thermal stability and thus an increase of the risk of

thermal runaway of the battery [92,770]. Above 4.2 V, the evolution of CO₂ gas and the generation of a heat flow from NMC cathodes [16] give evidence of such a reaction of the particles with the electrolyte. In addition, remaining at a highly delithiated state can cause significant electrolyte oxidation resulting in other side reactions [14]. To remedy this drawback, additives are employed in the electrolytes. In particular, a mixture with 2 wt.% prop-1-ene-1,3-sultone (PES) + 2 wt.% tris-(trimethyl-silyl) phosphite (TTSPi) + 2 wt.% 1,3,2-dioxathiolane-2,2-dioxide (DTD) in the control electrolyte (1 M LiPF₆ ethylene carbonate (EC): ethyl methyl carbonate (EMC) 3:7 w:w electrolyte), named PES211, can be used in Ni-rich cells to suppress the gas evolution [771]. In addition, rock-salt surface layers known to be formed with the use of VC are not formed with PES211. In practice, however, the Ni-rich cells should not be fully charged, which, however, implies a loss of energy density available with these batteries [772]. In addition, additives added to the electrolyte must help in the formation of the cathode–electrolyte interphase (CEI), but also of the solid–electrolyte interphase (SEI) on the anode side. In particular, in a full cell graphite/Ni-rich cathode, the dissolved Ni migrate to the graphite side and the strong correlation between Ni²⁺ and Li⁺ in the SEI is the main reason for the increase of SEI resistivity [773]. Many results are reported for full cells with graphite anode. However, other anodes can be chosen, in particular calcium tetrafluoroborate (Ca(BF₄)₂) as additive for the rational design of interfacial layers on both Li metal anode and Ni-rich cathode [774]. In this case, Li-Ca alloy suppressed the growth of Li dendrite by reducing the nucleation polarization. The preferential oxidation of BF₄⁻ in Ca(BF₄)₂ results in the formation of B-based CEI. For batteries with Ni-rich cathodes and Si-based anodes, we guide the reader to a recent review devoted to them [775]. In addition, we would like to mention a result too recent to be included in this review, dating from 2023. Huang et al. introduced tetravinylsilane (TVSi) as a multifunctional electrolyte additive into a commercial electrolyte to engineer tailored interphases simultaneously on Si anode and LiNi_{0.92}Mn_{0.05}Co_{0.03}O₂ cathode [776]. This full cell demonstrated a capacity retention of 83% after 200 cycles at 1 C. In addition, Zhang et al. proposed 3-Fluoro-5-(4,4,5,5-tetramethyl-1,3,2-dioxaborolan-2-yl)picolinonitrile (FTDP), which decomposed to form B-contained and cyano (CN) group-rich CEI, as well as LiF-, Li₃N-rich solid SEI, simultaneously, resulting in the integrity and stability of electrodes [777]. The 1.6 Ah NMC811/SiO_x pouch cell with 0.2 wt.% of this additive delivered a high-capacity retention of 84.0% after 300 cycles at the current of 1.0 A.

7.2.1. Additives

The surface reactivity of the layered cathodes is related to the presence of surface-active oxygen resulting from TM-O bond covalency, which increases with increasing Ni content [778]. The consequence is a dehydrogenation of the ethylene carbonate (EC), which has been observed on NMC811 electrodes at a voltage of 3.8 V vs. Li⁺/Li [779]. This oxidation of the carbonate solvent is considered as the main route for the electrolyte decomposition [780,781]. This oxidative decomposition of the electrolyte generates a CEI that must be homogeneous to protect the particles from further degradation [782], and thin enough to avoid a thick resistive CEI that would reduce the rate capability [783]. To construct such a CEI, an electrolyte additive is a good strategy [784,785]. The most popular additive for this purpose is fluoroethylene carbonate (FEC) [786–788]. The reason for the use of fluorinated carbonates is their lower HOMO and LUMO energies compared to their nonfluorinated counterparts, due to the strong electronegativity of fluorine. Therefore, they have higher oxidation potentials and higher reduction potentials, so that they can be used in high-voltage cells. In addition, they are known to generate a SEI protecting the anode.

Organic additives can be sacrificed at high voltages (4.3–4.5 V) because their HOMOs are higher than the HOMOs of organic solvents, so that they are able to prevent the

oxidative decomposition of the solvents [789]. The electro-polymerization of electrolyte additives can also provide electrons to counteract the decomposition of solvents [790]. Other solvents can be used to allow for the formation of more even CEIs, reducing contact between electrode surfaces and electrolytes [791].

Replacing Mn and Co with Ni in layered $\text{LiNi}_x\text{Mn}_y\text{Co}_{1-x-y}\text{O}_2$ (NMC) positive electrodes promotes the dehydrogenation of carbonate-based electrolytes on the oxide surface, which generates protic species to decompose LiPF_6 in the electrolyte. The stability of the surface of NMC can be enhanced by decreasing free-solvent activity in the electrolyte through controlling salt concentration and salt dissociation. In particular, NMC811 with capacities greater than 150 mAh g^{-1} (77% retention) after 500 cycles could be achieved by simply increasing the LiPF_6 concentration [792]. Otherwise, protection of the Ni-rich particles is needed to avoid thermal runaway due to the reaction of NMC with the LiPF_6 salt of the electrolyte. Forero-Saboya et al. used lithium hydridoaluminate as electrolyte additive, which acts as HF scavenger. Moreover, its oxidation results in the formation of an Al-rich protective layer on the cathode. With this additive in the electrolyte, the $\text{LiNi}_{0.86}\text{Mn}_{0.07}\text{Co}_{0.07}\text{O}_2$ exhibited a capacity retention of 66% at C/3 after 200 cycles with a graphite anode, raising at 87% with $\text{Li}_4\text{Ti}_5\text{O}_{12}$ anode [793]. Hu et al. proposed the dual additives of tetrabutyl titanate (TBT) and lithium difluoroxalate borate (LiDFOB) to form a stable Ti-, B-, and F-rich CEI [794]. The LiDFOB additive is functionalized by fluorine (F)-rich functional groups, which leads to the formation of the LiF-based SEI layers via reductive decomposition. In addition, TBT stabilized the electrolyte by removing $\text{H}_2\text{O}/\text{HF}$. The $\text{Li}|\text{NMC811}$ cell with the dual additives exhibited a capacity retention of 86% after 200 cycles at 1 C and a high cut-off voltage of 4.5 V. This is also the capacity retention obtained with *N,O*-bis(trimethylsilyl)acetamide additive [795]. $\text{Li}_3(\text{CB}_{11}\text{H}_{12})_2(\text{CB}_9\text{H}_{10})$ hydroborate electrolyte was successfully integrated in a NMC811 cell. With the Li-In anode, the cell had a discharge capacity at C/10 of $\sim 145 \text{ mAh g}^{-1}$ at room temperature. It retained 98% of the initial discharge capacity after 100 cycles at C/5 and 70% after 1000 cycles at C/2 [796]. Capacity retentions of 97% after 100 cycles at C/5 and 75% after 350 cycles at C/2 are also achieved with a graphite anode without any excess Li. The energy density per cathode composite weight of 460 Wh kg^{-1} is on par with the best solid-state batteries.

Hu et al. tuned the spatial linking structure of dipentacyclic anhydride (DPA) to obtain a new class of DPA-based additives to obtain robust CEI and SEI layers [797]. Among them, the best results were obtained with 1,2,3,4-cyclobutane-tetracarboxylic dianhydride (CBDA). The CBDA with a quaternary ring spatial linking structure changes Li^+ coordination, which decreases the content of organic species in the CEI. In addition, CBDA makes more PF_6^- and FEC to transfer to both of the electrodes' surfaces for decomposition owing to their stronger binding energies. As a result, a prototypical 216 Wh kg^{-1} (1.2 Ah) NMC811//graphite pouch cell with this additive in the electrolyte exhibited an ultrahigh capacity retention 94% over 800 cycles at a current density of 1 C. Moreover, prolonged stable cycling for 900 cycles (93% capacity retention at 1 C) in an NMC811//graphite pouch cell was enabled by CBDA, outperforming the best cycling performance of NMC811//Li-metal batteries incorporating monocyclic anhydride additives (83% after 200 cycles at 1 C) [798]. Jiang et al. employed glutaric anhydride (GA) as a multifunctional electrolyte additive to in situ construct a CEI, which significantly enhanced the cycling performance of $\text{Li}/\text{NMC811}$ cell [799]. Therefore, anhydride additives can be used with Ni-rich based batteries, although the functions and mechanisms of these additives are not well understood and need further investigations.

Qin et al. reported a Janus-faced CEI film constructed by succinonitrile (SN) and cylohexylbenzene (CHB) additives [800]. SN is adsorbed on electrode particles, while CHB is electrochemically polymerized generating an outer layer subsequently. The $\text{Li}/\text{LiNi}_{0.8}\text{Co}_{0.1}\text{Mn}_{0.1}\text{O}_2$ cell with SN+CHB electrolyte presented excellent long-cycle per-

formance with a capacity retention ~72.3% in 600 cycles at the rate of 0.5/1.0 C between 2.8–4.7 V.

VC is known to generate a poly(carbonate)-based SEI layer, but it usually hinders Li⁺ migration at the Ni-rich NCM interface [801,802]. A co-additive is thus recommended to compensate for the inferior properties of the VC additive. Kim et al. proposed the choice of LiDFOB as a co-additive of VC for Ni-rich NCM and SiO_x electrode materials [803]. The *LiNi_{0.83}Co_{0.11}Mn_{0.06}O₂* (NCM83) // SiO_x cell with this modifies electrolyte exhibited a capacity retention of 72.7% after 100 cycles at 1 C. Dai et al. selected LiNO₃ and LiBF₄ as dual additives. With an electrolyte consisting in 1.0 M LiPF₆ in SL/FEC/EMC with 0.5 wt.% LiBF₄–LiNO₃, NMC811-graphite cell retains 90.4% of the initial capacity after 200 cycles at 2 C (~6 mAh cm⁻²), owing to the formation of a uniform and LiF-inorganic (including B and S)-rich CEI and a dense, thin Li₃N–LiF-rich SEI [804].

Excessive Li is usually added in the preparation of NMC-based cathodes and tends to accumulate on the surface of particles and react with electrolytes to convert to lithium carbonate and hydroxide [423,805]. LiPF₆ can react with excessive alkaline Li on the surfaces of cathode particles to produce chemically stable Li₃PO₄ and LiF, and significantly suppress parasitic reactions caused by excessive Li [806]. Phelan et al. showed that higher concentration of LiPF₆ leads to formation of more Li_xPO_yF_z-/LiF-rich CEI that protects Ni-rich cathode materials [807]. Qiao et al. introduced Li₂O as a preloaded sacrificial agent on a NMC811 cathode to provide an additional Li source to offset the irreversible loss of Li, and employed fluorinated ether additive to neutralize O₂⁻ species released through Li₂O oxidation [808]. This led to the construction of a LiF-based layer at the CEI. The pouch cell constructed with this modified NMC811 cathode has a gravimetric energy density of 320 Wh kg⁻¹, maintaining 80% capacity after 300 cycles. On the other hand, reactions between LiPF₆ and trace amounts of water generate HF. To prevent such reactions, 3-IPTS can be used as an electrolyte additive: it can consume the trace amounts of water in electrolytes [789]. Zhang et al. demonstrated an effective approach to inhibit the dissolution of TM ions by using medium concentrated lithium bis(fluorosulfonyl)imide (LiFSI)-based electrolytes with an optimized fluoroethylene carbonate (FEC) content. In addition, this electrolyte creates the formation of a LiF-rich layer on the *LiNi_{0.90}Mn_{0.05}Co_{0.05}O₂* cathode surface [809]. Triallyl cyanurate (TAC) additive forms robust CEI via oxidation decomposition and inhibits LiPF₆ hydrolysis. It also modifies SEI on the anode through reduction decomposition. As a result, TAC substantially enhances the electrochemical performance of Ah-level pouch cells with various Ni-rich cathodes, achieving long cycle life at both room temperature and 45 °C, alongside improved high-temperature storage capabilities, with both graphite and graphite-SiO_x anodes [810] (see Figure 21). Zhuang et al. proposed bis(di-tert-butyl)-4-dimethylaminophenylphosphine (Bis-4TMPA) as electrolyte additive [811]. The phosphine group in Bis-4TMPA reacted with the oxygen species and formed a stable CEI, while the nitrogen-containing group reacted with HF to reduce the corrosion on the electrode. The *LiNi_{0.8}Co_{0.1}Mn_{0.1}O₂* with the addition of 0.5 wt.% Bis-4TMPA exhibited a capacity retention rate of 76.3% after 400 cycles (1 C = 200 mAh g⁻¹), against 69.1% for the pristine NMC811. Zou et al. utilized 4-fluoro-N, N-dimethylbenzenesulfonamide (FBSN) as an additive to refrain the dehydrogenation of EC [812]. This result is due to the formation of a CEI composed of LiF and benzene ring skeleton along with conductive S-rich and N-rich lithium species. Moreover, this CEI can be effectively self-repaired in time when damaged. As a result, the *LiNi_{0.9}Co_{0.05}Mn_{0.05}O₂* (NCM90) // Li cells with 2% FBSN-containing electrolyte delivers a capacity retention of 90.2% after 200 cycles at 1 C, and 83.1% after 200 cycles even at higher voltage of 4.5 V. With 2,4,6-triphenyl boroxine (TPBX) additive, the graphite/NMC811 maintained 84% of the initial discharged capacity after 100 cycles at 0.5 C (69% for the cells using the baseline electrolyte [813]. Zhang et al.

proposed a diazacyclo type additive, 2-fluoropyrazine (2-FP). When adding 0.2% 2-FP to the electrolyte, the capacity retention of single-crystal LiNi_{0.90}Co_{0.05}Mn_{0.05}O₂ (NCM90) cathode was promoted from 72.3% to 82.1% after 200 cycles at 1 C [814]. This improvement is attributed to the formation of a CEI film through ring-opening electrochemical polymerization of 2-FP upon the NCM90 electrode particles; This film suppressed of the decomposition of LiPF₆ and protected the cathode from side reactions with the electrolyte. Yang et al. fabricated a robust CEI through in situ polymerization of ethylene carbonate induced by aluminum isopropoxide [815]. This increased the capacity retention of the NMC811//Li cell at 1 C rate after the 3rd cycle from 80.8% to 97.8% with a highly reversible capacity of 176 mAh g⁻¹ after 200 cycles at 1 C.

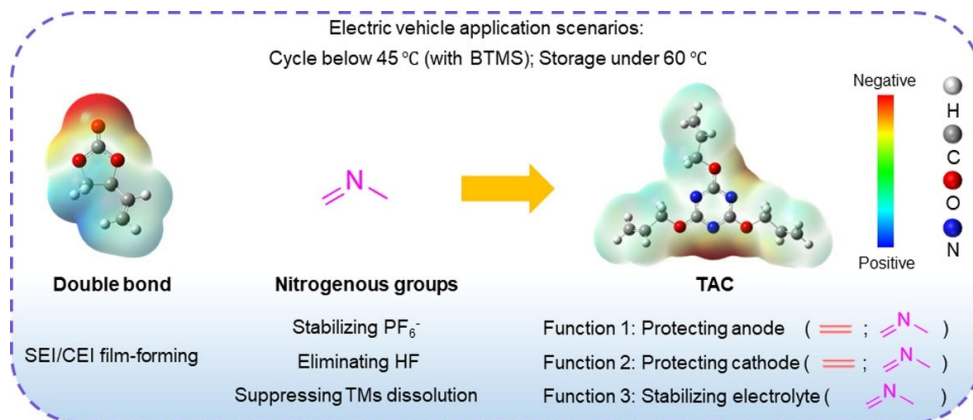


Figure 21. Structure of triallyl cyanurate (TAC) and how it reflects the ‘multi-in-one’ design strategy. TAC, a triple-functional additive, extends battery life by forming a protective SEI on the anode, a CEI on cathode, and stabilizing the electrolyte against hydrolysis and corrosivity. It significantly improves cycle life and high-temperature storage for Ni-rich cathode Li-ion cells. Reproduced from ref. [810]. Copyright 2025 Elsevier.

Sulfone and sulfonate additives are used to stabilize both CEI of Ni-rich cathodes and the SEI at the anode side [816]. Kim et al. constructed a sulfonate-based CEI layer that selectively protect the surface of the Ni-rich NCMA cathode materials and control parasitic reactions. They selected 3-(*N,N*-dimethylpalmitylammonio)propane sulfonate (PAPS), which features amphiphilic characteristics due to its combination of hydrophilic (sulfonate) and hydrophobic (carbon) functional group. Above the melting point of PAPS (242 °C), the liquefied PAPS evenly attached to the Ni-rich NCMA material, and a further increase in temperature decomposed the PAPS precursor to form the sulfonate-based CEI layer [817]. The capacity retention of the PAPS-modified NCMA cathode after 100 cycles at 0.5 C improved at both 25 °C (92.7%) and at 45 °C (86.4%) compared with that of the pristine NCMA cathode (58.5% and 28.8%, respectively). Enhanced performance of the NMC811//graphite cell was achieved with 2-thiophene sulfonamide (2-TS) additive [818]. After 500 cycles in the voltage range of 2.80–4.20 V, the cell with 1% 2-TS lost 8.40% of the initial discharge capacity (23.59% without the additive). Li et al. proposed p-toluene sulfonylmethyl isocyanide (TOSMIC) additive. The high reduction activity of TOSMIC additive is mainly contributed by its sulfone group, while the high oxidation activity is primarily caused by its phenyl group. The graphite/LiNi_{0.8}Co_{0.15}Al_{0.05}O₂ cell with 3 wt.% TOSMIC exhibited a capacity retention of 67% after 100 cycles at 0.5 C [819]. The 3,3-diethylene di-sulfite (DES)-functionalized electrolyte regulates both the graphite anode and the NMC811 cathode, increasing the capacity retention of the cell to 82.53% after 150 cycles at 1 C when the cut-off voltage is raised to 4.5 V [820]. A noticeable result was obtained with 4-(allyloxy)phenyl fluorosulfate (APFS) additive. On one hand, the radical copolymerization of vinylene carbonate (VC) with APFS via electrochemical initiation creates a

spatially deformable polymeric SEI on the SiG-C (30 wt.% graphite + 70 wt.% SiC composite) anode. On the other hand, it generates a thermally stable CEI containing S-O and S-F species on the NMC cathode material. The SiG-C/LiNi_{0.8}Co_{0.1}Mn_{0.1}O₂ full cell with the combined use of VC with APFS exhibited a capacity retention of 72.5% with a capacity of 143.5 mAh g⁻¹ after 300 cycles at 45 °C [821]. The crucial role of VC polymerization in enhancing CEI stability and mitigating surface reconstruction on NMC cathodes has been explored recently [822]. Liu et al. proposed bis(4-fluorophenyl) sulfone (BFS) as an additive, which improved the capacity retention of NMC811 from 75.19% to 83.04% after 100 cycles at the rate of 1 C [823]. This additive led to a stable CEI, and can be oxidized at state of charge into two sulfonates, which prevent the carbonate electrolyte from decomposition. Another sulfone-based additive, phenyl trans-styryl sulfone (PTSS) increases the capacity retention of NMC811//graphite full cell from 48% to 63% after 100 cycles at 1 C [824]. This is attributed to the formation of the CEI, but in addition, the PTSS induced-SEI film enhances the interphasial stability of graphite anode. A sulfonate-based CEI was obtained by using ammonium sulfate [825], increasing the capacity retention of NMC from 52.2% to 75.6% after 100 cycles at 0.5 C at 45 °C. Joung and Yim proposed *N,N,N,N*-tetraethylsulfamide to improve surface stability for Ni-rich oxides cathode [826]. This sulfone and amine group-based additive effectively constructed an effective CEI layer on NMC811 cathodes, inhibiting electrolyte decomposition. In addition, it lowered the fluoride concentration in the cell. Ahn et al. proposed allyl phenyl sulfone additive [827]. A sulfonate ester additive, 1,3-propane sultone, is effective to stabilize the CEI of NMC, and the SEI on the lithium anode by constructing a LiF/Li₂SO₃-rich interphase layer [828]. Like in the other sulfone-based additives already cited, the sulfone functional group effectively suppresses electrolyte decomposition during cycling. The allyl functional group promotes additional crosslinking reaction during CEI formation, which renders the CEI more durable. In addition, it scavenged fluoride (F⁻) species in the cell with NMC811. As a result, the capacity retention at a relatively high temperature of 45 °C where the standard electrolyte decomposition is accelerated, the capacity retention of the Li//NMC811 cell at 0.5 C raises from 64.3% with the pristine electrolyte, to 78.9% with 0.25 wt.% additive. A cell with SiO_x/C anode, NCM90 (LiNi_{0.9}Co_{0.05}Mn_{0.05}O₂) cathode, in electrolyte with allyl phenyl sulfone additive still delivered a capacity of 777 mAh g⁻¹ after 200 cycles at 0.5 C and 30 °C, corresponding to 79.3% capacity retention (57.8% capacity retention without the additive) [829]. Trimethylsilyl 2-(fluorosulfonyl) difluoroacetate (TMSFS) additive in the electrolyte enhanced the capacity retention of LiNi_{0.9}Co_{0.05}Mn_{0.05}O₂ (NCM90) from 73% to 85.1% at 1 C up to 200 cycles [830], compared to 78% obtained with bis(vinylsulphonyl)methane instead of TMSFS [831]. Another scavenger of HF is 1-(trimethylsilyloxy)cyclohexene (TMSCH) with functional groups (C=C, Si-O) electrolyte additive, which in addition regulars both the CEI and the SEI with lithium metal anode [832]. The retention of the Li//NMC811 batteries at 1 C are enhanced from 68.2% to 84.9% at 30 °C and 64.2% to 85.8% at 45 °C. with this additive. Choi et al. chose a sultone additive: 1,4-butane sultone (BS), because its HOMO is similar with that of the carbonate-based solvents, and can thus form a stable CEI. The Li[Ni_{0.75}Mn_{0.25}]O₂//graphite full cell using the carbonate-based electrolyte with 1 wt.% BS additive exhibited a capacity retention of ~80% after 200 cycles at 200 mA g⁻¹ (~68% in absence of BS) [833].

Phosphorous containing additives can also participate in the formation of stable and robust CEI, and scavenge HF. Jo et al. introduced monobasic sodium phosphate (NaH₂PO₄) additive, which improved the thermal stability of NMC811 and enhanced the electrochemical performance of graphite//NMC811 cell at 60 °C [834]. On the other hand, lithium bis(trimethylsilyl) phosphate (LiTMSP) was incorporated as an electrolyte additive in graphite/NMC811 for improving the low-temperature performance (at -10 °C).

Zhao et al. utilized carbonate-based electrolytes containing vinylene carbonate (VC) additive to stabilize graphite and phosphate compounds like triallyl phosphate (TPPC2) and tripropargyl phosphate (TPPC3) additives to stabilize the Ni-rich cathode. The artificial graphite/NMC811 with this modified electrolyte increased the capacity retention of NMC811/AG cells to 90.5% after 500 cycles at 1.0 C and 55 °C [835]. A better compromise between voltage drop, gas emission, and thermal stability in artificial graphite/NMC811 can be obtained with lithium difluoro(dioxalato)phosphate (LiDFDOP) additive, singly and in combination with co-additives fluoroethylene carbonate (FEC) and vinylene carbonate (VC) [836].

Allyltrimethylsilane additive has the same functions owing to C=C, Si-C groups, enhancing the capacity retention of NMC811 to from 46.4% to 82.9% after 200 cycles at 1 C [837]. We have already mentioned the improvement of the electrochemical performance of Ni-rich cathodes by coating the particles with siloxane [437]. 1,3,5-Trimethyl-1,3,5-tris(3,3,3-trifluoropropyl) cyclotrisiloxane (D_3F) as an electrolyte additive is also effective. 5 wt.% of this additive enhances the capacity retention of the graphite/NMC811 cell from 38 to 76% after 300 cycles at 1 C [838]. Among siloxane additives, propargyloxytrimethylsilane (PMSL), allyloxytrimethylsilane (AMSL), and trimethylmethoxysilane (TMSL) have been tested by Chen et al. They concluded that the highest cycle ability at 60 °C is obtained with PMSL, the artificial graphite//NMC811 cell with this additive exhibiting a capacity retention of 85% after 300 cycles at 0.5 C in the voltage range 3.0–4.3 V [839]. Ren et al. introduced cyano-groups into a siloxane to synthesize a novel cyano-siloxane additive, namely 2,2,7,7-tetramethyl-3,6-dioxa-2,7-disilaoctane-4,4,5,5-tetracarbonitrile (TDSTCN). 0.5 wt.% TDSTCN additive enables ultrahigh nickel LiNi_{0.9}Co_{0.05}Mn_{0.05}O₂//graphite (NCM90//Gr) full cells with significantly increased cycle life, especially at an elevated temperature of 50 °C and a high charging cut-off voltage of 4.5 V [840]. Zhang et al. introduced lithium hexamethyldisilazide (LiHMDS) with a low oxidation potential, which improve the cycling stability of Li//NMC811 batteries at high-stress conditions such as high voltage (4.5 V) and high temperature (60 °C) [841].

Fluorine-containing electrolyte additives have excellent kinetic reactivity, which can preferentially generate stable SEI films and uniform CEI [842]. Lithium difluoro(oxalato)borate (LiDFOB) additive is a film-forming additive protecting the surface of Ni-rich cathodes [843]. The same additive has been used with a fluorinated electrolyte composed of 1 M LiPF₆ as a lithium salt in fluoroethylene carbonate (FEC)/ethyl methyl carbonate (EMC)/2,2,2-trifluoroethyl acetate (TFA) (1:3:1 by volume) [844]. The NMC811 cathode with this electrolyte and 0.2 M LiDFOB additive exhibited superior discharge capability (247.2 mAh g⁻¹), cycling stability (81.4% retention at 200 cycles, 0.5 C) and rate performance (154.5 mAh g⁻¹ at 5 C) at 4.6 V compared to commercial electrolytes (66.2% retention at 200 cycles, 108.0 mAh g⁻¹ at 5 C) in Li//NMC811 half-cells. Ahn et al. proposed 2,4-difluorobiphenyl (FBP) as a fluorine-based additive to form a stable CEI, where the biphenyl provides an overcharge protection [845]. This additive successfully enhanced the high-voltage cycling stability of the Ni-rich NCM83 cathode. Chen et al. utilized LiDFOB and tris(trimethylsilyl)phosphate (TMSP) as dual additives, where TMSP was added to scavenge HF [846]. Owing to the synergistic effect of LiDFOB and TMSP, the Li/LiNi_{0.8}Co_{0.1}Mn_{0.1}O₂ half cells exhibited the capacity retention 76.3% after 500 cycles at a super high voltage of 4.7 V and 1 C rate. 2-aminoethyldiphenyl borate (AEDB) significantly improves long-term cycling of a graphite//LiNi_{0.85}Co_{0.1}Mn_{0.05}O₂ full cell, with a capacity retention of 88% after 100 cycles with cutoff voltage set to 4.35 V, by forming a stable CEI [847]. LiNi_{0.8}Mn_{0.1}Co_{0.1}O₂, or NMC811 is particularly attractive, as it can achieve a notably high specific capacity (200–220 mAh g⁻¹ at a relatively high average discharge voltage of ~3.8 V vs. Li⁺/Li), stable cycling with an ultrahigh cut-off voltage of 4.8 V

can be realized by using an appropriate amount of lithium difluorophosphate (LiPO_2F_2) in a common commercial electrolyte. The $\text{Li}^+/\text{LiNi}_{0.76}\text{Mn}_{0.14}\text{Co}_{0.10}\text{O}_2$ cell retains 97% of the initial capacity (235 mAh g^{-1}) after 200 cycles [848]. The decomposition products (Li_3PO_4 and LiF) of LiPO_2F_2 generated a protective SEI. This result is even better than the performance of NMC811 in presence of sulfonamide-based electrolyte [849].

Isocyanate additives also improve the electrochemical performance of Ni-rich cathodes [789]. Oh et al. proposed icosfluoro-15-crown-5-ether (IF-CE) as an additive [850]. Each molecule of this additive contains 20 fluorine atoms, which participate at the formation of SEI on the anode, and of CEI. A pouch-type full cell with 5 wt.% SiO_2 -graphite anode and $\text{LiNi}_{0.88}\text{Co}_{0.08}\text{Mn}_{0.04}\text{O}_2$ cathode, and IF-CE + FEC additives in the electrolyte, demonstrates an initial capacity of 194 mAh g^{-1} at 1 C, with capacity retention of 78% after 300 cycles. Peng et al. selected fluorine- and nitrogen-containing methyl-2-nitro-4-(trifluoromethyl)benzoate (MNTB) regulated with FEC to generate a robust CEI film while capturing HF [851] (see Figures 22 and 23). The NMC811//Li batteries with 15% MNTB-containing electrolyte exhibited a specific capacity of 150.12 mA h g^{-1} with a capacity retention of 81.10% after 300 cycles with 0.5 C charging and 1 C discharging in the voltage range of 3.0–4.3 V. Lei et al. chose pentafluorophenyl trifluoroacetate (PFTF) to adapt the NMC811 cell by forming LiF-rich CEI/SEI films and eliminate HF, extending the cycling stability of the symmetrical Li cell is expanded to 500 h [852]. Cyclopentyl isocyanate (CPI) with a single isocyanate ($-\text{NCO}$) functional group as a bifunctional electrolyte additive was used to improve the interfacial stability of Ni-rich cathode $\text{LiNi}_{0.83}\text{Co}_{0.12}\text{Mn}_{0.05}\text{O}_2$ [853]. Tan et al. utilized anhydride additives to improve the electrochemical performance of $\text{LiNi}_{0.5}\text{Mn}_{1.5}\text{O}_4$ cathode [854]. Han et al. used 4-fluorophenyl isocyanate (4-FI) as an additive to improve the low-temperature performance of the NMC811// $\text{SiO}_x@G$ battery due to the optimization of F in the SEI membrane components. The capacity retention of the NMC811// $\text{SiO}_x@G$ pouch cell increased from 92.5% (without additive) to 94.2% (with 1% 4-FI) after 200 cycles at 0.5 C. At -20°C , the cyclic stability of the NMC811// $\text{SiO}_x@G$ pouch cell increased from 83.2% (without additive) to 88.6% (with 1% 4-FI) after 100 cycles at 0.33 C [855]. 4-fluorobenzene isocyanate (4-FBC) electrolyte additive is also efficient to form a CEI film on Ni-rich cathodes. Tested in the NMC532// $\text{SiO}_2@\text{Graphite}$ pouch full cells with electrolytes containing a mass fraction of 1% 4-FBC additives demonstrate improved capacity retention of 81.3% after 200 cycles at 1 C (39.1% without additive) [856]. 1,2,4-1H-Triazole (HTZ) was added to the electrolyte to improve the interfacial stability of $\text{LiNi}_{0.9}\text{Co}_{0.05}\text{Mn}_{0.05}\text{O}_2$, resulting in an increase of both rate capability and cycle ability up to 60°C [857]. Owing to its $-\text{N}=\text{C}=\text{O}$ group, isocyanooethyl methacrylate additive improves the performance of NMC811//graphite, increasing the capacity retention from 62.8% to 81.9% after 150 cycles at 1 C in the voltage range 2.75–4.4 V [858].

Other HF scavengers include silane derivatives [859]. In particular, with 3% silane-based electrolyte additive, vinyltrimethylsilane (VTMS) in the LiPF_6 -based electrolyte, the graphite//NMC811 cell maintained a discharge capacity of 131.9 mAh g^{-1} after 500 cycles in the voltage range of 2.8–4.3 V at 1 C [860]. Cheng et al. reported that a dual additive containing lithium bis(oxalate)borate and dopamine produces a uniform inorganic/polymer CEI that eliminates undesirable interfacial side reactions [861]. Guan et al. synthesized niobium-doped strontium titanate (Nb-STO) via a facile solvothermal method and used it as a surface modification layer onto the NMC811 cathode. [862]. Not only did Nb-STO prevent the dissolution of the transition metals, it also alleviated the internal resistance growth from uncontrollable CEI evolution. With this protection, the capacity of NMC811 was $\sim 190 \text{ mAh g}^{-1}$ after 100 cycles under 1 C with capacity retention over 84% in the voltage range of 3.0–4.5 V (61% with pristine NMC811). Zhang et al. proposed an electrolyte additive, *cis*-1,2,3,6-tetrahydrophthalic anhydride (THPA), to enhance the interfacial

stability of the Ni-rich $\text{LiNi}_{0.90}\text{Co}_{0.05}\text{Mn}_{0.05}\text{O}_2$ (NCM90) cathode [863]. This additive not only hinders the oxidation of carbonate solvents, but also generates a conductive protective CEI film. The capacity retention of NCM90 with an electrolyte containing 2.0% THPA reached 93.2% after 120 cycles at 1 C ($1 \text{ C} = 180 \text{ mA g}^{-1}$) at 30°C , against 80.0% in absence of this additive. Zou et al. proposed a diboron electrolyte additive 5,5,5',5'-tetramethyl-2,2'-bi-1,3,2-dioxaborinane (TBDB) to construct a stable $\text{LiNi}_{0.9}\text{Co}_{0.05}\text{Mn}_{0.05}\text{O}_2$ (NCM90)/electrolyte interface [864]. With 0.3% TBDB-containing electrolyte, the NCM90 cathode shows a capacity retention of 84.3% after 200 cycles at 1 C at a charge cutoff of 4.4 V (70.1% with the baseline electrolyte). Zeng et al. employed Toluylene-2,4-diisocyanate (TDI) additive containing lone-pair electrons. With this additive in the electrolyte, the graphite//NMC811 cell exhibited a capacity retention of 94% at 1 C 1000 cycles at 25°C (78% in absence of this additive) [865]. The authors attributed this significant increase of the cycle ability to the isocyanate group playing a crucial role in inhibiting the generation of H_2O and HF, which leads to the formation of a thin and dense CEI. Lim et al. synthesized tetrakis(methacryloyloxyethyl)pyrophosphate additive to form a stable CEI, which increased the capacity retention of graphite/NMC811 cell to 82.2% after 300 cycles at a 1.0 C rate [866].

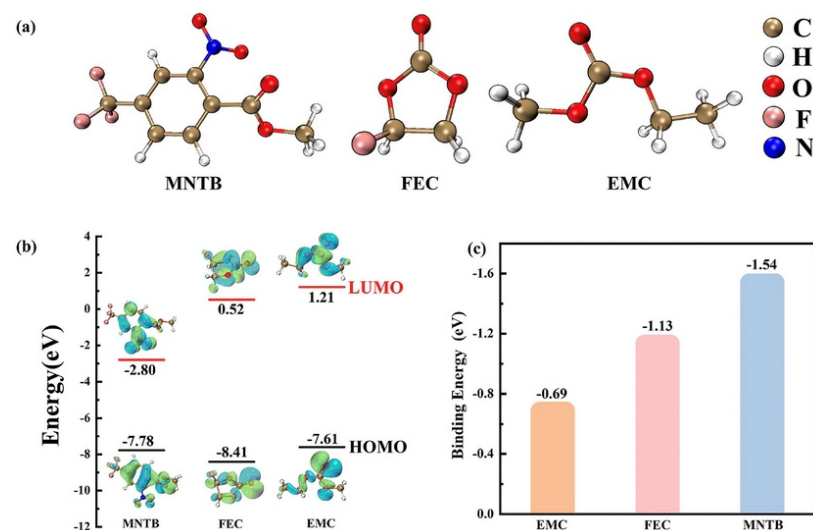


Figure 22. (a) Molecular structures of methyl-2-nitro-4-(trifluoromethyl)benzoate (MNTB), fluoroethylene carbonate (FEC), and ethyl methyl carbonate (EMC). (b) HOMO and LUMO energy levels of MNTB, FEC, and EMC. (c) Binding energies between Li^+ and solvents (binding energy = the energy of solvent after binding to Li^+ – the energy of solvent before binding to Li^+). The performance of NMC811 with MNTB/FEC electrolyte is reported in Figure 23. Reproduced from ref. [851]. Copyright 2024 American Chemical Society.

The oxidative decomposition of nitrile leads to the formation of a stable CEI responsible for the high-voltage stability of nitrile-containing electrolytes. Li et al. utilized lithium difluoro(oxalato)borate (LiDFOB) as the lithium salt and adiponitrile ($\text{C}_6\text{H}_8\text{N}_2$) as the additive. The $\text{LiNi}_{0.5}\text{Mn}_{1.5}\text{O}_4//\text{Li}$ half-cell with this electrolyte delivered a capacity of 100.9 mAh g^{-1} at 0.5 C, with a capacity retention of 81.2% after 50 cycles, significantly better than the result obtained in absence of the adiponitrile additive [867]. The additive adiponitrile complexed with Ni^{4+} ions on the surface of the cathode electrode inhibited the dissolution of Ni^{4+} and contributed to the formation of a CEI protective and conductive passivation film. The authors also calculated that the Ni^{4+} ion with a strong cathode potential and the cyanide group with a strong anode potential participated in charge transfer to stabilize the cathode material. In addition, adiponitrile also stabilizes the lithium anode, so that using 1 wt.% adiponitrile in 0.8 M LiTFSI + 0.2 M

$\text{LiDFOB} + 0.05 \text{ M LiPF}_6$ dissolved in EMC/FEC = 3:1 electrolyte, the Li/full concentration gradient $\text{Li}[\text{Ni}_{0.73}\text{Co}_{0.10}\text{Mn}_{0.15}\text{Al}_{0.02}]O_2$ battery achieves a cycle retention of 75% over 830 cycles under high-capacity loading of 1.8 mAh cm^{-2} and fast charge–discharge time of 2 h [868]. Another nitrile additive, 1,3,6-hexanetricarbonitrile was used to raise the capacity retention of $\text{LiNi}_{0.83}\text{Co}_{0.07}\text{Mn}_{0.1}\text{O}_2$ to 81.42% at 1 C after 300 cycles at a cutoff voltage of 4.5 V [869]. Note, however, that nitrile has a poor reductive stability. Therefore, it should not be used with lithium anode, unless another additive is added to form a SEI protecting the lithium or graphite anode.

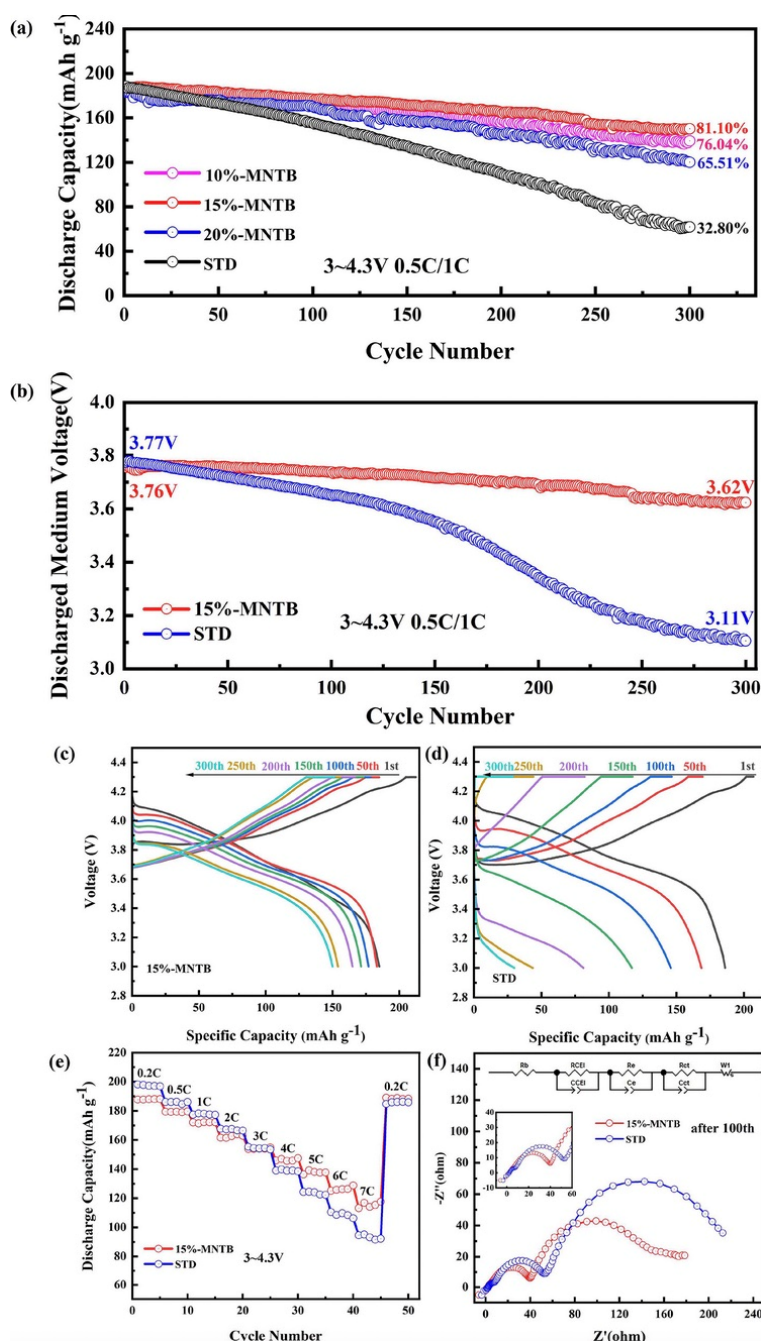


Figure 23. Electrochemical performance of NMC811 // Li cells. (a) cycling performance of standard electrolyte (STD) for reference, and different ratios of MNTB groups regulated with FEC after 300 cycles. (b) Discharged medium voltage. (c,d) Voltage–capacity graphs corresponding to different cycles. (e) Rate capability (0.2, 0.5, 1, 2, 3, 4, 5, 6, 7, and 0.2 C) diagrams. (f) EIS figure after 100 cycles. Reproduced from ref. [851]. Copyright 2024 American Chemical Society.

Qiu et al. designed 1-methyl-1-cyanopropylpyrrolidine bisfluoromethanesulfonimide salt (PYR_{1(4CN)}TFSI) to reduce the interface impedance on the NMC811 cathode side and enhance the compatibility between the electrolytes and the lithium metal anode. With the addition of 0.5 wt.% PYR_{1(4CN)}TFSI in the electrolyte, the Li//LiNi_{0.8}Co_{0.1}Mn_{0.1}O₂ cells delivered 107 mAh g⁻¹ after 200 cycles at 1 C [870]. The result is attributed to the combination of TFSI⁻ with pyrrole, which promotes the migration of Li⁺, while the cyano group can coordinate with oxygen atom electron pairs on TFSI⁻ to participate in the SEI film on the lithium anode. Park et al. utilized 5-methyl-4-((trifluoromethoxy)methyl)-1,3-dioxol-2-one and 5-methyl-4-((trimethylsilyloxy)methyl)-1,3-dioxol-2-one to provide spatial flexibility to the vinylene carbonate-derived SEI via polymeric propagation with the vinyl group of vinylene carbonate. This electrolyte was compatible with Si-C anode, and with high-voltage cathode, so the Si-C/NMC cell exhibited 81.5% capacity retention after 400 cycles at 1 C and fast-charging capability (1.9% capacity fading after 100 cycles at 3 C) [871]. Zhuang et al. introduced lithium tetrafluoro (1,2-dihydroxyethane-1,1,2,2-tetracarbonitrile) phosphate (LiTFTCP) additive, adding the effects of cyano-groups (—CN) into lithium fluorinated phosphate. NMC811 //SiO_x-graphite full cells (cathode loading 17.2 mg cm⁻², 3.5 mAh cm⁻²) using 0.5 wt.% LiTFTCP additive deliver a capacity retention of 90.24% (172.8 mAh g⁻¹/191.5 mAh g⁻¹) after 600 cycles at 1 C, 30 °C, in the voltage range 2.7–4.25 V, with an average Coulombic efficiency (ACE) of 99.91% [872]. This remarkable result is due to cyano-enriched CEI layer and the stable LiF-enriched SEI layer.

Song et al. reported a systematic study of electrolyte additives in single-crystal and bimodal artificial graphite/NMC811, including vinylene carbonate (VC), 1,3,2-dioxathiolane-2,2-dioxide (ethylene sulfate or DTD), fluoroethylene carbonate (FEC), lithium difluorophosphate (LFO), and lithium bis(oxalate) borate (LiBOB) [873]. They concluded that 2VC + 1DTD cells possess the best or close to the best performance on long-term cycling at 40 °C and 55 °C, but their high charge transfer resistance (R_{ct}) leads to relatively poor performance in 20 °C 1 C long-term cycling. 2FEC + 1LFO cells are also the top performer on formation gas and R_{ct} and possess lower R_{ct} and ΔR_{ct} than 2VC + 1DTD cells in cycling and storage tests, but perform slightly worse in capacity retention during cycling at 40 and 55 °C.

Innovative electrolyte solvent technologies are also a good strategy. We have already mentioned fluorinated solvents [146,833]. We can also cite fluoroacetonitrile (FAN) solvent enabling 4.5-V graphite//NMC811 pouch cells (1.2 Ah, 2.85 mAh cm⁻²) to achieve high reversibility (0.62 Ah) when the cells are charged and discharged even at -65 °C [874], fluorinated cyclic ether allowing Li (50 μm)//NMC811 (4 mAh cm⁻²) cells to maintain 80% capacity after 568 and 218 cycles at room temperature and 60 °C, respectively [875], and 1,2-difluorobenzene enabling highly stable cycling of Li//NMC811 cells (4.4 V) at C/3 charge and 1 C discharge (1 C = 2 mA cm⁻²) for 500 cycles with a capacity retention of 93% [876]. By dissolving fluorinated electrolytes into highly fluorinated non-polar solvents, the LiNi_{0.8}Co_{0.15}Al_{0.05}O₂//Li battery can still deliver ~50% of its room-temperature capacity at -85 °C [877]. With an all-fluorinated electrolyte containing fluoroethylene carbonate (FEC), and ethyl (2,2,2-trifluoroethyl) carbonate (ETFEC), the Li//NMC811 cell showed a capacity retention of 72.3% with an average CE of 99.8% at high voltage (up to 4.6 V) after 225 cycles at 1 C [878]. β-fluorinated sulfone-based electrolytes enable the very stable long-term cycling of graphite//LiNi_{0.6}Co_{0.2}Mn_{0.2}O₂ full cells [879].

10% sulfone plus 0.02 M Lithium difluoro(oxalato)borate (LiDFOB) enabling ~400 Wh kg⁻¹ NMC811//Li cells at 4.7 V to demonstrate an 82% capacity retention after 200 cycles [880]. Chen et al. chose ethyl butyrate (EB) as a solvent to be fluorinated because of its low melting point. In particular, ethyl heptafluorobutyrate (EHFB) enabled 4.5 V graphite//NMC811 pouch cells (1 Ah) to perform stably over 200 cycles at -10 °C with

only 2% capacity loss [881]. Xiao et al. enhanced the solubility of LiNO₃ in ester-based electrolytes by employing triethyl phosphate (TEP) as a co-solvent. As a result, NO₃⁻ is preferentially adsorbed on the electrode surface to derive a CEI layer with the homogeneous oxynitridation, while NO₃⁻ dominated weakly dissociated solvation clusters (NSC) suppress the dendrite formation on the lithium metal anode [882]. With this design, the Li//NMC811 full cell achieves 80% capacity retention after 300 cycles of 0.5 C. Another solubilizer, tris (2,2,2-trifluoroethyl) borate (TTFEB), utilizes its electron-deficient B atom to snatch electron-rich NO₃⁻ anion of insoluble LiNO₃ and thus forms a unique TTFEB-LiNO₃ solvation structure in carbonate electrolytes [883]. The full cell, featuring a thin Li anode (50 μm) and a high-loading NMC811 cathode (4.04 mAh cm⁻²) in the dual-additive electrolyte (FEC+TTFEB), demonstrated a capacity retention of 81.5% after 140 cycles at 1 C.

7.2.2. Electrolyte Formulations

An et al. designed a fire-resistant liquid electrolyte formulation consisting of propylene carbonate and 2,2,2-trifluoroethyl group-containing linear ester solvents paired with 1 mol L⁻¹ LiPF₆ salt and FEC additive. The replacement of linear carbonate with fluorinated linear ester yielded a fire-resistant and outperforming electrolyte under harsh condition. The fire-resistant electrolyte-incorporated industrial 730 mAh graphite//NMC811 Li-ion pouch battery achieved 82% retention after 400 cycles under 4.3 V charge voltage, 45 °C and 1 C [884]. Huang et al. designed an electrolyte consisting in 1 M LiPF₆ in FEC/acetonitrile (FEC/AN, 7/3 by vol.). Combining the FEC-dominated solvation structure and the AN-rich environment, the designed electrolyte triples the capacity of the 1 Ah graphite//NMC811 pouch cells at 8 C in comparison with the commercial electrolyte [885].

Other electrolytes have been formulated to improve the performance of batteries with Ni-rich cathodes. In particular, fluorinated linear carboxylate esters with low freezing point and low viscosity as co-solvents enhance the performance of such batteries at subzero temperatures [886,887], while perfluorinated electrolytes improve their thermal stability [888,889], and EC-free electrolytes are studied to enhance the high-voltage cycle life and safety [890–894].

Another class of electrolytes is obtained with substitution of LiPF₆ salt by other salts (LiTFSI, LiFSI, and LiDFOB). In particular, dual-salt LiDFOB-LiBF₄ in a sulfolane-based electrolyte with fluorobenzene additive to restrain the decomposition of sulfonate endowed graphite//NMC811 cell with capacity retentions of 83% after 500 cycles at 25 °C and 82% after 400 cycles at 60 °C [895]. Even better results were reported with 1.6 m LiFSI and (2-cyanoethyl)triethoxysilane (TEOSCN), which enabled long-term cycling mesocarbon microbead (MCMB)//NMC811 for 1000 cycles with an ultrahigh-capacity retention of 91% at 25 °C and for 500 cycles with a retention of 81% at 60 °C [896]. Xu et al. chose LiTFSI as the salt, and selected solvents with low donor number (DN < 10) and high dielectric constant to minimize Li⁺ desolvation energy, and thus the interfacial resistance, while still dissociating LiTFSI. These properties were fulfilled with an electrolyte consisting in 1 M LiTFSI dissolved into methyl difluoroacetate (MDFA), methyl 2,2-difluoro-2 (fluorosulfonyl)acetate (MDFSA), and 1,1,2,2-tetrafluoroethyl-2,2,3,3-tetrafluoropropylether (TTE). In addition, the fluorination endowed the electrolyte with non-flammability characteristics [897]. NMC811//graphite pouch cells with this lean electrolyte (2.5 grams per ampere hour) achieve stable cycling with an average Coulombic efficiency of more than 99.9 per cent at -30 °C. Su et al. developed a dual-anion regulated electrolyte using LiTFSI and lithium difluoro(bisoxalato)phosphate (LiDFBOP) as anion regulators. The incorporation of TFSI⁻ in the solvation sheath reduces the desolvation energy of Li⁺, and DFBOP⁻ promotes the formation of the CEI. As a result,

Li//LiNi_{0.83}Co_{0.11}Mn_{0.06}O₂ pouch cells exhibited 84.6% capacity retention at 0.1 C charge and 0.5 C discharge rates [898].

Chen et al. also utilized LiFSI as the primary salt and TTE as the dilutant. Moreover, trimethyl phosphate (TMP) provided the basis for the introduction of lithium nitrate (LiNO₃) as the secondary lithium salt. LiNO₃ regulated the solvation structure and successfully prepared the phosphate ester-based localized high-concentration electrolyte with an apparent Li⁺ concentration of 1.15 M. Meanwhile, NO₃⁻ generated nitride-dominated electrode/electrolyte interfaces on the lithium anode and nickel-rich cathode surfaces. As a result, the Li//NMC811 battery with this electrolyte maintained 81.7% capacity retention after 800 cycles at 4.3 V, 1 C, and 93.3% capacity retention after 200 cycles at a high voltage of 4.5 V [899]. On the other hand, Yang et al. kept a carbonate electrolyte, and used double salts synergistic effect (LiPF₆+LiFSI) to construct a super concentrated (DSSC) electrolyte of 1 M LiPF₆ + 8 M LiFSI in EC:DMC (LiPF₆: LiFSI = 1:8, EC:DMC = 1:1 by weight). The LiNi_{0.90}Co_{0.05}Mn_{0.05}O₂ (NCM9055)//Li cells with this electrolyte exhibited the capacity retention of 93.04% and reversible capacity of 173.8 mAh g⁻¹ after 100 cycles at 1 C rate. This result was attributed to the formation of a stable and uniform 2–3 nm rock-salt phase protection layer on the surface of NCM9055, induced by the electrolyte [900]. Zhang et al. proposed an electrolyte consisting of 1.9 m LiFSI in a mixture of 2,2,2-trifluoroethyl trifluoromethanesulfonate (TTMS) and 2,2,2-trifluoroethyl methanesulfonate (TM) (1:2 by volume). These two solvents integrate the properties of sulfonates and fluorination forming a Li-rich CEI and low impedance SEI layer containing S species on graphite, so that this electrolyte endows 4.6 V NMC811//graphite (1 Ah) with a high-capacity retention of 83% after 1000 cycles [901]. Zhang et al. fabricated an advanced ether-based localized high-concentration electrolyte (LHCE) consisting of LiFSI, 1,2-dimethoxyethane (DME) and TTE with a molar ratio of 1:1.2:3 [902]. The LiNi_{0.94}Co_{0.06}O₂ (NC94) in this advanced ether-based LHCE exhibited capacity retentions of 81.4% after 500 cycles at 25 °C and 91.6% after 100 cycles at 60 °C in the voltage range of 2.8–4.4 V in Li//NC94 cells at 1 C cycling rate.

Note, however, that the LiFSI corrodes aluminum of the current collector at voltage \geq 4.3 V [903], which is thus the limit of the upper potential range to be used, even if NMC is coated. Moreover, LiFSI and LiTFSI salts corrode the Ni-rich cathode materials [904], because the nickel ions induce the breakage of C-F bond of these fluor-lithium salts driven by voltage. To avoid these drawbacks, Qiao et al. designed a non-corrosive sulfonimide salt lithium((difluoromethanesulfonyl) (trifluoromethanesulfonyl)imide (LiDFTFSI)) [905]. The improvement of the electrochemical properties by the replacement of LiPF₆ or LiTFSI by this salt demonstrates the decisive role of the salt anion. Another demonstration is the outstanding improvement of the rate capability of Li//NMC811 pouch cell with an asymmetric Li salt, lithium 1,1,1-trifluoro-N-[2-[2-(2-methoxyethoxy)ethoxy]ethyl] methanesulfonamide (LiFEA) [906]. This pouch cell with LiFEA maintained 81% capacity after 100 cycles under fast-cycling conditions (charging: 1.46 mA cm⁻², discharging: 3.66 mA cm⁻²). A highly fluorinated (8-CF₃) aluminum-centered lithium salt of lithium perfluoropinacolatoaluminate (LiFPA) facilitates the formation of a passivating CEI layer (see Figure 24) [907]. A Li//NMC622 cell in a high loading of 3.5 mAh cm⁻² with LiFPA-EC/DMC electrolyte can perform 100 stable cycles delivered a capacity of 3.43 mAh cm⁻² after 100 cycles at 0.2 C, corresponding to a capacity retention rate of 97.7%. Wu et al. utilized a dual-anion ionic liquid, 0.8Pyr₁₄FSI-0.2LiTFSI. This salt allows for stable interfaces at both Li-metal and Ni-rich electrodes. With this specific electrolyte, the LiNi_{0.88}Co_{0.09}Mn_{0.03}O₂ (NCM88)//Li cell achieved an initial specific capacity of 214 mAh g⁻¹ and outstanding capacity retention of 88% over 1000 cycles at 0.3C, and an average Coulombic efficiency of 99.94% [908].

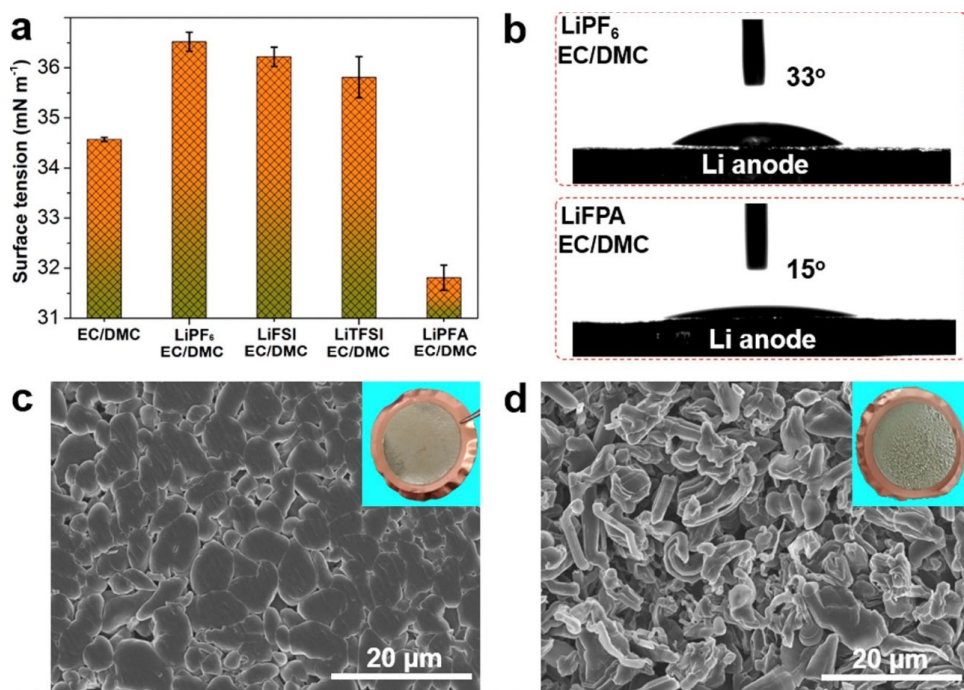


Figure 24. Effect of a highly fluorinated (8-CF_3) aluminum (Al)-centered lithium salt of lithium perfluoropinacolatoaluminate (LiFPA) on electrolyte wettability and Li deposition. (a) Surface tension of varied electrolytes. (b) Contact angle of 1 M LiPF₆-EC/DMC and 1 M LiFPA-EC/DMC to Li anode. Morphology of deposited Li on Cu foil using (c) 1 M LiFPA-EC/DMC and (d) 1 M LiPF₆-EC/DMC, at a current density of 0.5 mA cm^{-2} for 16 h. Insets in (c,d) are optical images of deposited Li on Cu foil. Reproduced from ref. [907]. Copyright 2022 American Chemical Society.

Since Li-derived impurities at the surface of the particles degrade the electrochemical performance, attempts have been made to remove them. Exposition of the Ni-rich layered materials in air results in the presence of LiOH and Li₂CO₃ impurities at the surface, which can react with the electrolyte to generate CO₂. Rinsing with water is a way to remove them [909]. Unfortunately, the water molecules induce the extraction of Li⁺ from the surface due to Li⁺/H⁺ exchange [910], triggering surface degradation and increasing the CEI [294]. We have mentioned earlier that the best strategy to remove the Li-derived impurities is coating. In addition, coating of NMC avoids the dehydrogenation of EC solvent, observed at voltage as low as 3.8 V on the surface of pristine NMC811 [779]. Wang et al. replaced the highly flammable organic solvents EC in conventional electrolytes with dimethyl methyl phosphonate (DMMP) and 1,1,2,2-tetrafluoroethyl-2,2,3,3-tetrafluoropropylether (HFE) to obtain an electrolyte having a wide potential window beyond 5.0 V, and forming an effective CEI. The Li//NMC622 battery with this electrolyte showed no capacity loss over 100 cycles, and an average CE of 99.6% at a high cutoff voltage of 4.5 V [911].

The interaction between the electrolytes and the Ni-rich materials is not yet well understood. A step has been made, however, by a recent work of Wang et al., who proposed a sp^2 -induction mechanism to address coordination deficiency through the coupling of interfacial orbitals between molecules and the cathode surface [912]. Among the sp^2 -hybrid high-fluorinated olefins in this work, (perfluorobutyl)ethylene (PFBE) is identified as an optimal inducing molecule. The Li//LiNi_{0.8}Mn_{0.1}Co_{0.1}O₂ (30 μm Li, high load 3.7 mAh cm^{-2} NMC811) cell with PFBE electrolyte achieving 80% capacity retention over 320 cycles (voltage range 2.8–4.4 V, charge/discharge 0.2/0.3 C), compared to 175 cycles with a PFBE-absent electrolyte. The electrolyte was composed of LiFSI salt and methoxytrimethylsilane (MOTMS) solvent, chosen because PFBE cannot dissolve salt (molar ratio LiFSI:MOTMS 1.2:2).

7.3. Recycling Ni-Rich Batteries

Lithium, cobalt, and nickel resources are limited [913,914]. To overcome this criticality and the energy costs and environmental hazards associated with the extraction of these metals, large-scale recycling of Ni-rich-based batteries is mandatory [915,916]. At present, only cobalt is recycled at a low price, taking into account the high cost of cobalt. Advancements in recycling technologies to mitigate environmental impact and recover valuable materials is thus desirable [917,918]. The industrial recycling processes of positive electrode materials comprise pyrometallurgy and hydrometallurgy. They are energy-intensive due to their reliance on high temperatures, and potentially damaging due to toxic chemicals. In hydrometallurgical processes, acidic leaching in the presence of a reducing agent is commonly used, including the use of H_2O_2 as a reducing agent for Co^{3+} [919]. To limit the extensive amount of chemicals used in hydrometallurgy, an alternative approach has emerged consisting of solid-state reactions to convert oxide-based materials into salts that are readily soluble in aqueous media. This approach, hereafter denoted salt conversion, has already been demonstrated for different salts including sulfates [920–922]. The fundamental understanding of the reactivity of layered compounds with these media has been investigated in this paper. The authors established the conditions to convert layered lithiated transition metal compounds into sulfate-based products targeting the stabilization of the metal into the langbeinite structure $K_2M_2(SO_4)_3$. This conversion enables subsequent metal recovery using only water as medium, which therefore prevents the classical use of highly acidic solutions usually used in hydrometallurgy to destabilize the oxidic compounds. To illustrate the possibility of recovering metals using salt conversion, the authors highlighted $LiCoO_2$ as an example. However, the langbeinite-type structure can accommodate different cations such as $M = Mg^{2+}, Ca^{2+}, Mn^{2+}, Fe^{2+}, Co^{2+}, Ni^{2+}, Zn^{2+}$, and Cd^{2+} [923]. Therefore, the extension of the salt conversion to NMC and NCA compounds supports the versatility of this method for different types of electrode chemistry of LIBs, opening practical outcomes to the vital question of battery recycling. Moreover, Wang et al. published a synthesis method of new cathodes, using as raw materials NMCs obtained from spent lithium-ion batteries recycling system [924]. Hamitouche et al. proposed a method to chemically convert lithiated transition metal oxides into readily water-soluble sulfate products [925]. This method comprises a temperature-driven solid-state reaction between the electrode material and potassium hydrogenosulfate molten salt yielding $K_2M_2(SO_4)_3$ and potassium/lithium sulfates.

Recently, Ji et al. [926] proposed a greener and more economic effective pathway, centered on “repair” to regenerate spent Ni-rich cathode materials, following a process already proposed to regenerate $LiFePO_4$ cathode by using a multifunctional organic lithium salt [927]. Ji et al. introduced a closed-loop upcycling strategy that leverages the detritus of the cathode and anode current collectors produced during dismantling process, involving two dopants (Al and Cu) in a ternary eutectic molten salt system ($NaCl-KCl-LiOH$). The two dopants work synergistically, as Al^{3+} tends to fill TM layer vacancies, strengthening bonding and reducing antisite defects, while Cu^{2+} tends to fill Li layer vacancies. The process was applied to highly degraded polycrystalline $LiNi_{0.83}Co_{0.12}Mn_{0.05}O_2$ cathode. The upcycled material achieved a first-cycle discharge capacity of over 215 mAh g^{-1} and maintained 93.3% capacity retention after 100 cycles at 1 C, and a fast-charging capability of 85 mAh g^{-1} at 15 C. The 1.2 Ah pouch cell using this upcycled cathode material retained 91.1% capacity retention after 200 cycles.

It is crucial to address the non-uniform lithium distribution among the repeatedly reacted cathode particles. The solution can be achieved by chemical relithiation by using a lithiation agent in the regeneration process [915,916,927–931]. The problem is that these reagents can cause overlithiation and structural damage. In particular, the introduction of

redox mediators (RMs), such as quinone-based and organic electron-donating materials avoid this problem and has proven more effective in the restoration of NMC cathode materials [932,933]. Recently, Kim et al. achieved 100% efficiency of chemical re lithiation of NMC622 assisted by the redox mediator 3,5-di-tert-butyl-o-benzoquinone (DTBQ) [934]. This result offers a facile and sustainable solution for Ni-rich battery recycling.

Zheng et al. proposed a different process. They investigated selective leaching of lithium from spent NCM using advanced oxidant ammonium persulfate $(\text{NH}_4)_2\text{S}_2\text{O}_8$, resulting in the recovery of lithium carbonate Li_2CO_3 . Then, the recovered Li_2CO_3 is combined with the selective leaching residue to synthesize fully-regenerated NCM via high-temperature solid-phase synthesis [935]

7.4. Safety Issues

Ni-rich lithium batteries suffer from severe thermal runaway under abuse conditions [936–938]. The release of oxygen by the cathode material is part of the problem, and cross-talking effects between cathode and anode play a critical role. The cross-talk of cathode-released oxygen to fully lithiated graphite anode [939,940], as well as the reaction between oxygen species and the electrolyte [941], can trigger the thermal runaway. It has also been suggested that the recombination of atomic hydrogen accumulated in graphite anode plays an important role [942]. LiH induced exothermic reactions at the anode side and H_2 generation and migration to the cathode side are also at the origin of thermal runaway [943–946]. The conclusion of these different works is that the thermal-induced cross-talking effects between the cathode and anode triggers the thermal runaway of the Ni-rich lithium batteries. This also implies that the stability of the CEI and SEI is more essential than that of the electrolyte components [947].

8. Conclusions

Progress in recent years on Ni-rich cathode elements have been made along different issues. Structural and chemical stability have been enhanced. Single-crystallized materials show better mechanical integrity compared to polycrystalline materials, reducing cracking and degradation. Efforts in research should then focus on this morphology. Introducing doping elements can stabilize the crystal structure, mitigate cation mixing, and improve thermal stability, and surface coating can suppress side reactions with electrolytes and reduce microcracking.

Progress has also been achieved to mitigate oxygen loss and electrolyte decomposition. High-voltage stable electrolytes with additives help reduce electrolyte decomposition at high voltages. Replacing liquid electrolytes with ceramic solid electrolytes can enhance stability and lifespan. Designing gradient Ni concentration across cathode particles can minimize oxygen release and improve cycle life.

Mechanical and microstructural improvements include crack-resistant design preventing the performance loss. Combining Ni-rich cathodes with other materials (e.g., Li-rich layered oxides) can balance energy density and stability.

Improved manufactory and scalability results from lower cobalt content, which reduces cobalt dependence, cuts costs, and improves sustainability.

An optimized sintering process has been achieved, due to advanced synthesis techniques like spray drying and atomic layer deposition, which can refine particle morphology and enhance material uniformity.

However, additional research is needed, and the future outlook depends on following research along the following lines:

- The interaction between the electrolytes and the Ni-rich materials and the related CEI needs further investigation. Newly-developed experimental set-ups, such as cryogenic

transmission electron microscopy revealing atomic-resolution CEI structures, should help for this purpose. An example is the dynamic evolution of over cycling and its impact on the performance of NMC811, revealed by the ultrafine images of CEI obtained by this process in presence of FEC-based electrolytes [948].

- Safety issues with high-voltage cathode materials would plead in favor of the use of solid electrolytes. As shown in this review, some attempts are promising, but the research should continue in the next years. The space charge layer between the cathode and a ceramic solid electrolyte may result in high polarization and capacity degradation. Another difficulty comes from the deterioration of the contact between the cathode and solid electrolyte upon cycling, due to the rigid ceramic nature of the solid electrolyte and the change in the lattice parameters of the cathode material, in particular at high charge. The columnar shape of the Ni-rich particles or actually any elongated form will help [949], pointing to the need for further investigation on the correlations between morphology, synthesis, and electrochemical performance. Elongated polymer electrolytes have already made possible the commercialization of LiFePO₄-based batteries, due to the low voltage (3.5 V) of the cells. With higher voltage cells, the same polymers cannot be used, because of their poor antioxidative ability. Further investigations on polymer electrolytes with wide electrochemical window are thus needed, and under studies [950]. Further research is needed to pair Ni-rich cathodes with lithium metal or silicon anodes. The reaction of the electrolytes with the Ni-rich cathode and the anode materials is not well understood, and further studies on the additives able to generate both a SEI and a CEI protecting the electrodes against side reactions with an electrolyte stable at high voltage are still needed.
- The application of AI to the research on Li-rich batteries is needed and most promising. It is possible today to predict material degradation pathways according to operating environments, which will help to optimize the design and composition of electrode materials for enhanced performance and durability of the Ni-rich cathode materials. Machine learning (ML) can accelerate the design of new Ni-rich cathode chemistries, and can also be used to build next-generation battery architectures. Many trials have been made to dope Ni-rich cathode materials with different single and multiple doping elements. ML models can **predict dopants** that improve stability without expensive trial-and-error experiments. In particular, deep learning models trained on large materials databases (e.g., Materials Project) predict stable Ni-rich structures with minimal degradation. ML will also help **designing single-crystal vs. polycrystalline** Ni-rich cathodes to reduce cracking. **Computer vision** models will be used to analyze SEM/TEM images to detect defects and suggest improvements in synthesis processes.

Ni-rich lithium-based cathode materials, particularly those in the layered LiNi_xCo_yMn_zO₂ (NCM) and LiNi_xCo_yAl_zO₂ (NCA) families, have emerged as frontrunners in the pursuit of high-energy-density lithium-ion batteries. Their increased nickel content directly contributes to elevated specific capacities, making them attractive for applications ranging from electric vehicles to grid storage. Over the past two decades, the field has experienced remarkable advancements in material synthesis, structural stabilization, and electrochemical performance optimization. This review has comprehensively explored the multifaceted aspects of Ni-rich LIBs, spanning from fundamental crystal chemistry and degradation mechanisms to cutting-edge approaches in coating, doping, and electrolyte engineering. Despite these advancements, the commercialization and long-term viability of Ni-rich cathodes are still hindered by persistent challenges. Chief among these are structural degradations during cycling, irreversible phase transitions, surface instability, gas evolution (notably O₂ and CO₂), transition metal dissolution, and thermal runaway risks at high states of charge. These degradation pathways are exacerbated by the high reactivity of Ni⁴⁺

and the increased lattice strain that arises during deep lithiation/delithiation cycles. Addressing these issues requires a deep understanding of bulk–surface–interface interactions under both normal and abusive conditions.

Innovations in material engineering, such as gradient compositions, core–shell morphologies, single-crystal structures, and atomic-scale doping, have demonstrated notable progress in mitigating degradation while improving thermal stability and capacity retention. Furthermore, the strategic development of advanced electrolytes, including localized high-concentration electrolytes (LHCEs), fluorinated solvents, and hybrid solid–liquid systems, has opened new frontiers in interfacial stability. Coupled with surface coatings based on metal oxides, phosphates, or ion-conductive polymers, these approaches form a synergistic framework to extend cycle life and enhance safety.

At the device level, progress in electrode architecture, electrode–electrolyte interface design, and formation protocols have collectively contributed to more robust, scalable battery systems. However, translating these laboratory-scale improvements into commercial viability necessitates further breakthroughs in synthesis cost reduction, scalable coating technologies, and recyclability strategies.

The field also stands to benefit from deeper integration of advanced characterization techniques—such as operando X-ray diffraction (XRD), transmission electron microscopy (TEM), neutron scattering, and synchrotron-based spectroscopy—alongside computational modeling and machine learning. These tools are critical for real-time insight into degradation pathways and for predictive materials discovery. Data-driven optimization and digital twin modeling may accelerate the design of next-generation Ni-rich cathode systems that are both high-performing and durable.

Looking forward, Ni-rich cathode chemistries will likely remain central to LIB technology for the foreseeable future, especially as efforts to reduce or eliminate cobalt become more urgent for ethical and economic reasons. Sustainable sourcing of nickel, closed-loop recycling systems, and lifecycle assessments will be crucial components of this ecosystem. Simultaneously, a holistic approach that incorporates safety engineering, environmental considerations, and total cost of ownership must guide the development and deployment of these advanced materials.

To our view, a breakdown of the best, most effective strategies-ranked by impact and practicality are as follows:

1. Surface coating to prevent electrolyte attack, suppress transition metal (TM) dissolution, and stabilize the cathode–electrolyte interface. The benefits are the reduction of surface reactivity, minimization of HF attack, and improvement of the cycling stability. To fulfill this goal, however, the coating must be uniform, thin (<10 nm), and ionically conductive to avoid impeding Li⁺ transport.
2. Doping, to enhance structural stability, suppress phase transitions, and reduce oxygen release. The cation doping stabilizes the layered structure and suppresses Li/Ni disorder, while anion doping, in particular F[−] (fluorination), strengthens TM–O bonds and suppresses oxygen evolution. The benefits are improved structural integrity, better capacity retention, and reduced gas generation.
3. Single-crystal morphology minimizes grain boundaries and microcracks, which are common initiation sites for degradation. The benefits are improved mechanical integrity, longer cycle life, and better thermal stability. However, there are drawbacks: this morphology is more difficult and costly to synthesize. It may require higher sintering temperatures.
4. Gradient composition or core–shell design combines a Ni-rich core for capacity with a stable outer shell (lower-Ni or doped) to buffer against side reactions. These architectures enhance thermal and chemical stability and delay impedance rise.

5. Optimized electrolyte formulations reduce parasitic reactions, stabilize CEI (cathode–electrolyte interface), and suppress gas generation.
6. Particle size and morphology engineering is useful to reduce mechanical stress and optimize Li⁺ diffusion. Spherical secondary particles with controlled porosity or dense, crack-resistant structures are preferred, resulting in improved structural stability and rate capability.
7. Thermal and pressure management during cycling, to reduce gas generation and mechanical damage. The strategy for this purpose is to use stack pressure or thermal management in cell design.
8. Advanced synthesis techniques, to achieve controlled doping, precise morphology, and homogeneous element distribution.

The efforts in the next years should then be focused on the integrated design combining the above approaches, such as the synthesis of a Ni-rich cathode with gradient composition, surface coating (e.g., LiNbO₃), W-doping, and used with a fluorinated LHCE, which will significantly outperform a conventional NMC811 cell in both energy density and cycle life, even at high voltages (>4.3 V).

In conclusion, while Ni-rich lithium-ion batteries have achieved a high level of maturity, their full potential will only be realized through continued interdisciplinary collaboration across materials science, electrochemistry, manufacturing, and systems engineering (see Table S1). The challenges are complex, but the rewards—in terms of decarbonizing transportation, stabilizing renewable grids, and powering the next generation of electronic devices—are immense. With sustained innovation and strategic investment, Ni-rich cathode technologies are well poised to drive the next wave of energy storage breakthroughs.

Supplementary Materials: The following supporting information can be downloaded at: <https://www.mdpi.com/article/10.3390/batteries11070254/s1>, Table S1: Highlights of top-performing Ni-rich cathodes [908,951–953].

Author Contributions: Conceptualization, A.M.; writing—original draft preparation, A.M.; writing—review and editing, C.M.J. All authors have read and agreed to the published version of the manuscript.

Funding: This research received no external funding.

Conflicts of Interest: The authors declare no conflicts of interest.

Abbreviations

The following abbreviations are used in this manuscript:

ALD	atomic layer deposition
ASSLBs	all-solid-state lithium batteries
CB	carbon black
CBDA	cyclobutane-tetracarboxylic dianhydride
CEI	cathode electrolyte interphase
COF	covalent organic framework
DFT	density functional theory
DMC	dimethyl carbonate
DTBQ	di-tert-butyl-o-benzoquinone
EPD	electrophoretic deposition
EV	electric vehicle
HOMO	Highest Occupied Molecular Orbital
HoMS	hollow multi-shell structure
LIBs	Lithium-ion batteries
LIPON	lithium phosphorus oxynitride

LLAO	$\text{Li}_{0.5}\text{La}_2\text{Al}_{0.5}\text{O}_4$
LUMO	Lowest Unoccupied Molecular Orbital
NASICON	sodium (Na) superionic conductor
NATM	$\text{LiNi}_{0.93}\text{Al}_{0.05}\text{Ti}_{0.01}\text{Mg}_{0.01}\text{O}_2$
NCA	$\text{LiNi}_x\text{Co}_y\text{Al}_z\text{O}_2$
NMC	$\text{LiNi}_{1-x-y}\text{Mn}_x\text{Co}_y\text{O}_2$
NMCA	$\text{LiNi}_x\text{Mn}_y\text{Co}_z\text{Al}_{(1-x-y-z)}\text{O}_2$
NMC811	$\text{LiNi}_{0.8}\text{Mn}_{0.1}\text{Co}_{0.1}\text{O}_2$
NMC333	$\text{LiNi}_{1/3}\text{Mn}_{1/3}\text{Co}_{1/3}\text{O}_2$
NMC622	$\text{LiNi}_{0.6}\text{Mn}_{0.2}\text{Co}_{0.2}\text{O}_2$
PANI	polyaniline
PEG	polyethylene glycol
PPC	pyrrole-co-citral nitrile
PPy	polypyrrole
SEI	solid-electrolyte interphase
SEM	scanning electron microscopy
SOC	state-of-charge
TM	transition metal
VC	vinylene carbonate
XRD	X-ray diffraction

References

1. You, L.Z.; Chu, B.B.; Li, G.X.; Huang, T.; Yu, A.S. H_3BO_3 washed $\text{LiNi}_{0.8}\text{Co}_{0.1}\text{Mn}_{0.1}\text{O}_2$ with enhanced electrochemical performance and storage characteristics. *J. Power Sources* **2021**, *482*, 228940. [[CrossRef](#)]
2. Yu, H.F.; Cao, Y.Q.; Chen, L.; Hu, Y.J.; Duan, X.Z.; Dai, S.; Jiang, H. Surface enrichment and diffusion enabling gradient-doping and coating of Ni-rich cathode toward Li ion batteries. *Nat. Commun.* **2021**, *12*, 4564. [[CrossRef](#)] [[PubMed](#)]
3. Rajkamal, A.; Sharma, A.; Pullagura, B.K.; Thapa, R.; Kim, H. Engineering lithium nickel cobalt manganese oxides cathodes: A computational and experimental approach to bridging gaps. *Chem. Eng. J.* **2024**, *481*, 148223. [[CrossRef](#)]
4. Ding, H.; Wang, X.; Wang, J.; Zhang, H.; Liu, G.; Yu, W.; Wang, J. Morphology-controllable synthesis and excellent electrochemical performance of Ni-rich layered NCM622 as cathode materials for lithium-ion batteries via glycerin-assisted solvothermal method. *J. Power Sources* **2023**, *553*, 232307. [[CrossRef](#)]
5. Kim, J.; Lee, I.; Kim, Y.-H.; Bae, J.H.; Hwang, K.; Kang, H.; Yoon, S. Ni-rich cathode material with isolated porous layer hindering crack propagation under 4.5 V high cut-off voltage cycling. *Chem. Eng. J.* **2023**, *455*, 140578. [[CrossRef](#)]
6. Liu, H.D.; Zhu, Z.Y.; Yan, Q.Z.; Yu, S.C.; He, X.; Chen, Y.; Liu, P. A disordered rock salt anode for fast-charging lithium-ion batteries. *Nature* **2020**, *585*, 63–67. [[CrossRef](#)]
7. Xie, H.; Peng, H.; Jiang, D.; Xiao, Z.; Liu, X.; Liang, H.; Wu, M.; Liu, D.; Li, Y.; Sun, Y.; et al. Structures, issues, and optimization strategies of Ni-rich and Co-low cathode materials for lithium-ion battery. *Chem. Eng. J.* **2023**, *470*, 144051. [[CrossRef](#)]
8. Tian, X.; Guo, R.; Bai, Y.; Li, N.; Wang, X.; Wang, J.; Wu, C. High-performance high-nickel multi-element cathode materials for lithium-ion batteries. *Batteries* **2023**, *9*, 319. [[CrossRef](#)]
9. Ryu, H.-H.; Namkoong, B.; Kim, J.H.; Belharouak, I.; Yoon, C.S.; Sun, Y.K. Capacity fading mechanisms in Ni-rich single-crystal NCM cathodes. *ACS Energy Lett.* **2021**, *6*, 2726–2734. [[CrossRef](#)]
10. Ding, Y.; Wang, R.; Wang, L.; Cheng, K.; Zhao, Z.; Mu, D.; Wu, B. A short review on layered $\text{LiNi}_{0.8}\text{Mn}_{0.1}\text{Co}_{0.1}\text{O}_2$ positive electrode material for lithium-ion batteries. *Energy Proc.* **2017**, *105*, 2941–2952. [[CrossRef](#)]
11. Mubarac, S.; Silva, M.N.; Silva, G.T.; Freitas, B.; Gonçalves, J.M.; Zanin, H. Super Ni-rich and Co-poor $\text{LiNi}_x\text{Co}_y\text{Mn}_{1-x-y}\text{O}_2$, $\text{LiNi}_x\text{Co}_y\text{Al}_{1-x-y}\text{O}_2$, and $\text{LiNi}_x\text{Co}_y\text{Mn}_z\text{Al}_{(1-x-y-z)}\text{O}_2$ ($x \geq 0.85$) based cathodes for lithium-ion batteries: A review on emerging trends, recent developments, and future perspectives. *J. Energy Storage* **2024**, *96*, 112612. [[CrossRef](#)]
12. Li, J.; Manthiram, A. A comprehensive analysis of the interfacial and structural evolution over long-term cycling of ultrahigh-nickel cathodes in lithium-ion batteries. *Adv. Energy Mater.* **2019**, *9*, 1902731. [[CrossRef](#)]
13. Cui, Z.; Xie, Q.; Manthiram, A. Zinc-doped high-nickel, low-cobalt layered oxide cathodes for high-energy-density lithium-ion batteries. *ACS Appl. Mater. Interfaces* **2021**, *13*, 15324–15332. [[CrossRef](#)]
14. Li, J.; Liu, H.; Xia, J.; Cameron, A.R.; Nie, M.; Botton, G.A.; Dahn, J.R. The impact of electrolyte additives and upper cut-off voltage on the formation of a rocksalt surface layer in $\text{LiNi}_{0.8}\text{Mn}_{0.1}\text{Co}_{0.1}\text{O}_2$ electrodes. *J. Electrochem. Soc.* **2017**, *164*, A655–A665. [[CrossRef](#)]

15. Xu, C.; Märker, K.; Lee, J.; Mahadevegowda, A.; Reeves, P.J.; Day, S.J.; Groh, M.F.; Emge, S.P.; Ducati, C.; Mehdi, B.L.; et al. Bulk fatigue induced by surface reconstruction in layered Ni-rich cathodes for Li-ion batteries. *Nat. Mater.* **2021**, *20*, 84–92. [CrossRef]
16. Li, J.; Downie, L.E.; Ma, L.; Qiu, W.; Dahn, J.R. Study of the failure mechanisms of $\text{LiNi}_{0.8}\text{Mn}_{0.1}\text{Co}_{0.1}\text{O}_2$ Cathode material for lithium ion batteries. *J. Electrochem. Soc.* **2015**, *162*, A1401–A1408. [CrossRef]
17. Zhang, N.; Li, J.; Li, H.; Liu, A.; Huang, Q.; Ma, L.; Li, Y.; Dahn, J.R. Structural, electrochemical, and thermal properties of nickel-rich $\text{LiNi}_x\text{Mn}_y\text{Co}_z\text{O}_2$ materials. *Chem. Mater.* **2018**, *30*, 8852–8860. [CrossRef]
18. Schipper, F.; Erickson, E.M.; Erk, C.; Shin, J.-Y.; Chesneau, F.F.; Aurbach, D. Review: Recent advances and remaining challenges for lithium-ion battery cathodes. *J. Electrochem. Soc.* **2017**, *164*, A6220–A6228. [CrossRef]
19. Kim, M.; Zhu, J.; Li, L.; Wang, C.; Chen, G. Understanding reactivities of Ni-rich $\text{Li}[\text{Ni}_x\text{Mn}_y\text{Co}_{1-x-y}]\text{O}_2$ single-crystal cathode materials. *ACS Appl. Energy Mater.* **2020**, *3*, 12238–12245. [CrossRef]
20. Xu, J.; Lin, F.; Doeff, M.M.; Tong, W. A review of Ni-based layered oxides for rechargeable Li-ion batteries. *J. Mater. Chem. A* **2017**, *5*, 874–901. [CrossRef]
21. Duh, Y.S.; Sun, Y.; Lin, X.; Zheng, J.; Wang, M.; Wang, Y.; Lin, X.; Jiang, X.; Zheng, Z.; Zheng, S.; et al. Characterization on thermal runaway of commercial 18650 lithium-ion batteries used in electric vehicles: A review. *J. Energy Storage* **2021**, *41*, 102888. [CrossRef]
22. Ohneseit, S.; Finster, P.; Floras, C.; Lubenau, N.; Uhlmann, N.; Seifert, H.J.; Zizebert, C. Thermal and mechanical safety assessment of type 21700 lithium-ion batteries with NMC, NCA and LFP cathodes—investigation of cell abuse by means of accelerating rate calorimetry (ARC). *Batteries* **2023**, *9*, 237. [CrossRef]
23. Huggins, R.A. *Energy Storage: Fundamentals, Materials and Applications*, 2nd ed.; Springer International Publishing: Cham, Switzerland, 2016; pp. 181–208.
24. Manthiram, A. An outlook on lithium-ion battery technology. *ACS Cent. Sci.* **2017**, *3*, 1063–1069. [CrossRef] [PubMed]
25. Singh, J.P.; Devnani, H.; Sharma, A.; Lim, W.C.; Dhyani, A.; Chae, K.H.; Lee, S. Challenges and opportunities using Ni-rich layered oxide cathodes in Li-ion rechargeable batteries: The case of nickel cobalt manganese oxides. *Energy Adv.* **2024**, *3*, 1869–1893. [CrossRef]
26. Ahangari, M.; Szalai, B.; Lujan, J.; Zhou, M.; Luo, H. Advancements and challenges in high-capacity Ni-rich cathode materials for lithium-ion batteries. *Materials* **2024**, *17*, 801. [CrossRef]
27. Butt, A.; Ali, G.; Kubra, K.T.; Sharif, R.; Salman, A.; Bashir, M.; Jamil, S. Recent advances in enhanced performance of Ni-rich cathode materials for Li-ion batteries: A review. *Energy Technol.* **2022**, *10*, 2100775. [CrossRef]
28. Jamil, S.; Wang, G.; Fasehullah, M.; Xu, M. Challenges and prospects of nickel-rich layered oxide cathode material. *J. Alloys Compd.* **2022**, *909*, 164727. [CrossRef]
29. Liu, W.; Oh, P.; Liu, X.; Lee, M.-J.; Cho, W.; Chae, S.; Kim, Y.; Cho, J. Nickel-rich layered lithium transition-metal oxide for high-energy lithium-ion batteries. *Angew. Chem. Int. Ed.* **2015**, *54*, 4440–4457. [CrossRef]
30. Yan, W.; Yang, S.; Huang, Y.; Yang, Y.; Yuan, G. A review on doping/coating of nickel-rich cathode materials for lithium-ion batteries. *J. Alloys Compd.* **2020**, *819*, 153048. [CrossRef]
31. Britala, L.; Marinaro, M.; Kucenskis, G. A review of the degradation mechanisms of NCM cathodes and corresponding mitigation strategies. *J. Energy Storage* **2023**, *73A*, 108875. [CrossRef]
32. Myung, S.T.; Maglia, F.; Park, K.J.; Yoon, C.S.; Lamp, P.; Kim, S.-J.; Sun, Y.-K. Nickel-rich layered cathode materials for automotive lithium-ion batteries: Achievements and perspectives. *ACS Energy Lett.* **2017**, *2*, 196–223. [CrossRef]
33. Hou, P.Y.; Yin, J.M.; Ding, M.; Huang, J.; Xu, X. Surface/interfacial structure and chemistry of high-energy nickel-rich layered oxide cathodes: Advances and perspectives. *Small* **2017**, *13*, 1701802. [CrossRef]
34. Jung, R.; Metzger, M.; Maglia, F.; Stirnner, C.; Gasteiger, H.A. Oxygen release and its effect on the cycling stability of $\text{LiNi}_x\text{Mn}_y\text{Co}_z\text{O}_2$ (NMC) cathode materials for Li-ion batteries. *J. Electrochem. Soc.* **2017**, *164*, A1361–A1377. [CrossRef]
35. Strehle, B.; Kleiner, K.; Jung, R.; Chesneau, F.; Mendez, M.; Gasteiger, H.A.; Piana, M. The role of oxygen release from Li- and Mn-rich layered oxides during the first cycles investigated by on-line electrochemical mass spectrometry. *J. Electrochem. Soc.* **2017**, *164*, A400–A406. [CrossRef]
36. Luo, Y.-H.; Pan, Q.-L.; Wei, H.-X.; Huang, Y.-D.; Tang, L.-B.; Wang, Z.-Y.; He, Z.-J.; Yan, C.; Mao, J.; Dai, K.-H.; et al. Towards Ni-rich layered oxides cathodes with low Li/Ni intermixing by mild molten-salt ion exchange for lithium-ion batteries. *Nano Energy* **2022**, *102*, 107626. [CrossRef]
37. Xiao, P.; Li, W.-H.; Chen, S.; Li, G.; Dai, Z.-J.; Feng, M.-D.; Chen, X.; Yang, W.-S. Effects of Oxygen pressurization on $\text{Li}^+/\text{Ni}^{2+}$ cation mixing and the oxygen vacancies of $\text{LiNi}_{0.8}\text{Co}_{0.15}\text{Al}_{0.05}\text{O}_2$ cathode materials. *ACS Appl. Mater. Interfaces* **2022**, *14*, 31851–31861. [CrossRef]
38. Chen, J.-N.; Yang, Y.; Tang, Y.-S.; Wang, Y.-F.; Li, H.; Xiao, X.-H.; Wang, S.-N.; Mariyam, S.D.D.; Etter, M.; Missyul, A.; et al. Constructing a thin disordered self-protective layer on the LiNiO_2 primary particles against oxygen release. *Adv. Funct. Mater.* **2022**, *33*, 2211515. [CrossRef]

39. Li, X.-H.; Wang, Q.; Guo, H.-Y.; Artrith, N.; Urban, A. Understanding the onset of surface degradation in LiNiO_2 cathodes. *ACS Appl. Energy Mater.* **2022**, *5*, 5730–5741. [CrossRef]
40. Duan, Y.; Chen, S.P.; Zhang, L.; Guo, L.; Shi, F.N. Review on oxygen release mechanism and modification strategy of nickel-rich NCM cathode materials for lithium-ion batteries: Recent advances and future directions. *Energy Fuel* **2024**, *38*, 5607–5631. [CrossRef]
41. Buchberger, I.; Seidlmayer, S.; Pokharel, A.; Piana, M.; Hattendorff, J.; Kudejova, P.; Gilles, R.; Gasteiger, H.A. Aging analysis of graphite/ $\text{LiNi}_{1/3}\text{Mn}_{1/3}\text{Co}_{1/3}\text{O}_2$ cells using XRD, PGAA, and AC impedance. *J. Electrochem. Soc.* **2015**, *162*, A2737–A2746. [CrossRef]
42. Komagata, S.; Itou, Y.; Kondo, H. Impact of surface layer formation during cycling on the thermal stability of the $\text{LiNi}_{0.8}\text{Co}_{0.1}\text{Mn}_{0.1}\text{O}_2$ cathode. *ACS Appl. Mater. Interfaces* **2022**, *14*, 8931–8937. [CrossRef]
43. Chen, S.; Zhang, P.; Zhou, X.; Wu, W.; Liu, X.; Liu, Y.; Feng, G.; Zhang, B.; Xing, W.; Zuo, M.; et al. Slightly Li-enriched chemistry enabling super stable $\text{LiNi}_{0.5}\text{Mn}_{0.5}\text{O}_2$ cathodes under extreme conditions. *Chem. Sci.* **2024**, *15*, 14415–14424. [CrossRef] [PubMed]
44. Deng, Z.; Liu, Y.; Wang, L.; Fu, N.; Li, Y.; Luo, Y.; Wang, J.; Xiao, X.; Wang, X.; Yang, X.; et al. Challenges of thermal stability of high-energy layered oxide cathode materials for lithium-ion batteries: A review. *Mater. Today* **2023**, *69*, 236–261. [CrossRef]
45. Lim, J.M.; Hwang, T.; Kim, D.; Park, M.-S.; Cho, K.; Cho, M. Intrinsic origins of crack generation in Ni-rich $\text{LiNi}_{0.8}\text{Co}_{0.1}\text{Mn}_{0.1}\text{O}_2$ layered oxide cathode material. *Sci. Rep.* **2017**, *7*, 39669. [CrossRef] [PubMed]
46. Lee, S.; Li, W.; Dolocan, A.; Celio, H.; Park, H.; Warner, J.H.; Manthiram, A. In-depth analysis of the degradation mechanisms of high-nickel, low/no-cobalt layered oxide cathodes for lithium-ion batteries. *Adv. Energy Mater.* **2021**, *11*, 2100858. [CrossRef]
47. Laakso, E.; Efimova, S.; Colalongo, M.; Kauranen, P.; Lahtinen, K.; Napolitano, E.; Ruiz, V.; Moskon, J.; Gaberscek, M.; Park, J.; et al. Aging mechanisms of NMC811/Si-Graphite Li-ion batteries. *J. Power Sources* **2024**, *599*, 234159. [CrossRef]
48. Wu, Z.; Zhang, C.; Yuan, F.; Lyu, M.; Yang, P.; Zhang, L.; Zhou, M.; Wang, L.; Zhang, S.; Wang, L. Ni-rich cathode materials for stable high-energy lithium-ion batteries. *Nano Energy* **2024**, *126*, 109620. [CrossRef]
49. Li, T.; Yuan, X.-Z.; Zhang, L.; Song, D.; Shi, K.; Bock, D. Degradation mechanisms and mitigation strategies of nickel-rich NMC-based lithium-ion batteries. *Electrochem. Energy Rev.* **2020**, *3*, 43–80. [CrossRef]
50. Xia, Y.; Zheng, J.; Wang, C.; Gu, M. Designing principle for Ni-rich cathode materials with high energy density for practical applications. *Nano Energy* **2018**, *49*, 434–452. [CrossRef]
51. Kim, J.; Zhang, X.; Zhang, J.; Manthiram, A.; Meng, Y.S.; Xu, W. A Review on the stability and surface modification of layered transition-metal oxide cathodes. *Mater. Today* **2021**, *46*, 155–182. [CrossRef]
52. Liu, X.; Zeng, Y.; Yuan, W.; Zhang, G.; Zheng, H.; Chen, Z. Advances in multi-scale design and fabrication processes for thick electrodes in lithium-ion batteries. *Energy Rev.* **2024**, *3*, 100066. [CrossRef]
53. Das, J.; Kleiman, A.; Rehman, A.U.; Verma, R.; Young, M.H. The cobalt supply chain and environmental life cycle impacts of lithium-ion battery energy storage systems. *Sustainability* **2024**, *16*, 1910. [CrossRef]
54. The Organisation for Economic Co-Operation and Development (OECD). Interconnected Supply Chains: A Comprehensive Look at Due Diligence Challenges and Opportunities Sourcing Cobalt and Copper from the Democratic Republic of the Congo. In *Responsible Business Conduct*; OECD: Paris, France, 2019. Available online: <https://mneguidelines.oecd.org/Interconnected-supply-chains-a-comprehensive-look-at-due-diligence-challenges-and-opportunities-sourcing-cobalt-and-copper-from-the-DRC.pdf> (accessed on 1 January 2019).
55. U.S. Geological Survey (USGS). *Mineral Commodity Summaries 2022-Cobalt*; U.S. Geological Survey: Reston, VA, USA, 2022. Available online: <https://pubs.usgs.gov/periodicals/mcs2022/mcs2022-cobalt.pdf> (accessed on 25 May 2023).
56. Cobalt Institute. State of Cobalt Market Report. 2021. Available online: https://www.cobaltinstitute.org/wp-content/uploads/2021/09/Cobalt-Institute-State-of-the-Cobalt-Market-Report_2020.pdf (accessed on 25 May 2023).
57. U.S. Department of Energy. *Energy Storage Grand Challenge: Energy Storage Market Report*; U.S. Department of Energy: Washington, DC, USA, 2020. Available online: https://www.energy.gov/sites/prod/files/2020/12/f81/Energy%20Storage%20Market%20Report%202020_0.pdf (accessed on 1 December 2020).
58. The White House. FACT SHEET: Securing a Made in America Supply Chain for Critical Minerals. 2022. Available online: <https://bidenwhitehouse.archives.gov/briefing-room/statements-releases/2022/02/22/fact-sheet-securing-a-made-in-america-supply-chain-for-critical-minerals/> (accessed on 22 February 2022).
59. Nriagu, J.O. Toxic metal pollution in Africa. *Sci. Total. Environ.* **1992**, *121*, 1–37. [CrossRef]
60. Banza, C.L.N.; Nawrot, T.S.; Haufroid, V.; Decrée, S.; De Putter, T.; Smolders, E.; Kabyla, B.I.; Luboya, O.N.; Ilunga, A.N.; Mutombo, A.M.; et al. High human exposure to cobalt and other metals in Katanga, a mining area of the Democratic Republic of Congo. *Environ. Res.* **2009**, *109*, 745–752. [CrossRef]
61. United Nations Environment Programme (UNEP). Water Issues in the Democratic Republic of Congo: Challenges and Opportunities—Technical Report. 2011. Available online: <https://www.ircwash.org/sites/default/files/Partow-2011-Water.pdf> (accessed on 1 January 2011).

62. Slack, J.F.; Kimball, B.E.; Shedd, K.B. *Cobalt Report 1802F. Professional Paper*; USGS Publications Warehouse: Reston, VA, USA, 2017. Available online: <https://pubs.er.usgs.gov/publication/pp1802F> (accessed on 25 May 2023).
63. Shengo, M.; Kime, M.-B.; Mambwe, M.; Nyembo, T. A review of the beneficiation of copper-cobalt-bearing minerals in the Democratic Republic of Congo. *J. Sustain. Min.* **2019**, *18*, 226–246. [CrossRef]
64. Muimba-Kankolongo, A.; Nkulu, C.B.L.; Mwitwa, J.; Kampemba, F.M.; Nabuyanda, M.M.; Haufroid, V.; Smolders, E.; Nemery, B. Contamination of water and food crops by trace elements in the African Copperbelt: A collaborative cross-border study in Zambia and the Democratic Republic of Congo. *Environ. Adv.* **2021**, *6*, 100103. [CrossRef]
65. Schmidt, T.; Buchert, M.; Schebek, L. Investigation of the primary production routes of nickel and cobalt products used for Li-ion batteries. *Resour. Conserv. Recycl.* **2016**, *112*, 107–122. [CrossRef]
66. Voronina, N.; Sun, Y.-K.; Myung, S.-T. Co-free layered cathode materials for high energy density lithium-ion batteries. *ACS Energy Lett.* **2020**, *5*, 1814–1824. [CrossRef]
67. Ryu, H.-H.; Sun, H.H.; Myung, S.-T.; Yoon, C.S.; Sun, Y.-K. Reducing cobalt from lithium-ion batteries for the electric vehicle era. *Energy Environ. Sci.* **2021**, *14*, 844–852. [CrossRef]
68. Gent, W.E.; Busse, G.M.; House, K.Z. The predicted persistence of cobalt in lithium-ion batteries. *Nat. Energy* **2022**, *7*, 1132. [CrossRef]
69. Chu, B.; Guo, Y.-J.; Shi, J.-L.; Yin, Y.-X.; Huang, T.; Su, H.; Yu, A.; Guo, Y.-G. Cobalt in high-energy-density layered cathode materials for lithium-ion batteries. *J. Power Sources* **2022**, *544*, 231873. [CrossRef]
70. Liu, T.; Yu, L.; Liu, J.; Lu, J.; Bi, X.; Dai, A.; Li, M.; Li, M.; Hu, Z.; Ma, L.; et al. Understanding Co roles towards developing Co-free Ni-rich cathodes for rechargeable batteries. *Nat. Energy* **2021**, *6*, 277–286. [CrossRef]
71. Ge, H.; Shen, Z.; Wang, Y.; Sun, Z.; Cao, X.; Wang, C.; Fan, X.; Bai, J.; Li, R.; Yang, T.; et al. Design of high-performance and sustainable Co-free Ni-rich cathodes for next-generation lithium-ion batteries. *SusMat* **2024**, *4*, 48–71. [CrossRef]
72. Wang, R.; Wang, L.; Fan, Y.; Yang, W.; Zhan, C.; Liu, G. Controversy on necessity of cobalt in nickel-rich cathode materials for lithium-ion batteries. *J. Ind. Eng. Chem.* **2022**, *110*, 120–130. [CrossRef]
73. Mallick, S.; Patel, A.; Sun, X.-G.; Paranthaman, M.P.; Mou, M.; Mugumya, J.H.; Jiang, M.; Rasche, M.L.; Lopez, H.; Gupta, R.B. Low-cobalt active cathode materials for high-performance lithium-ion batteries: Synthesis and performance enhancement methods. *J. Mater. Chem. A* **2023**, *11*, 3789–3821. [CrossRef]
74. Hussain, S.K.; Bang, J.H. Recent progress in Co-free, Ni-rich cathode materials for lithium-ion batteries. *Bull. Korean Chem. Soc.* **2024**, *45*, 4–15. [CrossRef]
75. Liu, X.; Xu, G.-L.; Yin, L.; Hwang, I.; Li, Y.; Lu, L.; Xu, W.; Zhang, X.; Chen, Y.; Ren, Y.; et al. Probing the thermal-driven structural and chemical degradation of Ni-rich layered cathodes by Co/Mn exchange. *J. Am. Chem. Soc.* **2020**, *142*, 19745. [CrossRef]
76. Choi, J.U.; Voronina, N.; Sun, Y.-K.; Myung, S.-T. Recent progress and perspective of advanced high-energy Co-less Ni-rich cathodes for Li-ion batteries: Yesterday, today, and tomorrow. *Adv. Energy Mater.* **2020**, *10*, 2002027. [CrossRef]
77. Song, Y.; Cui, Y.; Geng, L.; Li, B.; Ge, L.; Zhou, L.; Qiu, Z.; Nan, J.; Wu, W.; Xu, H.; et al. Li/Ni intermixing: The real origin of lattice oxygen stability in Co-free Ni-rich cathode materials. *Adv. Energy Mater.* **2024**, *14*, 2303207. [CrossRef]
78. Kim, Y.; Seong, W.M.; Manthiram, A. Cobalt-free, high-nickel layered oxide cathodes for lithium-ion batteries: Progress, challenges, and perspectives. *Energy Storage Mater.* **2021**, *34*, 250–259. [CrossRef]
79. Xiao, Y.; Liu, T.; Liu, J.; He, L.; Chen, J.; Zhang, J.; Chen, H. Insight into the origin of lithium/nickel ions exchange in layered $\text{Li}(\text{Ni}_x\text{Mn}_y\text{Co}_z)\text{O}_2$ cathode materials. *Nano Energy* **2018**, *49*, 77–85. [CrossRef]
80. Zheng, J.; Ye, Y.; Liu, T.; Xiao, Y.; Wang, F.; Pan, F. Ni/Li disordering in layered transition metal oxide: Electrochemical impact, origin, and control. *Acc. Chem. Res.* **2019**, *52*, 2201–2209. [CrossRef]
81. Wang, D.; Xin, C.; Zhang, M.; Bai, J.; Zheng, J.; Kou, R.; Ko, J.Y.P.; Huq, A.; Zhong, G.; Sun, C.-J.; et al. Intrinsic role of cationic substitution in tuning Li/Ni mixing in high-Ni layered oxides. *Chem. Mater.* **2019**, *31*, 2731–2740. [CrossRef]
82. Ben Kamel, K.; Amdouni, N.; Abdel-Ghany, A.; Zaghib, K.; Mauger, A.; Gendron, F.; Julien, C. Local structure and electrochemistry of $\text{LiNi}_y\text{Mn}_y\text{Co}_{1-2y}\text{O}_2$ electrode materials for Li-ion batteries. *Ionics* **2008**, *14*, 89–97. [CrossRef]
83. Zhang, J.; Wang, S.; Yang, X.; Liu, Y.; Wu, Z.; Li, H.; Indris, S.; Ehrenberg, H.; Hua, W. Unravelling the peculiar role of Co and Al in highly Ni-rich layered oxide cathode materials. *Chem. Eng. J.* **2024**, *484*, 149599. [CrossRef]
84. Lin, J.; Lian, X.; Wang, X.; Ma, Y.; Fang, L.; Suo, X. Effects of Al content on the electrochemical performance and thermal stability of $\text{Li}(\text{Ni}_{0.9}\text{Co}_{0.06}\text{Mn}_{0.04})_{1-x}\text{Al}_x\text{O}_2$ cathode materials for Li-ion batteries. *Ionics* **2023**, *29*, 2153–2162. [CrossRef]
85. Aishova, A.; Park, G.; Yoon, C.S.; Sun, Y. Cobalt-free high-capacity Ni-rich layered $\text{Li}[\text{Ni}_{0.9}\text{Mn}_{0.1}]\text{O}_2$ cathode. *Adv. Energy Mater.* **2020**, *10*, 1903179. [CrossRef]
86. Li, W.; Lee, S.; Manthiram, A. High-nickel NMA: A cobalt-free alternative to NMC and NCA cathodes for lithium-ion batteries. *Adv. Mater.* **2020**, *32*, 2002718. [CrossRef] [PubMed]
87. Mu, L.; Kan, W.H.; Kuai, C.; Yang, Z.; Li, L.; Sun, C.-J.; Sainio, S.; Avdeev, M.; Nordlund, D.; Lin, F. Structural and electrochemical impacts of Mg/Mn dual dopants on the LiNiO_2 cathode in Li-metal batteries. *ACS Appl. Mater. Interfaces* **2020**, *12*, 12874–12882. [CrossRef]

88. Muralidharan, N.; Essehli, R.; Hermann, R.P.; Parejiya, A.; Amin, R.; Bai, Y.; Du, Z.; Belharouak, I. $\text{LiNi}_x\text{Fe}_y\text{Al}_z\text{O}_2$, a new cobalt-free layered cathode material for advanced Li-ion batteries. *J. Power Sources* **2020**, *471*, 228389. [[CrossRef](#)]
89. Mu, L.; Zhang, R.; Kan, W.H.; Zhang, Y.; Li, L.; Kuai, C.; Zytlewski, B.; Rahman, M.M.; Sun, C.-J.; Sainio, S.; et al. Dopant distribution in Co-free high-energy layered cathode materials. *Chem. Mater.* **2019**, *31*, 9769–9776. [[CrossRef](#)]
90. Yang, Z.; Mu, L.; Hou, D.; Rahman, M.M.; Xu, Z.; Liu, J.; Nordlund, D.; Sun, C.; Xiao, X.; Lin, F. Probing dopant redistribution, phase propagation, and local chemical changes in the synthesis of layered oxide battery cathodes. *Adv. Energy Mater.* **2020**, *11*, 2002719. [[CrossRef](#)]
91. Li, H.; Cormier, M.; Zhang, N.; Inglis, J.; Li, J.; Dahn, J.R. Is cobalt needed in Ni-rich positive electrode materials for lithium ion batteries? *J. Electrochem. Soc.* **2019**, *166*, A429–A439. [[CrossRef](#)]
92. Cui, Z.; Xie, Q.; Manthiram, A. A cobalt- and manganese-free high-nickel layered oxide cathode for long-life, safer lithium-ion batteries. *Adv. Energy Mater.* **2021**, *11*, 2102421. [[CrossRef](#)]
93. Bianchini, M.; Roca-Ayats, M.; Hartmann, P.; Brezesinski, T.; Janek, J. There and back again—The journey of LiNiO_2 as a cathode active material. *Angew. Chem. Int. Ed.* **2019**, *58*, 10434–10458. [[CrossRef](#)]
94. Cui, J.; Ding, X.; Luo, D.; Xie, H.; Zhang, Z.; Zhang, B.; Tan, F.; Liu, C.; Lin, Z. Effect of cationic uniformity in precursors on Li/Ni mixing of Ni-rich layered cathodes. *Energy Fuels* **2021**, *35*, 1842–1850. [[CrossRef](#)]
95. Wang, S.; Hua, W.; Missyul, A.; Darma, M.S.D.; Tayal, A.; Indris, S.; Ehrenberg, H.; Liu, L.; Knapp, M. Kinetic control of long-range cationic ordering in the synthesis of layered Ni-rich oxides. *Adv. Funct. Mater.* **2021**, *31*, 2009949. [[CrossRef](#)]
96. Paidi, A.K.; Lee, A.T.; Paidi, V.K.; Ahn, H.; Lim, J.; Lee, K.-S.; Lee, S.; Ahn, D. Atomic-level insights into the first cycle irreversible capacity loss of Ni-rich layered cathodes for Li-ion batteries. *J. Mater. Chem. A* **2023**, *11*, 12002–12012. [[CrossRef](#)]
97. Hu, Q.; Wu, Y.Z.; Ren, D.S.; Liao, J.Y.; Song, Y.Z.; Liang, H.M.; Wang, A.P.; He, Y.F.; Wang, L.; Chen, Z.H.; et al. Revisiting the initial irreversible capacity loss of $\text{LiNi}_{0.6}\text{Co}_{0.2}\text{Mn}_{0.2}\text{O}_2$ cathode material batteries. *Energy Storage Mater.* **2022**, *50*, 373–379. [[CrossRef](#)]
98. Zhang, S.; Yang, Z.; Lu, Y.; Xie, W.; Yan, Z.; Chen, J. Insights into cation migration and intermixing in advanced cathode materials for lithium-ion batteries. *Adv. Energy Mater.* **2024**, *14*, 2402068. [[CrossRef](#)]
99. Wu, K.; Ran, P.; Yin, W.; He, L.; Wang, B.; Wang, F.; Zhao, E.; Zhao, J. Dynamic evolution of antisite defect and coupling anionic redox in high-voltage ultrahigh-Ni cathode. *Angew. Chem. Int. Ed.* **2024**, *63*, e202410326.
100. Shi, C.-G.; Peng, X.-X.; Dai, P.; Xiao, P.H.; Zheng, W.-C.; Li, H.-Y.; Li, H.; Indris, S.; Mangold, S.; Hong, Y.-H.; et al. Investigation and suppression of oxygen release by $\text{LiNi}_{0.8}\text{Co}_{0.1}\text{Mn}_{0.1}\text{O}_2$ cathode under overcharge conditions. *Adv. Energy Mater.* **2022**, *12*, 2200569. [[CrossRef](#)]
101. Gabrisch, H.; Yi, T.H.; Yazami, R. Transmission electron microscope studies of $\text{LiNi}_{1/3}\text{Mn}_{1/3}\text{Co}_{1/3}\text{O}_2$ before and after long-term aging at 70 °C. *Electrochem. Solid State Lett.* **2008**, *11*, A119–A124. [[CrossRef](#)]
102. Jung, S.K.; Gwon, H.; Hong, J.; Park, K.-Y.; Seo, D.-H.; Kim, H.; Kang, K. Understanding the degradation mechanisms of $\text{LiNi}_{0.5}\text{Co}_{0.2}\text{Mn}_{0.3}\text{O}_2$ cathode material in lithium-ion batteries. *Adv. Energy Mater.* **2014**, *4*, 1300787. [[CrossRef](#)]
103. Robert, R.; Villevieille, C.; Novák, P. Enhancement of the high potential specific charge in layered electrode materials for lithium-ion batteries. *J. Mater. Chem. A* **2014**, *2*, 8589–8598. [[CrossRef](#)]
104. Konishi, H.; Yoshikawa, M.; Hirano, T. The effect of thermal stability for high-Ni-content layer-structured cathode materials, $\text{LiNi}_{0.8}\text{Mn}_{0.1-x}\text{Co}_{0.1}\text{Mo}_x\text{O}_2$ ($x = 0, 0.02, 0.04$). *J. Power Sources* **2013**, *244*, 23–28. [[CrossRef](#)]
105. Wang, D.; Li, X.-H.; Wang, Z.X.; Guo, H.; Huang, Z.; Kong, L.; Ru, J. Improved high voltage electrochemical performance of Li_2ZrO_3 -coated $\text{LiNi}_{0.5}\text{Co}_{0.2}\text{Mn}_{0.3}\text{O}_2$ cathode material. *J. Alloys Compd.* **2015**, *647*, 612–619. [[CrossRef](#)]
106. Lin, F.; Markus, I.M.; Nordlund, D.; Weng, T.-C.; Asta, M.D.; Xin, H.L.; Doeff, M.M. Surface reconstruction and chemical evolution of stoichiometric layered cathode materials for lithium-ion batteries. *Nat. Commun.* **2014**, *5*, 3529. [[CrossRef](#)]
107. Hwang, S.; Chang, W.; Kim, S.M.; Su, D.; Kim, D.Y.; Lee, J.Y.; Chung, K.Y.; Stach, E.A. Investigation of changes in the surface structure of $\text{Li}_x\text{Ni}_{0.8}\text{Co}_{0.15}\text{Al}_{0.05}\text{O}_2$ cathode materials induced by the initial charge. *Chem. Mater.* **2014**, *26*, 1084–1092. [[CrossRef](#)]
108. Yang, J.; Hou, M.Y.; Haller, S.; Wang, Y.; Wang, C.; Xia, Y. Improving the cycling performance of the layered Ni-rich oxide cathode by introducing low content Li_2MnO_3 . *Electrochim. Acta* **2016**, *189*, 101–110. [[CrossRef](#)]
109. Yang, J.; Xia, Y.Y. Enhancement on the cycling stability of the layered Ni-rich oxide cathode by in situ fabricating nano-thickness cation-mixing layers. *J. Electrochem. Soc.* **2016**, *163*, A2665–A2672. [[CrossRef](#)]
110. Liu, J.; Du, Z.; Wang, X.; Tan, S.; Wu, X.; Geng, L.; Song, B.; Chien, P.-H.; Everett, S.M.; Hu, E. Anionic redox induced anomalous structural transition in Ni-rich cathodes. *Energy Environ. Sci.* **2021**, *14*, 6441–6454. [[CrossRef](#)]
111. Lu, Z.; Zhang, J.; Zhang, Q.; Wong, D.; Yin, W.; Zhang, N.; Chen, Z.; Gu, L.; Hu, Z.; Liu, X. Oxygen anion redox chemistry correlated with spin state in Ni-rich layered cathodes. *Adv. Sci.* **2023**, *10*, 2206442. [[CrossRef](#)]
112. Chu, Y.; Mu, Y.; Zou, L.; Wu, F.; Yang, L.; Feng, Y.; Zeng, L. Oxygen release in Ni-rich layered cathode for lithium-ion batteries: Mechanisms and mitigating strategies. *ChemElectroChem* **2024**, *11*, e20230065. [[CrossRef](#)]
113. Flores, E.; Vonrüti, N.; Novák, P.; Aschauer, U.; Berg, E.J. Elucidation of $\text{Li}_x\text{Ni}_{0.8}\text{Co}_{0.15}\text{Al}_{0.05}\text{O}_2$ redox chemistry by operando raman spectroscopy. *Chem. Mater.* **2018**, *30*, 4694–4703. [[CrossRef](#)]

114. Li, J.; Hua, H.; Kong, X.; Yang, H.; Dai, P.; Zeng, J.; Zhao, J. In-situ probing the near-surface structural thermal stability of high-nickel layered cathode materials. *Energy Storage Mater.* **2022**, *46*, 90–99. [[CrossRef](#)]
115. Lee, E.; Muhammad, S.; Kim, T.; Kim, H.; Lee, W.; Yoon, W.S. Tracking the influence of thermal expansion and oxygen vacancies on the thermal stability of Ni-rich layered cathode materials. *Adv. Sci.* **2020**, *7*, 1902413. [[CrossRef](#)] [[PubMed](#)]
116. Li, X.; Gao, A.; Tang, Z.; Meng, F.; Shang, T.; Guo, S.; Ding, J.; Luo, Y.; Xiao, D.; Wang, X.; et al. Robust surface reconstruction induced by subsurface Ni/Li antisites in Ni-rich cathodes. *Adv. Funct. Mater.* **2021**, *31*, 2010291. [[CrossRef](#)]
117. Chae, B.G.; Park, S.Y.; Song, J.H.; Lee, E.; Jeon, W.S. Evolution and expansion of Li concentration gradient during charge-discharge cycling. *Nat. Commun.* **2021**, *12*, 3814. [[CrossRef](#)]
118. Yin, S.; Deng, W.; Chen, J.; Gao, X.; Zou, G.; Hou, H.; Ji, X. Fundamental and solutions of microcrack in Ni-rich layered oxide cathode materials of lithium-ion batteries. *Nano Energy* **2021**, *83*, 105854. [[CrossRef](#)]
119. Hwang, S.; Kim, S.M.; Bak, S.-M.; Chung, K.Y.; Chang, W. Investigating the reversibility of structural modifications of $\text{Li}_x\text{Ni}_y\text{Mn}_z\text{Co}_{1-y-z}\text{O}_2$ cathode materials during initial charge/discharge, at multiple length scales. *Chem. Mater.* **2015**, *27*, 6044–6052. [[CrossRef](#)]
120. Ghanty, C.; Markovsky, B.; Erickson, E.M.; Talianker, M.; Haik, O.; Tal-Yossef, Y.; Mor, A.; Aurbach, D.; Lampert, J.; Volkov, A.; et al. Li^+ -ion extraction/insertion of Ni-rich $\text{Li}_{1+x}(\text{Ni}_y\text{Co}_z\text{Mn}_w)\text{O}_2$ ($0.005 < x < 0.03$; $y:z = 8:1$, $w \approx 1$) electrodes: In situ XRD and Raman spectroscopy study. *ChemElectroChem* **2015**, *2*, 1479–1486.
121. Wang, X.L.; An, K.; Cai, L.; Feng, Z.; Nagler, S.E.; Daniel, C.; Rhodes, K.J.; Stoica, A.D.; Skorpenske, H.D.; Liang, C.; et al. Visualizing the chemistry and structure dynamics in lithium-ion batteries by in situ neutron diffraction. *Sci. Rep.* **2012**, *2*, 747. [[CrossRef](#)]
122. Yang, J.; Xia, Y.Y. Suppressing the phase transition of the layered Ni-rich oxide cathode during high-voltage cycling by introducing low-content Li_2MnO_3 . *ACS Appl. Mater. Interfaces* **2016**, *8*, 1297–1308. [[CrossRef](#)]
123. Li, J.; Shunmugasundaram, R.; Doig, R. In situ X-ray diffraction study of layered Li–Ni–Mn–Co oxides: Effect of particle size and structural stability of core–shell materials. *Chem. Mater.* **2016**, *28*, 162–171. [[CrossRef](#)]
124. Yoon, S.; Park, H.G.; Koo, S.; Hwang, J.; Lee, Y.; Park, K.; Kim, D. An in-depth understanding of chemomechanics in Ni-rich layered cathodes for lithium-ion batteries. *J. Alloys Compd.* **2023**, *939*, 168531. [[CrossRef](#)]
125. Laubach, S.; Laubach, S.; Schmidt, P.; Ensling, D.; Schmid, S.; Jaegermann, W.; Thissen, A.; Nikolowski, K.; Ehrenberg, H. Changes in the crystal and electronic structure of LiCoO_2 and LiNiO_2 upon Li intercalation and de-intercalation. *Phys. Chem. Chem. Phys.* **2009**, *11*, 3278–3289. [[CrossRef](#)] [[PubMed](#)]
126. Yabuuchi, N.; Makimura, Y.; Ohzuku, T. Solid-state chemistry and electrochemistry of $\text{LiCo}_{1/3}\text{Ni}_{1/3}\text{Mn}_{1/3}\text{O}_2$ for advanced lithium-ion batteries. *J. Electrochem. Soc.* **2007**, *154*, A314–A321. [[CrossRef](#)]
127. Wang, S.Y.; Yan, M.Y.; Li, Y.; Vinado, C.; Yang, J. Separating electronic and ionic conductivity in mix-conducting layered lithium transition-metal oxides. *J. Power Sources* **2018**, *393*, 75–82. [[CrossRef](#)]
128. Cui, S.; Wei, Y.; Liu, T.; Deng, W.; Hu, Z.; Su, Y.; Li, H.; Li, M.; Guo, H.; Duan, Y.; et al. Optimized temperature effect of Li-ion diffusion with layer distance in $\text{Li}(\text{Ni}_x\text{Mn}_y\text{Co}_z)\text{O}_2$ cathode materials for high performance Li-ion battery. *Adv. Energy Mater.* **2016**, *6*, 1501309. [[CrossRef](#)]
129. Wu, F.; Liu, N.; Chen, L.; Su, Y.; Tan, G.; Bao, L.; Zhang, Q.; Lu, Y.; Wang, J.; Chen, S.; et al. Improving the reversibility of the H2–H3 phase transitions for layered Ni-rich oxide cathode towards retarded structural transition and enhanced cycle stability. *Nano Energy* **2019**, *59*, 50–57. [[CrossRef](#)]
130. Yoon, C.S.; Ryu, H.H.; Park, G.T.; Kim, J.H.; Kim, K.H.; Sun, Y.K. Extracting maximum capacity from Ni-rich $\text{Li}[\text{Ni}_{0.95}\text{Co}_{0.025}\text{Mn}_{0.025}]\text{O}_2$ cathodes for high-energy-density lithium-ion batteries. *J. Mater. Chem. A* **2018**, *6*, 4126–4132. [[CrossRef](#)]
131. Park, S.-H.; Lee, H.; Park, J.; Roh, Y.; Byun, S.; Lim, J.; Jung, S.; Kim, N.; Lee, K.-T.; Lee, Y.-M. A microcrack propagation-based life prediction model for lithium-ion batteries with Ni-rich cathode materials. *J. Energy Storage* **2023**, *58*, 106420. [[CrossRef](#)]
132. Park, N.-Y.; Kim, M.-C.; Han, S.-M.; Park, G.-T.; Kim, D.-H.; Kim, M.-S.; Sun, Y.-K. Mechanism behind the loss of fast charging capability in nickel-rich cathode materials. *Angew. Chem. Int. Ed.* **2024**, *63*, e202319707. [[CrossRef](#)] [[PubMed](#)]
133. Liu, T.; Yu, L.; Lu, J.; Zhou, T.; Huang, X.; Cai, Z.; Dai, A.; Gim, J.; Ren, Y.; Xiao, X.; et al. Rational design of mechanically robust Ni-rich cathode materials via concentration gradient strategy. *Nat. Commun.* **2021**, *12*, 6024. [[CrossRef](#)] [[PubMed](#)]
134. Park, G.T.; Ryu, H.H.; Park, N.Y.; Yoon, C.S.; Sun, Y.K. Tungsten doping for stabilization of $\text{Li}[\text{Ni}_{0.90}\text{Co}_{0.05}\text{Mn}_{0.05}]\text{O}_2$ cathode for Li-ion battery at high voltage. *J. Power Sources* **2019**, *442*, 227242. [[CrossRef](#)]
135. Lv, C.; Li, Z.; Ren, X.; Li, K.; Ma, J.; Duan, X. Revealing the degradation mechanism of Ni-rich cathode materials after ambient storage and related regeneration method. *J. Mater. Chem. A* **2021**, *9*, 3995–4006. [[CrossRef](#)]
136. Su, M.; Chen, Y.; Liu, H.; Li, J.; Fu, K.; Zhou, Y.; Dou, A.; Liu, Y. Storage degradation mechanism of layered Ni-rich oxide cathode material $\text{LiNi}_{0.8}\text{Co}_{0.1}\text{Mn}_{0.1}\text{O}_2$. *Electrochim. Acta* **2022**, *422*, 140559. [[CrossRef](#)]
137. Yang, J.; Liang, X.; Ryu, H.-H.; Yoon, C.S.; Sun, Y.-K. Ni-rich layered cathodes for lithium-ion batteries: From challenges to the future. *Energy Storage Mater.* **2023**, *63*, 102969. [[CrossRef](#)]

138. Lv, Y.; Huang, S.; Zhao, Y.; Ray, S.; Lu, X.; Hou, Y.; Zhang, J. A review of nickel-rich layered oxide cathodes: Synthetic strategies, structural characteristics, failure mechanism, improvement approaches and prospects. *Appl. Energy* **2022**, *305*, 117849. [[CrossRef](#)]
139. Quilty, C.-D.; West, P.-J.; Li, W.-Z.; Dunkin, M.-R.; Wheeler, G.-P.; Ehrlich, S.; Ma, L.; Jaye, C.; Fischer, D.-A.; Takeuchi, E.-S.; et al. Multimodal electrochemistry coupled microcalorimetric and X-ray probing of the capacity fade mechanisms of Nickel rich NMC—progress and outlook. *Phys. Chem. Chem. Phys.* **2022**, *24*, 11471–11485. [[CrossRef](#)]
140. Sun, H.-H.; Manthiram, A. Impact of microcrack generation and surface degradation on a nickel-rich layered $\text{Li}[\text{Ni}_{0.9}\text{Co}_{0.05}\text{Mn}_{0.05}]\text{O}_2$ cathode for lithium-ion batteries. *Chem. Mater.* **2017**, *29*, 8486–8493. [[CrossRef](#)]
141. Korsunsky, A.M.; Sui, T.; Song, B. Explicit formulae for the internal stress in spherical particles of active material within lithium-ion battery cathodes during charging and discharging. *Mater. Des.* **2015**, *69*, 247–252. [[CrossRef](#)]
142. Brandt, L.R.; Marie, J.-J.; Moxham, T.; Förstermann, D.P.; Salvati, E.; Besnard, C.; Papadaki, C.; Wang, Z.; Bruce, P.G.; Korsunsky, A.M. Synchrotron X-ray quantitative evaluation of transient deformation and damage phenomena in a single nickel-rich cathode particle. *Energy Environ. Sci.* **2020**, *13*, 3556–3566. [[CrossRef](#)]
143. Park, N.-Y.; Park, G.-T.; Kim, S.-B.; Jung, W.; Park, B.-C.; Sun, Y.-K. Degradation mechanism of Ni-rich cathode materials: Focusing on particle interior. *ACS Energy Lett.* **2022**, *7*, 2362–2369. [[CrossRef](#)]
144. Zhao, J.; Wang, Z.; Wang, J.; Guo, H.; Li, X.; Gui, W.; Chen, N.; Yan, G. Anchoring K^+ in Li^+ sites of $\text{LiNi}_{0.8}\text{Co}_{0.15}\text{Al}_{0.05}\text{O}_2$ cathode material to suppress its structural degradation during high-voltage cycling. *Energy Technol.* **2018**, *6*, 2358–2366. [[CrossRef](#)]
145. Lee, E.J.; Chen, Z.; Noh, H.-J.; Nam, S.C.; Kang, S.; Kim, D.H.; Amine, K.; Sun, Y.-K. Development of microstrain in aged lithium transition metal oxides. *Nano Lett.* **2014**, *14*, 4873–4880. [[CrossRef](#)]
146. Xu, G.-L.; Liu, Q.; Lau, K.K.S.; Liu, Y.; Liu, X.; Gao, H.; Zhou, X.; Zhuang, M.; Ren, Y.; Li, J.; et al. Building ultraconformal protective layers on both secondary and primary particles of layered lithium transition metal oxide cathodes. *Nat. Energy* **2019**, *4*, 484–494. [[CrossRef](#)]
147. Hu, J.; Li, L.; Hu, E.; Chae, S.; Jia, H.; Liu, T.; Wu, B.; Bi, J.; Amine, K.; Wang, C.; et al. Mesoscale-architecture-based crack evolution dictating cycling stability of advanced lithium-ion batteries. *Nano Energy* **2020**, *79*, 105420. [[CrossRef](#)]
148. Bi, Y.J.; Tao, J.H.; Wu, Y.Q.; Li, L.Z.; Xu, Y.B.; Hu, E.Y.; Wu, B.B.; Hu, J.T.; Wang, C.M.; Zhang, J.G.; et al. Reversible planar gliding and microcracking in a single-crystalline Ni-rich cathode. *Science* **2020**, *370*, 1313–1317. [[CrossRef](#)]
149. Tian, H.; Gao, L.T.; Guo, Z.-S. Microstructural adjusting crack evolution of polycrystalline NCM particle during charge/discharge cycle. *J. Electrochem. Soc.* **2022**, *169*, 090513. [[CrossRef](#)]
150. Han, G.-M.; Kim, Y.-S.; Ryu, H.-H.; Sun, Y.-K.; Yoon, C.S. Structural stability of single-crystalline Ni-rich layered cathode upon delithiation. *ACS Energy Lett.* **2022**, *7*, 2919–2926. [[CrossRef](#)]
151. Su, Y.F.; Zhang, Q.Y.; Chen, L.; Bao, L.Y.; Lu, Y.; Chen, S.; Wu, F. Stress accumulation in Ni-rich layered oxide cathodes: Origin, impact, and resolution. *J. Energy Chem.* **2022**, *65*, 236–253. [[CrossRef](#)]
152. Koo, J.K.; Ran, W.T.A.; Yun, Y.; Seo, J.K.; Kim, M.; Lee, J.; Lee, S.; Kim, J.; Hwang, S.M.; Kim, Y.-J. Probing intraparticle heterogeneity in Ni-rich layered cathodes with different carbon black contents using scanning probe microscopy. *J. Energy Storage* **2022**, *51*, 104395. [[CrossRef](#)]
153. Lee, S.; Song, G.; Yun, B.; Kim, T.; Choi, S.H.; Kim, H.; Doo, S.W.; Lee, K.T. Revealing the nanoscopic corrosive degradation mechanism of nickel-rich layered oxide cathodes at low state-of-charge levels: Corrosion cracking and pitting. *ACS Nano* **2024**, *18*, 10566–10581. [[CrossRef](#)] [[PubMed](#)]
154. Sharma, N.; Vasconcelos, L.S.; Hassan, S.; Zhao, K. Asynchronous-to-synchronous transition of li reactions in solid-solution cathodes. *Nano Lett.* **2022**, *22*, 5883–5890. [[CrossRef](#)]
155. Cheng, X.; Li, Y.; Cao, T.; Wu, R.; Wang, M.; Liu, H.; Liu, X.; Lu, J.; Zhang, Y. Real-time observation of chemomechanical breakdown in a layered nickel-rich oxide cathode realized by in situ scanning electron microscopy. *ACS Energy Lett.* **2021**, *6*, 1703–1710. [[CrossRef](#)]
156. Mu, L.; Lin, R.; Xu, R.; Han, L.; Xia, S.; Sokaras, D.; Steiner, J.D.; Weng, T.C.; Nordlund, D.; Doeff, M.M.; et al. Oxygen release induced chemomechanical breakdown of layered cathode materials. *Nano Lett.* **2018**, *18*, 3241–3249. [[CrossRef](#)]
157. Kim, U.H.; Ryu, H.H.; Kim, J.H.; Mücke, R.; Kaghazchi, P.; Yoon, C.S.; Sun, Y.-K. Microstructure-controlled Ni-rich cathode material by microscale compositional partition for next-generation electric vehicles. *Adv. Energy Mater.* **2019**, *9*, 1803902. [[CrossRef](#)]
158. Morzy, J.K.; Dose, W.M.; Vullum, P.E.; Lai, M.C.; Mahadevagowda, A.; De Volder, M.F.L.; Ducati, C. Origins and importance of intragranular cracking in layered lithium transition metal oxide cathodes. *ACS Appl. Energy Mater.* **2024**, *7*, 3945–3956. [[CrossRef](#)]
159. Park, K.-J.; Hwang, J.-Y.; Ryu, H.-H.; Maglia, F.; Kim, S.-J.; Lamp, P.; Yoon, C.S.; Sun, Y.-K. Degradation mechanism of Ni-enriched NCA cathode for lithium batteries: Are microcracks really critical? *ACS Energy Lett.* **2019**, *4*, 1394–1400. [[CrossRef](#)]
160. Li, W.; Asl, H.-Y.; Xie, Q.; Manthiram, A. Collapse of $\text{LiNi}_{1-x-y}\text{Co}_x\text{Mn}_y\text{O}_2$ lattice at deep charge irrespective of nickel content in lithium-ion batteries. *J. Am. Chem. Soc.* **2019**, *141*, 5097–5101. [[CrossRef](#)]
161. Yan, P.; Zheng, J.; Gu, M.; Xiao, J.; Zhang, J.-G.; Wang, C.-M. Intragranular cracking as a critical barrier for high-voltage usage of layer-structured cathode for lithium-ion batteries. *Nat. Commun.* **2017**, *8*, 14101. [[CrossRef](#)]

162. Li, W.; Song, B.; Manthiram, A. High-voltage positive electrode materials for lithium-ion batteries. *Chem. Soc. Rev.* **2017**, *46*, 3006–3059. [[CrossRef](#)]
163. Li, M.; Liu, T.; Bi, X.; Chen, Z.; Amine, K.; Zhong, C.; Lu, J. Cationic and anionic redox in lithium-ion based batteries. *Chem. Soc. Rev.* **2020**, *49*, 1688–1705. [[CrossRef](#)] [[PubMed](#)]
164. Ryu, H.H.; Park, K.J.; Yoon, C.S.; Sun, Y.K. Capacity fading of Ni-rich $\text{Li}[\text{Ni}_x\text{Co}_y\text{Mn}_{1-x-y}]\text{O}_2$ ($0.6 \leq x \leq 0.95$) cathodes for high-energy-density lithium-ion batteries: Bulk or surface degradation? *Chem. Mater.* **2018**, *30*, 1155–1163. [[CrossRef](#)]
165. Ryu, H.H.; Park, G.T.; Yoon, C.S.; Sun, Y.K. Microstructural degradation of Ni-rich $\text{Li}[\text{Ni}_x\text{Co}_y\text{Mn}_{1-x-y}]\text{O}_2$ cathodes during accelerated calendar aging. *Small* **2018**, *14*, 1803179. [[CrossRef](#)] [[PubMed](#)]
166. Hu, J.; Zhang, L.; Zhong, S.; Li, Z.; Zeng, M.; Fan, F.; Yan, T. Extended fast-charging life of ultrahigh-Ni layered oxides by adjusting the current density during the $\text{H}_2 \rightarrow \text{H}_3$ phase transition. *Energy Storage Mater.* **2022**, *50*, 757–759.
167. Dai, P.P.; Kong, X.B.; Yang, H.Y.; Li, J.Y.; Zeng, J.; Zhao, J.B. Single-crystal Ni-rich layered $\text{LiNi}_{0.9}\text{Mn}_{0.1}\text{O}_2$ enables superior performance of Co-free cathodes for lithium-ion batteries. *ACS Sustain. Chem. Eng.* **2022**, *10*, 4381–4390. [[CrossRef](#)]
168. Ryu, H.H.; Lee, S.B.; Yoon, C.S.; Sun, Y.K. Morphology-dependent battery performance of Ni-rich layered cathodes: Single-crystal versus refined polycrystal. *ACS Energy Lett.* **2022**, *7*, 3072–3079. [[CrossRef](#)]
169. Niu, S.; Xu, J.; Wu, K.; Liang, C.; Zhu, G.; Qu, Q.; Zheng, H. Different mechanical and electrochemical behavior between the two major Ni-rich cathode materials in Li-ion batteries. *Mater. Chem. Phys.* **2021**, *260*, 124046. [[CrossRef](#)]
170. Liang, W.; Zhao, Y.; Shi, L.; Wang, Z.; Yuan, S. Spheroidization: The impact of precursor morphology on solid-state lithiation process for high-quality ultrahigh-nickel oxide cathodes. *Angew. Chem. Int. Ed.* **2024**, *63*, e202407477. [[CrossRef](#)]
171. Zou, L.; Zhao, W.; Jia, H.; Zheng, J.; Li, L.; Abraham, D.P.; Chen, G.; Croy, J.R.; Zhang, J.-G.; Wang, X.C. The role of secondary particle structures in surface phase transitions of Ni-rich cathodes. *Chem. Mater.* **2020**, *32*, 2884–2892. [[CrossRef](#)]
172. Kim, U.-H.; Park, J.-H.; Aishova, A.; Ribas, R.M.; Monteiro, R.S.; Griffith, K.J.; Yoon, C.S.; Sun, Y.-K. Microstructure engineered Ni-rich layered cathode for electric vehicle batteries. *Adv. Energy Mater.* **2021**, *11*, 2100884. [[CrossRef](#)]
173. Park, G.-T.; Yoon, D.R.; Kim, U.-H.; Namkoong, B.; Lee, J.; Wang, M.M.; Lee, A.C.; Gu, X.W.; Chueh, W.C.; Yoon, C.S.; et al. Ultrafine-grained Ni-rich layered cathode for advanced Li-ion batteries. *Energy Environ. Sci.* **2021**, *14*, 6616–6626. [[CrossRef](#)]
174. Wang, L.; Liu, T.; Wu, T.; Lu, J. Strain-retardant coherent perovskite phase stabilized Ni-rich cathode. *Nature* **2022**, *611*, 61–67. [[CrossRef](#)] [[PubMed](#)]
175. Hou, D.; Xu, Z.; Yang, Z.; Kuai, C.; Du, Z.; Sun, C.-J.; Ren, Y.; Liu, J.; Xiao, X.; Lin, F. Effect of the grain arrangements on the thermal stability of polycrystalline nickel-rich lithium-based battery cathodes. *Nat. Commun.* **2022**, *13*, 3437. [[CrossRef](#)]
176. Namkoong, B.; Park, N.-Y.; Park, G.-T.; Shin, J.-Y.; Beierling, T.; Yoon, C.S.; Sun, Y.-K. High-energy Ni-rich cathode materials for long-range and long-life electric vehicles. *Adv. Energy Mater.* **2022**, *12*, 2200615. [[CrossRef](#)]
177. Trevisanello, E.; Ruess, R.; Conforto, G.; Richter, F.H.; Janek, J. Polycrystalline and single crystalline NCM cathode materials—Quantifying particle cracking, active surface area, and lithium diffusion. *Adv. Energy Mater.* **2021**, *11*, 2003400. [[CrossRef](#)]
178. Deng, X.; Zhang, R.; Zhou, K.; Gao, Z.; He, W.; Zhang, L.; Han, C.; Kang, F.; Li, B. A comparative investigation of single crystal and polycrystalline Ni-rich NCMs as cathodes for lithium-ion batteries. *Energy Environ. Mater.* **2022**, *6*, e12331. [[CrossRef](#)]
179. Zhang, R.; Wang, C.; Ge, M.; Xin, H.L. Accelerated degradation in a quasi-single-crystalline layered oxide cathode for lithium-ion batteries caused by residual grain boundaries. *Nano Lett.* **2022**, *22*, 3818–3824. [[CrossRef](#)] [[PubMed](#)]
180. Li, S.; Yao, Z.; Zheng, J.; Fu, M.; Cen, J.; Hwang, S.; Jin, H.; Orlov, A.; Gu, L.; Wang, S.; et al. Direct observation of defect-aided structural evolution in a nickel-rich layered cathode. *Angew. Chem. Int. Ed.* **2020**, *59*, 22092–22099. [[CrossRef](#)]
181. Lin, Q.; Guan, W.; Zhou, J.; Meng, J.; Huang, W.; Chen, T.; Gao, Q.; Wei, X.; Zeng, Y.; Li, J.; et al. Ni-Li anti-site defect induced intragranular cracking in Ni-rich layer-structured cathode. *Nano Energy* **2020**, *76*, 105021. [[CrossRef](#)]
182. Meng, X.H.; Lin, T.; Mao, H.; Shi, J.L.; Sheng, H.; Zou, Y.G.; Fan, M.; Jiang, K.; Xiao, R.J.; Xiao, D.; et al. Kinetic origin of planar gliding in single-crystalline Ni-rich cathodes. *J. Am. Chem. Soc.* **2022**, *144*, 11338–11347. [[CrossRef](#)] [[PubMed](#)]
183. Wang, C.; Wang, X.; Zhang, R.; Lei, T.; Kisslinger, K.; Xin, H.L. Resolving complex intralayer transition motifs in high-Ni-content layered cathode materials for lithium-ion batteries. *Nat. Mater.* **2023**, *22*, 235–241. [[CrossRef](#)] [[PubMed](#)]
184. Sun, J.; Cao, X.; Yang, H.; He, P.; Dato, M.A.; Cabana, J.; Zhou, H. The origin of high-voltage stability in single-crystal layered Ni-rich cathode materials. *Angew. Chem.* **2022**, *134*, e202207225. [[CrossRef](#)]
185. Saaid, F.I.; Kasim, M.F.; Winie, T.; Elong, K.A.; Azahidi, A.; Basri, N.D.; Yaakob, M.K.; Mastuli, M.S.; Shaffee, S.N.A.; Yaakob, M.K.; et al. Ni-rich lithium nickel manganese cobalt oxide cathode materials: A review on the synthesis methods and their electrochemical performances. *Heliyon* **2024**, *10*, e23968. [[CrossRef](#)]
186. Zhang, Y.J.; Du, K.; Cao, Y.B.; Lu, Y.; Peng, Z.D.; Fan, J.; Hu, G. Hydrothermal preparing agglomerate $\text{LiNi}_{0.8}\text{Co}_{0.1}\text{Mn}_{0.1}\text{O}_2$ cathode material with submicron primary particle for alleviating microcracks. *J. Power Sources* **2020**, *477*, 228701. [[CrossRef](#)]
187. Li, Y.; He, J.J.; Luo, L.; Li, X.; Chen, Z.; Zhang, Y.B.; Deng, L.; Dong, P.; Yang, S.; Wu, K.; et al. Highly dispersed micrometer nickel-rich single-crystal construction: Benefits of supercritical reconstruction during hydrothermal synthesis. *ACS Appl. Energy Mater.* **2022**, *5*, 6302–6312. [[CrossRef](#)]

188. Gu, H.; Wang, J.; Wang, Z.; Tong, J.; Qi, N.; Han, G.; Zhang, M. Self-assembled porous $\text{LiNi}_{0.8}\text{Co}_{0.1}\text{Mn}_{0.1}\text{O}_2$ cathode materials with micro/nano-layered hollow morphologies for high-power lithium-ion batteries. *Appl. Surf. Sci.* **2021**, *539*, 148034. [[CrossRef](#)]
189. Li, S.Y.; Liang, W.B.; Xie, J.; Wei, Y.; Cui, X.L. Synthesis of hollow microspheres $\text{LiNi}_{0.5}\text{Mn}_{1.5}\text{O}_4$ coated with Al_2O_3 and characterization of the electrochemical capabilities. *J. Electrochem. Energy Convers. Storage* **2020**, *17*, 031007.
190. Guo, J.; Li, W. Synthesis of single-crystal $\text{LiNi}_{0.7}\text{Co}_{0.15}\text{Mn}_{0.15}\text{O}_2$ materials for Li-ion batteries by a sol-gel method. *ACS Appl. Energy Mater.* **2022**, *5*, 397–406. [[CrossRef](#)]
191. Bai, X.; Wei, A.J.; He, R.; Li, W.; Li, X.H.; Zhang, L.H.; Liu, Z. The structural and electrochemical performance of Mg-doped $\text{LiNi}_{0.85}\text{Co}_{0.10}\text{Al}_{0.05}\text{O}_2$ prepared by a solid-state method. *J. Electroanal. Chem.* **2020**, *858*, 113771. [[CrossRef](#)]
192. Zheng, L.; Bennett, J.C.; Obrovac, M.N. All-dry synthesis of single crystal NMC cathode materials for Li-ion batteries. *J. Electrochem. Soc.* **2020**, *167*, 130536. [[CrossRef](#)]
193. Wang, Z.; Yang, L.; Xu, C.; Cheng, J.; Zhao, J.; Huang, Q.; Yang, C. Advances in reactive co-precipitation technology for preparing high-performance cathodes. *Green Carbon* **2023**, *1*, 193–209. [[CrossRef](#)]
194. He, F.R.; Tian, Z.Q.; Xiang, W.; Yang, W.; Zheng, B.P.; Cai, J.Y.; Guo, X.D. Insight into the surface reconstruction-induced structure and electrochemical performance evolution for Ni-rich cathodes with postannealing after washing. *ACS Appl. Mater. Interfaces* **2023**, *15*, 9160–9170. [[CrossRef](#)]
195. Liang, W.; Zhao, Y.; Shi, L.; Wang, Z.; Wang, Y.; Zhang, M.; Yuan, S. Advances of high-performance $\text{LiNi}_{1-x-y}\text{Co}_x\text{M}_y\text{O}_2$ cathode materials and their precursor particles via co-precipitation process. *Particuology* **2024**, *86*, 67–85. [[CrossRef](#)]
196. Wang, L.; Shi, Q.; Zhan, C.; Liu, G. One-step solid-state synthesis of Ni-rich cathode materials for lithium-ion batteries. *Materials* **2023**, *16*, 3079. [[CrossRef](#)]
197. El Kouihen, F.; Chakir, M.; Faik, A. The effect of synthesis methods on cation mixing degree in cobalt-free, nickel-rich NMA materials. *Chem. Pap.* **2025**, *79*, 2411–2420. [[CrossRef](#)]
198. Li, X.; Zhang, K.; Wang, S.; Wang, M.; Jiang, F.; Liu, Y.; Huang, Y.; Zheng, J. Optimal synthetic conditions for a novel and high-performance Ni-rich cathode material of $\text{LiNi}_{0.68}\text{Co}_{0.10}\text{Mn}_{0.22}\text{O}_2$. *Sustain. Energy Fuels* **2018**, *2*, 1772–1780.
199. Ying, B.X.; Fitzpatrick, J.R.; Teng, Z.J.; Chen, T.X.; Lo, T.W.B.; Siozios, V.; Murray, C.A.; Brand, H.E.A.; Day, S.; Tang, C.C.; et al. Monitoring the formation of nickel-poor and nickel-rich oxide cathode materials for lithium-ion batteries with synchrotron radiation. *Chem. Mater.* **2023**, *35*, 1514–1526. [[CrossRef](#)]
200. Han, Q.; Cai, L.L.; Yang, Z.F.; Hu, Y.J.; Jiang, H.; Li, C.Z. New insights into the pre-lithiation kinetics of single-crystalline Ni-rich cathodes for long-life Li-ion batteries. *Green Energy Environ.* **2024**, *9*, 556–564. [[CrossRef](#)]
201. Xiao, X.; Wang, L.; Li, J.T.; Zhang, B.; Hu, Q.; Liu, J.L.; Wu, Y.Q.; Gao, J.H.; Chen, Y.B.; Song, S.L.; et al. Rational synthesis of high-performance Ni-rich layered oxide cathode enabled via probing solid-state lithiation evolution. *Nano Energy* **2023**, *113*, 108528. [[CrossRef](#)]
202. Liu, J.J.; Yuan, Y.F.; Zheng, J.H.; Wang, L.G.; Ji, J.; Zhang, Q.; Yang, L.; Bai, Z.Y.; Lu, J. Understanding the synthesis kinetics of single-crystal Co-free Ni-rich cathodes. *Angew. Chem. Int. Ed.* **2023**, *62*, e202302547. [[CrossRef](#)] [[PubMed](#)]
203. Wolfman, M.; Wang, X.P.; Garcia, J.C.; Barai, P.; Stubbs, J.E.; Eng, P.J.; Kahvecioglu, O.; Kinnibrugh, T.L.; Madsen, K.E.; Iddir, H.; et al. Spheroidization: The impact of precursor morphology on solid-state lithiation process for high-quality ultrahigh-nickel oxide cathodes. *Adv. Energy Mater.* **2022**, *12*, 2102951. [[CrossRef](#)]
204. Xu, Z.R.; Jiang, Z.S.; Kuai, C.G.; Xu, R.; Qin, C.D.; Zhang, Y.; Rahman, M.M.; Wei, C.; Nordlund, D.; Sun, C.-J.; et al. Charge distribution guided by grain crystallographic orientations in polycrystalline battery materials. *Nat. Commun.* **2020**, *11*, 83. [[CrossRef](#)] [[PubMed](#)]
205. Polierer, S.; Guse, D.; Wild, S.; Delgado, K.H.; Otto, T.N.; Zevaco, T.A.; Kind, M.; Sauer, J.; Studt, F.; Pitter, S. Enhanced direct dimethyl ether synthesis from CO_2 rich syngas with $\text{Cu}/\text{ZnO}/\text{ZrO}_2$ catalysts prepared by continuous co-precipitation. *Catalysts* **2020**, *10*, 816. [[CrossRef](#)]
206. Ahmed, R.R.; Mubarak, T.H.; Mohamed, I.H. A study of structural and chemical properties of $\text{Ni}_{1-x}\text{Zn}_x\text{Fe}_2\text{O}_4$ ferrite powder prepared by co-precipitation method. *Digest J. Nanomater. Biostruct.* **2022**, *17*, 741–748. [[CrossRef](#)]
207. Entwistle, T.; Sanchez-Perez, E.; Murray, G.J.; Anthonisamy, N.; Cussen, S.A. Co-precipitation synthesis of nickel-rich cathodes for Li-ion batteries. *Energy Rep.* **2022**, *8*, 67–73. [[CrossRef](#)]
208. Lee, S.H.; Kwon, K.Y.; Choi, B.K.; Yoo, H.D. A kinetic descriptor to optimize Co-precipitation of Nickel-rich cathode precursors for lithium-ion batteries. *J. Electroanal. Chem.* **2022**, *924*, 116828. [[CrossRef](#)]
209. Heo, K.; Lee, J.S.; Kim, H.S.; Kim, M.Y.; Jeong, H.; Kim, J.; Lim, J. Ionic conductor- $\text{LiNi}_{0.8}\text{Co}_{0.1}\text{Mn}_{0.1}\text{O}_2$ composite synthesized by simultaneous co-precipitation for use in lithium-ion batteries. *J. Electrochem. Soc.* **2018**, *165*, A2955–A2960. [[CrossRef](#)]
210. Xu, L.P.; Zhou, F.; Kong, J.Z.; Zhou, H.B.; Zhang, Q.C.; Wang, Q.Z.; Yan, G. Influence of precursor phase on the structure and electrochemical properties of $\text{LiNi}_{0.6}\text{Mn}_{0.2}\text{Co}_{0.2}\text{O}_2$ cathode materials. *Solid State Ion.* **2018**, *324*, 49–58. [[CrossRef](#)]
211. Zhang, X.; Hu, G.R.; Peng, Z.D.; Cao, Y.B.; Li, L.Y.; Tan, C.P.; Du, K. Synthesis and characterization of mono-dispersion $\text{LiNi}_{0.8}\text{Co}_{0.1}\text{Mn}_{0.1}\text{O}_2$ micrometer particles for lithium-ion batteries. *Ceram. Int.* **2021**, *47*, 25680–25688. [[CrossRef](#)]

212. Pollen, H.N.; Tolchard, J.R.; Svensson, A.M.; Wagner, N.P. A single-pot co-precipitation synthesis route for Ni-rich layered oxide materials with high cycling stability. *ChemElectroChem* **2022**, *9*, e202200859. [[CrossRef](#)]
213. Para, M.L.; Alidoost, M.; Shiea, M.; Boccardo, G.; Buffo, A.; Barresi, A.A.; Marchisio, D. A modelling and experimental study on the co-precipitation of $\text{Ni}_{0.8}\text{Mn}_{0.1}\text{Co}_{0.1}(\text{OH})_2$ as precursor for battery cathodes. *Chem. Eng. Sci.* **2022**, *254*, 117634. [[CrossRef](#)]
214. Zhang, H.W.; Cen, T.; Tian, Y.H.; Zhang, X.J. Synthesis of high-performance single-crystal $\text{LiNi}_{0.8}\text{Co}_{0.1}\text{Mn}_{0.1}\text{O}_2$ cathode materials by controlling solution super-saturation. *J. Power Sources* **2022**, *532*, 231037. [[CrossRef](#)]
215. Kumar, D.; Kurian, E.; Ramesha, K. Synthesis of quasi-spherical $\text{LiNi}_{0.86}\text{Mn}_{0.1}\text{Co}_{0.04}\text{O}_2$ cathode particles via hydroxide coprecipitation: Influence of pH on precursor particle size in enhancing capacity and stability of Ni-rich cathode for lithium-ion batteries. *Energy Technol.* **2025**, *24*, 02418. [[CrossRef](#)]
216. Duan, J.H.; Zhang, R.C.; Zhu, Q.H.; Xiao, H.; Huang, Q.S. The effect of controlling strategies of pH and ammonia concentration on preparing full concentration gradient $\text{Ni}_{0.8}\text{Co}_{0.1}\text{Mn}_{0.1}(\text{OH})_2$ via co-precipitation in a pilot-scale reactor. *Energy Technol.* **2020**, *8*, 1901437. [[CrossRef](#)]
217. Park, B.H.; Kim, T.; Park, H.; Sohn, Y.; Shin, J.; Kang, M. Electrochemical performance of layer-structured $\text{Ni}_{0.8}\text{Co}_{0.1}\text{Mn}_{0.1}\text{O}_2$ cathode active materials synthesized by carbonate co-precipitation. *Nanomaterials* **2022**, *12*, 3610. [[CrossRef](#)]
218. Shen, W.-Z.; Ma, Y.; Yao, C.; Liang, F. Controlling the precursor morphology of Ni-rich $\text{LiNi}_{0.8}\text{Co}_{0.1}\text{Mn}_{0.1}\text{O}_2$ cathode for lithium-ion battery. *Nano* **2019**, *14*, 100–108. [[CrossRef](#)]
219. Hu, K.H.; He, Y.Y.; Zhu, C.Q.; Zhou, K.; Chen, Q.; Yang, Z.M.; Wan, B.-R.; Yang, E.-Q.; Zhang, T.-T.; Qin, Y.-D. Insight into the evolution of precursor and electrochemical performance of Ni-rich cathode modulated by ammonia during hydroxide precipitation. *J. Alloys Compd.* **2019**, *803*, 538–545. [[CrossRef](#)]
220. Liang, H.L.; Yuan, S.; Shi, L.Y.; Zhao, Y.; Wang, Z.Y.; Zhu, J.F. Highly-ordered microstructure and well performance of $\text{LiNi}_{0.6}\text{Mn}_{0.2}\text{Co}_{0.2}\text{O}_2$ cathode material via the continuous microfluidic synthesis. *Chem. Eng. J.* **2020**, *394*, 124846. [[CrossRef](#)]
221. Zou, L.; Li, J.; Liu, Z.; Wang, G.; Manthiram, A.; Wang, C. Lattice doping regulated interfacial reactions in cathode for enhanced cycling stability. *Nat. Commun.* **2019**, *10*, 3447. [[CrossRef](#)] [[PubMed](#)]
222. Park, H.W.; Hwang, J.U.; Im, J.S.; Lee, J.D. Electrochemical properties of $\text{LiNi}_{0.9}\text{Co}_{0.1}\text{O}_2$ cathode material prepared by co-precipitation using an eco-friendly chelating agent. *J. Solid State Electrochem.* **2022**, *26*, 1567–1576. [[CrossRef](#)]
223. Li, F.; Liu, Z.; Shen, J.; Xu, X.; Zeng, L.; Zhang, B.; Zhu, H.; Liu, Q.; Liu, J.; Zhu, M. A nanorod-like Ni-rich layered cathode with enhanced Li^+ diffusion pathways for high-performance lithium-ion batteries. *J. Mater. Chem.* **2021**, *9*, 2830–2839. [[CrossRef](#)]
224. Wang, X.; Wang, S.; Ren, L.; Wu, W.; Zuo, M.; Xing, W.; Zhang, B.; Fan, W.; He, Z.; Yu, Z.; et al. Micro-structure tuning and evolution of hydroxide precursor with radially oriented grains during industrial-scale continuous precipitation process. *J. Alloys Compd.* **2024**, *977*, 173458. [[CrossRef](#)]
225. Zhou, X.; Hong, F.; Wang, S.; Zhao, T.; Peng, J.; Zhang, B.; Fan, W.; Xing, W.; Zuo, M.; Zhang, P.; et al. Precision engineering of high-performance Ni-rich layered cathodes with radially aligned microstructure through architectural regulation of precursors. *eScience* **2024**, *4*, 100276. [[CrossRef](#)]
226. Zhu, Q.H.; Xiao, H.; Zhang, R.C.; Geng, S.J.; Huang, Q.S. Effect of impeller type on preparing spherical and dense $\text{Ni}_{1-x-y}\text{Co}_x\text{Mn}_y(\text{OH})_2$ precursor via continuous co-precipitation in pilot scale: A case of $\text{Ni}_{0.6}\text{Co}_{0.2}\text{Mn}_{0.2}(\text{OH})_2$. *Electrochim. Acta* **2019**, *318*, 1–13. [[CrossRef](#)]
227. Wu, J.; Li, H.; Liu, Y.; Ye, Y.; Yang, Y. Facile synthesis and electrochemical performance of lithium-rich layered oxides with stable hierarchical structure through HEPES-assisted co-precipitation method. *Electrochim. Acta* **2022**, *401*, 139485. [[CrossRef](#)]
228. Zhang, J.; Zhai, X.; Zhao, T.; Yang, X.; Wang, Q.; Chen, Z.; Chen, M.-C.; Ma, J.-J.; Lu, Y.-R.; Hung, S.-F.; et al. What impact does ammonia have on the microstructure of the precursor and the electrochemical performance of Ni-rich layered oxides? *J. Mater. Chem. A* **2025**, *13*, 1181–1190. [[CrossRef](#)]
229. Kim, E.; Cho, Y.H.; Shin, J.H.; Eun, H.J.; Song, H.I.; Lee, S.-H.; Suk, J.; Moon, S. Unlocking the superior performance of Ni-rich layered materials through precise precursor engineering. *J. Eur. Ceram. Soc.* **2025**, *45*, 117280. [[CrossRef](#)]
230. Lao, J.; Lu, Y. Synthesis of nano cubic microstructure $\text{LiNi}_{0.8}\text{Co}_{0.1}\text{Mn}_{0.1}\text{O}_2$ cathode materials via rapid precipitation assisted with hydrothermal treatment. *Heliyon* **2024**, *10*, e40201. [[CrossRef](#)]
231. Chen, A.; Wang, K.; Li, J.; Mao, Q.; Xiao, Z.; Zhu, D.; Wang, G.; Liao, P.; He, J.; You, Y.; et al. The formation, detriment and solution of residual lithium compounds on Ni-rich layered oxides in lithium-ion batteries. *Front. Energy Res.* **2020**, *8*, 593009. [[CrossRef](#)]
232. Li, W.D.; Erickson, E.M.; Manthiram, A. High-nickel layered oxide cathodes for lithium-based automotive batteries. *Nat. Energy* **2020**, *5*, 26–34. [[CrossRef](#)]
233. Wang, L.; Liu, T.; Dai, A.; De Andrade, V.; Ren, Y.; Xu, W.; Lee, S.; Zhang, Q.; Gu, L.; Wang, S.; et al. Reaction inhomogeneity coupling with metal rearrangement triggers electrochemical degradation in lithium-rich layered cathode. *Nat. Commun.* **2021**, *12*, 5370. [[CrossRef](#)] [[PubMed](#)]
234. Wang, J.; Lu, X.; Zhang, Y.; Zhou, J.; Wang, J.; Xu, S. Grain size regulation for balancing cycle performance and rate capability of $\text{LiNi}_{0.9}\text{Co}_{0.055}\text{Mn}_{0.045}\text{O}_2$ single crystal nickel-rich cathode materials. *J. Energy Chem.* **2022**, *65*, 681–687. [[CrossRef](#)]

235. Jeyakumar, J.; Seenivasan, M.; Wu, Y.-S.; Wu, S.-H.; Chang, J.-K.; Jose, R.; Yang, C.-C. Preparation of long-term cycling stable Ni-rich concentration-gradient NCMA cathode materials for li-ion batteries. *J. Colloid Interface Sci.* **2023**, *639*, 145–159. [[CrossRef](#)] [[PubMed](#)]
236. Liang, W.; Jin, F.; Zhao, Y.; Shi, L.; Liu, Q.; Wang, Z.; Wang, Y.; Zhang, M.; Zhu, J.; Yuan, S. Synthesis of single-crystal $\text{LiNi}_{0.8}\text{Co}_{0.1}\text{Mn}_{0.1}\text{O}_2$ materials for Li-ion batteries by microfluidic technology. *Chem. Eng. J.* **2023**, *464*, 142656. [[CrossRef](#)]
237. Riewald, F.; Kurzhals, P.; Bianchini, M.; Sommer, H.; Janek, J.; Gasteiger, H.A. The LiNiO_2 cathode active material: A comprehensive study of calcination conditions and their correlation with physicochemical properties part II. Morphology. *J. Electrochem. Soc.* **2022**, *169*, 020529. [[CrossRef](#)]
238. Yu, Z.; Qu, X.; Wan, T.; Dou, A.; Zhou, Y.; Peng, X.; Su, M.; Liu, Y.; Chu, D. Synthesis and mechanism of high structural stability of nickel-rich cathode materials by adjusting Li-excess. *ACS Appl. Mater. Interfaces* **2020**, *12*, 40393–40403. [[CrossRef](#)]
239. Kan, H.; Yang, Z.; Meng, Q.; Dong, P.; Zhang, Y. Preparation and electrochemical performance of the Ni-rich Co-free cathode material $\text{LiNi}_{0.94}\text{Mn}_{0.04}\text{Al}_{0.02}\text{O}_2$. *Energy Fuels* **2024**, *38*, 6420–6426. [[CrossRef](#)]
240. Kim, Y.; Park, H.; Warner, J.H.; Manthiram, A. Unraveling the intricacies of residual lithium in high-Ni cathodes for lithium-ion batteries. *ACS Energy Lett.* **2021**, *6*, 941–948. [[CrossRef](#)]
241. Li, J.; Liang, G.; Zheng, W.; Zhang, S.; Davey, K.; Pang, W.K.; Guo, Z. Addressing cation mixing in layered structured cathodes for lithium-ion batteries: A critical review. *Nano Mater. Sci.* **2023**, *5*, 404–420. [[CrossRef](#)]
242. Li, X.Q.; Xiong, X.; Wang, Z.; Chen, Q. Effect of sintering temperature on cycling performance and rate performance of $\text{LiNi}_{0.8}\text{Co}_{0.1}\text{Mn}_{0.1}\text{O}_2$. *Trans. Nonferr. Met. Soc. China* **2014**, *24*, 4023–4029. [[CrossRef](#)]
243. Ding, Y.; Mu, D.; Wu, B.; Wang, R.; Zhao, Z.; Wu, F. Recent progresses on nickel-rich layered oxide positive electrode materials used in lithium-ion batteries for electric vehicles. *Appl. Energy* **2017**, *195*, 586–599. [[CrossRef](#)]
244. Wang, L.; Lei, X.; Liu, T.; Dai, A.; Su, D.; Amine, K.; Lu, J.; Wu, T. Regulation of surface defect chemistry toward stable Ni-rich cathodes. *Adv. Mater.* **2022**, *34*, 2200744. [[CrossRef](#)]
245. Xu, Z.; Wang, Z.; Tan, X.; Guo, H.; Peng, W.; Li, X.; Wang, J.; Yan, G. Correlating morphological and structural evolution with the electrochemical performance of nickel-rich cathode materials: From polycrystal to single crystal. *J. Electrochem. Soc.* **2022**, *169*, 090520. [[CrossRef](#)]
246. Allen, E.; Shin, Y.; Judge, W.; Wolfman, M.; De Andrade, V.; Cologna, S.M.; Cabana, J. 3D quantification of elemental gradients within heterostructured particles of battery cathodes. *ACS Energy Lett.* **2023**, *8*, 1371–1378. [[CrossRef](#)]
247. Lee, W.; Lee, D.; Kim, Y.; Choi, W.; Yoon, W.-S. Enhancing the structural durability of Ni-rich layered materials by post-process: Washing and heat-treatment. *J. Mater. Chem. A* **2020**, *8*, 10206–10216. [[CrossRef](#)]
248. Karger, L.; Kornevychuk, S.; Sicolo, S.; Li, H.; van der Bergh, W.; Zhang, R.; Indris, S.; Kondrakov, A.; Janek, J.; Brezesinski, T. Decoupling substitution effects from point defects in layered Ni-rich oxide cathode materials for lithium-ion batteries. *Adv. Funct. Mater.* **2024**, *34*, 2402444. [[CrossRef](#)]
249. Wang, T.; Ren, K.; Xiao, W.; Dong, W.; Qiao, H.; Duan, A.; Pan, H.; Yang, Y.; Wang, H. Tuning the Li/Ni disorder of the NMC811 cathode by thermally driven competition between lattice ordering and structure decomposition. *J. Phys. Chem. C* **2020**, *124*, 5600–5607. [[CrossRef](#)]
250. Mo, Y.; Liu, S.; Yuan, G.; Li, Z.; Zhang, M.; Guo, L. Enhancing the reversibility of the chemical evolution of the Ni-rich $\text{LiNi}_{0.8}\text{Co}_{0.1}\text{Mn}_{0.1}\text{O}_2$ cathode via a simple pre-oxidation process. *RSC Adv.* **2024**, *14*, 2889–2895. [[CrossRef](#)] [[PubMed](#)]
251. Xu, X.; Huo, H.; Jian, J.-Y.; Wang, L.-G.; Zhu, H.; Xu, S.; He, X.-S.; Yin, G.-P.; Du, C.-Y.; Sun, X.-L. Radially oriented single-crystal primary nanosheets enable ultrahigh rate and cycling properties of $\text{LiNi}_{0.8}\text{Co}_{0.1}\text{Mn}_{0.1}\text{O}_2$ cathode material for lithium-ion batteries. *Adv. Energy Mater.* **2019**, *9*, 1803963. [[CrossRef](#)]
252. Wang, T.; Ren, K.; He, M.; Dong, W.; Xiao, W.; Pan, H.; Yang, J.; Yang, Y.; Liu, P.; Cao, Z.; et al. Synthesis and manipulation of single-crystalline lithium nickel manganese cobalt oxide cathodes: A review of growth mechanism. *Front. Chem.* **2020**, *8*, 747. [[CrossRef](#)] [[PubMed](#)]
253. Liu, Y.; Harlow, J.; Dahn, J. Microstructural observations of “single crystal” positive electrode materials before and after long term cycling by cross-section scanning electron microscopy. *J. Electrochem. Soc.* **2020**, *167*, 020512. [[CrossRef](#)]
254. Kong, X.; Zhang, Y.; Peng, S.; Zeng, J.; Zhao, J. Superiority of single crystal to polycrystalline $\text{LiNi}_x\text{Co}_y\text{Mn}_{1-x-y}\text{O}_2$ cathode materials in storage behaviors for lithium-ion batteries. *ACS Sustain. Chem. Eng.* **2020**, *8*, 14938–14948. [[CrossRef](#)]
255. Lüther, M.J.; Jiang, S.-K.; Lange, M.A.; Buchmann, J.; Martin, A.G.; Schmuck, R.; Placke, T.; Hwang, B.J.; Winter, M.; Kasnatscheew, J. Systematic “apple-to-apple” comparison of single-crystal and polycrystalline Ni-rich cathode active materials: From comparable synthesis to comparable electrochemical conditions. *Small* **2024**, *5*, 2400119. [[CrossRef](#)]
256. Qian, G.; Zhang, Y.; Li, L.; Zhang, R.; Xu, J.; Chen, Z.; Xie, S.; Wang, H.; Rao, Q.; He, Y.; et al. Single-crystal nickel-rich layered-oxide battery cathode materials: Synthesis, electrochemistry, and intra-granular fracture. *Energy Storage Mater.* **2020**, *27*, 140–149. [[CrossRef](#)]

257. Fan, X.-M.; Hu, G.-R.; Zhang, B.; Ou, X.; Zhang, J.-F.; Zhao, W.-G.; Jia, H.-P.; Zou, L.F.; Li, P.; Yang, Y. Crack-free single crystalline Ni-rich layered NCM cathode enable superior cycling performance of lithium-ion batteries. *Nano Energy* **2020**, *70*, 104450. [[CrossRef](#)]
258. Pang, P.; Tan, X.; Wang, Z.; Cai, Z.; Nan, J.; Xing, Z.; Li, H. Crack-free single-crystal $\text{LiNi}_{0.83}\text{Co}_{0.10}\text{Mn}_{0.07}\text{O}_2$ as cycling/thermal stable cathode materials for high-voltage lithium-ion batteries. *Electrochim. Acta* **2021**, *365*, 137380. [[CrossRef](#)]
259. Han, Y.; Xu, J.; Wang, W.; Long, F.; Qu, Q.; Wang, Y.; Zheng, H. Implanting an electrolyte additive on a single crystal Ni-rich cathode surface for improved cycle ability and safety. *J. Mater. Chem. A* **2020**, *8*, 24579–24589. [[CrossRef](#)]
260. Chen, X.; Tang, Y.; Fan, C.; Han, S. A highly stabilized single crystalline nickel-rich $\text{LiNi}_{0.8}\text{Co}_{0.1}\text{Mn}_{0.1}\text{O}_2$ cathode through a novel surface spinel-phase modification. *Electrochim. Acta* **2020**, *341*, 136075. [[CrossRef](#)]
261. Ge, M.; Wi, S.; Liu, X.; Bai, J.; Ehrlich, S.; Lu, D.; Lee, W.K.; Chen, Z.; Wang, F. Kinetic limitations in single-crystal high-nickel cathodes. *Angew. Chem. Int. Ed.* **2021**, *60*, 17350–17355. [[CrossRef](#)]
262. You, B.; Wang, Z.; Shen, F.; Chang, Y.; Peng, W.; Li, X.; Guo, H.; Hu, Q.; Deng, C.; Yang, S.; et al. Research progress of single-crystal nickel-rich cathode materials for lithium-ion batteries. *Small Methods* **2021**, *5*, 2100234. [[CrossRef](#)] [[PubMed](#)]
263. Wang, Y.; Wang, E.; Zhang, X.; Yu, H. High-voltage “single-crystal” cathode materials for lithium-ion batteries. *Energy Fuels* **2021**, *35*, 918–932. [[CrossRef](#)]
264. Han, Y.; Lei, Y.; Ni, J.; Zhang, Y.; Geng, Z.; Ming, P.; Zhang, C.; Tian, X.; Shi, J.-L.; Guo, Y.; et al. Single-crystalline cathodes for advanced Li-ion batteries: Progress and challenges. *Small* **2022**, *18*, 2107048. [[CrossRef](#)]
265. Zhao, W.; Zou, L.; Zhang, L.; Fan, X.; Zhang, H.; Pagani, F.; Brack, E.; Seidl, L.; Ou, X.; Egorov, K.; et al. Assessing long-term cycling stability of single-crystal versus polycrystalline nickel-rich NCM in pouch cells with 6 mAh cm^{-2} electrodes. *Small* **2022**, *18*, 2107357. [[CrossRef](#)]
266. Zhang, F.; Lou, S.; Li, S.; Yu, Z.; Liu, Q.; Dai, A.; Cao, C.; Toney, M.F.; Ge, M.; Xiao, X.; et al. Surface regulation enables high stability of single-crystal lithium-ion cathodes at high voltage. *Nat. Commun.* **2020**, *11*, 3050. [[CrossRef](#)]
267. Hu, J.; Li, L.; Bi, Y.; Tao, J.; Lochala, J.; Liu, D.; Wu, B.; Cao, X.; Chae, S.; Wang, C.; et al. Locking oxygen in lattice: A quantifiable comparison of gas generation in polycrystalline and single crystal Ni-rich cathodes. *Energy Storage Mater.* **2022**, *47*, 195–202. [[CrossRef](#)]
268. Ge, J.; Xie, M.; Zhao, Q.; Zhang, S.; Sun, H. Advances in Co-free layered cathode materials for Li-ion batteries. *Int. J. Electrochem. Sci.* **2023**, *18*, 100292. [[CrossRef](#)]
269. Huang, H.; Zhang, L.; Tian, H.; Yan, J.; Tong, J.; Liu, X.; Zhang, H.; Huang, H.; Hao, S.; Gao, J.; et al. Pulse high temperature sintering to prepare single-crystal high nickel oxide cathodes with enhanced electrochemical performance. *Adv. Energy Mater.* **2023**, *13*, 2203188. [[CrossRef](#)]
270. Li, H.; Wang, L.; Song, Y.; Zhang, Z.; Du, A.; Tang, Y.; Wang, J.; He, X. Why the synthesis affects performance of layered transition metal oxide cathode materials for Li-ion batteries. *Adv. Mater.* **2024**, *36*, 2312292. [[CrossRef](#)] [[PubMed](#)]
271. Ma, Y.; Lv, F.; Wang, Z.; Feng, J.; Wu, M.; Liu, Z.; Chen, L.; Gu, Y. Open-channel [011] facet CeO_2 with a shorter pathway of Li^+ migration as a modification material for $\text{LiNi}_{0.8}\text{Co}_{0.1}\text{Mn}_{0.1}\text{O}_2$ toward high-rate lithium-ion batteries. *ACS Sustain. Chem. Eng.* **2020**, *8*, 8795–8802. [[CrossRef](#)]
272. Liu, H.-W.; Parthasarathi, S.-K.; Thi, S.; Weng, Y.-T.; Bolloju, S.; Chen, C.C.; Jeng, R.-J.; Wu, N.-L. A comparative study of polycrystal/single-crystal $\text{LiNi}_{0.8}\text{Co}_{0.1}\text{Mn}_{0.1}\text{O}_2$ in all-solid-state Li-ion batteries with halide-based electrolyte under low stacking pressure. *Energy Technol.* **2023**, *11*, 2201439. [[CrossRef](#)]
273. Zhang, Q.; Wang, Y.; Deng, Q.; Chu, Y.; Dong, P.; Chen, C.; Wang, Z.; Xia, Z.; Yang, C. In situ and real-time monitoring the chemical and thermal evolution of lithium-ion batteries with single-crystalline Ni-rich layered oxide cathode. *Angew. Chem. Int. Ed.* **2024**, *63*, e202401716. [[CrossRef](#)]
274. Liu, X.; Zheng, B.; Zhao, J.; Zhao, W.; Liang, Z.; Su, Y.; Xie, C.; Zhou, K.; Xiang, Y.; Zhu, J.; et al. Electrochemo-mechanical effects on structural integrity of Ni-rich cathodes with different microstructures in all solid-state batteries. *Adv. Energy Mater.* **2021**, *11*, 2003583. [[CrossRef](#)]
275. Zhu, H.; Tang, Y.; Wiaderek, K.M.; Borkiewicz, O.J.; Ren, Y.; Zhang, J.; Ren, J.; Fan, L.; Li, C.C.; Li, D.; et al. Spontaneous strain buffer enables superior cycling stability in single-crystal nickel-rich NCM cathode. *Nano Lett.* **2021**, *21*, 9997–10005. [[CrossRef](#)]
276. Ran, A.; Chen, S.; Cheng, M.; Liang, Z.; Li, B.; Zhou, G.; Kang, F.; Zhang, X.; Wei, G. A single-crystal nickel-rich material as a highly stable cathode for lithium-ion batteries. *J. Mater. Chem. A* **2022**, *10*, 19680–19689. [[CrossRef](#)]
277. Han, Q.; Yu, H.; Cai, L.; Jiang, H. Unique insights into the design of low-strain single-crystalline Ni-rich cathodes with superior cycling stability. *Proc. Natl. Acad. Sci. USA* **2024**, *121*, e2317282121. [[CrossRef](#)]
278. Cha, H.; Kim, J.; Lee, H.; Kim, N.; Hwang, J.; Sung, J.; Yoon, M.; Kim, K.; Cho, J. Boosting reaction homogeneity in high-energy lithium-ion battery cathode materials. *Adv. Mater.* **2020**, *32*, 2003040. [[CrossRef](#)]
279. Kong, X.; Zhang, Y.; Li, J.; Yang, H.; Dai, P.; Zeng, J.; Zhao, J. Single-crystal structure helps enhance the thermal performance of Ni-rich layered cathode materials for lithium-ion batteries. *Chem. Eng. J.* **2022**, *434*, 134638. [[CrossRef](#)]

280. Wang, C.; Zhang, R.; Siu, C.; Ge, M.; Kisslinger, K.; Shin, Y.; Xin, H.L. Chemomechanically stable ultrahigh-Ni single-crystalline cathodes with improved oxygen retention and delayed phase degradations. *Nano Lett.* **2021**, *21*, 9797–9804. [CrossRef] [PubMed]
281. Van den Bergh, W.; Karger, L.; Murugan, S.; Janek, J.; Kondrakov, A.; Brezesinski, T. Single crystal layered oxide cathodes: The relationship between particle size, rate capability, and stability. *ChemElectroChem* **2023**, *10*, e202300165. [CrossRef]
282. Ni, L.; Zhang, S.; Di, A.; Deng, W.; Zou, G.; Hou, H.; Ji, X. A comparative investigation of single crystal and polycrystalline Ni-rich layered cathodes. *Energy Environ. Mater.* **2022**, *12*, 2201510.
283. Zhou, X.; Wang, X.; Xu, Z.; Wang, Q.; Lu, C.; Ma, R.; Zheng, Y.; Ruan, M.; Mao, Q.; Xu, J.; et al. Facile ball-milling synthesis of pseudo-single-crystalline nickel-rich layered oxide cathodes towards long-lifespan lithium-ion batteries. *J. Electron. Mater.* **2024**, *53*, 7355–7366. [CrossRef]
284. Leng, J.; Wang, J.; Peng, W.; Tang, Z.; Xu, S.; Liu, Y.; Wang, J. Highly-dispersed submicrometer single-crystal nickel-rich layered cathode: Spray synthesis and accelerated lithium-ion transport. *Small* **2021**, *17*, e2006869. [CrossRef]
285. Zhang, X.; Liu, Y.; Wang, M.; Guo, Z.; Cao, L.; Xiao, Y.; Chen, L.; Cheng, Y.-J.; Xia, Y. Simultaneous enhancement of ordered layered structure and inhibition of micro-cracks via porous structure to improve stability for Ni-rich cathode. *J. Energy Storage* **2024**, *76*, 109936. [CrossRef]
286. Chen, J.; Feng, S.; Deng, J.; Zhou, Y. Insights into the porosity and radial structure for precursor of Ni-rich $\text{LiNi}_{0.9}\text{Co}_{0.05}\text{Mn}_{0.05}\text{O}_2$ cathode materials. *Chem. Engin. Sci.* **2025**, *304*, 121092. [CrossRef]
287. Zou, K.; Xie, S.; Jiang, M.; Wang, P.; Ning, T.; Tan, L.; Li, H.; Zhou, Y.; Wang, W.; Li, L. Insights into the precursor specific surface area for engineering Co-free Ni-rich cathodes with tailororable properties. *Chem. Eng. J.* **2024**, *483*, 149189. [CrossRef]
288. Song, S.H.; Kim, H.S.; Hong, S.; Jeon, H.; Lim, J.; Jung, Y.H.; Ahn, H.; Jang, J.D.; Kim, M.-H.; Seo, J.H.; et al. Toward a nanoscale-defect-free Ni-rich layered oxide Cathode through Regulated pore evolution for long-lifespan Li rechargeable batteries. *Adv. Func. Mater.* **2024**, *34*, 2306654. [CrossRef]
289. Lv, F.; Zhang, Y.; Wu, M.; Gu, Y. A molten-salt method to synthesize ultrahigh-nickel single-crystalline $\text{LiNi}_{0.92}\text{Co}_{0.06}\text{Mn}_{0.02}\text{O}_2$ with superior electrochemical performance as cathode material for lithium-ion batteries. *Small* **2022**, *18*, 2201946. [CrossRef]
290. Zhou, W.; Huang, H.; Liu, X.; Gao, J.; Hao, S.; Yang, Y.; Qiu, J. Perspective on the preparation methods of single crystalline high nickel oxide cathode materials. *Adv. Energy Mater.* **2023**, *13*, 2300378. [CrossRef]
291. Yoo, Y.-W.; Kang, C.-Y.; Kim, H.-K.; Lee, J.-K.; Kumar, R.V.; Kim, K.-N.; Yoon, J.-R.; Lee, S.-H. Enhanced structure/interfacial properties of single-crystal Ni-rich $\text{LiNi}_{0.92}\text{Co}_{0.04}\text{Mn}_{0.04}\text{O}_2$ cathodes synthesized via LiCl-NaCl molten-salt method. *Energy Environ. Mater.* **2025**, *8*, e12778. [CrossRef]
292. Kim, S.; Park, K. Electrode design to mitigate the kinetic issue of cathodes in high energy lithium-ion batteries. *J. Power Sources* **2022**, *547*, 231916. [CrossRef]
293. Guo, F.; Xie, Y.; Zhang, Y. Low-temperature strategy to synthesize single-crystal $\text{LiNi}_{0.8}\text{Co}_{0.1}\text{Mn}_{0.1}\text{O}_2$ with enhanced cycling performances as cathode material for lithium-ion batteries. *Nano Res.* **2022**, *15*, 2052–2059. [CrossRef]
294. Lee, W.; Lee, S.; Lee, E.; Choi, M.; Thangavel, R.; Lee, Y.; Yoon, W.-S. Destabilization of the surface structure of Ni-rich layered materials by water-washing process. *Energy Storage Mater.* **2022**, *44*, 441–451. [CrossRef]
295. Ryu, H.-H.; Lim, H.-W.; Lee, S.G.; Sun, Y.-K. Near-surface reconstruction in Ni-rich layered cathodes for high-performance lithium-ion batteries. *Nat. Energy* **2024**, *9*, 47–56. [CrossRef]
296. Hu, B.-R.; Yuan, Y.-Y.; Wang, Y.-C.; Xiong, X.-H. Simultaneously enhanced electrochemical performance and air stability of Ni-rich cathode with a modified washing process. *Rare Met.* **2023**, *43*, 87–97. [CrossRef]
297. Wang, R.; Li, Q.; Wang, F.; Ding, J.; An, B.; Rua, J.; Sun, D.; Fang, F.; Wang, F. One-step molten-salt-assisted approach for direct preparation and regeneration of $\text{LiNi}_{0.6}\text{Co}_{0.2}\text{Mn}_{0.2}\text{O}_2$ cathode. *Small* **2024**, *20*, 2400762. [CrossRef]
298. Guo, Z.; Jian, Z.; Zhang, S.; Feng, Y.; Kou, W.; Ji, H.; Yang, G. The effect of Ni oxidation state on the crystal structure and electrochemical properties of $\text{LiNi}_{0.8}\text{Co}_{0.1}\text{Mn}_{0.1}\text{O}_2$ cathode material for highly reversible lithium storage. *J. Alloys Compd.* **2021**, *882*, 160642. [CrossRef]
299. Gao, C.; Liu, H.; Zhang, J.; Guo, Z.; Huang, H. Simplified crystal grain boundary engineering of solid electrolyte-infused $\text{LiNi}_{0.5}\text{Mn}_{1.5}\text{O}_4$ cathodes for high cycling stability lithium-ion batteries. *J. Power Sources* **2023**, *582*, 233434. [CrossRef]
300. Wu, Y.; Wu, H.; Deng, J.; Han, Z.; Xiao, X.; Wang, L.; Chen, Z.; Deng, Y.; He, X. Insight of synthesis of single crystal Ni-rich $\text{LiNi}_{1-x-y}\text{Co}_x\text{Mn}_y\text{O}_2$ cathodes. *Adv. Energy Mater.* **2024**, *14*, 2303758. [CrossRef]
301. Tayal, A.; Barai, P.; Zhong, H.; Kahvecioglu, O.; Wang, X.; Pupek, K.Z.; Ma, L.; Ehrlich, N.; Srinivasan, V.; Qu, X.; et al. In situ insights into cathode calcination for predictive synthesis: Kinetic crystallization of LiNiO_2 from hydroxides. *Adv. Mater.* **2024**, *36*, 2312027. [CrossRef]
302. Huang, H.; Zhu, H.; Gao, J.; Wang, J.; Shao, M.; Zhou, W. Grain-growth inhibitor with Three-section-sintering for highly dispersed single-crystal NCM90 cubes. *Angew. Chem. Int. Ed.* **2024**, *136*, e202314457. [CrossRef]
303. Choi, J.H.; Embleton, T.J.; Ko, K.; Yang, H.; Son, Y.; Park, J.; Lee, S.; Oh, P. A perspective on the requirements of Ni-rich cathode surface modifications for application in lithium-ion batteries and all-solid-state lithium-ion batteries. *ChemElectroChem* **2024**, *11*, e202300705. [CrossRef]

304. Yu, H.; Pei, D. A review of the origin, adverse influence and modification method of residual surface lithium in Ni-rich cathodes. *Int. J. Electrochem. Sci.* **2024**, *19*, 100391. [[CrossRef](#)]
305. Han, B.; Key, B.; Lipton, A.S.; Vaughey, J.T.; Hughes, B.; Trevey, J.; Dogan, F. Influence of coating protocols on alumina-coated cathode material: Atomic layer deposition versus wet-chemical coating. *J. Electrochem. Soc.* **2019**, *166*, A3679–A3684. [[CrossRef](#)]
306. Cheng, X.; Zheng, J.; Lu, J.; Li, Y.; Yan, P.; Zhang, Y. Realizing superior cycling stability of Ni-rich layered cathode by combination of grain boundary engineering and surface coating. *Nano Energy* **2019**, *62*, 30–37. [[CrossRef](#)]
307. Sim, S.-J.; Lee, S.-H.; Jin, B.-S.; Kim, H.-S. Use of carbon coating on $\text{LiNi}_{0.8}\text{Co}_{0.1}\text{Mn}_{0.1}\text{O}_2$ cathode material for enhanced performances of lithium-ion batteries. *Sci. Rep.* **2020**, *10*, 11114. [[CrossRef](#)]
308. Chen, G.; Peng, B.; Han, R.; Chen, N.; Wang, Z.; Wang, Q. A robust carbon coating strategy toward Ni-rich lithium cathodes. *Ceram. Int.* **2020**, *46*, 20985. [[CrossRef](#)]
309. Qiu, Y.; Wei, X.; Liu, N.; Song, Y.; Bi, L.; Long, X.; Chen, Z.; Wang, S.; Liao, J. Plasma-induced amorphous N-nano carbon shell for improving structural stability of $\text{LiNi}_{0.8}\text{Co}_{0.1}\text{Mn}_{0.1}\text{O}_2$ cathode. *Electrochim. Acta* **2022**, *428*, 140973. [[CrossRef](#)]
310. Jan, S.S.; Nurgul, S.; Shi, X.; Xia, H.; Pang, H. Improvement of chemical performance of $\text{LiNi}_{0.8}\text{Co}_{0.1}\text{Mn}_{0.1}\text{O}_2$ cathode material by graphene nanosheets modification. *Electrochim. Acta* **2014**, *149*, 86–93. [[CrossRef](#)]
311. Du, Z.; Li, J.; Wood, M.; Mao, C.; Daniel, C.; Wood, D.L. Three-dimensional conductive network formed by carbon nanotubes in aqueous processed NMC electrode. *Electrochim. Acta* **2018**, *270*, 54–61. [[CrossRef](#)]
312. Wu, Z.; Han, X.; Zheng, J.; Wei, Y.; Qiao, R.; Shen, F.; Dai, J.; Hu, L.; Xu, K.; Lin, Y.; et al. Depolarized and fully active cathode based on $\text{Li}(\text{Ni}_{0.5}\text{Co}_{0.2}\text{Mn}_{0.3})\text{O}_2$ embedded in carbon nanotube network for advanced batteries. *Nano Lett.* **2014**, *14*, 4700–4706. [[CrossRef](#)] [[PubMed](#)]
313. Kang, J.; Pham, H.Q.; Kang, D.-H.; Park, H.-Y.; Song, S.-W. Improved rate capability of highly loaded carbon fiber-interwoven $\text{LiNi}_{0.6}\text{Co}_{0.2}\text{Mn}_{0.2}\text{O}_2$ cathode material for high-power Li-ion batteries. *J. Alloys Compd.* **2016**, *657*, 464–471. [[CrossRef](#)]
314. Ning, R.; Yuan, K.; Zhang, K.; Shen, C.; Xie, K. A scalable snowballing strategy to construct uniform rGO-wrapped $\text{LiNi}_{0.8}\text{Co}_{0.1}\text{Mn}_{0.1}\text{O}_2$ with enhanced processability and electrochemical performance. *Appl. Surf. Sci.* **2021**, *542*, 148663. [[CrossRef](#)]
315. Poursalehi, F.; Javanbakht, M.; Daryakenari, A.A.; Gao, B. Preparing a binder-free cathode composed of NMC811/sulfonated reduced graphene oxide sheets/carbon black via in-situ electrophoretic deposition to enhance cycleability of Li-ion batteries. *J. Electroanal. Chem.* **2024**, *971*, 118593. [[CrossRef](#)]
316. She, S.; Zhou, Y.; Hong, Z.; Huang, Y.; Wu, Y. Surface coating of NCM-811 cathode materials with g-C₃N₄ for enhanced electrochemical performance. *ACS Omega* **2022**, *7*, 24851–24857. [[CrossRef](#)]
317. Park, C.W.; Lee, J.-H.; Seo, J.K.; Jo, W.Y.; Whang, D.; Hwang, S.M.; Kim, Y.-J. Graphene collage on Ni-rich layered oxide cathodes for advanced lithium-ion batteries. *Nat. Commun.* **2021**, *12*, 2145. [[CrossRef](#)]
318. Ryu, H.H.; Lim, H.-W.; Kang, G.-C.; Park, N.-Y.; Sun, Y.-K. Long-lasting Ni-rich NCMA cathodes via simultaneous microstructural refinement and surface modification. *ACS Energy Lett.* **2023**, *8*, 1354–1361. [[CrossRef](#)]
319. Cho, W.; Kim, S.-M.; Song, J.-H.; Yim, T.; Kim, J.-S.; Kim, Y.-J. Improved electrochemical and thermal properties of nickel rich $\text{LiNi}_{0.6}\text{Co}_{0.2}\text{Mn}_{0.2}\text{O}_2$ cathode materials by SiO₂ coating. *J. Power Sources* **2015**, *282*, 45–50. [[CrossRef](#)]
320. Han, B.; Xu, S.; Zhao, S.; Lin, G.-X.; Feng, Y.-Z.; Chen, L.-B.; Ivey, G.-D.; Wang, P.; Wei, W.-F. Enhancing the structural stability of Ni-rich layered oxide cathodes with a preformed Zr-concentrated defective nanolayer. *ACS Appl. Mater. Interfaces* **2018**, *10*, 39599–39607. [[CrossRef](#)] [[PubMed](#)]
321. Yao, L.; Liang, F.; Jin, J.; Chowdari, B.V.R.; Yang, J.; Wen, Z. Improved electrochemical property of Ni-rich $\text{LiNi}_{0.6}\text{Co}_{0.2}\text{Mn}_{0.2}\text{O}_2$ cathode via in-situ ZrO₂ coating for high energy density lithium-ion batteries. *Chem. Eng. J.* **2020**, *389*, 124403. [[CrossRef](#)]
322. Kitsche, D.; Tang, Y.; Hemmelmann, H.; Walther, F.; Bianchini, M.; Kondrakov, A.; Janek, J.; Brezesinski, T. Atomic layer deposition derived zirconia coatings on Ni-rich cathodes in solid-state batteries: Correlation between surface constitution and cycling performance. *Small Sci.* **2023**, *3*, 2200073. [[CrossRef](#)]
323. Chen, Y.; Zhang, Y.; Chen, B.; Wang, Z.; Lu, C. An approach to application for $\text{LiNi}_{0.6}\text{Co}_{0.2}\text{Mn}_{0.2}\text{O}_2$ cathode material at high cutoff voltage by TiO₂ coating. *J. Power Sources* **2014**, *256*, 20–27. [[CrossRef](#)]
324. Li, W.-W.; Zhang, X.-J.; Si, J.-J.; Yang, J.; Sun, X.-Y. TiO₂-coated $\text{LiNi}_{0.9}\text{Co}_{0.08}\text{Al}_{0.02}\text{O}_2$ cathode materials with enhanced cycle performance for Li-ion batteries. *Rare Met.* **2021**, *40*, 1719–1726. [[CrossRef](#)]
325. Wang, W.-C.; Lee, C.-H.; Yu, D.; Kondo, Y.; Miyahara, Y.; Abe, T.; Miyazaki, K. Effects of a solid solution outer layer of TiO₂ on the surface and electrochemical properties of $\text{LiNi}_{0.6}\text{Co}_{0.2}\text{Mn}_{0.2}\text{O}_2$ cathodes for lithium-ion batteries through the use of thin-film electrodes. *ACS Appl. Energy Mater.* **2022**, *5*, 5117–5126. [[CrossRef](#)]
326. Su, S.; Zheng, W.; Qin, Y.; Wu, J.; Ke, J.; Sun, Y.; Lin, X. Controllable construction of CeO₂ shells with a nanoscale thickness to enhance the high-voltage electrochemical performance of Ni-rich cathodes. *ACS Appl. Nano Mater.* **2025**, *8*, 3039–3049. [[CrossRef](#)]
327. Arumugam, R.S.; Ma, L.; Li, J.; Xia, X.; Paulsen, J.M.; Dahn, J.R. Special synergy between electrolyte additives and positive electrode surface coating to enhance the performance of $\text{Li}[\text{Ni}_{0.6}\text{Mn}_{0.2}\text{Co}_{0.2}]\text{O}_2$ /graphite cells. *J. Electrochem. Soc.* **2016**, *163*, A2531–A2538. [[CrossRef](#)]

328. Kong, J.Z.; Chen, Y.; Cao, Y.Q.; Wang, Q.-Z.; Li, A.-D.; Li, H.; Zhou, F. Enhanced electrochemical performance of Ni-rich $\text{LiNi}_{0.6}\text{Co}_{0.2}\text{Mn}_{0.2}\text{O}_2$ coated by molecular layer deposition derived dual-functional $\text{C-Al}_2\text{O}_3$ composite coating. *J. Alloys Compd.* **2019**, *799*, 89–98. [CrossRef]
329. Neudeck, S.; Strauss, F.; Garcia, G.; Wolf, H.; Janek, J.; Hartmann, P.; Brezesinski, T. Room temperature, liquid-phase Al_2O_3 surface coating approach for Ni-rich layered oxide cathode material. *Chem. Commun.* **2019**, *55*, 2174–2177. [CrossRef]
330. Liu, W.; Li, X.F.; Xiong, D.B.; Hao, Y.C.; Li, J.W.; Kou, H.R.; Yan, B.; Li, D.J.; Lu, S.G.; Koo, A.; et al. Significantly improving cycling performance of cathodes in lithium-ion batteries: The effect of Al_2O_3 and LiAlO_2 coatings on $\text{LiNi}_{0.6}\text{Co}_{0.2}\text{Mn}_{0.2}\text{O}_2$. *Nano Energy* **2018**, *44*, 111–120. [CrossRef]
331. Wu, Y.Q.; Li, M.L.; Wahyudi, W.; Sheng, G.; Miao, X.H.; Anthopoulos, T.D.; Huang, K.W.; Li, Y.X.; Lai, Z.P. Performance and stability improvement of layered NCM lithium-ion batteries at high voltage by a microporous Al_2O_3 sol–gel coating. *ACS Omega* **2019**, *4*, 13972–13980. [CrossRef] [PubMed]
332. Zhu, W.; Huang, X.; Liu, T.; Xie, Z.; Wang, Y.; Tian, K.; Bu, L.; Wang, H.; Gao, L.; Zhao, J. Ultrathin Al_2O_3 coating on $\text{LiNi}_{0.8}\text{Co}_{0.1}\text{Mn}_{0.1}\text{O}_2$ cathode material for enhanced cycle ability at extended voltage ranges. *Coatings* **2019**, *9*, 92. [CrossRef]
333. Hu, D.; Du, F.; Cao, H.; Zhou, Q.; Sun, P.; Xu, T.; Mei, C.; Hao, Q.; Fan, Z.; Zheng, J. An effective strategy to control thickness of Al_2O_3 coating layer on nickel-rich cathode materials. *J. Electroanal. Chem.* **2021**, *880*, 114910. [CrossRef]
334. Anh, V.T.; Vu, H.-A.T.; Nguyen, V.; Nang, H.X.; Do, L.T.; Dao, V.-D.; Vu, N.H. Enhancing electrochemical performance of Ni-rich cathodes for Li-ion batteries through spatial atomic layer deposition of ZnO coatings. *Mater. Chem. Phys.* **2025**, *336*, 130544. [CrossRef]
335. Ma, F.; Wu, Y.; Wei, G.; Qiu, S.; Qu, J. Enhanced electrochemical performance of $\text{LiNi}_{0.8}\text{Co}_{0.1}\text{Mn}_{0.1}\text{O}_2$ cathode via wet-chemical coating of MgO . *J. Solid State Electrochem.* **2019**, *23*, 2213–2224. [CrossRef]
336. Liu, W.; Gao, F.; Zang, Y.; Qu, J.; Xu, J.; Ji, S.; Huo, Y.; Qiu, J. Boosting cycle stability of NMC811 cathode material via 2D Mg-Al-LDO nanosheet coating for lithium-ion battery. *J. Alloys Compd.* **2021**, *867*, 159079. [CrossRef]
337. Mohanty, D.; Dahlberg, K.; King, D.-M.; David, L.-A.; Sefat, A.-S.; Wood, D.-L.; Daniel, C.; Dhar, S.; Mahajan, V.; Lee, M.; et al. Modification of Ni-rich FCG NMC and NCA cathodes by atomic layer deposition: Preventing surface phase transitions for high-voltage lithium-ion batteries. *Sci. Rep.* **2016**, *6*, 26532. [CrossRef]
338. Zhang, X.; Zhang, P.; Zeng, T.; Yu, Z.; Qu, X.; Peng, X.; Zhou, Y.; Duan, X.; Dou, A.; Su, M.; et al. Improving the structure stability of $\text{LiNi}_{0.8}\text{Co}_{0.15}\text{Al}_{0.05}\text{O}_2$ by double modification of tantalum surface coating and doping. *ACS Appl. Energy Mater.* **2021**, *4*, 8641–8652. [CrossRef]
339. Xia, Y.; Chen, A.; Wang, K.; Mao, Q.; Huang, H.; Zhang, J.; He, X.; Gan, Y.; Xiao, Z.; Zhang, W. Industrial modification comparison of Ni-Rich cathode materials towards enhanced surface chemical stability against ambient air for advanced lithium-ion batteries. *Chem. Eng. J.* **2022**, *450*, 138382. [CrossRef]
340. Chen, J.; Wang, X.L.; Jin, E.M.; Moon, S.-G.; Jeong, S.M. Optimization of B_2O_3 coating process for NCA cathodes to achieve long-term stability for application in lithium-ion batteries. *Energy* **2021**, *222*, 119913. [CrossRef]
341. Cui, X.; Ai, L.; Mao, L.; Xie, Y.; Liang, Y.; Zhang, N.; Feng, Y.; Wang, S.; Li, S. Enhanced electrochemical properties of $\text{LiNi}_{0.6}\text{Co}_{0.2}\text{Mn}_{0.2}\text{O}_2$ cathode material by the diffusional Al_2O_3 coating layer. *Ionics* **2019**, *25*, 411–419. [CrossRef]
342. Negi, R.S.; Elm, M.T. Reproducible long-term cycling data of Al_2O_3 coated $\text{LiNi}_{0.70}\text{Co}_{0.15}\text{Mn}_{0.15}\text{O}_2$ cathodes for lithium-ion batteries. *Sci. Data* **2022**, *9*, 127. [CrossRef]
343. Ahangari, M.; Xia, F.; Szalai, B.; Zhou, M.; Luo, H. Advancing lithium-ion batteries' electrochemical performance: Ultrathin alumina coating on $\text{Li}(\text{Ni}_{0.8}\text{Co}_{0.1}\text{Mn}_{0.1})\text{O}_2$ cathode materials. *Micromachines* **2024**, *15*, 894. [CrossRef]
344. Woo, S.G.; Han, J.H.; Kim, K.J.; Kim, J.-H.; Yu, J.-S.; Kim, Y.-J. Surface modification by sulfated zirconia on high-capacity nickel-based cathode materials for Li-ion batteries. *Electrochim. Acta* **2015**, *153*, 115–121. [CrossRef]
345. Wang, Y.; Meng, D.; Li, Z.; Huan, Y.; Cheng, G.; Ren, Z.; Liu, X.; Wang, K.; Chen, L.; Gu, H.; et al. Breaking the cycle of heterogeneous degradation: Surface-targeted protection for Ni-rich cathodes in practical high-energy batteries. *ACS Energy Lett.* **2025**, *10*, 1457–1465. [CrossRef]
346. Cheng, X.; Yan, T.; Qin, D.; Leng, L.; Tian, J.; Sun, T.; Lu, J.; Liu, X.; Zhang, Y. Optimizing annealing strategy to achieve effective grain boundary modification with aluminum oxide for stable cycling Ni-rich cathodes. *ACS Appl. Mater. Interfaces* **2025**, *17*, 13988–13996. [CrossRef]
347. Mitra, S.; Mudiyanselage, T.R.; Wang, X.; Lohar, G.; Dubal, D. Bolstering the rate performance of Co-free Ni-rich layered oxide cathode through a rapid heating method. *Batter. Supercaps* **2025**, *e202400782*. [CrossRef]
348. Meng, K.; Wang, Z.; Guo, H.; Li, X.; Wang, D. Improving the cycling performance of $\text{LiNi}_{0.8}\text{Co}_{0.1}\text{Mn}_{0.1}\text{O}_2$ by surface coating with Li_2TiO_3 . *Electrochim. Acta* **2016**, *211*, 822–831. [CrossRef]
349. Hou, L.; Liu, Q.; Mu, D.; Li, L.; Wu, F.; Chen, R. Surface reconstruction reduces internal stress of Ni-rich cathode particles. *Small* **2025**, *21*, 2406495. [CrossRef] [PubMed]
350. Kong, J.-Z.; Wang, S.-S.; Tai, G.-A.; Zhu, L.; Wang, L.-G.; Zhai, H.-F.; Wu, D.; Li, A.-D.; Li, H. Enhanced electrochemical performance of $\text{LiNi}_{0.5}\text{Co}_{0.2}\text{Mn}_{0.3}\text{O}_2$ cathode material by ultrathin ZrO_2 coating. *J. Alloys Compd.* **2016**, *657*, 593–600. [CrossRef]

351. Schipper, F.; Bouzaglo, H.; Dixit, M.; Erickson, E.M.; Weigel, T.; Talianker, M.; Grinblat, J.; Burstein, L.; Schmidt, M.; Lampert, J.; et al. From Surface ZrO₂ coating to bulk Zr doping by high temperature annealing of nickel-rich lithiated oxides and their enhanced electrochemical performance in lithium-ion batteries. *Adv. Energy Mater.* **2018**, *8*, 1701682. [CrossRef]
352. Guan, P.; Min, J.; Chen, F.; Zhang, S.; Hu, L.; Ma, Z.; Han, Z.; Zhou, L.; Jia, H.; Liu, Y.; et al. Enhancing the electrochemical properties of nickel-rich cathode by surface coating with defect-rich strontium titanate. *ACS Appl. Mater. Interfaces* **2023**, *15*, 29308–29320. [CrossRef]
353. Lou, F.; Xie, Q.; Luo, X.; Xie, Y.; Wang, M.; Hao, H.; Wang, Z.; Yang, L.; Wang, G.; Chen, J.; et al. Preventing structural collapse and thermal runaway to improve the electrochemical performance and safety of LiNi_{0.8}Co_{0.1}Mn_{0.1}O₂ by a negative-thermal-expansion material of Al₂(WO₃)₄. *Ind. Eng. Chem. Res.* **2022**, *61*, 4588–4600. [CrossRef]
354. Wustrow, A.; Hancock, J.C.; Incorvati, J.T.; Vaughey, J.T.; Poeppelmeier, K.R. Effect of fluoride doping on lithium diffusivity in layered molybdenum oxide. *ACS Appl. Energy Mater.* **2019**, *2*, 2080–2086. [CrossRef]
355. Salehi, M.; Maleksaeedi, S.; Bin Sapari, M.A.; Nai, M.L.S.; Meenashisundaram, G.K.; Gupta, M. Additive manufacturing of magnesium–zinc–zirconium (ZK) alloys via capillary-mediated binderless three-dimensional printing. *Mater. Des.* **2019**, *169*, 107683. [CrossRef]
356. Park, S.-B.; Kang, C.-Y.; Hwang, D.-Y.; Yoo, Y.-W.; Park, H.-J.; Park, J.-H.; Kim, H.-S.; Lee, S.-H. Effect of MoO₃ surface coating on electrochemical performances of LiNi_{0.8}Co_{0.1}Mn_{0.1}O₂ cathode. *Current Appl. Phys.* **2022**, *44*, 1–5. [CrossRef]
357. Yuan, Y.; Wang, L.; Sun, Q.; Nie, W.; Chang, L.; Chen, S.; Cheng, H. Architecting versatile NiFe₂O₄ coating for enhancing structural stability and rate capability of layered Ni-rich cathodes. *Chem. Eng. J.* **2023**, *470*, 144210. [CrossRef]
358. Sun, Q.; Liu, X.; Chang, L.; Liu, Y.; Zhang, J.; Yuan, Y.; Lu, X.; Cheng, H. Promoting durability of Ni-rich layered oxide via inverse spinel NiFe₂O₄ interface layer for high-voltage lithium-ion batteries. *ACS Appl. Energy Mater.* **2024**, *7*, 6236–6247. [CrossRef]
359. Wang, L.; Mu, D.; Wu, B.; Yang, G.; Gai, L.; Liu, Q.; Fan, Y.; Peng, Y.; Wu, F. Enhanced electrochemical performance of lithium metasilicate-coated LiNi_{0.6}Co_{0.2}Mn_{0.2}O₂ Ni-rich cathode for Li-ion batteries at high cutoff voltage. *Electrochim. Acta* **2016**, *222*, 806–813. [CrossRef]
360. Qu, X.; Huang, H.; Wan, T.; Hu, L.; Yu, Z.; Liu, Y.; Dou, A.; Zhou, Y.; Su, M.; Peng, X.; et al. An integrated surface coating strategy to enhance the electrochemical performance of nickel-rich layered cathodes. *Nano Energy* **2022**, *91*, 16665. [CrossRef]
361. Zhou, X.; Chen, A.; Lu, C.; Ma, R.; Fang, R.; Gan, Y.; Wang, G.; Xu, J.; Mao, Q.; Lu, X.; et al. Ultra-low-dose Nb₂O₅ coating promotes electrochemical kinetics and rate capability of Ni-rich oxide cathode. *J. Solid State Electrochem.* **2024**, 1–10. [CrossRef]
362. Ahaliabadeh, Z.; Miikkulainen, V.; Mänttimäki, M.; Mousavihashemi, S.; Lahtinen, J.; Lide, Y.; Yang, H.; Mizohata, K.; Kankaanpää, T.; Kallio, T. Understanding the stabilizing effects of nanoscale metal oxide and Li-metal oxide coatings on lithium-ion battery positive electrode materials. *ACS Appl. Mater. Interfaces* **2021**, *13*, 42773–42790. [CrossRef] [PubMed]
363. Sun, H.H.; Ryu, H.-H.; Kim, U.-H.; Weeks, J.A.; Heller, A.; Sun, Y.-K.; Mullins, C.B. Beyond doping and coating: Prospective strategies for stable high-capacity layered Ni-rich cathodes. *ACS Energy Lett.* **2020**, *5*, 1136–1146. [CrossRef]
364. Lee, D.-J.; Scrosati, B.; Sun, Y.-K. Ni₃(PO₄)₂-coated Li[Ni_{0.8}Co_{0.15}Al_{0.05}]O₂ lithium battery electrode with improved cycling performance at 55 °C. *J. Power Sources* **2011**, *196*, 7742–7746. [CrossRef]
365. Kim, T.; Goh, M.S.; Moon, H.; Shin, H.; Lee, J.; Jeong, H.; Joo, S.W.; Kim, Y.S.; Im, Y.; Kang, M. Enhanced battery capacity and cycle life due to suppressed side reactions on the surface of Ni-rich LiNi_{0.8}Co_{0.1}Mn_{0.1}O₂ cathode materials coated with Co₃(PO₄)₂. *J. Colloid Int. Sci.* **2024**, *670*, 729–741. [CrossRef]
366. Huang, B.; Li, X.; Wang, Z.; Guo, H. A facile process for coating amorphous FePO₄ onto LiNi_{0.8}Co_{0.15}Al_{0.05}O₂ and the effects on its electrochemical properties. *Mater. Lett.* **2014**, *131*, 210–213. [CrossRef]
367. Zha, G.; Luo, Y.; Hu, N.; Ouyang, C.; Hou, H. Surface modification of the LiNi_{0.8}Co_{0.1}Mn_{0.1}O₂ cathode material by coating with FePO₄ with a yolk–shell structure for improved electrochemical performance. *ACS Appl. Mater. Interfaces* **2020**, *12*, 36046–36053. [CrossRef]
368. Qi, R.; Shi, J.; Zhang, X.; Zeng, X. Improving the stability of LiNi_{0.80}Co_{0.15}Al_{0.05}O₂ by AlPO₄ nanocoating for lithium-ion batteries. *Sci. China Chem.* **2017**, *60*, 1230–1235. [CrossRef]
369. Wu, Y.; Cheng, W.; Hao, S.; Li, L.; Ran, Q.; Liu, L.; Ji, Y.; Huo, J.; Liu, X. Utilizing dual functions of LaPO₄ to enhance the electrochemical performance of LiNi_{0.87}Co_{0.09}Al_{0.04}O₂ cathode material. *Nanotechnology* **2023**, *34*, 075706. [CrossRef] [PubMed]
370. Zou, P.; Lin, Z.; Fan, M.; Wang, F.; Liu, Y.; Xiong, X. Facile and efficient fabrication of Li₃PO₄-coated Ni-rich cathode for high-performance lithium-ion battery. *Appl. Surf. Sci.* **2020**, *504*, 144506. [CrossRef]
371. Liang, J.; Zhu, Y.; Li, X.; Luo, J.; Deng, S.; Zhao, Y.; Sun, Y.; Wu, D.; Hu, Y.; Li, W.; et al. A gradient oxy-thiophosphate-coated Ni-rich layered oxide cathode for stable all-solid-state Li-ion batteries. *X. Sun. Nat. Commun.* **2023**, *14*, 146. [CrossRef]
372. Park, H.G.; Kwon, D.; Cho, W.; Yoon, S.; Kim, D.; Park, K. Correlation between grain boundary coating and chemomechanics in Ni-rich layered Li cathodes. *Chem. Eng. J.* **2023**, *452*, 139442. [CrossRef]
373. Luo, Z.; Ding, C.; Wang, W.; Hu, G.; Du, K.; Cao, Y.; Peng, Z. Improving storage performance and lattice oxygen stability of single crystal LiNi_{0.925}Co_{0.03}Mn_{0.045}O₂ by integrating utilization of surface residual lithium and lattice modulation. *Appl. Surf. Sci.* **2024**, *665*, 160238. [CrossRef]

374. Chen, Z.; Kim, G.T.; Guang, Y.; Bresser, D.; Diemant, Y.; Huang, M.; Copley, R.; Behm, J.; Passerini, S.; Shen, Z. Manganese phosphate coated Li[Ni_{0.6}Co_{0.2}Mn_{0.2}]O₂ cathode material: Towards superior cycling stability at elevated temperature and high voltage. *J. Power Sources* **2018**, *402*, 263–271. [CrossRef]
375. Peng, Z.-D.; Huang, M.; Wang, W.-G.; Du, K.; Guan, D.-C.; Hu, G.; Cao, Y.-B. Enhancing the structure and interface stability of LiNi_{0.83}Co_{0.12}Mn_{0.05}O₂ cathode material for Li-ion batteries via facile CeP₂O₇ coating. *ACS Sustain. Chem. Eng.* **2022**, *10*, 4881–4893. [CrossRef]
376. Min, K.; Park, K.; Park, S.Y.; Seo, S.W.; Choi, B.; Cho, E. Improved electrochemical properties of LiNi_{0.91}Co_{0.06}Mn_{0.03}O₂ cathode material via Li-reactive coating with metal phosphates. *Sci. Rep.* **2017**, *7*, 7151. [CrossRef]
377. Peng, F.; Zhang, L.; Yang, G.; Li, Y.; Pan, Q.; Li, Y.; Hu, S.; Zheng, F.; Wang, H.; Li, Q. Nanoscale surface modification to suppress capacity fade of Ni-rich layered oxide material at high cut-off voltage. *Chem. Eng. J.* **2023**, *451*, 138911. [CrossRef]
378. Zeng, L.; Shi, K.; Qiu, B.; Liang, H.; Li, J.; Zhao, W.; Li, S.; Zhang, W.; Liu, Z.; Liu, Q. Hydrophobic surface coating against chemical environmental instability for Ni-rich layered oxide cathode materials. *Chem. Eng. J.* **2022**, *437*, 135276. [CrossRef]
379. Huang, Y.; Li, P.-Y.; Wei, H.-X.; Luo, Y.-H.; Tang, L.-B.; Chen, H.-Z.; Zhang, X.; Zheng, J. Suppress moisture sensitivity of Ni-rich cathode materials by bioinspired self-assembly hydrophobic layer. *Chem. Eng. J.* **2023**, *477*, 146850. [CrossRef]
380. Jo, M.; Oh, P.; Kim, J.; Choi, J.-H.; Kim, S.; Ha, S.; Son, Y. Electrochemical lithium storage performance at high voltage and temperature of LiNi_{0.6}Co_{0.2}Mn_{0.2}O₂ cathode for Lithium-ion batteries by facile Mn₃(PO₄)₂ dry coating. *Appl. Surf. Sci.* **2013**, *613*, 156018. [CrossRef]
381. Yang, C.; Shao, R.; Mi, Y.; Shen, L.; Zhao, B.; Wang, Q.; Wu, K.; Lui, W.; Gao, P.; Zhou, H. Stable interstitial layer to alleviate fatigue fracture of high nickel cathode for lithium-ion batteries. *J. Power Sources* **2018**, *376*, 200–206. [CrossRef]
382. Ahn, J.; Jang, E.K.; Yoon, S.; Lee, S.-J.; Sung, S.-J.; Kim, D.-H.; Cho, K.Y. Ultrathin ZrO₂ on LiNi_{0.5}Mn_{0.3}Co_{0.2}O₂ electrode surface via atomic layer deposition for high-voltage operation in lithium-ion batteries. *Appl. Surf. Sci.* **2019**, *484*, 701–709. [CrossRef]
383. Sun, X.; Wang, L.; Ma, J.; Yu, X.; Zhang, S.; Zhou, X.; Cui, G. A bifunctional chemomechanics strategy to suppress electrochemomechanical failure of Ni-rich cathodes for all-solid-state lithium batteries. *ACS Appl. Mater. Interfaces* **2022**, *14*, 17674–17681. [CrossRef]
384. Jeyakumar, J.; Wu, Y.; Wu, S.; Jose, R.; Yang, C. Surface-modified quaternary layered Ni-rich cathode materials by Li₂ZrO₃ for improved electrochemical performance for high-power Li-ion batteries. *ACS Appl. Energy Mater.* **2022**, *5*, 4796–4807. [CrossRef]
385. Hu, Y.; Guo, F.; Zhu, C.; Qiu, L.; Zhou, J.; Deng, Y.; Zheng, Z.; Liu, Y.; Sun, Y.; Zhong, B.; et al. Effective and low-cost in situ surface engineering strategy to enhance the interface stability of an ultrahigh Ni-rich NCMA cathode. *ACS Appl. Mater. Interfaces* **2022**, *14*, 51835–51845. [CrossRef]
386. Qiao, Y.; Hao, R.; Shi, X.; Li, Y.; Wang, Y.; Zhang, Y.; Tang, C.; Li, G.; Wang, G.; Liu, J.; et al. Improving the cycling stability of LiNi_{0.8}Co_{0.1}Mn_{0.1}O₂ by enhancing the structural integrity via synchronous Li₂SiO₃ coating. *ACS Appl. Energy Mater.* **2022**, *5*, 4885–4892. [CrossRef]
387. Huang, X.; Zhu, W.; Yao, J.; Bu, L.; Li, X.; Tian, K.; Lu, H.; Quan, C.; Xu, S.; Xu, K.; et al. Suppressing structural degradation of Ni-rich cathode materials towards improved cycling stability enabled by a Li₂MnO₃ coating. *J. Mater. Chem. A* **2020**, *8*, 17429–17441. [CrossRef]
388. Dong, L.; Guan, X.; Zhou, Y.; Tang, S.; Chen, F. Supplying active lithium to single-crystal Li(Ni_{0.90}Co_{0.05}Mn_{0.05})_{0.98}Ta_{0.02}O₂ with Li₂MnO₃ coating served as cathode for Li-ion batteries. *Particuology* **2024**, *95*, 303–318. [CrossRef]
389. Kim, A.-Y.; Strauss, F.; Bartsch, T.; Teo, J.-H.; Janek, J.; Brezesinski, T. Effect of surface carbonates on the cyclability of LiNbO₃-coated NCM622 in all-solid-state batteries with lithium thiophosphate electrolytes. *Sci. Rep.* **2021**, *11*, 5367. [CrossRef] [PubMed]
390. Yu, H.; Wang, S.; Hu, Y.; He, G.; Quo, L.; Parkin, B.P.; Iang, H. Lithium-conductive LiNbO₃ coated high-voltage LiNi_{0.5}Co_{0.2}Mn_{0.3}O₂ cathode with enhanced rate and cyclability. *Green Energy Environ.* **2022**, *7*, 266–274. [CrossRef]
391. Liu, H.; Zhao, X.; Xie, Y.; Luo, S.; Wang, Z.; Zhu, L.; Zhang, X. Insights into capacity fading mechanism and coating modification of high-nickel cathodes in lithium-ion batteries. *ACS Appl. Mater. Interfaces* **2022**, *14*, 55491–55502. [CrossRef]
392. Zuo, J.; Wang, J.; Duan, R.; Bai, Y.; Xu, K.; Zhang, K.; Wang, J.; Zhang, K.; Yang, Z.; Li, M.; et al. Grain binding derived reinforced interfacial mechanical behavior of Ni-rich layered cathode materials. *Nano Energy* **2024**, *121*, 109214. [CrossRef]
393. Xie, J.; Sendek, A.-D.; Cubuk, E.-D.; Zhang, X.; Lu, Z.; Gong, Y.; Wu, T.; Shi, F.; Liu, W.; Reed, E.-J.; et al. Atomic layer deposition of stable LiAlF₄ lithium-ion conductive interfacial layer for stable cathode cycling. *ACS Nano* **2017**, *11*, 7019–7027. [CrossRef] [PubMed]
394. Susai, F.A.; Sclar, H.; Maiti, S.; Burstein, L.; Perkal, O.; Grinblat, J.; Taliander, M.; Ruthstein, S.; Erk, C.; Hartmann, P.; et al. Stabilized behavior of LiNi_{0.85}Co_{0.10}Mn_{0.05}O₂ cathode materials induced by their treatment with SO₂. *ACS Appl. Energy Mater.* **2020**, *3*, 3609–3618. [CrossRef]
395. Tan, X.; Peng, W.; Duan, H.; Wang, Z.; Guo, H.; Luo, G.; Yuan, R.; Li, X.; Wang, J. A scalable dry chemical method for lithium borate coating to improve the performance of LiNi_{0.90}Co_{0.06}Mn_{0.04}O₂ cathode material. *Solid State Ion.* **2022**, *28*, 2073–2082. [CrossRef]

396. Yang, J.; Li, Y.; Xi, X.; Zheng, J.; Yu, J.; He, Z. Suppressed internal intrinsic stress engineering in high-performance Ni-Rich cathode via multilayered in situ coating structure. *Energy Environ. Mater.* **2022**, *24*, 12574. [[CrossRef](#)]
397. Llanos, S.; Ahaliabadeh, Z.; Miikkulainen, V.; Kong, X.; Obrezkov, F.; Lahtinen, J.; Yao, L.; Jiang, H.; Lassi, U.; Kallio, T. Structural and interfacial stability of a coated Ni-rich layered oxide cathode at high-voltage operation. *Mater. Today Energy* **2025**, *50*, 101862. [[CrossRef](#)]
398. Byeon, Y.S.; Lee, H.B.; Hong, Y.; Kim, H.; Cho, W.; Park, M.-S. Cation-deficient Li_xWO_3 surface coating on Ni-rich cathodes materials for lithium-ion batteries. *ACS Appl. Interfaces* **2025**, *17*, 9322–9331. [[CrossRef](#)]
399. Yu, J.; Peng, J.; Huang, W.; Wang, L.; Wei, Y.; Yang, N.; Li, L. Inhibition of excessive SEI-forming and improvement of structure stability for $\text{LiNi}_{0.8}\text{Co}_{0.1}\text{Mn}_{0.1}\text{O}_2$ by Li_2MoO_4 . *Ionics* **2021**, *27*, 2867–2876. [[CrossRef](#)]
400. You, M.J.; Jung, J.; Byeon, Y.S.; Jung, J.Y.; Hong, Y.; Park, M.-S. Controlled crystallinity of LiTaO_3 surface layer for single-crystalline Ni-rich cathodes for lithium-ion batteries and all-solid-state batteries. *Chem. Engin. J.* **2024**, *483*, 149199. [[CrossRef](#)]
401. Herzog, M.J.; Gauquelin, N.; Esken, D.; Verbeeck, J.; Janek, J. Increased performance improvement of lithium-ion batteries by dry powder coating of high-nickel NMC with nanostructured fumed ternary lithium metal oxides. *ACS Appl. Energy Mater.* **2021**, *4*, 8832–8848. [[CrossRef](#)]
402. Tang, W.; Chen, Z.; Xiong, F.; Chen, F.; Huang, C.; Gao, Q.; Wang, T.; Yang, Z.; Zhang, W. An effective etching-induced coating strategy to shield $\text{LiNi}_{0.8}\text{Co}_{0.1}\text{Mn}_{0.1}\text{O}_2$ electrode materials by LiAlO_2 . *J. Power Sources* **2019**, *412*, 246–254. [[CrossRef](#)]
403. Ran, Q.; Zhao, H.; Hu, Y.; Shen, Q.; Liu, W.; Liu, J.; Shu, X.; Zhang, M.; Liu, S.; Tan, M.; et al. Enhanced electrochemical performance of dual-conductive layers coated Ni-rich $\text{LiNi}_{0.6}\text{Co}_{0.2}\text{Mn}_{0.2}\text{O}_2$ cathode for Li-ion batteries at high cut-off voltage. *Electrochim. Acta* **2018**, *289*, 82–93. [[CrossRef](#)]
404. Wang, H.; Chu, Y.; Pan, Q.; Yang, G.; Lai, A.; Liu, Z.; Zheng, F.; Hu, S.; Huang, Y.; Li, Q. Enhanced interfacial reaction interface stability of Ni-rich cathode materials by fabricating dual-modified layer coating for lithium-ion batteries. *Electrochim. Acta* **2021**, *366*, 137476. [[CrossRef](#)]
405. Zhang, H.; Xu, J.; Zhang, J. Surface-coated $\text{LiNi}_{0.8}\text{Co}_{0.1}\text{Mn}_{0.1}\text{O}_2$ (NMC811) cathode materials by Al_2O_3 , ZrO_2 , and $\text{Li}_2\text{O}-2\text{B}_2\text{O}_3$ thin-layers for improving the performance of lithium-ion batteries. *Front. Mater.* **2019**, *6*, 309. [[CrossRef](#)]
406. Jamil, S.; Ran, Q.; Yang, L.; Huang, Y.; Cao, S.; Yang, X.; Wang, X. Improved high-voltage performance of $\text{LiNi}_{0.87}\text{Co}_{0.1}\text{Al}_{0.03}\text{O}_2$ by Li^+ -conductor coating. *Chem. Eng. J.* **2021**, *407*, 126442. [[CrossRef](#)]
407. Wu, K.; Li, Z.; Chen, X. Designing a corrosion inhibiting layer to enhance cycling stability of 4.7 V Ni-rich cathode. *Adv. Func. Mater.* **2024**, *34*, 15327. [[CrossRef](#)]
408. Du, F.; Sun, P.; Zhou, Q.; Zeng, D.; Hu, D.; Fan, Z.; Hao, Q.; Mei, C.; Xu, T.; Zheng, J. Interlinking primary grains with lithium boron oxide to enhance the stability of $\text{LiNi}_{0.8}\text{Co}_{0.15}\text{Al}_{0.05}\text{O}_2$. *ACS Appl. Mater. Interfaces* **2020**, *12*, 56963–56973. [[CrossRef](#)]
409. Lin, J.; Guo, H.; Sun, K.; Fang, L. A nickel-rich oxide, $\text{Li}(\text{Ni}_{0.90}\text{Co}_{0.06}\text{Mn}_{0.04})_{0.995}\text{Al}_{0.005}\text{O}_2$, with a dual conductive coating. *J. Alloys Compd.* **2023**, *940*, 168870. [[CrossRef](#)]
410. Xiao, P.; Cao, Y.; Li, W.; Li, G.; Yu, Y.; Dai, Z.; Du, Z.; Chen, X.; Sun, J.; Yang, W. Simple strategy for synthesizing $\text{LiNi}_{0.8}\text{Co}_{0.15}\text{Al}_{0.05}\text{O}_2$ using Co Al-LDH nanosheet-coated Ni(OH)_2 as the precursor: Dual effects of the buffer layer and synergistic diffusion. *ACS Appl. Mater. Interfaces* **2021**, *13*, 29714–29725. [[CrossRef](#)]
411. Chen, J.; Zhu, L.; Jia, D.; Jiang, X.; Wu, Y.; Hao, Q.; Xia, X.; Ouyang, Y.; Peng, L.; Tang, W.; et al. $\text{LiNi}_{0.8}\text{Co}_{0.15}\text{Al}_{0.05}\text{O}_2$ cathodes exhibiting improved capacity retention and thermal stability due to a lithium iron phosphate coating. *Electrochim. Acta* **2019**, *312*, 179–187. [[CrossRef](#)]
412. Zhang, J.; Lan, Z.; Xi, R.; Li, Y.; Zhang, C. The cycle stability and rate performance of $\text{LiNi}_{0.8}\text{Mn}_{0.1}\text{Co}_{0.1}\text{O}_2$ enhanced by Mg doping and LiFePO_4 coating. *ChemElectroChem* **2022**, *9*, e202101654. [[CrossRef](#)]
413. Yan, P.; Zheng, J.; Liu, J.; Wang, B.; Cheng, X.; Zhang, Y.; Sun, C.; Wang, X.; Zhang, J. Tailoring grain boundary structures and chemistry of Ni-rich layered cathodes for enhanced cycle stability of lithium-ion batteries. *Nat. Energy* **2018**, *3*, 600–605. [[CrossRef](#)]
414. Gan, Q.; Qin, N.; Wang, Z.; Li, Z.; Zhu, Y.; Li, Y.; Gu, S.; Yuan, H.; Luo, W.; Lu, L.; et al. Revealing mechanism of Li_3PO_4 coating suppressed surface oxygen release for commercial Ni-rich layered cathodes. *ACS Appl. Energy Mater.* **2020**, *3*, 7445–7455. [[CrossRef](#)]
415. Sattar, T.; Sim, S.; Jin, B.; Kim, H. Dual function Li-reactive coating from residual lithium on Ni-rich NCM cathode material for Lithium-ion batteries. *Sci. Rep.* **2021**, *11*, 18590. [[CrossRef](#)]
416. Fan, X.; Zhang, J.; Zhou, X.; Chen, J.; Shi, Y.; Kalimudina, G.; Wang, F.; Belgibayeva, A.; Kong, L. Basicity regulation of Ni-rich layered oxide cathodes for all-solid-state Li-ion batteries. *J. Energy Chem.* **2025**, *105*, 454–460. [[CrossRef](#)]
417. Cheng, W.; Hao, S.; Ji, Y.; Li, L.; Liu, L.; Xiao, Y.; Wu, Y.; Huo, J.; Tang, F.; Liu, X. Optimizing surface residual alkali and enhancing electrochemical performance of $\text{LiNi}_{0.8}\text{Co}_{0.15}\text{Al}_{0.05}\text{O}_2$ cathode by LiH_2PO_4 . *Nanotechnology* **2022**, *33*, 045404. [[CrossRef](#)]
418. Yang, H.; Wang, J.; Xu, C.; Wu, K.; Zou, F.; Hu, X.; Hu, Z. $\text{LiZr}_2(\text{PO}_4)_3$ surface coating towards stable layer structure $\text{Li}_{1.2}\text{Mn}_{0.54}\text{Ni}_{0.13}\text{Co}_{0.13}\text{O}_2$ cathode materials with long cycle performance. *Nano Res.* **2023**, *16*, 2373–2382. [[CrossRef](#)]
419. Chen, F.; Zhu, X.; Dai, W.; Yao, C.; Qian, J.; Chen, Z.; Liu, C. Optimized Ni-rich $\text{LiNi}_{0.83}\text{Co}_{0.06}\text{Mn}_{0.06}\text{Al}_{0.05}\text{O}_2$ cathode material with a $\text{Li}_{1.3}\text{Al}_{0.3}\text{Ti}_{1.7}(\text{PO}_4)_3$ fast ion conductor coating for Lithium-ion batteries. *J. Alloys Compd.* **2022**, *923*, 166277. [[CrossRef](#)]

420. Lv, Z.C.; Wang, F.F.; Wang, J.C.; Wang, P.F.; Yi, T.F. Durable lithium-ion insertion/extraction and migration behavior of LiF-encapsulated cobalt-free lithium-rich manganese-based layered oxide cathode. *J. Colloid Interface Sci.* **2023**, *649*, 175–184. [CrossRef] [PubMed]
421. Julien, C.M.; Mauger, A. Functional behavior of AlF₃ coatings for high-performance cathode materials for lithium-ion batteries. *AIMS Mater. Sci.* **2019**, *6*, 406–440. [CrossRef]
422. Li, J.; Wang, J.; Lu, X.; Jiang, H.; Zhang, Q.; Wang, B.; Lai, C. Enhancing high-potential stability of Ni-rich LiNi_{0.8}Co_{0.1}Mn_{0.1}O₂ cathode with PrF₃ coating. *Ceram. Int.* **2021**, *47*, 6341–6351. [CrossRef]
423. Kaufman, L.A.; McCloskey, B.D. Surface lithium carbonate influences electrolyte degradation via reactive oxygen attack in lithium-excess cathode materials. *Chem. Mater.* **2021**, *33*, 4170–4176. [CrossRef]
424. Kang, W.; Jiang, A.; Chen, S.; Cao, X.; Yu, X.; Luo, Y.; Deng, W. High-performance Ti-doped V₂O₅ coating on the Ni-rich layered cathode: Construction and theoretical calculation. *J. Alloys Compd.* **2024**, *970*, 172700. [CrossRef]
425. Li, L.; Xu, M.; Yao, Q.; Chen, Z.; Song, L.; Zhang, Z.; Gao, C.; Wang, P.; Yu, Z.; Lai, Y. Alleviating surface degradation of nickel-rich layered oxide cathode material by encapsulating with nanoscale Li-ions/electrons superionic conductors hybrid membrane for advanced Li-ion batteries. *ACS Appl. Mater. Interfaces* **2016**, *8*, 30879–30889. [CrossRef]
426. Qu, J.; Sadighi, Z.; Yuan, H.; Zuin, L.; Goward, G.R.; Botton, G.A. Effective recovery of the air-exposed Ni-rich lithium transition metal oxide cathodes with a coating-stabilized surface. *J. Power Sources* **2024**, *614*, 234983. [CrossRef]
427. Wu, Y.-S.; Pham, Q.-T.; Yang, C.-C.; Chern, C.-S.; Babulal, L.M.; Seenivasan, M.; Jeyakumar, J.; Mengesha, T.H.; Placke, T.; Brunklaus, G.; et al. Coating of a novel lithium-containing hybrid oligomer additive on nickel-rich LiNi_{0.8}Co_{0.1}Mn_{0.1}O₂ cathode materials for high-stability and high-safety lithium-ion batteries. *ACS Sustain. Chem. Eng.* **2022**, *10*, 7394–7408. [CrossRef]
428. Nie, H.; Shang, C.; Hu, P.; Li, Y. In-situ electrochemical polymerization of polypyrrole on LiNi_{0.8}Co_{0.1}Mn_{0.1}O₂ cathode with improved performance for lithium-ion batteries. *Mater. Lett.* **2023**, *335*, 133768. [CrossRef]
429. Kim, H.I.; Jang, H.J.; Park, E.J.; Kim, S.-J.; Son, J.-T. Dramatic enhancement of the electrochemical property of nano-fiber Li[Ni_{0.9}Co_{0.05}Al_{0.05}]O₂ as a lithium-ion battery cathode material using a polypyrrole coating. *J. Korean Phys. Soc.* **2021**, *79*, 567–572. [CrossRef]
430. Han, Y.; Heng, S.; Wang, Y.; Qu, Q.; Zheng, H. Anchoring interfacial nickel cations on single-crystal LiNi_{0.8}Co_{0.1}Mn_{0.1}O₂ cathode surface via controllable electron transfer. *ACS Energy Lett.* **2020**, *5*, 2421–2433. [CrossRef]
431. Gan, Q.; Qin, N.; Zhu, Y.; Huang, Z.; Zhang, F.; Gu, S.; Xie, J.; Zhang, K.; Lu, L.; Lu, Z. Polyvinylpyrrolidone-induced uniform surface-conductive polymer coating endows Ni-rich LiNi_{0.8}Co_{0.1}Mn_{0.1}O₂ with enhanced cyclability for lithium-ion batteries. *ACS Appl. Mater. Interfaces* **2019**, *11*, 12594–12604. [CrossRef]
432. Yoon, Y.; Shin, S.; Shin, M.W. Fundamental understanding of the effect of a polyaniline coating layer on cation mixing and chemical states of LiNi_{0.9}Co_{0.085}Mn_{0.015}O₂ for Li-ion batteries. *ACS Appl. Polym. Mater.* **2023**, *5*, 1344–1353. [CrossRef]
433. He, P.; Zhang, M.; Wang, S.; Wan, M.; Wang, D.Y.; Wang, Y.; Yan, D.; Zhang, X.; Sun, Y. Enhanced high-rate and cyclic performance of Co-free and Ni-rich LiNi_{0.95}Mn_{0.05}O₂ cathodes by coating electronic/Li⁺ conductive PANI-PEG layer. *J. Solid State Electrochem.* **2024**, *28*, 4259–4272. [CrossRef]
434. Huang, J.; Zhang, L.; Tang, H.; Huang, S.; Tang, Y.; Ma, J.; Huang, B.; Li, Y.; Sun, Y.; Xiao, S.; et al. A Mo/PANI co-modified ultra-high nickel NCM9622 cathode composite with excellent cycle stability and high-rate performance for power batteries. *J. Mater. Chem. A* **2024**, *12*, 21412–21424. [CrossRef]
435. Huang, Y.; Tao, M.; Mo, L.; Zhang, L.; Su, D.; Jiang, J.; Pan, Q.; Hu, S.; Wang, H.; Li, Q.; et al. Organic coating strategy with oxidized oxygen anion capture to suppress lattice oxygen evolution of Ni-rich cathode materials at high voltage. *Chem. Eng. J.* **2024**, *493*, 152525. [CrossRef]
436. Li, Z.-W.; Lin, F.; Zhang, X.-D.; Zhang, X.-S.; Wen, R.; Li, X.; Zheng, Z.-J. Stress-relieving protective elastomeric interphase for stable Ni-rich cathodes. *Adv. Func. Mater.* **2025**, *35*, 2415035. [CrossRef]
437. Liu, C.; Liao, C.M.; Li, Z.; Nie, S.; Yi, Z.; Xiao, W. Revealing the origin of enhanced structural stability for nickel-rich LiNi_{0.83}Co_{0.11}Mn_{0.06}O₂ cathodes in situ modified with multifunctional polysiloxane. *Chem. Eng. J.* **2024**, *491*, 152078. [CrossRef]
438. Lin, K.; Yang, S.; Shi, Z.; Fan, Q.; Liu, Z.; Liu, L. Knitting a sweater with UV-induced in situ polymerization of poly(pyrrole-co-citral nitrile) on Ni-rich layer oxide cathode materials for lithium ion batteries. *J. Power Sources* **2022**, *520*, 230768. [CrossRef]
439. Yoon, Y.; Shin, M.W. Cationic covalent organic framework coating of the Ni-rich cathode surface for the significant improvement of the interfacial Li⁺ transport and structural stability. *ACS Appl. Energy Mater.* **2024**, *7*, 5244–5252. [CrossRef]
440. Zhao, R.; Liang, J.; Huang, J.; Zeng, R.; Zhang, J.; Chen, H.; Shi, G. Improving the Ni-rich LiNi_{0.5}Co_{0.2}Mn_{0.3}O₂ cathode properties at high operating voltage by double coating layer of Al₂O₃ and AlPO₄. *J. Alloys Compd.* **2017**, *724*, 1109–1116. [CrossRef]
441. Wu, F.; Shi, Q.; Chen, L.; Dong, J.; Zhao, J.; Wang, H.; Gao, F.; Liu, J.; Zhang, H.; Li, N.; et al. New insights into dry-coating-processed surface engineering enabling structurally and thermally stable high-performance Ni-rich cathode materials for lithium-ion batteries. *Chem. Eng. J.* **2023**, *470*, 144045. [CrossRef]

442. Bai, H.; Yuan, K.; Zhang, C.; Zhang, W.; Tang, X.; Jiang, S.; Jin, T.; Ma, Y.; Kou, L.; Shen, C.; et al. Advantageous surface engineering to boost single-crystal quaternary cathodes for high-energy-density lithium-ion batteries. *Energy Storage Mater.* **2023**, *61*, 102879. [[CrossRef](#)]
443. Liu, Y.; Zeng, T.; Li, G.; Wan, T.; Li, M.; Zhang, X.; Li, M.; Su, M.; Dou, A.; Zeng, W.; et al. The surface double-coupling on single-crystal $\text{LiNi}_{0.8}\text{Co}_{0.1}\text{Mn}_{0.1}\text{O}_2$ for inhibiting the formation of intragranular cracks and oxygen vacancies. *Energy Storage Mater.* **2022**, *52*, 534–546. [[CrossRef](#)]
444. Mohsen, M.; Rahim, L.; Hossein, E.; Manesha, M. Preparation and characteristics of graphene/ $\text{Y}_2\text{O}_3/\text{LiNi}_{0.8}\text{Co}_{0.15}\text{Al}_{0.05}\text{O}_2$ composite for the cathode of lithium-ion battery. *J. Electroanal. Chem.* **2020**, *862*, 113971.
445. Yua, J.; Zhang, J.; Zhang, Y.; Wang, Z.; Chen, Z.; Gao, A.; Zhang, J.; Wang, Y.; Zhao, R. Electrostatic adsorption facilitating dual-layer coating for stabilized cathode-electrolyte interphases and boosted lithium intercalation thereof in $\text{LiNi}_{0.8}\text{Co}_{0.1}\text{Mn}_{0.1}\text{O}_2$ cathode. *Appl. Surf. Sci.* **2022**, *577*, 151716. [[CrossRef](#)]
446. Liu, G.; Li, Z.; Zeng, L.; Lin, J.; Zheng, B.; Liu, H.; Chen, L.; Wu, F. Single-crystal Ni-rich layered oxide cathodes with LiNbO_3 - Li_3BO_3 coating for sulfide all-solid-state batteries. *Nano Energy* **2025**, *137*, 110798. [[CrossRef](#)]
447. Yang, G.; Liu, B.; Lai, F.; Xue, K.; Zhang, X.; Wang, H.; Xie, M.; Wang, C. Low-temperature synthesis of amorphous $\text{LiF}/\text{Li}_3\text{BO}_3$ interfaces with F, B co-doped subsurface for long-cycling and high-rate Ni-rich cathodes. *Nano Energy* **2025**, *140*, 111009. [[CrossRef](#)]
448. Rambukwella, I.; Ponnuru, H.; Yan, C. The role of dopants in mitigating the chemo-mechanical degradation of Ni-rich cathode: A critical review. *EcoEnergy* **2025**, *3*, 321–353. [[CrossRef](#)]
449. Dang, R.; Qu, Y.; Ma, Z.; Yu, L.; Duan, L.; Lü, W. The effect of elemental doping on nickel-rich NCM cathode materials of lithium ion batteries. *J. Phys. Chem. C* **2022**, *126*, 151–159. [[CrossRef](#)]
450. Byeon, Y.S.; Lee, W.; Park, S.; Kim, D.; Jung, J.; Park, M.-S.; Yoon, W.-S. Comprehensive understanding of elemental doping and substitution of Ni-rich cathode materials for lithium-ion batteries via in situ operando analyses. *Small Sci.* **2024**, *4*, 2400165. [[CrossRef](#)]
451. Nguyen, T.T.; Kim, U.-H.; Yoon, C.S.; Sun, Y.-K. Enhanced cycling stability of Sn-doped $\text{Li}[\text{Ni}_{0.90}\text{Co}_{0.05}\text{Mn}_{0.05}]\text{O}_2$ via optimization of particle shape and orientation. *Chem. Eng. J.* **2021**, *405*, 126887. [[CrossRef](#)]
452. Chen, M.M.; Zhao, E.Y.; Chen, D.F.; Wu, M.; Han, S.; Huang, Q.; Yang, L.; Xiao, X.; Hu, Z. Decreasing Li/Ni disorder and improving the electrochemical performances of Ni-rich $\text{LiNi}_{0.8}\text{Co}_{0.1}\text{Mn}_{0.1}\text{O}_2$ by Ca doping. *Inorg. Chem.* **2017**, *56*, 8355–8362. [[CrossRef](#)]
453. Ko, G.; Jeong, S.; Park, S.; Lee, J.; Kim, S.; Shin, Y.; Kim, W.; Kwo, K.J. Doping strategies for enhancing the performance of lithium nickel manganese cobalt oxide cathode materials in lithium-ion batteries. *Energy Storage Mater.* **2023**, *60*, 102840. [[CrossRef](#)]
454. Susai, F.A.; Kovacheva, D.; Kravchuk, T.; Ravikumar, R.; Talianker, M.; Grinblat, J.; Burstein, L.; Kauffmann, Y.; Major, D.T.; Markovski, B.; et al. Improving performance of $\text{LiNi}_{0.8}\text{Co}_{0.1}\text{Mn}_{0.1}\text{O}_2$ cathode materials for lithium-ion batteries by doping with molybdenum-ions: Theoretical and experimental studies. *ACS Appl. Energy Mater.* **2019**, *2*, 4521–4534. [[CrossRef](#)]
455. Sattar, T.; Lee, S.-H.; Jin, B.-S.; Kim, H.-S. Influence of Mo addition on the structural and electrochemical performance of Ni-rich cathode material for lithium-ion batteries. *Sci. Rep.* **2020**, *10*, 8562. [[CrossRef](#)]
456. Park, G.-T.; Namkoong, B.; Kim, S.-B.; Liu, J.; Yoon, C.-S.; Sun, Y.-K. Introducing high-valence elements into cobalt-free layered cathodes for practical lithium-ion batteries. *Nat. Energy* **2022**, *7*, 946–954. [[CrossRef](#)]
457. Ryu, H.-H.; Lim, H.-W.; Lee, S.G.; Sun, Y.-K. Optimization of molybdenum-doped Ni-rich layered cathodes for long-term cycling. *Energy Storage Mater.* **2023**, *59*, 102771. [[CrossRef](#)]
458. Ryu, H.-H.; Park, G.-T.; Yoon, C.-S.; Sun, Y.-K. Suppressing detrimental phase transitions via tungsten doping of LiNiO_2 cathode for next generation lithium-ion batteries. *J. Mater. Chem. A* **2019**, *7*, 18580–18588. [[CrossRef](#)]
459. Ryu, H.-H.; Park, K.-J.; Yoon, D.-R.; Aishova, A.; Yoon, C.-S.; Sun, Y.-K. $\text{Li}[\text{Ni}_{0.9}\text{Co}_{0.09}\text{W}_{0.01}]\text{O}_2$: A new type of layered oxide cathode with high cycling stability. *Adv. Energy Mater.* **2019**, *9*, 1902698. [[CrossRef](#)]
460. Kim, U.-H.; Park, N.-Y.; Park, G.-T.; Kim, H.; Yoon, C.-S.; Sun, Y.-K. High-energy W-doped $\text{Li}[\text{Ni}_{0.95}\text{Co}_{0.04}\text{Al}_{0.01}]\text{O}_2$ cathodes for next-generation electric vehicles. *Energy Storage Mater.* **2020**, *33*, 399–407. [[CrossRef](#)]
461. Wang, J.-L.; Liu, C.-J.; Wang, Q.; Xu, G.-L.; Miao, C.; Xu, M.-B.; Wang, C.-J.; Xiao, W. Investigation of W^{6+} -doped in high-nickel $\text{LiNi}_{0.83}\text{Co}_{0.11}\text{Mn}_{0.06}\text{O}_2$ cathode materials for high-performance lithium-ion batteries. *J. Colloid Interface Sci.* **2022**, *628*, 338–349. [[CrossRef](#)] [[PubMed](#)]
462. Cheng, Y.; Zhang, X.; Leng, Q.; Yang, X.; Jiao, T.; Gong, Z.; Wang, M.-S.; Yang, Y. Boosting electrochemical performance of Co-free Ni-rich cathodes by combination of Al and high-valence elements. *Chem. Eng. J.* **2023**, *474*, 145869. [[CrossRef](#)]
463. Li, L.; Chen, Q.; Jiang, M.; Ning, T.; Tan, L.; Zhang, X.; Zheng, J.; Wang, J.; Wu, Q.; Ji, X.; et al. Uncovering mechanism behind tungsten bulk/grain-boundary modification of Ni-rich cathode. *Energy Storage Mater.* **2025**, *75*, 104016. [[CrossRef](#)]
464. Huang, Y.; Liu, X.; Yu, R.; Cao, S.; Pei, Y.; Luo, Z.; Zhao, Q.; Chang, B.; Wang, Y.; Wang, X. Tellurium surface doping to enhance the structural stability and electrochemical performance of layered Ni-rich cathodes. *ACS Appl. Mater. Interfaces* **2019**, *11*, 40022–40033. [[CrossRef](#)]

465. Jamil, S.; Yu, R.; Wang, Q.; Fasehullah, M.; Huang, Y.; Yang, Z.; Yang, X.; Wang, X. Enhanced cycling stability of nickel-rich layered oxide by tantalum doping. *J. Power Sources* **2020**, *473*, 228597. [CrossRef]
466. Kim, U.-H.; Park, G.-T.; Son, B.-K.; Nam, G.-W.; Liu, J.; Kuo, L.-Y.; Kaghazchi, P.; Yoon, C.-S.; Sun, Y.-K. Heuristic solution for achieving long-term cycle stability for Ni-rich layered cathodes at full depth of discharge. *Nat. Energy* **2020**, *5*, 860–869. [CrossRef]
467. Chu, B.; Liu, S.; You, L.; Liu, D.; Huang, T.; Li, Y.; Yu, A. Enhancing the cycling stability of Ni-rich $\text{LiNi}_{0.6}\text{Co}_{0.2}\text{Mn}_{0.2}\text{O}_2$ cathode at a high cutoff voltage with Ta doping. *ACS Sustain. Chem. Eng.* **2020**, *8*, 3082–3090. [CrossRef]
468. Sun, H.-H.; Kim, U.-H.; Park, J.-H.; Park, S.-W.; Seo, D.-H.; Heller, A.; Mullins, C.-B.; Yoon, C.-S.; Sun, Y.-K. Transition metal-doped Ni-rich layered cathode materials for durable Li-ion batteries. *Nat. Commun.* **2021**, *12*, 6552. [CrossRef]
469. Li, X.; Ge, W.; Zhang, K.; Zhang, K.; Peng, G.; Fu, Y.; Ma, X. Comprehensive study of tantalum doping on morphology, structure, and electrochemical performance of Ni-rich cathode materials. *Electrochim. Acta* **2022**, *403*, 139653. [CrossRef]
470. Zhang, H.; Zhang, X.; Zeng, T.; Dou, A.; Zhang, P.; Su, M.; Zhou, Y.; Liu, Y. Conversion of residual lithium into fast ionic conductor coating to achieve one-step double modification strategy in $\text{LiNi}_{0.8}\text{Co}_{0.15}\text{Al}_{0.05}\text{O}_2$. *J. Alloys Compd.* **2023**, *931*, 167638. [CrossRef]
471. Monsees, F.; Misiewicz, C.; Dalkilic, M.; Diddens, D.; Heuer, A. Enhancing the stability and performance of Ni-rich cathode materials through Ta doping: A combined theoretical and experimental study. *Phys. Chem. Chem. Phys.* **2025**, *27*, 834–843. [CrossRef]
472. Fan, F.; Zheng, R.; Zeng, C.; Zeng, C.; Xu, H.; Wang, X.; Tian, G.; Wang, S.; Liu, P.; Shu, C. Synergistically dissipating the local strain and restraining lattice oxygen escape by fine-tuning of microstructure enabling Ni-rich cathodes with superior cyclabilities. *J. Energy Chem.* **2025**, *105*, 24–34. [CrossRef]
473. Tian, F.; Zhang, Y.; Liu, Z.; Monteiro, R.S.; Ribas, R.M.; Gao, P.; Zhu, Y.; Yu, H.; Ben, L.; Huang, X. Investigation of structure and cycling performance of Nb⁵⁺ doped high-nickel ternary cathode materials. *Solid State Ion.* **2021**, *359*, 115520. [CrossRef]
474. Li, J.; Zhang, M.; Zhang, D.; Yan, Y.; Li, Z. An effective doping strategy to improve the cyclic stability and rate capability of Ni-rich $\text{LiNi}_{0.8}\text{Co}_{0.1}\text{Mn}_{0.1}\text{O}_2$ cathode. *Chem. Eng. J.* **2020**, *402*, 126195. [CrossRef]
475. Liu, L.-H.; Li, M.-C.; Chu, L.-H.; Jiang, B.; Lin, R.-X.; Zhu, X.-P.; Cao, G.-Z. Layered ternary metal oxides: Performance degradation mechanisms as cathodes, and design strategies for high performance batteries. *Prog. Mater. Sci.* **2020**, *111*, 100655.
476. Kim, U.-H.; Lee, S.-B.; Park, N.-Y.; Kim, S.-J.; Yoon, C.-S.; Sun, Y.-K. High-energy-density Li-ion battery reaching full charge in 12 min. *ACS Energy Lett.* **2022**, *7*, 3880–3888. [CrossRef]
477. Wang, J.-L.; Yi, Z.-C.; Liu, C.-J.; He, M.-Y.; Miao, C.; Li, J.-Q.; Xu, G.-L.; Xiao, W. Revealing the effect of Nb⁵⁺ on the electrochemical performance of nickel-rich layered $\text{LiNi}_{0.83}\text{Co}_{0.11}\text{Mn}_{0.06}\text{O}_2$ oxide cathode for lithium-ion batteries. *J. Colloid Interface Sci.* **2023**, *635*, 295–304. [CrossRef]
478. Wu, F.; Li, Q.; Chen, L.; Lu, Y.; Su, Y.; Bao, L.; Chen, R.; Chen, S. Use of Ce to reinforce the interface of Ni-rich $\text{LiNi}_{0.8}\text{Co}_{0.1}\text{Mn}_{0.1}\text{O}_2$ cathode materials for lithium-ion batteries under high operating voltage. *ChemSusChem* **2019**, *12*, 935–943. [CrossRef]
479. Li, Q.; Li, Z.; Wu, S.; Wang, Z.; Liu, X.; Li, W.; Li, N.; Wang, J.; Zhuang, W. Utilizing diverse functions of zirconium to enhance the electrochemical performance of Ni-rich layered cathode materials. *ACS Appl. Energy Mater.* **2020**, *3*, 11741–11751. [CrossRef]
480. Che, W.; Wan, X.-W.; Zhang, D.-Y.; Chang, C.-K. Stabilized performance of $\text{LiNi}_{0.90}\text{Co}_{0.07}\text{Al}_{0.03}\text{O}_2$ cathodes via Zr⁴⁺ doping upon 4.5 V application due to the suppression of H2–H3 phase transitions. *ACS Sustain. Chem. Eng.* **2021**, *9*, 5536–5545. [CrossRef]
481. Ni, J.-X.; Tan, Y.-Y.; Xu, K.; Jiang, Y.-J.; Chang, W.-Y.; Lai, C.-Y.; Liu, H. Cobalt-free nickel-rich layered $\text{LiNi}_{0.9}\text{Al}_{0.1-x}\text{Zr}_x\text{O}_2$ cathode for high energy density and stable lithium-ion batteries. *J. Taiwan Inst. Chem. Eng.* **2022**, *136*, 104421. [CrossRef]
482. Tang, Y.; Huang, Z.; Wang, W.; Wen, Y.; Zhang, S.; Chen, X.; Zhang, Z.; Yin, Z.; Yang, T.; Li, T.; et al. Superior fast-charging Ni-rich cathode via promoted kinetic-mechanical performance. *Nano Energy* **2024**, *128*, 109908. [CrossRef]
483. Zhang, Z.; Hong, B.; Yi, M.-Y.; Fan, X.-M.; Zhang, Z.; Huang, X.-B.; Lai, Y.-Q. In situ co-doping strategy for achieving long-term cycle stability of single-crystal Ni-rich cathodes at high voltage. *Chem. Eng. J.* **2022**, *445*, 136825. [CrossRef]
484. Kim, J.H.; Kim, H.; Kim, W.-J.; Kim, Y.-C.; Jung, J.Y.; Rhee, D.Y.; Song, J.H.; Cho, W.; Park, M.-S. Incorporation of titanium into Ni-rich layered cathode materials for lithium-ion batteries. *ACS Appl. Energy Mater.* **2020**, *3*, 12204–12211. [CrossRef]
485. Yang, R.-K.; Wu, Z.-G.; Li, Y.-C.; Li, R.; Qiu, L.; Wang, D.; Yang, L.; Guo, X.-D. Optimization of the electrochemical properties of $\text{LiNi}_{0.8}\text{Co}_{0.1}\text{Mn}_{0.1}\text{O}_2$ cathode material by titanium doping. *Ionics* **2020**, *26*, 3223–3230. [CrossRef]
486. Wang, N.; Zhu, Y.; Yao, J.; Zhao, M.; Xu, Y. Improved cycling stability of Ni-rich $\text{LiNi}_{0.8}\text{Co}_{0.1}\text{Mn}_{0.1}\text{O}_2$ cathode materials by optimizing Ti doping. *Funct. Mater. Lett.* **2021**, *14*, 2150002. [CrossRef]
487. Liu, W.; Cheng, X.; Wang, C.; Zhao, B.; Huang, B. Enhancing high cycle stability of Ni-rich $\text{LiNi}_{0.94}\text{Co}_{0.04}\text{Al}_{0.02}\text{O}_2$ layered cathode material. *Ionics* **2021**, *27*, 4619–4628. [CrossRef]
488. Yi, Z.; Liu, C.; Miao, C.; Wang, Z.; Wang, J.; Xin, Y.; Xiao, W. In-situ Ti⁴⁺-doped modification of layer-structured Ni-rich $\text{LiNi}_{0.83}\text{Co}_{0.11}\text{Mn}_{0.06}\text{O}_2$ cathode materials for high-energy lithium-ion batteries. *J. Colloid Interface Sci.* **2025**, *677*, 91–100. [CrossRef]
489. He, J.; Li, Y.; Luo, W.; Cao, Y.; Zhao, C.; Dong, P.; Duan, J.; Wang, D.; Wang, X.; Zhou, Z.; et al. Enhanced reversibility of single crystal Ni-rich cathode materials via Ti doping. *Electrochim. Acta* **2024**, *479*, 143855. [CrossRef]

490. Zhao, Z.; Zhang, Y.; Cao, H.; Peng, Y.; Ding, G.; Hua, Y.; Zhao, J.; Cui, C.; Huang, S. Enhancing the cycling stability of Ni-rich cathodes via dual-site modification induced by slight Ti-rich doping. *J. Power Sources* **2025**, *628*, 235913. [\[CrossRef\]](#)
491. Yang, Z.-F.; Wang, Z.-H.; Zhu, Y.-H.; Jiang, H.; Li, C.-Z. Enhancing surface-to-bulk stability of layered Co-free Ni-rich cathodes for long-life Li-ion batteries. *Battery Energy* **2022**, *2*, 20220048. [\[CrossRef\]](#)
492. Wang, B.; Cai, F.; Chu, C.; Fu, B.; Swierczek, K.; Li, L.; Zhao, H. Modification of the Ni-rich layered cathode material by Hf addition: Synergistic microstructural engineering and surface stabilization. *ACS Appl. Mater. Interfaces* **2024**, *16*, 12599–12611. [\[CrossRef\]](#)
493. Jeyakumar, J.; Seenivasan, M.; Wu, Y.-S.; Kuo, L.-Y.; Wu, S.-H.; Chang, J.-K.; Yang, C.-C. Sn-doped/coated Ni-rich $\text{LiNi}_{0.90}\text{Co}_{0.04}\text{Mn}_{0.03}\text{Al}_{0.03}\text{O}_2$ cathode materials for improved electrochemical performance of Li-ion batteries. *ACS Appl. Energy Mater.* **2024**, *7*, 4919–4934. [\[CrossRef\]](#)
494. Wang, R.; Li, Z.; Yang, Z.; Zhang, M.; Zhang, D.; Yan, Y. Synergistic effect of Ce^{4+} modification on the electrochemical performance of $\text{LiNi}_{0.6}\text{Co}_{0.2}\text{Mn}_{0.2}\text{O}_2$ cathode materials at high cut-off voltage. *Ceram. Int.* **2021**, *47*, 1268–1276. [\[CrossRef\]](#)
495. Xiong, Y.; Cao, G.; Li, Y.; Zhu, J.; Zheng, J.; Tan, Z.; Xi, X.; Yang, J. The synergistic Effect of Gd modification on improving the electrochemical performance of $\text{LiNi}_{0.88}\text{Co}_{0.09}\text{Al}_{0.03}\text{O}_2$ cathode materials. *J. Electrochem. Soc.* **2021**, *168*, 0305510. [\[CrossRef\]](#)
496. Jeong, M.; Kim, H.; Lee, W.; Ahn, S.-J.; Lee, E.; Yoon, W.-S. Stabilizing effects of Al-doping on Ni-rich $\text{LiNi}_{0.80}\text{Co}_{0.15}\text{Mn}_{0.05}\text{O}_2$ cathode for Li rechargeable batteries. *J. Power Sources* **2020**, *474*, 228592. [\[CrossRef\]](#)
497. Cheng, L.; Zhang, B.; Su, S.L.; Ming, L.; Zhao, Y.; Tan, X.X. Al-doping enables high stability of single-crystalline $\text{LiNi}_{0.7}\text{Co}_{0.1}\text{Mn}_{0.2}\text{O}_2$ lithium-ion cathodes at high voltage. *RSC Adv.* **2020**, *11*, 124–128. [\[CrossRef\]](#)
498. Zhang, C.; Wan, J.; Li, Y.; Zheng, S.; Zhou, K.; Wang, D.; Wang, D.; Hong, C.; Gong, Z.; Yang, Y.; et al. Restraining the polarization increase of Ni-rich and low-Co cathodes upon cycling by Al-doping. *J. Mater. Chem.* **2020**, *8*, 6893–6901. [\[CrossRef\]](#)
499. Kim, U.-H.; Lee, S.-B.; Ryu, J.-H.; Yoon, C.-S.; Sun, Y.-G. Optimization of Ni-rich $\text{Li}[\text{Ni}_{0.92-x}\text{Co}_{0.04}\text{Mn}_{0.04}\text{Al}_x]\text{O}_2$ cathodes for high energy density lithium-ion batteries. *J. Power Sources* **2023**, *564*, 232850. [\[CrossRef\]](#)
500. Xi, R.-H.; Zhang, J.-N.; Lan, Z.-W.; Yuan, Y.-X.; Kang, J.-L.; Li, Y.-Y.; Wang, J.-T.; Zhang, C.-H.; Hou, X.-Y. High-nickel and cobalt-free layered $\text{LiNi}_{0.90}\text{Mn}_{0.06}\text{Al}_{0.04}\text{O}_2$ cathode for lithium-ion batteries. *Ceram. Int.* **2022**, *48*, 36690–36696. [\[CrossRef\]](#)
501. Liu, Q.; Wu, Z.; Sun, J.-Y.; Xu, R.-M.; Li, X.-W.; Yu, X.; Liu, Y. Facile synthesis of crack-free single-crystalline Al-doped Co-free Ni-rich cathode material for lithium-ion batteries. *Electrochim. Acta* **2023**, *437*, 141473. [\[CrossRef\]](#)
502. Kong, X.; Li, D.; Fedorovskaya, E.O.; Kallio, T.; Ren, X. New insights in Al-doping effects on the LiNiO_2 positive electrode material by a sol-gel method. *Int. J. Energy Res.* **2021**, *45*, 10489–10499. [\[CrossRef\]](#)
503. Yang, C.; Li, Y.; Su, W.; Zhu, X.; Hao, L.; Wang, X.; Wu, S.; Chen, L.; Cao, D.; Su, Y.; et al. Aluminium doping in single-crystal nickel-rich cathodes: Insights into electrochemical degradation and enhancement. *J. Mater. Chem. A* **2024**, *12*, 20910–20920. [\[CrossRef\]](#)
504. Yan, H.; Ha, Y.; Ye, T.; Gao, X.; Yue, X.; Li, Z. High performance of Co-free $\text{LiNi}_x\text{Mn}_{1-x}\text{O}_2$ cathodes realized by nonmagnetic ion substitution for Li-ion batteries. *Chem. Eng. J.* **2023**, *465*, 142926. [\[CrossRef\]](#)
505. Li, Y.; Chang, S.-H.; Zheng, J.-C.; Zhang, D.-W.; Yang, J.-C.; Chen, Y.-X.; Guo, J.; Zhu, J.; Xiong, Y.; Li, W. Dual-modification of Gd_2O_3 on the high-voltage electrochemical properties of $\text{LiNi}_{0.8}\text{Co}_{0.1}\text{Mn}_{0.1}\text{O}_2$ cathode materials via the solid-state method. *J. Solid State Electrochem.* **2020**, *24*, 863–872. [\[CrossRef\]](#)
506. Sallard, S.; Billaud, J.; Sheptyakov, D.; Novak, P.; Villevieille, C. Cr-doped Li-rich nickel cobalt manganese oxide as a positive electrode material in Li-ion batteries to enhance cycling stability. *ACS Appl. Energy Mater.* **2020**, *3*, 8646–8657. [\[CrossRef\]](#)
507. Xu, Y.-D.; Zhang, J.; Wu, Z.-G.; Xu, C.-L.; Li, Y.-C.; Xiang, W.; Wang, Y.; Zhong, Y.-J.; Guo, X.-D.; Chen, H. Stabilizing the structure of nickel-rich lithiated oxides via Cr doping as cathode with boosted high-voltage/temperature cycling performance for Li-ion battery. *Energy Technol.* **2020**, *8*, 1900498. [\[CrossRef\]](#)
508. Zhang, B.; Zhang, H.; Su, Y.; Dong, J.; Yan, K.; Liu, J.; Lu, Y.; Wang, H.; Wang, C.; Wu, F.; et al. Rare-earth doping induced pinning effect with enhanced chemo-mechanical stability in Ni-rich cathodes for lithium-ion batteries. *Chin. J. Chem.* **2025**, *43*, 889–896. [\[CrossRef\]](#)
509. Luo, Z.; Li, H.; Wang, W.; Fang, Z.; Zhao, B.; Hu, G.; Peng, Z.; Du, K.; Cao, Y. Mitigating irreversible phase transition of Y-doped $\text{LiNi}_{0.925}\text{Co}_{0.03}\text{Mn}_{0.045}\text{O}_2$ by lattice engineering. *Ceram. Int.* **2024**, *50*, 9535–9547. [\[CrossRef\]](#)
510. Huang, Y.; Cao, S.; Xie, X.; Wu, C.; Jamil, S.; Zhao, Q.L.; Chang, B.B.; Wang, Y.; Wang, X.Y. Improving the structure and cycling stability of Ni-rich layered cathodes by dual modification of yttrium doping and surface coating. *ACS Appl. Mater. Interfaces* **2020**, *12*, 19483–19494. [\[CrossRef\]](#)
511. Zheng, H.; Liu, Z.; Chen, Y.; Gao, X. La-doped ultrahigh-nickel layered oxide cathode with enhanced cycle stability for Li-ion batteries. *ACS Appl. Mater. Interfaces* **2023**, *15*, 35043–35051. [\[CrossRef\]](#)
512. Lv, Y.; Cheng, X.; Qiang, W.; Huang, B. Improved electrochemical performances of Ni-rich $\text{LiNi}_{0.83}\text{Co}_{0.12}\text{Mn}_{0.05}\text{O}_2$ by Mg-doping. *J. Power Sources* **2020**, *450*, 227718. [\[CrossRef\]](#)
513. Weber, R.; Li, H.-Y.; Chen, W.-F.; Kim, C.-Y.; Plucknett, K.; Dahn, J.-R. In situ XRD studies during synthesis of single-crystal LiNiO_2 , $\text{LiNi}_{0.975}\text{Mg}_{0.025}\text{O}_2$, and $\text{LiNi}_{0.95}\text{Al}_{0.05}\text{O}_2$ cathode materials. *J. Electrochem. Soc.* **2020**, *167*, 100501. [\[CrossRef\]](#)

514. Liu, A.; Zhang, N.; Stark, J.E.; Arab, P.; Li, H.; Dahn, J.R. Synthesis of Co-free Ni-rich single crystal positive electrode materials for lithium-ion batteries: Part I. Two-step lithiation method for Al or Mg-doped LiNiO_2 . *J. Electrochem. Soc.* **2021**, *168*, 040531. [[CrossRef](#)]
515. Liu, A.; Zhang, N.; Stark, J.E.; Arab, P.; Li, H.; Dahn, J.R. Synthesis of Co-Free Ni-rich single crystal positive electrode materials for lithium-ion batteries: Part II. One-step lithiation method of Mg-doped LiNiO_2 . *J. Electrochem. Soc.* **2021**, *168*, 050506. [[CrossRef](#)]
516. Yu, H.-F.; Zhu, H.-W.; Yang, Z.-F.; Liu, M.-M.; Jiang, H.; Li, C.-Z. Bulk Mg-doping and surface polypyrrole-coating enable high-rate and long-life for Ni-rich layered cathodes. *Chem. Eng. J.* **2021**, *412*, 128625. [[CrossRef](#)]
517. Xiao, W.; Nie, Y.; Miao, C.; Wang, J.; Tan, Y.; Wen, M. Structural design of high-performance Ni-rich $\text{LiNi}_{0.83}\text{Co}_{0.11}\text{Mn}_{0.06}\text{O}_2$ cathode materials enhanced by Mg^{2+} doping and Li_3PO_4 coating for lithium-ion battery. *J. Colloid Interface Sci.* **2022**, *607*, 1071–1082. [[CrossRef](#)]
518. Lin, Y.; Abram, C.M.; Shi, X.; McKendry, I.G.; Wang, Z.; Zhong, H.; Zhao, H.; Yang, X.; Koel, B.E.; Yan, C.; et al. Enhanced thermal stability of aerosol-synthesized Ni-rich Li-ion battery cathode materials via concentration-gradient Ca doping. *ACS Appl. Energy Mater.* **2022**, *5*, 10751–10757. [[CrossRef](#)]
519. Wang, L.-C.; Chu, Y.-Q.; Nong, Y.-T.; Zheng, F.-H.; Li, Y.; Huang, Y.-Z.; Li, Y.-H.; Pan, Q.-C.; Wang, H.; Li, Q. Sr-based sub/surface integrated layer and bulk doping to enhance high-voltage cycling of a Ni-rich cathode material. *ACS Sustain. Chem. Eng.* **2022**, *10*, 7883–7895. [[CrossRef](#)]
520. Wang, J.; Wang, Y.; Zheng, M.; Cai, F. Strontium doping promotes low-temperature growth of single-crystalline Ni-rich cathodes with enhanced electrochemical performance. *Materials* **2025**, *18*, 1320. [[CrossRef](#)] [[PubMed](#)]
521. Jeong, S.; Park, S.; Park, J.; Beak, M.; Lee, J.; Kwon, E.E.; Kwon, K. The enhancement of cyclability of Ni-rich $\text{LiNi}_{0.9}\text{Co}_{0.05-x}\text{Mn}_{0.05}\text{Zn}_x$ cathode materials by the substitution of Zn for Co. *Int. J. Energy Res.* **2022**, *46*, 19177. [[CrossRef](#)]
522. Kang, Y.; Zhang, Y.; Zhao, L.; Zhang, Y.; Tang, H.; Xu, Y.; Tan, Y.; Hou, X.; Wang, J. Improving the electrochemical performance of Ag-doped Ni-rich $\text{Li}(\text{Ni}_{0.88}\text{Co}_{0.09}\text{Al}_{0.03})_{1-x}\text{O}_2$ layered cathode material. *Appl. Phys. A* **2025**, *131*, 177. [[CrossRef](#)]
523. Hu, Y.; Qin, Z.; Pei, J.; Cong, B.; Yang, X.; Chen, G. Reduced lithium/nickel disorder degree of sodium-doped lithium-rich layered oxides for cathode materials: Experiments and calculations. *ChemElectroChem* **2020**, *7*, 246–251. [[CrossRef](#)]
524. Li, S.-C.; Liu, Y.-Y.; Zhang, Y.-G.; He, W.; Zheng, H.-F.; Guo, W.-B.; Wu, H.-L.; Gao, G.-Y.; Sa, B.-S.; Wang, L.-S.; et al. Interfacial oxygen coordination environment regulation towards high-performance Li-rich layered oxide cathode. *Chem. Eng. J.* **2023**, *462*, 142194. [[CrossRef](#)]
525. Li, C.-F.; Chen, L.-D.; Wu, L.; Liu, Y.; Hu, Z.-Y.; Cui, W.-J.; Dong, W.-D.; Liu, X.; Yu, W.-B.; Li, Y.; et al. Directly revealing the structure-property correlation in Na^+ -doped cathode materials. *Appl. Surf. Sci.* **2023**, *612*, 155810. [[CrossRef](#)]
526. Chen, Y.H.; Zhang, J.; Li, Y.; Zhang, Y.F.; Huang, S.P.; Lin, W.; Chen, W.K. Effects of doping high-valence transition metal (V, Nb and Zr) ions on the structure and electrochemical performance of LIB cathode material $\text{LiNi}_{0.8}\text{Co}_{0.1}\text{Mn}_{0.1}\text{O}_2$. *Phys. Chem. Chem. Phys.* **2021**, *23*, 11528–11537. [[CrossRef](#)]
527. Li, X.; Lai, T.; Sheng, A.; Yang, J.; Li, Y.; Xiao, S.; Li, W.; Tan, H.; Huang, B. Effects of Nb-doping on cycle life, self-discharge and crack resistance of Ni-rich $\text{LiNi}_{0.94}\text{Co}_{0.02}\text{Al}_{0.04}\text{O}_2$ cathode for Li-ion batteries. *J. Energy Storage* **2023**, *72*, 108262. [[CrossRef](#)]
528. Li, L.; Huang, Y.; Liu, Z.; Zhao, N.; Liang, H.; Zhou, M.; Zou, K.; Tan, L.; Ning, T. Revealing the mechanism of Zr coating modification on Ni-rich cathode materials through solid-phase diffusion. *Chin. Chem. Lett.* **2025**, *111079*. [[CrossRef](#)]
529. Välikangas, J.; Laine, P.; Hietaniemi, M.; Hu, T.; Selent, M.; Tynjälä, P.; Lassi, U. Correlation of aluminum doping and lithiation temperature with electrochemical performance of $\text{LiNi}_{1-x}\text{Al}_x\text{O}_2$ cathode material. *J. Solid State Electrochem.* **2023**, *27*, 641–654. [[CrossRef](#)]
530. Lu, Y.; Jin, H.; Mo, Y.; Qu, Y.; Du, B.; Chen, Y. Synthesis and characterization of Cu-doped $\text{LiNi}_{0.6}\text{Co}_{0.2}\text{Mn}_{0.2}\text{O}_2$ materials for Li-ion batteries. *J. Alloys Compd.* **2020**, *844*, 156180. [[CrossRef](#)]
531. Ryu, H.-H.; Park, N.-Y.; Seo, J.-H.; Yu, Y.-S.; Sharma, M.; Mucke, R.; Kaghazchi, P.; Yoon, C.-S.; Sun, Y.-K. A highly stabilized Ni-rich NCA cathode for high-energy lithium-ion batteries. *Mater. Today* **2020**, *36*, 73–82. [[CrossRef](#)]
532. Wu, C.Y.; Bao, Q.; Tsai, Y.T.; Duh, J.G. Tuning (003) interplanar space by boric acid co-sintering to enhance Li^+ storage and transfer in $\text{Li}(\text{Ni}_{0.8}\text{Co}_{0.1}\text{Mn}_{0.1})\text{O}_2$ cathode. *J. Alloys Compd.* **2021**, *865*, 158806. [[CrossRef](#)]
533. Liu, Y.; Fan, X.-M.; Luo, B.; Zhao, Z.-W.; Shen, J.-X.; Liu, Z.-H.; Xiao, Z.-M.; Zhang, B.; Zhang, J.-F.; Ming, L. Understanding the enhancement effect of boron doping on the electrochemical performance of single-crystalline Ni-rich cathode materials. *J. Colloid Interface Sci.* **2021**, *604*, 776–784. [[CrossRef](#)]
534. Roitzheim, C.; Kuo, L.-Y.; Sohn, Y.J.; Finsterbusch, M.; Möller, S.; Sebold, D.; Valencia, H.; Meledina, M.; Mayer, J.; Breuer, U.; et al. Boron in Ni-rich NMC811 cathode material: Impact on atomic and microscale properties. *ACS Appl. Energy Mater.* **2022**, *5*, 524–538. [[CrossRef](#)]
535. Zhao, R.; Yang, Z.; Liang, J.; Lu, D.; Liang, C.; Guan, X.; Gao, A.; Chen, H. Understanding the role of Na-doping on Ni-rich layered oxide $\text{LiNi}_{0.5}\text{Co}_{0.2}\text{Mn}_{0.3}\text{O}_2$. *J. Alloys Compd.* **2016**, *689*, 318–325. [[CrossRef](#)]

536. Shen, Y.; Yao, X.; Zhang, J.; Wang, S.; Zhang, D.; Yin, D.; Wang, L.; Zhang, Y.; Hu, J.; Cheng, Y.; et al. Sodium doping derived electromagnetic center of lithium layered oxide cathode materials with enhanced lithium storage. *Nano Energy* **2022**, *94*, 106900. [[CrossRef](#)]
537. He, T.; Chen, L.; Su, Y.; Lu, Y.; Bao, L.; Chen, G.; Zhang, Q.; Chen, S.; Wu, F. The effects of alkali metal ions with different ionic radii substituting in Li sites on the electrochemical properties of Ni-Rich cathode materials. *J. Power Sources* **2019**, *441*, 22719. [[CrossRef](#)]
538. Vanaphuti, P.; Chen, J.; Cao, J.; Bigham, K.; Chen, B.; Yang, L.; Chen, H.; Wang, Y. Enhanced electrochemical performance of the lithium-manganese-rich cathode for Li-ion batteries with Na and F co-doping. *ACS Appl. Mater. Interfaces* **2019**, *11*, 37842–37849. [[CrossRef](#)]
539. Kim, Y.S.; Kim, J.H.; Sun, Y.K.; Yoon, C.S. Evolution of a radially aligned microstructure in boron-doped $\text{LiNi}_{0.95}\text{Co}_{0.04}\text{Al}_{0.01}\text{O}_2$ cathode particles. *ACS Appl. Mater. Interfaces* **2022**, *14*, 17500–17508. [[CrossRef](#)]
540. Kim, H.; Kim, S.-B.; Park, D.-H.; Park, K.-W. Fluorine-doped $\text{LiNi}_{0.8}\text{Mn}_{0.1}\text{Co}_{0.1}\text{O}_2$ cathode for high-performance lithium-ion batteries. *Energies* **2020**, *13*, 4808. [[CrossRef](#)]
541. Qiu, Q.-Q.; Yuan, S.-S.; Bao, J.; Wang, Q.-C.; Yue, X.-Y.; Li, X.-L.; Wu, X.-J.; Zhou, Y.-N. Suppressing irreversible phase transition and enhancing electrochemical performance of Ni-rich layered cathode $\text{LiNi}_{0.9}\text{Co}_{0.05}\text{Mn}_{0.05}\text{O}_2$ by fluorine substitution. *J. Energy Chem.* **2021**, *61*, 574–581. [[CrossRef](#)]
542. Wang, J.; Liu, C.; Xu, G.; Miao, C.; Wen, M.; Xu, M.; Wang, C.; Xiao, W. Strengthened the structural stability of *in-situ* F^- doping Ni-rich $\text{LiNi}_{0.8}\text{Co}_{0.15}\text{Al}_{0.05}\text{O}_2$ cathode materials for lithium-ion batteries. *Chem. Eng. J.* **2022**, *438*, 135537. [[CrossRef](#)]
543. Ahn, S.-Y.; Park, D.-H.; Kim, J.-H.; Jang, J.-S.; Kim, W.-C.; Lee, G.-I.; Lim, J.-W.; Hong, J.-M.; Park, K.-W. F-doped Co-free $\text{LiNi}_x\text{Mn}_{1-x}\text{O}_2$ ($0.7 \leq x \leq 0.9$) cathodes for ameliorating electrochemical performance of Li-ion batteries. *Mater. Today Energy* **2024**, *41*, 101520. [[CrossRef](#)]
544. Azhari, L.; Sousa, B.; Ahmed, R.; Wang, R.; Yang, Z.; Gao, G.; Han, Y.; Wang, Y. Stability enhancement and microstructural modification of Ni-rich cathodes via halide doping. *ACS Appl. Mater. Interfaces* **2022**, *14*, 46523–46536. [[CrossRef](#)]
545. Eilers-Rethwisch, M.; Winter, M.; Schappacher, F.M. Synthesis, electrochemical investigation and structural analysis of doped $\text{Li}[\text{Ni}_{0.6}\text{Mn}_{0.2}\text{Co}_{0.2-x}\text{M}_x]\text{O}_2$ ($x = 0, 0.05$; M = Al, Fe, Sn) cathode materials. *J. Power Sources* **2018**, *387*, 101–107. [[CrossRef](#)]
546. Eilers-Rethwisch, M.; Hildebrand, S.; Evertz, M.; Ibing, L.; Dagger, T.; Winter, M.; Schappacher, F.M. Comparative study of Sn-doped $\text{Li}[\text{Ni}_{0.6}\text{Mn}_{0.2}\text{Co}_{0.2-x}\text{Sn}_x]\text{O}_2$ cathode active materials ($x = 0 – 0.5$) for lithium ion batteries regarding electrochemical performance and structural stability. *J. Power Sources* **2018**, *397*, 68–78. [[CrossRef](#)]
547. Li, Z.; Yu, X.; Lv, Y.; Qi, L.; Ma, Y.; Zhang, H.; Song, D.; Shi, X.; Zhang, L. Investigation on the structure and electrochemical performance of $\text{LiNi}_{0.8}\text{Co}_{0.1}\text{Mn}_{0.1}\text{O}_2$ modified with Sn. *Electrochim. Acta* **2021**, *400*, 139468. [[CrossRef](#)]
548. Angellinnov, F.; Subhan, A.; Drew, A.J.; Syahrial, A.Z. Synthesis of Sn doped and rice husk derived activated carbon surface coating NMC 811 through solution combustion method. *Heliyon* **2024**, *10*, e23199. [[CrossRef](#)]
549. Huang, Z.J.; Wang, Z.X.; Zheng, X.B.; Guo, H.; Li, X.; Jing, Q.; Yang, Z. Effect of Mg doping on the structural and electrochemical performance of $\text{LiNi}_{0.6}\text{Co}_{0.2}\text{Mn}_{0.2}\text{O}_2$ cathode materials. *Electrochim. Acta* **2015**, *182*, 795–802. [[CrossRef](#)]
550. Zhou, K.; Xie, Q.; Li, B.; Manthiram, A. An in-depth understanding of the effect of aluminum doping in high-nickel cathodes for lithium-ion batteries. *Energy Storage Mater.* **2021**, *34*, 229–240. [[CrossRef](#)]
551. Yi, M.; Dolocan, A.; Manthiram, A. Stabilizing the interphase in cobalt-free, ultrahigh-nickel cathodes for lithium-ion batteries. *Adv. Funct. Mater.* **2023**, *33*, 2213164. [[CrossRef](#)]
552. Park, N.; Kim, S.; Kim, M.; Han, S.; Kim, D.; Kim, M.; Sun, Y. Mechanism of doping with high-valence elements for developing Ni-rich cathode materials. *Adv. Energy Mater.* **2023**, *13*, 2301530. [[CrossRef](#)]
553. Zybert, M.; Rondura, H.; Rarog-Pilecka, W.; Wieczorek, W. Application of rare earth elements as modifiers for Ni-rich cathode materials for Li-ion batteries: A mini review. *Front. Energy Res.* **2023**, *11*, 1248641. [[CrossRef](#)]
554. Kim, U.H.; Jun, D.-W.; Park, K.-J.; Zhang, Q.; Kaghazchi, P.; Aurbach, D.; Major, D.T.; Goobes, G.; Dixit, M.; Leifer, N.; et al. Pushing the limit of layered transition metal oxide cathodes for high-energy density rechargeable Li ion batteries. *Energy Environ. Sci.* **2018**, *11*, 1271–1279. [[CrossRef](#)]
555. Cheng, L.; Zhao, Y.; Huang, B.; Zho, Z.; Li, Y.; Li, W. Effects of W-doping on precursor growth of $\text{LiNi}_{0.88}\text{Co}_{0.09}\text{Mn}_{0.03}\text{O}_2$ and its electrochemical performance. *Trans. Nonferr. Met. Soc. China* **2024**, *34*, 1251–1262. [[CrossRef](#)]
556. Zhu, H.; Wang, Z.; Chen, L.; Hu, Y.; Jiang, H.; Li, C. Strain engineering of Ni-rich cathode enables exceptional cyclability in pouch-type full cells. *Adv. Mater.* **2023**, *35*, 2209357. [[CrossRef](#)]
557. Wu, J.; Zhu, H.; Yu, H.; Wang, Z.; Jiang, H.; Li, C. Enhancing surface and crystal stability of the Ni-high NCA cathode for high-energy and durable lithium-ion batteries. *Ind. Eng. Chem. Res.* **2022**, *61*, 2817–2824. [[CrossRef](#)]
558. Chu, M.; Huang, Z.; Zhang, T.; Wang, R.; Shao, T.; Wang, C.; Zhu, W.; He, L.; Chen, J.; Zhao, W.; et al. Enhancing the electrochemical performance and structural stability of Ni-rich layered cathode materials via dual-site doping. *ACS Appl. Mater. Interfaces* **2021**, *13*, 19950–19958. [[CrossRef](#)]

559. Zhang, L.; Liu, D.; Huang, J.; Peng, J.; Xie, H.; Huang, B.; Li, Y.; Sun, Y.; Xiao, S.; Wang, R. Effective reinforcement on the structural stability and electrochemical performances of ultra-high nickel cobalt free cathode material by co-doping. *J. Energy Storage* **2024**, *78*, 110073. [[CrossRef](#)]
560. Yao, Z.; Lum, Y.; Johnston, A.; Mejia-Mendoza, L.M.; Zhou, X.; Wen, Y.; Aspuru-Guzik, A.; Sargent, E.H.; She, Z.W. Machine learning for a sustainable energy future. *Nat. Rev. Mater.* **2022**, *8*, 202–215. [[CrossRef](#)] [[PubMed](#)]
561. Kim, M.; Kang, S.; Park, H.G.; Park, K.; Min, K. Maximizing the energy density and stability of Ni-rich layered cathode materials with multivalent dopants via machine learning. *Chem. Eng. J.* **2023**, *452*, 139254. [[CrossRef](#)]
562. Zhang, H.; Zhang, J. An overview of modification strategies to improve $\text{LiNi}_{0.8}\text{Co}_{0.1}\text{Mn}_{0.1}\text{O}_2$ (NMC811) cathode performance for automotive lithium-ion batteries. *eTransportation* **2021**, *7*, 100105. [[CrossRef](#)]
563. Zha, G.; Hu, W.; Agarwal, S.; Ouyang, C.; Hu, N.; Hou, H. High performance layered $\text{LiNi}_{0.8}\text{Co}_{0.07}\text{Fe}_{0.03}\text{Mn}_{0.1}\text{O}_2$ cathode materials for Li-ion battery. *Chem. Eng. J.* **2021**, *409*, 128343. [[CrossRef](#)]
564. Kondrakov, A.O.; Schmidt, A.; Xu, J.; Geßwein, H.; Mönig, R.; Hartmann, P.; Sommer, H.; Brezesinski, T.; Janek, J. Anisotropic lattice strain and mechanical degradation of high- and low-nickel NCM cathode materials for Li-ion batteries. *J. Phys. Chem. C* **2017**, *121*, 3286–3294. [[CrossRef](#)]
565. Jo, E.; Park, J.-H.; Park, J.; Hwang, J.; Chung, K.Y.; Nam, K.-W.; Kim, S.M.; Chang, W. Different thermal degradation mechanisms: Role of aluminum in Ni-rich layered cathode materials. *Nano Energy* **2020**, *78*, 105367. [[CrossRef](#)]
566. Jung, S.H.; Kim, U.-H.; Kim, J.-H.; Jun, S.; Yoon, C.S.; Jung, Y.S.; Sun, Y.-K. Ni-rich layered cathode materials with electrochemomechanically compliant microstructures for all-solid-state Li batteries. *Adv. Energy Mater.* **2020**, *10*, 1903360. [[CrossRef](#)]
567. Ikuerowo, T.O.; Tomomewo, O.; Akande, S.O. Unlocking the potential of Ni-rich $\text{LiNi}_{0.9}\text{Co}_{0.1}\text{O}_2$ cathodes: A DFT investigation of performance-limiting factors. *Phys. Chem. Chem. Phys.* **2025**, *27*, 1494–1502. [[CrossRef](#)]
568. Yang, K.; Yi, Y.; Yi, Z.; Yang, C.; Liu, F.; Wang, K.; Cao, J.; Chen, Z. Regulating the internal structure by magnesium doping to enhance cycle stability of full-concentration-gradient Ni-rich layered cathodes. *Chem. Eng. J.* **2023**, *474*, 145554. [[CrossRef](#)]
569. Jamil, S.; Yue, L.; Li, C.; Fasehullah, M.; Aizaz Uddin, M.; Yang, W.; Bao, S.; Xu, M. Significance of gallium doping for high Ni, low Co/Mn layered oxide cathode material. *Chem. Eng. J.* **2022**, *441*, 135821. [[CrossRef](#)]
570. Bunyanidhi, P.; Phattharasupakun, N.; Duangdangchote, S.; Prempluem, S.; Joraleechanchai, N.; Sawangphruk, M. Exploring the impact of metal oxide coating and metal atom doping on the electrochemical performance of Ni-rich cathode materials. *J. Mater. Chem. A* **2023**, *11*, 23223–23227. [[CrossRef](#)]
571. Gao, D.; Che, W.; Xu, Q.; Zhao, X.; Huang, Y.; Chang, C. W doping improves the electrochemical performance of $\text{LiNi}_{0.94}\text{Co}_{0.04}\text{Al}_{0.02}\text{O}_2$ cathode through dual enhanced electronic and ionic conductivities: A study from DFT calculations and experimental results. *Scr. Mater.* **2023**, *234*, 115586. [[CrossRef](#)]
572. Yang, J.; Gao, D.; Zhang, D.; Chang, C. Effect of dual improved electronic and cationic conductivity via W doping on cyclability and rate performance of $\text{LiNi}_{0.90}\text{Co}_{0.04}\text{Mn}_{0.03}\text{Al}_{0.03}\text{O}_2$ cathode for rechargeable LiBs. *J. Energy Storage* **2023**, *63*, 107088. [[CrossRef](#)]
573. Liu, B.; Liu, J.; Yang, J.; Wang, D.; Ye, C.; Wang, D.; Avdeev, M.; Shi, S.; Yang, J.; Zhang, W. Ab initio thermodynamic optimization of Ni-rich Ni–Co–Mn oxide cathode coatings. *J. Power Sources* **2020**, *450*, 227693. [[CrossRef](#)]
574. Zheng, X.; Yu, R.; Sun, J.; Chen, Y.; Chen, J.; He, J.; Zhang, Y.; Han, B.; Liao, G.; Wu, J.S.; et al. Precursor-oriented ultrathin Zr-based gradient coating on Ni-riched cathodes. *Nano Energy* **2023**, *105*, 108000. [[CrossRef](#)]
575. Hu, S.; Wang, J.; Lu, Y.; Yang, L.; Xiong, L.; Zhao, S.; Bai, L.; Huang, C.; Zhou, C.; Zhu, J.; et al. An epitaxial coating with preferred orientation stabilizing High-Energy Ni-Rich NCA cathodes. *Appl. Surf. Sci.* **2022**, *579*, 152183. [[CrossRef](#)]
576. Lee, H.B.; Hoang, T.D.; Byeon, Y.S.; Jung, H.; Moon, J.; Park, M.S. Surface stabilization of Ni-rich layered cathode materials via surface engineering with LiTaO_3 for lithium-ion batteries. *ACS Appl. Mater. Interfaces* **2022**, *14*, 2731–2741. [[CrossRef](#)] [[PubMed](#)]
577. Wang, J.; Yuan, Q.; Ren, Z.; Sun, C.; Zhang, J.; Wang, R.; Qian, M.; Shi, Q.; Shao, R.; Mu, D.; et al. Thermochemical cyclization constructs bridged dual-coating of Ni-rich layered oxide cathodes for high-energy Li-ion batteries. *Nano Lett.* **2022**, *22*, 5221–5229. [[CrossRef](#)]
578. Cho, H.; Kim, J.; Kim, M.; An, H.; Min, K.; Park, K. A review of problems and solutions in Ni-rich cathode-based Li-ion batteries from two research aspects: Experimental studies and computational insights. *J. Power Sources* **2024**, *597*, 234132. [[CrossRef](#)]
579. Wang, Y.; Huang, X.; Ji, W.; Wu, Y.; Zhao, S.; Li, Y.; Zhou, N. Insights into the doping rules of heteroatom on Ni-rich ternary cathode stability by integrating high throughput calculation and machine learning. *J. Energy Chem.* **2025**, *106*, 161–172. [[CrossRef](#)]
580. Xu, X.; Liu, J.; Wang, B.; Wang, J.; Wang, Y.; Meng, W.; Cai, F. A Study on the microstructure regulation effect of niobium doping on $\text{LiNi}_{0.88}\text{Co}_{0.05}\text{Mn}_{0.07}\text{O}_2$ and the electrochemical performance of the composite material under high voltage. *Materials* **2024**, *17*, 2127. [[CrossRef](#)] [[PubMed](#)]
581. Park, G.-T.; Park, N.-Y.; Noh, T.-C.; Namkoong, B.; Ryu, H.-H.; Shin, J.-Y.; Beierling, T.; Yoon, C.S.; Sun, Y.-K. High-performance Ni-rich $\text{Li}[\text{Ni}_{0.9-x}\text{Co}_{0.1}\text{Al}_x]\text{O}_2$ cathodes via multi-stage microstructural tailoring from hydroxide precursor to the lithiated oxide. *Energy Environ. Sci.* **2021**, *14*, 5084–5095. [[CrossRef](#)]
582. Park, N.-Y.; Ryu, H.-H.; Park, G.-T.; Noh, T.-C.; Sun, Y.-K. Optimized Ni-rich NCMA cathode for electric vehicle batteries. *Adv. Energy Mater.* **2021**, *11*, 2003767. [[CrossRef](#)]

583. Park, N.-Y.; Ryu, H.-H.; Kuo, L.-Y.; Kaghazchi, P.; Yoon, C.S.; Sun, Y.-K. High-energy cathodes via precision microstructure tailoring for next-generation electric vehicles. *ACS Energy Lett.* **2021**, *6*, 4195–4202. [[CrossRef](#)]
584. Ryu, H.-H.; Park, N.-Y.; Yoon, D.R.; Kim, U.-H.; Yoon, C.S.; Sun, Y.-K. New class of Ni-rich cathode materials $\text{Li}[\text{Ni}_x\text{Co}_y\text{B}_{1-x-y}]\text{O}_2$ for next lithium batteries. *Adv. Energy Mater.* **2020**, *10*, 2000495. [[CrossRef](#)]
585. Wang, S.; Zhou, X.; Zhao, T.; Peng, J.; Zhang, B.; Xing, W.; Zuo, M.; Zhang, P.; Fan, W.; Lv, G.; et al. Precise regulation of particle orientation for Ni-rich cathodes with ultra-long cycle life. *Nano Energy* **2024**, *129*, 110008. [[CrossRef](#)]
586. Meng, Z.; Ma, X.; Azhari, L.; Hou, J.; Wang, Y. Morphology controlled performance of ternary layered oxide cathodes. *Commun. Mater.* **2023**, *4*, 90. [[CrossRef](#)]
587. Wu, Z.-W.; Zhou, Y.; Hai, C.-X.; Zeng, J.-B.; Ren, X.-F.; Sun, Y.-X.; Shen, Y.; Li, X.; Dong, S.-D.; Zhang, G.-T. Improving electrochemical performance of NMC811 cathodes for lithium-ion batteries via consistently arranging the hexagonal nanosheets with exposed {104} facets. *Ceram. Int.* **2022**, *48*, 17279–17288. [[CrossRef](#)]
588. Shang, M.; Han, E.; Tian, Y.; He, Y.; Sun, L.; Zhu, L. The effects of multiple metals (K, Cu, Al) substitution on $\text{LiNi}_{0.66}\text{Co}_{0.20}\text{Mn}_{0.14}\text{O}_2$ for lithium-ion batteries. *Ionics* **2020**, *26*, 2699–2713. [[CrossRef](#)]
589. Ahaliabadeh, Z.; Kong, X.; Fedorovskaya, E.; Kallio, T. Extensive comparison of doping and coating strategies for Ni-rich positive electrode materials. *J. Power Sources* **2022**, *540*, 231633. [[CrossRef](#)]
590. Darjazi, H.; Gonzalo, E.; Acebedo, B.; Cid, R.; Zarrabeitia, M.; Bonilla, F.; Munoz-Marquez, M.A.; Nobili, F. Improving high-voltage cycling performance of nickel-rich NMC layered oxide cathodes for rechargeable lithium-ion batteries by Mg and Zr co-doping. *Mater. Today Sustain.* **2022**, *20*, 100236. [[CrossRef](#)]
591. Zhang, B.; Zheng, C.; Xiao, Z.; Xian, K.; Wen, H.; Lu, N.; He, X.; Ye, L.; Wang, J.; Ou, X.; et al. Synergistic doping chemistry enable the cycling properties of single-crystal Ni-rich cathode for lithium-ion batteries. *Appl. Surface Sci.* **2025**, *684*, 161839. [[CrossRef](#)]
592. Zhang, H.; Yu, H.; Chen, L.; Demir, M.; Cheng, Q.; Jiang, H. Limiting cationic mixing and lattice oxygen loss of single-crystalline Ni-rich Co-poor cathodes for high-voltage Li-ion batteries. *Green Energy Environ.* **2025**. [[CrossRef](#)]
593. Yao, W.; Liu, Y.; Li, D.; Zhang, Q.; Zhong, S.; Cheng, H.; Yan, Z. Synergistically enhanced electrochemical performance of Ni-rich cathode materials for lithium-ion batteries by K and Ti Co-modification. *J. Phys. Chem. C* **2020**, *124*, 2346–2356. [[CrossRef](#)]
594. He, X.; Shen, J.; Zhang, B.; Xiao, Z.; Ye, L.; Mao, Q.; Zhong, Q.; Ou, X. Surface $\text{Li}^+/\text{Ni}^{2+}$ antisite defects construction for achieving high-voltage stable single-crystal Ni-rich cathode by anion/cation co-doping. *Adv. Func. Mater.* **2024**, *34*, 2401300. [[CrossRef](#)]
595. Yang, K.; Chen, Z.; Yang, C.; Shi, W.; Yang, Y.; Yin, C.; Yi, Y.; Cao, J. Aluminium–sodium targeted co-doping to boost the electrochemical stability of full concentration gradient Ni-rich $\text{LiNi}_{0.80}\text{Co}_{0.05}\text{Mn}_{0.15}\text{O}_2$ cathodes. *J. Colloid Interface Sci.* **2025**, *683*, 335–346. [[CrossRef](#)]
596. Xiang, W.; Zhu, C.-Q.; Zhang, J.; Shi, H.; Liang, Y.T.; Yu, M.H.; Zhu, X.-M.; He, F.-R.; Lv, G.-P.; Guo, X.-D. Synergistic coupling effect of sodium and fluorine co-substitution on enhancing rate capability and cycling performance of Ni-rich cathode for lithium-ion battery. *J. Alloys Compd.* **2019**, *786*, 56–64. [[CrossRef](#)]
597. Wang, Z.; Wang, J.; Shi, H.; Wang, C.; Li, W.; Wang, Z.; Zhang, W.; Xiong, Z.; Gao, Y.; Yan, X. Synergistic effect of B-Nb co-modified to achieve crystal structure and interface tuning for Ni-rich cathode. *Electrochim. Acta* **2024**, *474*, 143475. [[CrossRef](#)]
598. Li, J.; Yang, H.; Deng, Q.; Li, W.; Zhang, Q.; Zhang, Z.; Chu, Y.; Yang, C. Stabilizing Ni-rich Single-crystalline $\text{LiNi}_{0.83}\text{Co}_{0.07}\text{Mn}_{0.10}\text{O}_2$ Cathodes using Ce/Gd Co-doped High-entropy Composite Surfaces. *Angew. Chem. Int. Ed.* **2024**, *63*, e202318042. [[CrossRef](#)]
599. Park, J.; Yim, T. Boron- and calcium-interspersed cathode-electrolyte interphases on Ni-rich layered oxide cathodes for advanced performance lithium-ion batteries. *Appl. Surface Sci.* **2024**, *663*, 160195. [[CrossRef](#)]
600. Usman, A.; Murtaza, G.; Ayyaz, A.; Al-Muhimeed, T.; Farid, G. Synthesis, characterization, and evaluation of improved electrochemical performance of vanadium and zinc co-doped Ni-rich oxide cathode materials: Experimental and first-principles study. *Ionics* **2024**, *30*, 5989–6001. [[CrossRef](#)]
601. Wu, F.; Liu, N.; Chen, L.; Li, N.; Lu, Y.; Cao, D.; Xu, M.; Wang, Z.; Su, Y. A universal method for enhancing the structural stability of Ni-rich cathodes via the synergistic effect of dual-element cosubstitution. *ACS Appl. Mater. Interfaces* **2021**, *13*, 24925–24936. [[CrossRef](#)]
602. Si, Z.; Shi, B.; Huang, J.; Yu, Y.; Han, Y.; Zhang, J.; Li, W. Titanium and fluorine synergistic modification improves the electrochemical performance of $\text{Li}(\text{Ni}_{0.8}\text{Co}_{0.1}\text{Mn}_{0.1})\text{O}_2$. *J. Mater. Chem. A* **2021**, *9*, 9354–9363. [[CrossRef](#)]
603. Sun, W.; Zhang, Q.; Sun, X.-G.; Li, C.; Huang, Y.; Mu, W.; Tan, J.; Li, J.; Liu, K.; Zheng, S.; et al. An epitaxial surface heterostructure anchoring approach for high-performance Ni-rich layered cathodes. *J. Energy Chem.* **2025**, *105*, 158–169. [[CrossRef](#)]
604. Mao, D.; Tan, X.; Fan, Z.; Song, L.; Zhang, Y.; Zhang, P.; Su, S.; Liu, G.; Wang, H.; Chu, W. Unveiling the roles of trace Fe and F Co-doped into high-Ni Li-rich layered oxides in performance improvement. *ACS Appl. Mater. Interfaces* **2023**, *15*, 10774–10784. [[CrossRef](#)]
605. Lv, Y.; Huang, S.; Lu, S.; Jia, T.; Liu, Y.; Ding, W.; Yu, X.; Kang, F.; Zhang, J.; Cao, Y. Engineering of cobalt-free Ni-rich cathode material by dual-element modification to enable 4.5 V-class high-energy-density lithium-ion batteries. *Chem. Eng. J.* **2023**, *455*, 140652. [[CrossRef](#)]

606. Park, H.G.; Min, K.; Park, K. A synergistic effect of Na^+ and Al^{3+} Dual doping on electrochemical performance and structural stability of $\text{LiNi}_{0.88}\text{Co}_{0.08}\text{Mn}_{0.04}\text{O}_2$ cathodes for Li-ion batteries. *ACS Appl. Mater. Interfaces* **2022**, *14*, 5168–5176. [CrossRef]
607. Peng, F.; Chu, Y.; Li, Y.; Pan, Q.; Yang, G.; Zhang, L.; Hu, S.; Zheng, F.; Wang, H.; Li, Q. Mg,Ti-base surface integrated layer and bulk doping to suppress lattice oxygen evolution of Ni-rich cathode material at a high cut-off voltage. *J. Energy Chem.* **2022**, *71*, 434–444. [CrossRef]
608. Zhang, Y.D.; Liu, J.D.; Xu, W.C.; Lu, Y.; Ma, H.; Cheng, F.Y.; Chen, J. Gradient doping Mg and Al to stabilize Ni-rich cathode materials for rechargeable lithium-ion batteries. *J. Power Sources* **2022**, *535*, 231445. [CrossRef]
609. Zhang, H.; Qin, L.; Sedlacik, M.; Saha, P.; Cheng, Q.; Yu, H.; Jiang, H. Enhanced Li-ion intercalation kinetics and lattice oxygen stability in single-crystalline Ni-rich Co-poor layered cathodes. *J. Mater. Chem. A* **2024**, *12*, 3682–3688. [CrossRef]
610. Jamil, S.; Bin Yousaf, A.; Yoon, S.H.; Han, D.S.; Yang, L.; Kasak, P.; Wang, X. Dual cationic modified high Ni-low co layered oxide cathode with a heteroepitaxial interface for high energy-density lithium-ion batteries. *Chem. Eng. J.* **2021**, *416*, 129118. [CrossRef]
611. Ziraki, S.; Kanani, M.; Hashemi, B.; Loghavi, M.M. Effect of sodium and yttrium co-doping on electrochemical performance of $\text{LiNi}_{0.8}\text{Co}_{0.15}\text{Al}_{0.05}\text{O}_2$ cathode material for Li-ion batteries: Computational and experimental investigation. *J. Energy Storage* **2023**, *70*, 107983. [CrossRef]
612. Feng, H.; Xu, Y.; Zhou, Y.; Song, J.; Yang, J.; Tan, Q. The Y^{3+} and W^{6+} co-doping into Ni-rich Co-free single-crystal cathode $\text{LiNi}_{0.9}\text{Mn}_{0.1}\text{O}_2$ for achieving high electrochemical properties in lithium-ion batteries. *J. Alloys Compd.* **2024**, *976*, 173043. [CrossRef]
613. Zhang, B.; Wen, H.; Xian, K.; Lu, N.; Zheng, C.; Xiao, Z.; He, X.; Ye, L.; Wang, J.; Ming, L.; et al. Synergistically regulating the structural tolerance of Co-free Ni-rich cathode materials at high-rate through multi-heteroatoms substitution. *J. Colloid Interface Sci.* **2025**, *682*, 589–598. [CrossRef]
614. Shen, J.; Li, H.; Qi, H.; Lin, Z.; Li, Z.; Zheng, C.; Du, W.; Chen, H.; Zhang, S. Enhancing thermodynamic stability of single-crystal Ni-rich cathode material via a synergistic dual-substitution strategy. *J. Energy Chem.* **2024**, *88*, 428–436. [CrossRef]
615. Vanaphuti, P.; Bai, J.; Ma, L.; Ehrlich, S.; Kisslinger, K.; Wang, F.; Wang, Y. Unraveling Na and F coupling effects in stabilizing Li, Mn-rich layered oxide cathodes via local ordering modification. *Energy Storage. Mater.* **2020**, *31*, 459–469. [CrossRef]
616. Ko, G.; Park, S.; Kim, W.; Kwon, K. Synergistic effect of Na and Al co-doping on the electrochemical properties of $\text{Li}[\text{Ni}_{0.8}\text{Mn}_{0.1}\text{Co}_{0.1}]\text{O}_2$ cathode materials for Li-ion batteries. *J. Alloys Compd.* **2022**, *925*, 166678. [CrossRef]
617. Liu, Z.-C.; Wang, F.; Wang, W.-N.; Liu, S.; Gao, X.-P. Enhancing structural rigidity of ultrahigh-Ni oxide through Al and Nb dual-bulk-doping for high-voltage lithium-ion batteries. *Small Methods* **2024**, *8*, 2400224. [CrossRef] [PubMed]
618. Lee, S.-B.; Park, N.-Y.; Park, G.-T.; Kim, U.-H.; Sohn, S.-J.; Kang, M.-S.; Ribas, R.M.; Monteiro, R.S.; Sun, Y.-K. Doping strategy in developing Ni-rich cathodes for high-performance lithium-ion batteries. *ACS Energy Lett.* **2024**, *9*, 740–747. [CrossRef]
619. Zhu, C.; Xu, M.; Huang, K.; Lian, C.; Su, H.; Liu, H. Al- and Nb-comodified Ni-rich NCM cathode for high-performance lithium-ion batteries. *Ind. Eng. Chem. Res.* **2024**, *63*, 2740–2749. [CrossRef]
620. Seo, J.-H.; Kim, U.-H.; Sun, Y.-K.; Yoon, C.-S. Multi-doped (Ga, B) $\text{Li}[\text{Ni}_{0.885}\text{Co}_{0.100}\text{Al}_{0.015}]\text{O}_2$ cathode. *J. Electrochem. Soc.* **2020**, *167*, 100557. [CrossRef]
621. Wang, Y.; Wang, Y.; Liu, S.; Li, G.; Zhou, Z.; Xu, N.; Wu, M.; Gao, X. Building the stable oxygen framework in high-Ni layered oxide cathode for high-energy-density Li-ion batteries. *Energy Environ. Mater.* **2022**, *5*, 1260–1269. [CrossRef]
622. Feng, Z.; Rajagopalan, R.; Zhang, S.; Sun, D.; Tang, Y.-G.; Ren, Y.; Wang, H.-Y. A three in one strategy to achieve zirconium doping, boron doping, and interfacial coating for stable $\text{LiNi}_{0.8}\text{Co}_{0.1}\text{Mn}_{0.1}\text{O}_2$ cathode. *Adv. Sci.* **2020**, *8*, 2001809. [CrossRef]
623. Choi, C.-M.; Park, J.-H.; Sun, Y.-K.; Yoon, C.-S. Ultra-stable cycling of multi-doped (Zr,B) $\text{Li}[\text{Ni}_{0.885}\text{Co}_{0.100}\text{Al}_{0.015}]\text{O}_2$ cathode. *J. Power Sources* **2021**, *513*, 230548. [CrossRef]
624. Ming, Y.; Xiang, W.; Qiu, L.; Hua, W.-B.; Li, R.; Wu, Z.-G.; Xu, C.-L.; Li, Y.-C.; Wang, D.; Chen, Y.-X.; et al. Dual elements coupling effect induced modification from the surface into the bulk lattice for Ni-rich cathodes with suppressed capacity and voltage decay. *ACS Appl. Mater. Interfaces* **2020**, *12*, 8146–8156. [CrossRef]
625. Cheng, X.; Zhong, F.; Wang, T.; Cao, X.; Liang, M.; Liu, Y.; Wu, B.; Li, J. The dual modification of La and Zr of Ni-rich cathodes for improved cycling stability at elevated voltage and temperature. *J. Power Sources* **2024**, *612*, 234801. [CrossRef]
626. Kumar, D.; Ramesha, K. Comprehensive study of Ti and Ta co-doping in Ni-rich cathode material $\text{LiNi}_{0.8}\text{Mn}_{0.1}\text{Co}_{0.1}\text{O}_2$ towards improving the electrochemical performance. *ChemPhysChem* **2024**, *25*, e202400064. [CrossRef]
627. Guan, S.; Tao, L.; Tang, P.; Fang, R.; Wu, H.; Piao, N.; Yang, H.; Hu, G.; Geng, X.; Li, L.; et al. Regulating interfacial chemistry and kinetic behaviors of F/Mo co-doping Ni-rich layered oxide cathode for long-cycling lithium-ion batteries over $-20\text{ }^\circ\text{C}$ – $60\text{ }^\circ\text{C}$. *J. Energy Chem.* **2024**, *94*, 449–457. [CrossRef]
628. Rambukwella, I.; Firestein, K.L.; Xu, Y.; Sun, Z.; Zhang, S.; Yan, C. Unveiling the effect of molybdenum and titanium co-doping on degradation and electrochemical performance in Ni-rich cathodes. *Mater. Rep. Energy* **2025**, *5*, 100314. [CrossRef]
629. Hou, L.; Liu, Q.; Chen, X.; Yang, Q.; Zhang, F.; Mu, D.; Li, L.; Wu, F.; Chen, R. Al & Ti Synergy enhancing ionic diffusion and stabilizing lattice oxygen for the high voltage single crystal Ni-rich layered oxide cathode materials. *J. Power Sources* **2024**, *603*, 234439.

630. Han, E.; Du, X.; Yang, P.; Han, Y. The effects of copper and titanium co-substitution on $\text{LiNi}_{0.6}\text{Co}_{0.15}\text{Mn}_{0.25}\text{O}_2$ for lithium-ion batteries. *Ionics* **2018**, *24*, 393–401. [CrossRef]
631. Zhu, F.; Shi, Y.; Hu, G.; Peng, Z.; Cao, Y.; Sun, Q.; Xue, Z.; Zhang, Y.; Du, K. Enhanced electrochemical performance of $\text{LiNi}_{0.8}\text{Co}_{0.1}\text{Mn}_{0.1}\text{O}_2$ via titanium and boron co-doping. *Ceram. Int.* **2021**, *47*, 3070–3078.
632. He, Z.; Zhang, M.; Zhou, K.; Cheng, Y.; Luo, M.; Su, Y.; Hao, J.; Sun, Y.; Li, Y.; Yang, Y. Enabling excellent thermal stability of an ultrahigh nickel-rich cathode ($\text{LiNi}_{0.90}\text{Co}_{0.05}\text{Mn}_{0.05}\text{O}_2$) by a magnesium and titanium codoping strategy. *ACS Appl. Energy Mater.* **2023**, *6*, 3422–3431. [CrossRef]
633. Xie, Y.; Guo, F.; Zhang, Y. Multifunctional Ti-Mg co-doping strategy to enhance long-term cycling performance for Ni-rich cathode materials. *J. Alloys Compd.* **2024**, *981*, 173592. [CrossRef]
634. Zhou, Y.; Zhang, H.; Wang, Y.; Wan, T.; Guan, P.; Zhou, X.; Wang, X.; Chen, Y.; Shi, H.; Dou, A.; et al. Relieving stress concentration through anion–cation codoping toward highly stable nickel-rich cathode. *ACS Nano* **2023**, *17*, 20621–20633. [CrossRef]
635. Zhang, X.-Y.; Qiu, Y.-G.; Cheng, F.-Y.; Wei, P.; Li, Y.-Y.; Liu, Y.; Sun, S.-X.; Xu, Y.; Li, Q.; Fang, C.; et al. Realization of a high-voltage and high-rate nickel-rich NCM cathode material for LIBs by Co and Ti dual modification. *ACS Appl. Mater. Interfaces* **2021**, *13*, 17707–17716. [CrossRef]
636. Xiao, Z.M.; Zhang, B.; He, X.Y.; Ou, X. Cobalt/aluminum co-substitution in a $\text{LiNi}_{0.9}\text{Mn}_{0.1}\text{O}_2$ layered cathode for improving kinetics. *Chem. Commun.* **2023**, *59*, 7935–7938. [CrossRef]
637. Shi, H.; Zeng, T.; Zhang, H.; Zhou, Y.; Su, M.; Li, X.; Zhang, P.; Dou, A.; Naveed, A.; Liu, Y. Enhanced structure and electrochemical stability of single crystal nickel-rich cathode material by $\text{La}_2\text{Li}_{0.5}\text{Co}_{0.5}\text{O}_4$ surface coating. *Ceram. Int.* **2022**, *48*, 17548–17555. [CrossRef]
638. Yoon, M.; Dong, Y.-H.; Hwang, J.; Sung, J.; Cha, H.; Ahn, K.; Huang, Y.; Kang, S.-J.; Cho, J. Reactive boride infusion stabilizes Ni-rich cathodes for lithium-ion batteries. *Nat. Energy* **2021**, *6*, 362–371. [CrossRef]
639. Kim, Y.; Kim, H.; Shin, W.; Jo, E.; Manthiram, A. Insights into the microstructural engineering of cobalt-free, high-nickel cathodes based on surface energy for lithium-ion batteries. *Adv. Energy Mater.* **2023**, *13*, 2204054. [CrossRef]
640. Zeng, C.; Zheng, R.; Fan, F.; Wang, X.; Tian, G.; Liu, S.; Liu, P.; Wang, C.; Wang, S.; Shu, C. Phase compatible surface engineering to boost the cycling stability of single-crystalline Ni-rich cathode for high energy density lithium-ion batteries. *Energy Storage Mater.* **2024**, *72*, 103788. [CrossRef]
641. Kuo, L.-Y.; Roitzheim, C.; Valencia, H.; Mayer, J.; Möller, S.; Myung, S.-T.; Finsterbusch, M.; Guillon, O.; Fattakhova-Rohlfing, D.; Kaghazchi, P. Doping-induced surface and grain boundary effects in Ni-rich layered cathode materials. *Small* **2024**, *20*, 2307678. [CrossRef]
642. Guo, Y.-J.; Zhang, C.-H.; Xin, S.; Shi, J.-L.; Wang, W.-P.; Fan, M.; Chang, Y.-X.; He, W.-H.; Wang, E.; Zou, Y.-G.; et al. Competitive doping chemistry for nickel-rich layered oxide cathode materials. *Angew. Chem. Int. Ed.* **2022**, *61*, e202116865. [CrossRef]
643. Ou, X.; Liu, T.; Zhong, W.; Fan, X.; Guo, X.; Huang, X.; Cao, L.; Hu, J.; Zhang, B.; Chu, Y.S.; et al. Enabling high energy lithium metal batteries via single-crystal Ni-rich cathode material co-doping strategy. *Nat. Commun.* **2022**, *13*, 2319. [CrossRef] [PubMed]
644. Zhang, W.; Tang, X.; Xiao, L.; Xiao, Z. Influence of Al^{3+} and PO_4^{3-} co-doping on structure and electrochemical performance of $\text{LiNi}_{0.8}\text{Co}_{0.1}\text{Mn}_{0.1}\text{O}_2$ cathode materials. *J. Solid State Electrochem.* **2023**, *27*, 1185–1194. [CrossRef]
645. Reissig, F.; Lange, M.A.; Haneke, L.; Placke, T.; Zeier, W.G.; Winter, M.; Schmuck, R.; Gomez-Martin, A. Synergistic effects of surface coating and bulk doping in Ni-rich lithium nickel cobalt manganese oxide cathode materials for high-energy lithium-ion batteries. *ChemSusChem* **2022**, *15*, e202102220. [CrossRef]
646. Park, G.-T.; Yoon, J.I.; Kim, G.-H.; Park, N.-Y.; Park, B.-C.; Sun, Y.-K. Ni-rich cathode materials enabled by cracked-surface protection strategy for high-energy lithium batteries. *Mater. Sci. Eng. R Rep.* **2025**, *164*, 100945. [CrossRef]
647. Gong, M.; Fu, Y.; Yao, W.; Rao, X.; Zhang, Q.; Zhong, S.; Sun, Q.; Cheng, H. Profiting the Co-modifications of Li_2SnO_3 coating and Sn^{4+} doping in Co-free Ni-rich cathode particles for lithium-ion batteries. *ACS Appl. Energy Mater.* **2023**, *6*, 1248–1258. [CrossRef]
648. Luo, Z.; Hu, G.; Wang, W.; Du, K.; Peng, Z.; Zeng, J.; Li, L.; Cao, Y. Enhancing the electrochemical performance of Co-less Ni-rich $\text{LiNi}_{0.925}\text{Co}_{0.03}\text{Mn}_{0.045}\text{O}_2$ cathode material via Co-modification with $\text{Li}_2\text{B}_4\text{O}_7$ coating and B^{3+} doping. *J. Power Sources* **2022**, *548*, 232092. [CrossRef]
649. Li, L.; Fu, L.; Li, M.; Wang, C.; Zhao, Z.; Xie, S.; Lin, H.; Wu, X.; Liu, H.; Zhang, L.; et al. B-doped and $\text{La}_4\text{NiLiO}_8$ -coated $\text{LiNi}_{0.825}\text{Co}_{0.115}\text{Mn}_{0.06}\text{O}_2$ cathode with enhanced structural and interfacial stability for lithium-ion batteries. *J. Energy Chem.* **2022**, *71*, 588–594.
650. Yang, H.; Wu, H.H.; Ge, M.; Li, L.; Yuan, Y.; Yao, Q.; Chen, J.; Xia, L.; Zheng, J.; Chen, Z.; et al. Simultaneously dual modification of Ni-rich layered oxide cathode for high-energy lithium-ion batteries. *Adv. Funct. Mater.* **2019**, *29*, 1808825. [CrossRef]
651. Sattar, T.; Sim, S.-J.; Doo, S.-G.; Jin, B.-S.; Kim, H.-S. A synergistic modification approach toward high-capacity Ni-rich cathode materials for next generation lithium-ion batteries. *Solid State Ion.* **2022**, *387*, 116053. [CrossRef]
652. Shen, J.; Zhang, B.; He, X.; Xiao, B.; Xiao, Z.; Li, X.; Ou, X. Synergistic regulation of kinetic reaction pathway and surface structure degradation in single-crystal high-nickel cathodes. *J. Colloid Interface Sci.* **2023**, *629*, 388–398. [CrossRef]

653. Lv, Y.; Huang, S.-F.; Lu, S.-R.; Ding, W.-B.; Yu, X.-L.; Liang, G.-M.; Zou, J.-S.; Kang, F.-Y.; Zhang, J.-J.; Cao, Y.-D. $\text{B}_2\text{O}_3/\text{LiBO}_2$ dual-modification layer stabilized Ni-rich cathode for lithium-ion battery. *J. Power Sources* **2022**, *536*, 231510. [[CrossRef](#)]
654. Su, Y.; Li, L.; Chen, L.; Wang, L.; Lu, Y.; Zhang, Q.; Bao, L.; Wu, F. Enhanced electrochemical performance of Ni-rich cathode materials with an in situ-formed $\text{LiBO}_2/\text{B}_2\text{O}_3$ hybrid coating layer. *ACS Appl. Energy Mater.* **2022**, *5*, 2231–2241. [[CrossRef](#)]
655. Xu, M.; Lu, J.; Sun, Z.; Yang, M.; Sheng, B.; Chen, M.; Chen, J.; Zhang, Q.; Han, X. Lanthanum doping and surface Li_3BO_3 passivating layer enabling 4.8 V nickel-rich layered oxide cathodes toward high energy lithium-ion batteries. *J. Colloid Interface Sci.* **2024**, *673*, 386–394. [[CrossRef](#)]
656. Tang, W.; Shu, Z.; Li, A.; Huang, X.; Li, W. Enhancing structural integrity and long-term cycling stability of high-voltage single-crystalline Ni-rich cathodes via surface/subsurface dual-functional modification engineering. *Energy Storage Mater.* **2025**, *77*, 104185. [[CrossRef](#)]
657. Zhang, J.; Zhang, J.; Ou, X.; Wang, C.; Peng, C.; Zhang, B. Enhancing high-voltage performance of Ni-rich cathode by surface modification of self-assembled NASICON fast ionic conductor $\text{LiZr}_2(\text{PO}_4)_3$. *ACS Appl. Mater. Interfaces* **2019**, *11*, 15507–15516. [[CrossRef](#)]
658. Xin, F.; Zhou, H.; Zong, Y.; Zuba, M.; Chen, Y.; Chernova, N.A.; Bai, J.; Pei, B.; Goel, A.; Rana, J.; et al. What is the role of Nb in nickel-rich layered oxide cathodes for lithium-ion batteries? *ACS Energy Lett.* **2021**, *6*, 1377–1382. [[CrossRef](#)]
659. Xin, F.; Zhou, H.; Chen, X.; Zuba, M.; Chernova, N.; Zhou, G.; Whittingham, M. Li–Nb–O coating/substitution enhances the electrochemical performance of the $\text{LiNi}_{0.8}\text{Mn}_{0.1}\text{Co}_{0.1}\text{O}_2$ (NMC 811) cathode. *ACS Appl. Mater. Interfaces* **2019**, *11*, 34889–34894. [[CrossRef](#)] [[PubMed](#)]
660. Zhang, M.; Lv, M.; Zhang, D.; Yan, Y.; Wang, Y.; Li, J.; Li, Z. Enhanced electrochemical properties of NMC811 cathode material due to synergistic modification with Sm as doping and coating agent. *J. Alloys Compd.* **2022**, *909*, 164712. [[CrossRef](#)]
661. Kim, Y. Thermochemical investigation of Zr doping in $\text{LiNi}_{8/12}\text{Co}_{2/12}\text{Mn}_{2/12}\text{O}_2$ based on phase equilibria simulation. *Int. J. Quant. Chem.* **2019**, *119*, e26028. [[CrossRef](#)]
662. Tan, X.; Peng, W.; Wang, M.; Luo, G.; Wang, Z.; Yan, G.; Guo, H.; Li, Q.; Wang, J. Al, Zr dual-doped cobalt-free nickel-rich cathode materials for lithium-ion batteries. *Prog. Nat. Sci. Mater. Int.* **2023**, *33*, 108–115. [[CrossRef](#)]
663. Dai, Z.; Liu, Y.; Zhao, H.; Bai, Y. Ultra-high temperature operated Ni-rich cathode stabilized by thermal barrier for high-energy lithium-ion batteries. *Adv. Mater.* **2024**, *36*, 2313500. [[CrossRef](#)]
664. Yang, K.; Yi, Y.; Hu, G.; Yang, C.; Liu, F.; Yin, C.; Cao, J.; Chen, Z. Enhancing the cycling stability of full-concentration-gradient Ni-rich layered cathodes via in-situ Zr doping. *Chem. Eng. J.* **2024**, *493*, 152872. [[CrossRef](#)]
665. Wang, Y.-Y.; Gao, M.-Y.; Liu, S.; Li, G.-R.; Gao, X.-P. Yttrium surface gradient doping for enhancing structure and thermal stability of high-Ni layered oxide as cathode for Li-ion batteries. *ACS Appl. Mater. Interfaces* **2021**, *13*, 7343–7354. [[CrossRef](#)]
666. Luo, Z.; Hu, G.; Wang, W.; Zhao, B.; Li, H.; Peng, Z.; Du, K.; Cao, Y. Ni-rich Co-less cathode materials with LiYO_2 and Y^{3+} modification toward improved storage performance against ambient air for lithium-ion batteries. *ACS Sustain. Chem. Eng.* **2024**, *12*, 24–36. [[CrossRef](#)]
667. Bizzotto, F.; Dachraoui, W.; Grissa, R.; Zhao, W.; Pagani, F.; Querel, E.; Khünel, R.-S.; Battaglia, C. Modification of NMC811 with titanium for enhanced cycling and high-voltage stability. *Electrochim. Acta* **2023**, *462*, 142758. [[CrossRef](#)]
668. Fan, Q.; Lin, K.; Yang, S.; Guan, S.; Chen, J.; Feng, S.; Liu, J.; Liu, L.; Li, J.; Shi, Z. Constructing effective TiO_2 nano-coating for high-voltage Ni-rich cathode materials for lithium-ion batteries by precise kinetic control. *J. Power Sources* **2020**, *477*, 228745. [[CrossRef](#)]
669. Wang, W.; Wu, L.; Li, Z.; Huang, K.; Jiang, J.; Chen, Z.; Qi, X.; Dou, H.; Zhang, X. In situ tuning residual lithium compounds and constructing TiO_2 coating for surface modification of a nickel-rich cathode toward high-energy lithium-ion batteries. *ACS Appl. Energy Mater.* **2020**, *3*, 12423–12432. [[CrossRef](#)]
670. Sun, Y.; Huang, W.; Zhao, G.; Liu, Q.; Duan, L.; Wang, S.; An, Q.; Wang, H.; Yang, Y.; Zhang, C.; et al. $\text{LiNi}_{0.9}\text{Co}_{0.09}\text{Mo}_{0.01}\text{O}_2$ cathode with Li_3PO_4 coating and Ti doping for next-generation lithium-ion batteries. *ACS Energy Lett.* **2023**, *8*, 1629–1638. [[CrossRef](#)]
671. Hou, Y.; Ren, Y.; Shi, T.; Li, J.; Li, H.; Zhang, L.; Liu, Y.; Wan, Y.; Zhang, S.; Liu, Y.; et al. The surface Al_2O_3 coating and bulk Zr doping drastically improve the voltage fade and cycling stability of $\text{Li}(\text{Ni}_{0.8}\text{Mn}_{0.1}\text{Co}_{0.1})\text{O}_2$ cathode materials. *J. Alloys Compd.* **2023**, *939*, 168778. [[CrossRef](#)]
672. Chen, S.; Zhou, X.; Wang, S.; Zhang, P.; Zu, W.; Liu, X.; Feng, G.; Zhang, B.; Xing, W.; Zuo, M.; et al. High-performance single crystal Ni-rich cathode with regulated lattice and interface constructed by separated lithiation and crystallization calcination. *Green Chem. Eng.* **2024**. [[CrossRef](#)]
673. Shi, H.; Zheng, J.; Wan, T.; Wang, H.; Wen, Z.; Zheng, F.; Su, M.; Dou, A.; Zhou, Y.; Naveed, A.; et al. Constructing electrochemically stable single crystal Ni-rich cathode material via modification with high valence metal oxides. *J. Energy Chem.* **2025**, *101*, 392–401. [[CrossRef](#)]
674. Song, W.; Gao, A.; Liu, Y.; Liu, A.; Peng, H.; Li, M.; Yang, R.; Wang, F. Tungsten-doped Ni-rich $\text{LiNi}_{0.8}\text{Mn}_{0.18}\text{Al}_{0.02}\text{O}_2$ cathode with fast kinetics and stable surface structure. *J. Alloys Compd.* **2025**, *1010*, 177611. [[CrossRef](#)]

675. Xiao, Z.; Zhou, C.; Song, L.; Cao, Z.; Jiang, P. Dual-modification of WO_3 -coating and Mg-doping on $\text{LiNi}_{0.8}\text{Co}_{0.1}\text{Mn}_{0.1}\text{O}_2$ cathodes for enhanced electrochemical performance at high voltage. *Ionics* **2021**, *27*, 1909–1917. [CrossRef]
676. Xiao, W.; Wang, J.-L.; Yi, Z.-C.; Liu, C.-J.; Miao, C.; Xin, Y.; Nie, S.-Q. Dual modification of $\text{LiNi}_{0.83}\text{Co}_{0.11}\text{Mn}_{0.06}\text{O}_2$ cathode materials by K^+ doping and Li_3PO_4 coating for lithium ions batteries. *Rare Met.* **2024**, *43*, 3007–3018. [CrossRef]
677. Shen, L.; Gu, Y.; Xu, T.; Zhou, Q.; Peng, P.; Chan, Y.; Du, F.; Zheng, J. Dual modification of phosphate toward improving electrochemical performance of LiNiO_2 cathode materials. *J. Colloid Interface Sci.* **2024**, *662*, 505–515. [CrossRef]
678. Liu, C.; Yi, Z.; Wan, J.; Miao, C.; Wang, Z.; Wang, J.; Xiao, W. Nb^{5+} ions doping and Li_3PO_4 artificial layer synergetic strategy to strengthen structure, stabilize interface, and promote ions migration for high-performance Ni-rich cathode. *Chem. Eng. J.* **2025**, *503*, 158633. [CrossRef]
679. Lin, H.; Shen, Y.; Wei, L.; Song, R.; Wu, F.; Wei, P.; Yang, Z.; Ren, Y.; Qu, K.; Ding, Z. Enhancing structural stability and electrochemical performance of ultra-high Ni-rich Co-free cathode via MgHPO_4 dual-functional modification. *Chem. Res. Chin. Univ.* **2025**, *41*, 333–342. [CrossRef]
680. Tang, Y.; Chen, Z.; Lin, F.; Zhu, H.; Wen, J.; Wang, Y.; Bai, M.; Duan, J. Synergistic role of Sb doping and surface modification in high performance ultrahigh-nickel layered oxides cathode materials. *J. Alloys Compd.* **2023**, *959*, 170552. [CrossRef]
681. Sun, G.; Zhuang, S.; Jiang, S.; Ren, Y.; Sun, Y.; Pan, X.; Wen, Y.; Li, X.; Tu, F. Elevating cycle stability of Ni-rich NMC811 cathode via single-crystallization integrating dual-modification strategy for lithium-ion batteries. *J. Alloys Compd.* **2024**, *976*, 173097. [CrossRef]
682. Yu, H.; Zhu, H.; Jiang, H.; Su, X.; Hu, Y.; Jiang, H.; Li, C. Restraining the escape of lattice oxygen enables superior cyclic performance towards high-voltage Ni-rich cathodes. *Natl. Sci. Rev.* **2023**, *10*, nwac166. [CrossRef]
683. Li, X.; Chen, Y.; Lv, K.; Liu, J.; Bayaguud, A.; Li, X. Surface-to-bulk synergistic modification enables stable interface of Ni-rich oxide cathode for all-solid-state lithium batteries. *Electrochim. Acta* **2024**, *497*, 144595. [CrossRef]
684. Liu, L.; Zhao, Y.; Shan, L.; Jiang, G.; Zhang, Y.; Meng, Q.; Dong, P. Improved electrochemical performance of Co-free Ni-rich cathode material for lithium-ion battery through multi-element composite modification. *Electrochim. Acta* **2024**, *477*, 143804. [CrossRef]
685. Wang, R.; Zhang, X.; Li, Z.; Wu, L.; Chen, J.; Liu, X.; Hu, H.; Ding, H.; Cao, S.; Wei, Q.; et al. Improving structure stability of single-crystalline Ni-rich cathode at high voltage by element gradient doping and interfacial modification. *J. Energy Chem.* **2025**, *101*, 630–640. [CrossRef]
686. Wang, H.; Dong, J.; Zhang, H.; Liu, J.; Lu, Y.; Liu, Y.; Wang, X.; Li, N.; Huang, Q.; Wu, F.; et al. Enhancing structural and thermal stability of ultrahigh-Ni cathodes via anion-cation codoping induced surface reconstruction strategy. *J. Energy Chem.* **2025**, *106*, 9–19. [CrossRef]
687. Chen, S.; He, T.; Su, Y.; Lu, Y.; Chen, L.; Zhang, Q.; Wang, J.; Chen, R.; Wu, F. Ni-rich $\text{LiNi}_{0.8}\text{Co}_{0.1}\text{Mn}_{0.1}\text{O}_2$ oxide coated by dual-conductive layers as high-performance cathode material for lithium-ion batteries. *ACS Appl. Mater. Interfaces* **2017**, *9*, 29732–29743. [CrossRef]
688. Ma, Y.; Xu, M.; Zhang, J.; Liu, R.; Wang, Y.; Xiao, H.; Huang, Y.; Yuan, G. Improving electrochemical performance of Ni-rich $\text{LiNi}_{0.8}\text{Co}_{0.1}\text{Mn}_{0.1}\text{O}_2$ cathode for Li-ion batteries by dual-conductive coating layer of PPy and LiAlO_2 . *J. Alloys Compd.* **2020**, *848*, 156387. [CrossRef]
689. Yang, H.; Wu, K.; Hu, G.; Peng, Z.; Cao, Y.; Du, K. Design and synthesis of double-functional polymer composite layer coating to enhance the electrochemical performance of the Ni-rich cathode at the upper cutoff voltage. *ACS Appl. Mater. Interfaces* **2019**, *11*, 8556–8566. [CrossRef] [PubMed]
690. Tan, Z.; Chen, X.; Lin, J.; Huang, Y.; Cheng, W.; Liu, Q.; Zhang, H.; Ren, F.; Huang, Y.; Liu, Z.; et al. Restraining planar gliding in single-crystalline $\text{LiNi}_{0.9}\text{Co}_{0.05}\text{Mn}_{0.05}\text{O}_2$ cathodes by combining bulk and surface modification strategies. *Angew. Chem. Inter. Ed.* **2025**, *64*, e202419903. [CrossRef]
691. Cheng, W.-D.; Li, L.; Hao, S.-L.; Wu, Y.-X.; Huo, J.-S.; Ji, Y.-Y.; Liu, X.-Q. Face-lifting the surface of $\text{LiNi}_{0.8}\text{Co}_{0.15}\text{Al}_{0.05}\text{O}_2$ cathode via $\text{Y}(\text{PO}_3)_3$ to form an in situ triple composite Li-ion conductor coating layer with the enhanced electrochemical performance. *Nanotechnology* **2022**, *33*, 375701. [CrossRef]
692. Li, Q.; Dang, R.; Chen, M.; Lee, Y.; Hu, Z.-B.; Xiao, X.-L. A synthesis method for long cycle life lithium-ion cathode material: Ni-rich core-shell $\text{LiNi}_{0.8}\text{Co}_{0.1}\text{Mn}_{0.1}\text{O}_2$. *ACS Appl. Mater. Interfaces* **2018**, *10*, 17850–17860. [CrossRef] [PubMed]
693. Ryu, H.-H.; Park, N.-Y.; Noh, T.-C.; Kang, G.-C.; Maglia, F.; Kim, S.-J.; Yoon, C.-S.; Sun, Y.-K. Microstrain alleviation in high-energy Ni-rich NCMA cathode for long battery life. *ACS Energy Lett.* **2021**, *6*, 216–223. [CrossRef]
694. Bi, Y.-J.; Liu, M.; Xiao, B.-W.; Jiang, Y.; Lin, H.; Zhang, Z.-G.; Chen, G.-X.; Sun, Q.; He, H.-Y.; Huang, F.; et al. Highly stable Ni-rich layered oxide cathode enabled by a thick protective layer with bio-tissue structure. *Energy Storage Mater.* **2020**, *24*, 291–296. [CrossRef]
695. Maeng, S.; Chung, Y.; Min, S.; Shin, Y. Enhanced mechanical strength and electrochemical performance of core–shell structured high–nickel cathode material. *J. Power Sources* **2020**, *448*, 227395. [CrossRef]

696. Park, G.-T.; Sun, H.H.; Noh, T.-C.; Maglia, F.; Kim, S.-J.; Lamp, P.; Sun, Y.-K. Nanostructured Co-free layered oxide cathode that affords fast-charging lithium-ion batteries for electric vehicles. *Adv. Energy Mater.* **2022**, *12*, 2202719. [CrossRef]
697. Rathore, D.; Garayt, M.; Liu, Y.-L.; Geng, C.-X.; Johnson, M.; Dahn, J.-R.; Yang, C.-Y. Preventing interdiffusion during synthesis of Ni-rich core-shell cathode materials. *ACS Energy Lett.* **2022**, *7*, 2189–2195. [CrossRef]
698. Bae, J.H.; Hwang, K.; Kim, J.; Kang, H.; Lee, I.; Park, C.W.; Sohn, H.; Yoon, S. Enhanced electrochemical performance of Ni-rich cathode for lithium-ion batteries under elevated cut-off voltage (4.5 V): Elongated cycle stability of cathode by relaxed mechanical stress in the presence of internal porous layer. *J. Electroanal. Chem.* **2024**, *957*, 118123. [CrossRef]
699. Shi, H.; Wang, X.; Hou, P.; Zhou, E.; Guo, J.; Zhang, J.; Wang, D.; Guo, F.; Song, D.; Shi, X.; et al. Core–shell structured $\text{Li}[(\text{Ni}_{0.8}\text{Co}_{0.1}\text{Mn}_{0.1})_{0.7}(\text{Ni}_{0.45}\text{Co}_{0.1}\text{Mn}_{0.45})_{0.3}]\text{O}_2$ cathode material for high-energy lithium ion batteries. *J. Alloys Compd.* **2024**, *587*, 710–716. [CrossRef]
700. Xia, Y.; Chen, A.; Wang, K.; Xiao, Z.; Mao, Q.; Lu, X.; Wang, G.; Lu, C.; Zhang, J.; Huang, H.; et al. Binary-compositional core–shell structure Ni-rich cathode material with radially oriented primary particles in shell for long cycling lifespan lithium-ion batteries. *Mater. Today Energy* **2023**, *34*, 101292. [CrossRef]
701. Ye, T.; Li, Z.M.; Yan, H.L.; Ha, Y.; Zhang, D.Y.; Zhou, C.Y.; Wang, L.J.; Li, L.; Xiang, Q.X. Magnetic frustration effect on the rate performance of $\text{LiNi}_{0.6}\text{Co}_{0.4-x}\text{Mn}_x\text{O}_2$ cathodes for lithium-ion batteries. *Adv. Energy Mater.* **2022**, *12*, 2201556. [CrossRef]
702. Han, S.-M.; Park, G.-T.; Kim, D.-H.; Seo, M.-G.; Park, N.-Y.; Sun, Y.-K. Introducing Co nanoshells onto Ni-rich cathode materials for high long-life Li-ion batteries. *ACS Energy Lett.* **2024**, *9*, 5859–5868. [CrossRef]
703. Xue, H.; Liang, Y.; Huang, Y.; Ji, Y.; Xu, Z.; Chen, X.; Wang, H.; Liu, J.; Amine, K.; Liu, T.; et al. In situ conversion of artificial proton-rich shell to inorganic maskant toward stable single-crystal Ni-rich cathode. *Adv. Mater.* **2025**, *37*, 2415860. [CrossRef]
704. Song, G.; Zhong, H.; Dai, Y.; Zhou, X.; Yang, J. WO_3 membrane-encapsulated layered $\text{LiNi}_{0.6}\text{Co}_{0.2}\text{Mn}_{0.2}\text{O}_2$ cathode material for advanced Li-ion batteries. *Ceram. Int.* **2019**, *45*, 6774–6781. [CrossRef]
705. Liu, J.-K.; Yang, X.-R.; Wang, C.-W.; Yin, Z.-W.; Hu, Y.-Y.; Deng, L.; Wang, Z.; Zhou, Y.; Li, J.-T. Surface-to-bulk engineering with high-valence W^{6+} enabling stabilized single-crystal $\text{LiNi}_{0.9}\text{Co}_{0.05}\text{Mn}_{0.05}\text{O}_2$ cathode. *J. Energy Chem.* **2024**, *98*, 67–76. [CrossRef]
706. Chu, B.; Xu, R.; Li, G.; Chen, J.; Xu, Z.; Huang, T.; Wang, B.; Yu, A. Simultaneous B/W dual coating on ultra-high nickel single crystal cathode material for lithium-ion batteries. *J. Power Sources* **2023**, *577*, 233260. [CrossRef]
707. Du, F.; Qu, H.; Yu, X.; Ding, L.; Zhang, P.; Wang, Y.; Chen, Y.; Wang, Y.; Zhang, X.; Zheng, J. Pre-introducing Li_4NiWO_6 defect phase by tungsten modification enables highly stabilized Ni-rich cathode. *Chem. Eng. J.* **2024**, *492*, 152357. [CrossRef]
708. Ding, H.; Wang, X.; Zhao, J.; Wang, X.; Zhang, H.; Liu, G.; Yu, W.; Dong, X.; Wang, J. Construction of hollow multi-shell structural NCM622 as cathode to improve the cycling stability of its Li-ion batteries. *J. Energy Storage* **2025**, *107*, 114835. [CrossRef]
709. Yoon, C.-S.; Sun, Y.K.; Kim, U.-H.; Park, K.-J.; Ryu, H.-H.; Kim, H.-S.; Sun, Y.-K. Microstructure evolution of concentration gradient $\text{Li}[\text{Ni}_{0.75}\text{Co}_{0.10}\text{Mn}_{0.15}]\text{O}_2$ cathode for lithium-ion batteries. *Adv. Funct. Mater.* **2018**, *28*, 1802090. [CrossRef]
710. Wu, K.; Wang, J.-Y.; Li, Q.; Yang, Y.-Q.; Deng, X.; Dang, R.-B.; Wu, M.-M.; Wu, Z.-J.; Xiao, X.-L.; Yu, X.-Q. In situ synthesis of nickel concentration gradient structure promising superior electrochemical properties of Ni-rich $\text{LiNi}_{0.8}\text{Co}_{0.15}\text{Al}_{0.05}\text{O}_2$ at high cut-off voltage. *Nanoscale* **2020**, *12*, 11182–11191. [CrossRef] [PubMed]
711. Shang, M.-W.; Chen, X.; Niu, J.-J. Nickel-rich layered $\text{LiNi}_{0.8}\text{Mn}_{0.1}\text{Co}_{0.1}\text{O}_2$ with dual gradients on both primary and secondary particles in lithium-ion batteries. *Cell Rep. Phys. Sci.* **2022**, *3*, 100767. [CrossRef]
712. Yerkinbekova, Y.; Kumarov, A.; Tatykayev, B.; Mentbayeva, A.; Repo, E.; Laasko, E. Ni-rich cathode materials with concentration gradients for high-energy and safe lithium-ion batteries: A comprehensive review. *J. Power Sources* **2025**, *626*, 235686. [CrossRef]
713. Noh, H.-J.; Chen, Z.-H.; Yoon, C.-S.; Lu, J.; Amine, K.; Sun, Y.-K. Cathode material with nanorod structure—An application for advanced high-energy and safe lithium batteries. *Chem. Mater.* **2013**, *25*, 2109–2115. [CrossRef]
714. Wang, X.; Zhou, X.; Liu, X.; Feng, G.; Wang, S.; Zhang, B.; Zhang, P.; Zuo, M.; Xing, W.; Fan, W.; et al. Surface reactivity versus microcracks in Ni-rich layered oxide cathodes: Which is critical for long cycle life? *Chem. Eng. J.* **2024**, *488*, 150795. [CrossRef]
715. Wu, Z.; Zhou, Y.; Hai, C.; Zeng, J.; Sun, Y.; Ren, X.; Shen, Y.; Li, X.; Zhang, G. Analysis of the growth mechanism of hierarchical structure $\text{Ni}_{0.8}\text{Co}_{0.1}\text{Mn}_{0.1}(\text{OH})_2$ agglomerates as precursors of $\text{LiNi}_{0.8}\text{Co}_{0.1}\text{Mn}_{0.1}\text{O}_2$ in the presence of aqueous ammonia. *Appl. Surf. Sci.* **2023**, *619*, 156379. [CrossRef]
716. Wu, Z.; Zhou, Y.; Zeng, J.; Hai, C.; Sun, Y.; Ren, X.; Shen, Y.; Li, X. Investigating the effect of pH on the growth of coprecipitated $\text{Ni}_{0.8}\text{Co}_{0.1}\text{Mn}_{0.1}(\text{OH})_2$ agglomerates as precursors of cathode materials for Li-ion batteries. *Ceram. Int.* **2023**, *49*, 15851–15864. [CrossRef]
717. Liu, Y.; Zhang, C.; Lin, L.; Ai, X.; Gui, S.; Guo, W.; Li, S.; Wang, L.; Yang, H.; Peng, D.-L.; et al. Intrinsic highly conductive and mechanically robust Li-rich cathode materials enabled by microstructure engineering for enhanced electrochemical properties. *Adv. Funct. Mater.* **2023**, *34*, 2308494. [CrossRef]
718. Guo, W.; Wang, Z.; Yu, H.; Demir, M.; Cheng, Q.; Jiang, H. Robust concentration gradient Co-free Ni-rich cathodes enable long-life and safe operations in high-voltage Li-ion batteries. *Energy Fuels* **2025**, *39*, 4507–4514. [CrossRef]
719. He, X.; Su, S.; Zhang, B.; Xiao, Z.; Zhang, Z.; Ou, X. Alleviating the anisotropic microstructural change and boosting the lithium ions diffusion by grain orientation regulation for Ni-rich cathode materials. *J. Energy Chem.* **2024**, *88*, 213–222. [CrossRef]

720. Park, N.Y.; Cho, G.; Kim, S.B.; Sun, Y.K. Multifunctional doping strategy to develop high-performance Ni-rich cathode material. *Adv. Energy Mater.* **2023**, *13*, 2204291. [[CrossRef](#)]
721. Wu, Z.; Li, X.; Hai, C.; Ren, X.; Zeng, J.; Shen, Y.; Zhou, Y. Anionic-surfactant-assisted synthesis of $\text{Ni}_{0.8}\text{Co}_{0.1}\text{Mn}_{0.1}(\text{OH})_2$ as precursors of high-performance cathode materials for lithium-ion batteries. *J. Power Sources* **2024**, *615*, 235092. [[CrossRef](#)]
722. Chen, H.; Yuan, H.; Dai, Z.; Feng, S.; Zheng, M.; Zheng, C.; Jin, J.; Wu, M.; Wu, X.; Lu, J.; et al. Surface gradient Ni-rich cathode for Li-ion batteries. *Adv. Mater.* **2024**, *36*, 2401052. [[CrossRef](#)] [[PubMed](#)]
723. Wang, J.-P.; Du, C.Y.; Xu, X.; He, X.; Yin, G.; Ma, Y.; Zuo, P.; Cheng, X.; Gao, Y. Lithium phosphorus oxynitride coated concentration gradient $\text{Li}[\text{Ni}_{0.73}\text{Co}_{0.12}\text{Mn}_{0.15}]\text{O}_2$ cathode material with enhanced electrochemical properties. *Electrochim. Acta* **2016**, *192*, 340–345. [[CrossRef](#)]
724. Liu, Z.; Zheng, S.; Zhou, Y.; Tian, X. Enhancing the electrochemical performance of single-crystal $\text{LiNi}_{0.8}\text{Co}_{0.1}\text{Mn}_{0.1}\text{O}_2$ cathode material by phosphorus doping. *Chem. Eng. Sci.* **2024**, *285*, 119627. [[CrossRef](#)]
725. Choi, J.H.; Hwang, J.; Embleton, T.J.; Ko, K.; Jo, M.; Lee, C.; Yun, J.; Park, S.; Son, Y.; Oh, P. Selective outer surface modification of polycrystalline Ni-rich cathode for sulfide all-solid-state lithium-ion battery. *Korean J. Chem. Eng.* **2023**, *40*, 548–554. [[CrossRef](#)]
726. Park, G.-T.; Ryu, H.-H.; Noh, T.-C.; Kang, G.-C.; Sun, Y.-K. Microstructure-optimized concentration-gradient NCM cathode for long-life Li-ion batteries. *Mater. Today* **2022**, *52*, 9–18. [[CrossRef](#)]
727. Wu, T.; Liu, X.; Zhang, X.; Lu, Y.; Wang, B.; Deng, Q.; Yang, Y.; Wang, E.; Lyu, Z.; Li, Y.; et al. Full concentration gradient-tailored Li-rich layered oxides for high-energy lithium-ion batteries. *Adv. Mater.* **2021**, *33*, 2001358. [[CrossRef](#)]
728. Zhang, C.; Li, T.; Xue, B.; Wu, X.; Li, L.; Guo, Y.; Zhang, L. Synergistic modification of Ni-rich full concentration gradient materials with enhanced thermal stability. *Chem. Eng. J.* **2023**, *451*, 138518. [[CrossRef](#)]
729. Sun, H.-H.; Weeks, J.A.; Heller, A.; Mullins, C.B. Nanorod gradient cathode: Preventing electrolyte penetration into cathode particles. *ACS Appl. Energy Mater.* **2019**, *2*, 6002–6011. [[CrossRef](#)]
730. Huang, Z.; Yan, J.; Liu, Z.; Wang, W.; Zhang, Z.; Tang, Y.; Zhang, Z.; Yang, T.; Wang, X.; Li, X.; et al. Achieving long-life Ni-rich cathodes with improved mechanical-chemical properties via concentration gradient structure. *Adv. Func. Mater.* **2024**, *34*, 2400956. [[CrossRef](#)]
731. Song, L.; Xiao, M.; Du, J.; Li, L.; Zhao, T.; Xia, Y.; Xiang, Y.; Chen, T.; Jiang, L.; Xiao, Z.; et al. An effective gradient coating strategy to improve the structure stability of Ni-rich nickel-cobalt-manganese ternary layer oxide cathode. *J. Energy Storage* **2024**, *98*, 113123. [[CrossRef](#)]
732. Sitnikova, L.A.; Savina, A.; Morozov, A.V.; Golubnichiy, A.A.; Dolzhikova, E.A.; Moiseev, I.A.; Luchkin, S.Y.; Abakumov, A.M. Improving electrochemical performance of Ni-rich layered cathode material with combining Co-enriched compositional gradient and radial microstructure. *J. Power Sources* **2024**, *602*, 234302. [[CrossRef](#)]
733. Guo, W.; Yu, H.; Wang, M.; Wu, M.; Chen, L.; Jiang, H.; Li, C. Compositional gradient design of Ni-rich Co-poor cathodes enhanced cyclability and safety in high-voltage Li-ion batteries. *ACS Nano* **2025**, *19*, 8371–8380. [[CrossRef](#)]
734. Zhang, Y.; Li, H.; Liu, J.; Zhang, J.; Cheng, F.; Chen, J. $\text{LiNi}_{0.90}\text{Co}_{0.07}\text{Mg}_{0.03}\text{O}_2$ cathode materials with Mg-concentration gradient for rechargeable lithium-ion batteries. *J. Mater. Chem. A* **2019**, *7*, 20958–20964. [[CrossRef](#)]
735. Tao, J.; Mu, A.; Geng, S.; Xiao, H.; Zhang, L.; Huang, Q. Influences of direction and magnitude of Mg^{2+} doping concentration gradient on the performance of full concentration gradient cathode material. *J. Solid State Electrochem.* **2021**, *25*, 1959–1974. [[CrossRef](#)]
736. Mu, Y.; Chen, X.; Ming, H.; Zhang, S.; Zhu, X.; Qiu, J. Oriented gradient doping of zirconium in Ni-rich cathode to achieve ultrahigh stability and rate capability. *ACS Appl. Mater. Interfaces* **2023**, *15*, 49289–49298. [[CrossRef](#)]
737. Zhang, Y.; Li, H.; Liu, J.; Liu, J.; Ma, H.; Cheng, F. Enhancing LiNiO_2 cathode materials by concentration-gradient yttrium modification for rechargeable lithium-ion batteries. *J. Energy Chem.* **2021**, *63*, 312–319. [[CrossRef](#)]
738. Wu, H.; Zhou, X.; Yang, C.; Xu, D.; Zhu, Y.-H.; Zhou, T.; Xin, S.; You, Y. Concentration-gradient Nb-doping in a single-crystal $\text{LiNi}_{0.83}\text{Co}_{0.12}\text{Mn}_{0.05}\text{O}_2$ cathode for high-rate and long-cycle lithium-ion batteries. *ACS Appl. Mater. Interfaces* **2023**, *15*, 18828–18835. [[CrossRef](#)]
739. Yang, S.; Yang, K.; Mi, J.; Guo, S.; An, X.; Su, H.; He, Y. Electrolyte engineering and interphase chemistry toward high-performance nickel-rich cathodes: Progress and perspectives. *Mater. Rep. Energy* **2025**, *5*, 100317. [[CrossRef](#)]
740. Maleki Kheimeh Sari, H.; Li, X. Controllable cathode–electrolyte interface of $\text{Li}[\text{Ni}_{0.8}\text{Co}_{0.1}\text{Mn}_{0.1}]\text{O}_2$ for lithium ion batteries: A review. *Adv. Energy Mater.* **2019**, *9*, 1901597. [[CrossRef](#)]
741. Xu, Z.; Wang, X.; Wang, Z.; Li, X.; Liu, J.; Bayaguud, A.; Zhang, L. Interface problems, modification strategies and prospects of Ni-rich layered oxide cathode materials in all-solid-state lithium batteries with sulfide electrolytes. *J. Power Sources* **2023**, *571*, 233079. [[CrossRef](#)]
742. Wu, J.H.; Shen, L.; Zhang, Z.H.; Liu, G.Z.; Wang, Z.Y.; Zhou, D.; Wan, H.L.; Xu, X.X.; Yao, X.Y. All-solid-state lithium batteries with sulfide electrolytes and oxide cathodes. *Electro. Energy. Rev.* **2020**, *4*, 411. [[CrossRef](#)]
743. Payandeh, S.; Strauss, F.; Mazilkin, A.; Kondrakov, A.; Brezesinski, T. Tailoring the LiNbO_3 coating of Ni-rich cathode materials for stable and high-performance all-solid-state batteries. *Nano Res. Energy* **2022**, *1*, e9120016. [[CrossRef](#)]

744. Walther, F.; Strauss, F.; Wu, X.; Mogwitz, B.; Hertle, J.; Sann, J.; Rohnke, M.; Brezesinski, T.; Janek, J. The working principle of a $\text{Li}_2\text{CO}_3/\text{LiNbO}_3$ coating on NCM for thiophosphate-based all-solid-state batteries. *Chem. Mater.* **2021**, *33*, 2110–2125. [[CrossRef](#)]
745. Liu, S.; Zhou, L.; Han, J.; Wen, K.; Guan, S.; Xue, C.; Zhang, Z.; Xu, B.; Lin, Y.; Shen, Y.; et al. Super long-cycling all-solid-state battery with thin $\text{Li}_6\text{PS}_5\text{Cl}$ -based electrolyte. *Adv. Energy Mater.* **2022**, *12*, 2200660. [[CrossRef](#)]
746. Lee, J.Y.; Noh, S.; Seong, J.Y.; Lee, S.; Park, Y.J. Suppressing unfavorable interfacial reactions using polyanionic oxides as efficient buffer layers: Low-cost Li_3PO_4 coatings for sulfide-electrolyte-based all-solid-state batteries. *ACS Appl. Mater. Interfaces* **2023**, *15*, 12998–13011. [[CrossRef](#)]
747. Zhou, X.; Deng, L.; Zhang, K.; Zhang, Z.; Zhang, L.; Li, Z.; Kong, T.; Xie, Y.; Wang, Y. High-performance sulfide all-solid-state batteries enabled by high-voltage Ni-rich cathode with a conformal and conductive protective layer. *ACS Appl. Energy Mater.* **2024**, *7*, 2524–2532. [[CrossRef](#)]
748. Lin, C.; Liu, Y.; Su, H.; Zhong, Y.; Wang, X.; Gu, C.; Tu, J. Elevating cycle stability and reaction kinetics in Ni-rich cathodes through tailored bulk and interface chemistry for sulfide-based all-solid-state lithium batteries. *Adv. Funct. Mater.* **2024**, *34*, 2311564. [[CrossRef](#)]
749. Su, Y.; Liu, X.; Yan, H.; Zhao, J.; Cheng, Y.; Luo, Y.; Gu, J.; Zhong, H.; Fu, A.; Wang, K.; et al. Assembly of an elastic & sticky interfacial layer for sulfide-based all-solid-state batteries. *Nano Energy* **2023**, *113*, 108572.
750. Kim, J.S.; Jung, S.; Kwak, H.; Han, Y.; Kim, S.; Lim, J.; Lee, Y.M.; Jung, Y.S. Synergistic halide-sulfide hybrid solid electrolytes for Ni-rich cathodes design guided by digital twin for all-solid-State Li batteries. *Energy Storage Mater.* **2023**, *55*, 193–204. [[CrossRef](#)]
751. Li, Y.; Li, J.; Zeng, Z.; Xu, X.; Cheng, J.; Zhang, H.; Li, J.; Rao, Y.; Deng, Y.; Ci, L.; et al. Surface to bulk design empowering Ni-rich layered oxide cathode in sulfide-based All-Solid-State batteries. *Chem. Eng. J.* **2024**, *498*, 155029. [[CrossRef](#)]
752. Wang, Y.; Wang, Z.; Wu, D.; Niu, Q.; Lu, P.; Ma, T.; Su, Y.; Chen, L.; Li, H.; Wu, F. Stable Ni-rich layered oxide cathode for sulfide-based all-solid-state lithium battery. *eScience* **2022**, *2*, 537–545. [[CrossRef](#)]
753. Kitsche, D.; Tang, Y.; Ma, Y.; Goonetilleke, D.; Sann, J.; Walther, F.; Bianchini, M.; Janek, J.; Brezesinski, T. High performance all-solid-state batteries with a Ni-rich NCM cathode coated by atomic layer deposition and lithium thiophosphate solid electrolyte. *ACS Appl. Energy Mater.* **2021**, *4*, 7338–7345. [[CrossRef](#)]
754. Gao, X.; Liu, B.; Hu, B.; Ning, Z.; Jolly, D.S.; Zhang, S.; Perera, J.; Bu, J.; Liu, J.; Doerrer, C.; et al. Solid-state lithium battery cathodes operating at low pressures. *Joule* **2022**, *6*, 636–646. [[CrossRef](#)]
755. Zheng, H.; Peng, S.; Liang, S.; Yang, W.; Chen, C.; Wang, C.; Yu, R. Progress and challenges of Ni-rich layered cathodes for all-solid-state lithium batteries. *Adv. Funct. Mater.* **2025**, *35*, 2418274. [[CrossRef](#)]
756. Kim, S.; Kim, M.; Ku, M.; Park, J.; Lee, J.; Kim, Y.-B. Coating robust layers on Ni-rich cathode active materials while suppressing cation mixing for all-solid-state lithium-ion batteries. *ACS Nano* **2024**, *18*, 25096–25106. [[CrossRef](#)]
757. Zhao, W.; Zhang, R.; Ren, F.; Karger, L.; Dreyer, S.L.; Lin, J.; Ma, Y.; Cheng, Y.; Pal, A.S.; Velazquez-Rizo, M.; et al. Protective coating of single-crystalline Ni-rich cathode enables fast charging in all-solid-state batteries. *ACS Nano* **2025**, *19*, 8595–8607. [[CrossRef](#)]
758. Asano, T.; Sakai, A.; Ouchi, S.; Sakaida, M.; Miyazaki, A.; Hasegawa, S. Solid halide electrolytes with high lithium-ion conductivity for application in 4 V class bulk-type all-solid-state-batteries. *Adv. Mater.* **2018**, *30*, 1803075. [[CrossRef](#)]
759. Park, K.-H.; Kaup, K.; Assoud, A.; Zhang, Q.; Wu, X.; Nazar, L.F. High-voltage superionic halide solid electrolytes for all-solid-state Li-ion batteries. *ACS Energy Lett.* **2020**, *5*, 533–539. [[CrossRef](#)]
760. Zhou, L.; Kwok, C.Y.; Shyamsunder, A.; Zhang, Q.; Wu, X.; Nazar, L.F. A new halospinel superionic conductor for high-voltage all solid-state lithium batteries. *Energy Environ. Sci.* **2020**, *13*, 2056–2063. [[CrossRef](#)]
761. Kim, S.Y.; Kaup, K.; Park, K.-H.; Assoud, A.; Zhou, L.; Liu, J.; Wu, X.; Nazar, L.F. Lithium ytterbium-based halide solid electrolytes for high voltage all-solid-state batteries. *ACS Mater. Lett.* **2021**, *3*, 930–938. [[CrossRef](#)]
762. Zhou, L.; Zuo, T.-T.; Kwok, C.Y.; Kim, S.Y.; Assoud, A.; Zhang, Q.; Janek, J.; Nazar, L.F. High areal capacity, long cycle life 4 V ceramic all-solid-state Li-ion batteries enabled by chloride solid electrolytes. *Nat. Energy* **2022**, *7*, 83–93. [[CrossRef](#)]
763. Kim, S.-Y.; Cha, H.; Kostecki, R.; Chen, G.-Y. Composite cathode design for high-energy all-solid-state lithium batteries with long cycle life. *ACS Energy Lett.* **2023**, *8*, 521–528. [[CrossRef](#)]
764. Liu, H.-W.; Chen, H.; Thi, S.; Yu, P.-J.; Chen, J.-L.; Pao, C.-W.; Chang, P.-Y.; Haw, S.-C.; Liao, Y.-F.; Shao, Y.-C.; et al. High-capacity Ni-rich composite cathodes having chemically fused interface with Li_3InCl_6 electrolyte towards low-pressure operating all-solid-state Li-ion batteries. *Compos. Part B Eng.* **2025**, *293*, 112133. [[CrossRef](#)]
765. Seong, W.M.; Cho, K.H.; Park, J.W.; Park, H.; Eum, D.; Lee, M.H.; Kim, I.S.; Lim, J.; Kang, K. Controlling residual lithium in high-nickel (>90%) lithium layered oxides for cathodes in lithium-ion batteries. *Angew. Chem. Int. Ed.* **2020**, *59*, 18662–18669. [[CrossRef](#)] [[PubMed](#)]
766. Li, L.; Chen, J.; Huang, H.; Tan, L.; Song, L.; Wu, H.H.; Wang, C.; Zhao, Z.; Yi, H.; Duan, J.; et al. Role of residual Li and oxygen vacancies in Ni-rich cathode materials. *ACS Appl. Mater. Interfaces* **2021**, *13*, 42554–42563. [[CrossRef](#)]

767. Klein, S.; Bärmann, P.; Fromm, O.; Borzutzki, K.; Reiter, J.; Fan, Q.; Winter, M.; Placke, T.; Kasnatscheew, J. Prospects and limitations of single-crystal cathode materials to overcome cross-talk phenomena in high-voltage lithium ion cells. *J. Mater. Chem. A* **2021**, *9*, 7546–7555. [[CrossRef](#)]
768. Hou, X.; Liu, X.; Wang, H.; Zhang, X.; Zhou, J.; Wang, M. Specific countermeasures to intrinsic capacity decline issues and future direction of LiMn_2O_4 cathode. *Energy Storage Mater.* **2023**, *57*, 577–606. [[CrossRef](#)]
769. Wang, B.; Zhang, F.-L.; Zhou, X.A.; Wang, P.; Wang, J.; Ding, H.; Dong, H.; Liang, W.B.; Zhang, N.S.; Li, S.Y. Which of the nickel-rich NCM and NCA is structurally superior as a cathode material for lithium-ion batteries? *J. Mater. Chem. A* **2021**, *9*, 13540–13551. [[CrossRef](#)]
770. Wang, Z.P.; Yuan, J.; Zhu, X.Q.; Wang, H.; Huang, W.; Wang, Y.; Xu, S. Overcharge-to-thermal-runaway behavior and safety assessment of commercial lithium-ion cells with different cathode materials: A comparison study. *J. Energy Chem.* **2021**, *55*, 484–498. [[CrossRef](#)]
771. Xiong, D.J.; Hynes, T.; Ellis, L.D.; Dahn, J.R. Effects of surface coating on gas evolution and impedance growth at $\text{LiNi}_x\text{Mn}_y\text{Co}_{1-x-y}\text{O}_2$ Positive electrodes in Li-ion cells. *J. Electrochem. Soc.* **2017**, *164*, A3174–A3181. [[CrossRef](#)]
772. Wang, X.X.; Ding, Y.L.; Deng, Y.P.; Chen, Z.W. Ni-rich/Co-poor layered cathode for automotive Li-ion batteries: Promises and challenges. *Adv. Energy Mater.* **2020**, *10*, 1903864. [[CrossRef](#)]
773. Xu, H.; Li, Z.; Liu, T.; Han, C.; Guo, C.; Zhao, H.; Li, Q.; Lu, J.; Amine, K.; Qiu, X. Impacts of dissolved Ni^{2+} on the solid electrolyte interphase on a graphite anode. *Angew. Chem. Int. Ed.* **2022**, *61*, e202202894. [[CrossRef](#)]
774. Kim, Y.M.; Choi, J.I.; Park, B.K.; Han, J.W.; Lee, J.-W.; Kim, H.; Kim, K.J. Two-in-one strategy: Discretely functionalized electrolyte additive for stable lithium metal batteries coupled with Ni-rich cathode. *Chem. Eng. J.* **2024**, *486*, 150354. [[CrossRef](#)]
775. Zhang, X.; Cui, Z.; Jo, E.; Manthiram, A. Inhibition of transition-metal dissolution with advanced electrolytes in batteries with silicon-graphite anodes and high-nickel cathodes. *Energy Storage Mater.* **2023**, *56*, 562–571. [[CrossRef](#)]
776. Huang, Y.; Ji, Y.; Zheng, G.; Cao, H.; Xue, H.; Yao, X.; Wang, L.; Chen, S.; Yin, Z.; Pan, F.; et al. Tailored construction for enhanced Si anode and Ni-rich cathode performance in lithium-ion batteries. *Chin. Chem. Soc. Chem.* **2025**, *7*, 429–439.
777. Zhang, Y.; Zhang, Y.; Wang, X.; Gong, H.; Cao, Y.; Ma, K.; Zhang, S.; Wang, S.; Yang, W.; Wang, L.; et al. Trace multifunctional additive enhancing 4.8 V ultra-high voltage performance of Ni-rich cathode and SiO_x anode battery. *Adv. Energy Mater.* **2025**, *15*, 2403751. [[CrossRef](#)]
778. Yu, Y.; Karayaylali, P.; Katayama, Y.; Giordano, L.; Gauthier, M.; Maglia, F.; Jung, R.; Lund, I.; Shao-Horn, Y. Coupled LiPF_6 decomposition and carbonate dehydrogenation enhanced by highly covalent metal oxides in high-energy Li-ion batteries. *J. Phys. Chem. C* **2018**, *122*, 27368–27382. [[CrossRef](#)]
779. Zhang, Y.; Katayama, Y.; Tatara, R.; Giordano, L.; Yu, Y.; Fragedakis, D.; Sun, J.G.; Maglia, F.; Jung, R.; Bazant, M.Z.; et al. Revealing electrolyte oxidation via carbonate dehydrogenation on Ni-based oxides in Li-ion batteries by in situ Fourier transform infrared spectroscopy. *Energy Environ. Sci.* **2020**, *13*, 183–199. [[CrossRef](#)]
780. Dose, W.M.; Temprano, I.; Allen, J.P.; Bjorklund, E.; O’Keefe, C.A.; Li, W.; Mehdi, B.L.; Weatherup, R.S.; De Volder, M.F.L.; Grey, C.P. Electrolyte reactivity at the charged Ni-rich cathode interface and degradation in Li-ion batteries. *ACS Appl. Mater. Interfaces* **2022**, *14*, 13206–13222. [[CrossRef](#)]
781. Rinkel, B.L.D.; Vivek, J.P.; Garcia-Araez, N.; Grey, C.P. Two electrolyte decomposition pathways at nickel-rich cathode surfaces in lithium-ion batteries. *Energy Environ. Sci.* **2022**, *15*, 3416–3438. [[CrossRef](#)] [[PubMed](#)]
782. Dong, J.; Wu, F.; Zhao, J.; Shi, Q.; Lu, Y.; Li, N.; Cao, D.; Li, W.; Hao, J.; Yang, X.; et al. Multifunctional self-reconstructive cathode/electrolyte interphase layer for cobalt-free Li-rich layered oxide cathode. *Energy Storage Mater.* **2023**, *60*, 102798. [[CrossRef](#)]
783. Zhao, J.; Liang, Y.; Zhang, X.; Zhang, Z.; Wang, E.; He, S.; Wang, B.; Han, Z.; Lu, J.; Amine, K.; et al. In situ construction of uniform and robust cathode–electrolyte interphase for Li-rich layered oxides. *Adv. Funct. Mater.* **2020**, *31*, 2009192. [[CrossRef](#)]
784. Wu, F.; Dong, J.; Chen, L.; Bao, L.; Li, N.; Cao, D.; Lu, Y.; Xue, R.; Liu, N.; Wei, L.; et al. High-voltage and high-safety nickel-rich layered cathode enabled by a self-reconstructive cathode/electrolyte interphase layer. *Energy Storage Mater.* **2021**, *41*, 495–504. [[CrossRef](#)]
785. Dong, T.; Zhang, S.; Ren, Z.; Huang, L.; Xu, G.; Liu, T.; Wang, S.; Cui, G. Electrolyte engineering toward high performance high nickel ($\text{Ni} \geq 80\%$) lithium-ion batteries. *Adv. Sci.* **2024**, *11*, 2305753. [[CrossRef](#)]
786. Liu, L.L.; Wang, S.L.; Zhang, Z.Y.; Fan, J.; Qi, W.; Chen, S. Fluoroethylene carbonate as an electrolyte additive for improving interfacial stability of high-voltage $\text{LiNi}_{0.6}\text{Co}_{0.2}\text{Mn}_{0.2}\text{O}_2$ cathode. *Ionics* **2019**, *25*, 1035–1043. [[CrossRef](#)]
787. Wang, L.; Liu, S.; Zhao, K.; Li, J.; Yang, Y.; Gia, G. Improving the rate performance and stability $\text{LiNi}_{0.6}\text{Co}_{0.2}\text{Mn}_{0.2}\text{O}_2$ in high voltage lithium-ion battery by using fluoroethylene carbonate as electrolyte additive. *Ionics* **2018**, *24*, 3337–3346. [[CrossRef](#)]
788. Kang, Y.; Wang, J.; Wang, M.; Tang, X.; Cao, Z.; Wang, C.; Shi, Q.; Qian, Y.; Deng, Y. Multifunctional fluoroethylene carbonate for improving high-temperature performance of $\text{LiNi}_{0.8}\text{Mn}_{0.1}\text{Co}_{0.1}\text{O}_2 \parallel \text{SiO}_x$ @graphite lithium-ion batteries. *ACS Appl. Energy Mater.* **2020**, *3*, 9989–10000. [[CrossRef](#)]

789. Wang, S.; Chen, S.; Gao, W.; Liu, L.; Zhang, S. A new additive 3-isocyanatopropyltriethoxysilane to improve electrochemical performance of Li/NCM622 half-cell at high voltage. *J. Power Sources* **2019**, *423*, 90–97. [[CrossRef](#)]
790. Zhu, C.Y.; Liu, J.; Yu, X.; Zhang, Y.; Jiang, X.; Dong, P.; Zhang, Y. 4-bromoanisole (4BA) as additive for overcharge protection of lithium-ion batteries. *Int. J. Electrochem. Sci.* **2019**, *14*, 4571–4579. [[CrossRef](#)]
791. Cao, Z.; Hashinokuchi, M.; Doi, T.; Inaba, M. Improved cycle performance of $\text{LiNi}_{0.8}\text{Co}_{0.1}\text{Mn}_{0.1}\text{O}_2$ positive electrode material in highly concentrated LiBF_4/DMC . *J. Electrochem. Soc.* **2019**, *166*, A82–A88. [[CrossRef](#)]
792. Tataro, R.; Yu, Y.; Karayaylali, P.; Chan, A.K.; Zhang, Y.; Jung, R.; Maglia, F.; Giordano, L.; Shao-Horn, Y. Enhanced cycling performance of Ni-rich positive electrodes (NMC) in Li-ion batteries by reducing electrolyte free-solvent activity. *ACS Appl. Mater. Interfaces* **2019**, *11*, 34973–34988. [[CrossRef](#)]
793. Forero-Saboya, J.; Moiseev, I.A.; Vlara, M.-L.; Foix, D.; Deschamps, M.; Abakumov, A.M.; Tarascon, J.-M.; Mariyappan, S. A Hydridoaluminate additive producing a protective coating on Ni-rich cathode materials in lithium-ion batteries. *Adv. Energy Mater.* **2024**, *14*, 2402051. [[CrossRef](#)]
794. Hu, J.; Cheng, F.; Fang, C.; Han, J. High-voltage electrolyte design for a Ni-rich layered oxide cathode for lithium-ion batteries. *Sci. China Mater.* **2023**, *66*, 3046–3053. [[CrossRef](#)]
795. Zheng, Y.; Xu, N.; Chen, S.; Liao, Y.; Zhong, G.; Zhang, Z.; Yang, Y. Construction of a stable $\text{LiNi}_{0.8}\text{Co}_{0.1}\text{Mn}_{0.1}\text{O}_2$ (NMC811) cathode interface by a multifunctional organosilicon electrolyte additive. *ACS Appl. Energy Mater.* **2020**, *3*, 2837–2845. [[CrossRef](#)]
796. Braun, H.; Asakura, R.; Remhof, A.; Battaglia, C. Hydroborate solid-state lithium battery with high-voltage NMC811 cathode. *ACS Energy Lett.* **2024**, *9*, 707–714. [[CrossRef](#)]
797. Hu, R.; Mao, C.; Zhuo, H.; Dai, X.; Yang, L.; Shu, X.; Li, Y.; Li, Z.; Ruan, W.; Yang, F.; et al. Molecular space linkage of dipentacyclic anhydride additives for long-lifespan Li-metal batteries with Ni-rich cathode. *Energy Storage Mater.* **2025**, *75*, 104033. [[CrossRef](#)]
798. Yang, S.; Li, G.; Lin, X.; Mo, C.; Zhou, X.; Quan, L.; Zhou, K.; Li, S.; Wang, H.; Li, W. Highly improved cyclic stability of Ni-rich/Li batteries with succinic anhydride as electrolyte additive and underlying mechanism. *J. Energy Chem.* **2023**, *78*, 80–90. [[CrossRef](#)]
799. Jiang, S.; Xu, X.; Yin, J.; Zhu, X.; Wei, L.; Xi, K.; Zhang, L.; Lan, Y.; Wu, H.; Gao, Y. Tailoring electrode-electrolyte interphases to enable the cycling stability of lithium metal batteries with $\text{LiNi}_{0.8}\text{Co}_{0.1}\text{Mn}_{0.1}\text{O}_2$ cathode. *J. Power Sources* **2022**, *529*, 231195. [[CrossRef](#)]
800. Qin, Y.; Cheng, H.; Zhou, J.; Liu, M.; Ding, X.; Li, Y.; Huang, Y.; Chen, Z.; Shen, C.; Wang, D.; et al. A tough Janus-faced CEI film for high voltage layered oxide cathodes beyond 4.6 V. *Energy Storage Mater.* **2023**, *57*, 411–420. [[CrossRef](#)]
801. He, Y.; Liu, N.; Kohl, P.A. High conductivity, lithium ion conducting polymer electrolyte based on hydrocarbon backbone with pendent carbonate. *J. Electrochem. Soc.* **2020**, *167*, 100517. [[CrossRef](#)]
802. Jie, Y.; Ren, X.; Cao, R.; Cai, W.; Jiao, S. Advanced liquid electrolytes for rechargeable Li metal batteries. *Adv. Funct. Mater.* **2020**, *30*, 1910777. [[CrossRef](#)]
803. Kim, H.N.; Kim, S.Y.; Ahn, J.; Yim, T. Simultaneous realization of multilayer interphases on a Ni-rich NCM cathode and a SiO_x anode by the combination of vinylene carbonate with lithium difluoro(oxalato)borate. *ACS Appl. Mater. Interfaces* **2024**, *16*, 14940–14953. [[CrossRef](#)]
804. Dai, P.; Kong, X.; Yang, H.; Kuang, S.; Zeng, J.; Zhao, J. Synergistic effect of dual-anion additives promotes the fast dynamics and high-voltage performance of Ni-rich lithium-ion batteries by regulating the electrode/electrolyte interface. *ACS Appl. Mater. Interfaces* **2022**, *14*, 39927–39938. [[CrossRef](#)] [[PubMed](#)]
805. Xiao, B.; Sun, X. Surface and subsurface reactions of lithium transition metal oxide cathode materials: An overview of the fundamental origins and remedying approaches. *Adv. Energy Mater.* **2018**, *8*, 1802057. [[CrossRef](#)]
806. Zhang, S.S.; Fan, X.L.; Wang, C.S. Enhanced electrochemical performance of Ni-rich layered cathode materials by using LiPF_6 as a cathode additive. *ChemElectroChem* **2019**, *6*, 1536–1541. [[CrossRef](#)]
807. Phelan, C.M.E.; Björklund, E.; Singh, J.; Fraser, M.; Didwal, P.N.; Rees, G.J.; Ruff, Z.; Ferrer, P.; Grinter, D.C.; Grey, C.P.; et al. Role of salt concentration in stabilizing charged Ni-rich cathode interfaces in Li-ion batteries. *Chem. Mater.* **2024**, *36*, 3334–3344. [[CrossRef](#)]
808. Qiao, Y.; Yang, H.; Chang, Z.; Deng, H.; Li, X.; Zhou, H. A high-energy-density and long-life initial-anode-free lithium battery enabled by a Li_2O sacrificial agent. *Nat. Energy* **2021**, *6*, 653–662. [[CrossRef](#)]
809. Jiang, Q.; Li, M.; Li, J.; Wang, J.; Zhang, G.; Wang, J.; Zuo, J.; Cao, G.; Duan, R.; Hao, Y.; et al. LiF-rich cathode electrolyte interphases homogenizing Li^+ fluxes toward stable interface in Ni-rich Mn-based cathodes. *Adv. Mater.* **2025**, *37*, 2417620. [[CrossRef](#)]
810. Min, X.; Wang, L.; Shen, M.; Ma, G.; He, X. A multifunctional additive extending the calendar life of Ni-rich cathode-based lithium-ion batteries for electric vehicles. *Mater. Today* **2025**, *83*, 157–165. [[CrossRef](#)]
811. Zhuang, Y.; Zhao, Y.; Bao, Y.; Zhang, W.; Guan, M. Bis(di-tert-butyl)-4-dimethylaminophenylphosphine as electrolyte additive to improve the electrochemical performance of $\text{LiNi}_{0.8}\text{Co}_{0.1}\text{Mn}_{0.1}\text{O}_2$. *Electrochim. Acta* **2023**, *441*, 141745. [[CrossRef](#)]

812. Zou, Y.; Zheng, Q.; Tang, Y.; Yan, Y.; Zhou, S.; Liao, H.-G.; Qiao, Y.; Bao, J.; Sun, S.-G. Self-repaired cathode electrolyte interphase to stabilize the high-nickel cathode interface by a sustained-release multifunctional electrolyte additive. *Chem. Eng. J.* **2024**, *488*, 151153. [[CrossRef](#)]
813. Li, G.; Liao, Y.; Li, Z.; Xu, N.; Lu, Y.; Lan, G.; Sun, G.; Li, W. Constructing a low-impedance interface on a high-voltage $\text{LiNi}_{0.8}\text{Co}_{0.1}\text{Mn}_{0.1}\text{O}_2$ cathode with 2,4,6-triphenyl boroxine as a film-forming electrolyte additive for Li-ion batteries. *ACS Appl. Mater. Interfaces* **2020**, *12*, 37013–37026. [[CrossRef](#)]
814. Zhang, X.; Liu, G.; Zhou, K.; Cheng, Y.; Jiao, T.; Huang, L.; Zou, Y.; Wang, M.S.; Yang, Y.; Zheng, J. Dictating the interfacial stability of nickel-rich $\text{LiNi}_{0.90}\text{Co}_{0.05}\text{Mn}_{0.05}\text{O}_2$ via a diazacyclo electrolyte additive—2-Fluoropyrazine. *J. Colloid Interface Sci.* **2022**, *618*, 431–441. [[CrossRef](#)]
815. Yang, J.; Liu, X.; Wang, Y.; Zhou, X.; Weng, L.; Liu, Y.; Ren, Y.; Zhao, C.; Dahbi, M.; Alami, J.; et al. Electrolytes polymerization-induced cathode-electrolyte-interphase for high voltage lithium-ion batteries. *Adv. Energy Mater.* **2021**, *11*, 2101956. [[CrossRef](#)]
816. Kong, X.; Liu, J.; Zhang, Y.; Zeng, J.; Zhao, J. An effective electrolyte design to improve the high-voltage performance of high-capacity NMC811/ SiO_x -Gr batteries. *Electrochim. Acta* **2020**, *349*, 136356. [[CrossRef](#)]
817. Kim, S.Y.; Lee, S.; Yoon, S.C.; Yim, T. Amphiphilic surfactant-assisted cathode-electrolyte interphases for prolonged cycling performance in Ni-rich NCMA cathode materials of lithium-ion batteries. *J. Power Sources* **2025**, *633*, 236447. [[CrossRef](#)]
818. Li, S.; Yang, T.; Wang, W.; Lu, J.; Zhao, X.; Fan, W.; Zuo, X.; Nan, J. 2-Thiophene sulfonamide (2-TS)-contained multi-functional electrolyte matching high-voltage $\text{LiNi}_{0.8}\text{Mn}_{0.1}\text{Co}_{0.1}\text{O}_2$ /graphite batteries with enhanced performances. *Electrochim. Acta* **2020**, *352*, 136492. [[CrossRef](#)]
819. Li, Z.; Lin, X.; Zhou, H.; Xing, L.; Lan, G.; Zhang, W.; Chen, J.; Liu, M.; Huang, Q.; Li, W. Stabilizing the interphasial layer of Ni-rich cathode and graphite anode for lithium-ion battery with multifunctional additive. *J. Power Sources* **2020**, *467*, 228343. [[CrossRef](#)]
820. Li, S.; Li, C.; Yang, T.; Wang, W.; Lu, J.; Fan, W.; Zhao, X.; Zuo, X.; Tie, S.; Nan, J. 3,3-diethylene di-sulfite (DES) as a high-voltage electrolyte additive for 4.5 V $\text{LiNi}_{0.8}\text{Co}_{0.1}\text{Mn}_{0.1}\text{O}_2$ /graphite batteries with enhanced performances. *ChemElectroChem* **2021**, *8*, 745–754. [[CrossRef](#)]
821. Moon, H.; Nam, H.; Kim, M.P.; Lee, S.M.; Kim, H.; Jeon, M.H.; Lee, Y.-S.; Kim, K.; Chun, J.-H.; Kwak, S.K.; et al. Elastic interfacial layer enabled the high-temperature performance of lithium-ion batteries via utilization of synthetic fluorosulfate additive. *Adv. Func. Mater.* **2023**, *33*, 2303029. [[CrossRef](#)]
822. Dai, H.; Gomes, L.; Maxwell, D.; Zamani, S.; Yang, K.; Atienza, D.; Dale, N.; Mukerjee, S. Exploring the role of an electrolyte additive in suppressing surface Reconstruction of a Ni-rich NMC cathode at ultrahigh Voltage via enhanced in situ and operando characterization methods. *ACS Appl. Mater. Interfaces* **2024**, *16*, 8639–8654. [[CrossRef](#)]
823. Liu, L.; Gao, W.; Cui, Y.; Chen, S. A bifunctional additive bi(4-fluorophenyl) sulfone for enhancing the stability and safety of nickel-rich cathode-based cells. *J. Alloys Compd.* **2020**, *820*, 153069. [[CrossRef](#)]
824. Lan, G.; Xing, L.; Bedrov, D.; Chen, J.; Guo, R.; Che, Y.; Li, Z.; Zhou, H.; Li, W. Enhanced cyclic stability of Ni-rich lithium-ion battery with electrolyte film-forming additive. *J. Alloys Compd.* **2020**, *821*, 153236. [[CrossRef](#)]
825. Song, H.J.; Jang, S.H.; Choi, K.; Nam, S.C.; Mun, J.; Yim, T. Sulfonate-based artificial cathode-electrolyte interface to enhance electrochemical performance of Ni-rich layered oxide cathode materials. *ACS Sustain. Chem. Eng.* **2020**, *8*, 7316–7323. [[CrossRef](#)]
826. Jung, K.; Yim, T. High-performance lithium-ion batteries combined with bi-functionalized electrolyte additive and nickel-rich layered oxides. *J. Alloys Compd.* **2020**, *834*, 155155. [[CrossRef](#)]
827. Ahn, J.; Yim, T. Ni-rich $\text{LiNi}_{0.8}\text{Co}_{0.1}\text{Mn}_{0.1}\text{O}_2$ oxide functionalized by allyl phenyl sulfone as high-performance cathode material for lithium-ion batteries. *J. Alloys Compd.* **2021**, *867*, 159153. [[CrossRef](#)]
828. Zheng, W.-C.; Shi, C.-G.; Dai, P.; Huang, Z.; Lin, J.-X.; Chen, H.; Sun, M.-L.; Shen, C.-H.; Luo, C.-X.; Wang, Q.; et al. A functional electrolyte additive enabling robust interphases in high-voltage Li// $\text{LiNi}_{0.8}\text{Co}_{0.1}\text{Mn}_{0.1}\text{O}_2$ batteries at elevated temperatures. *J. Mater. Chem. A* **2022**, *10*, 21912–21922. [[CrossRef](#)]
829. Liu, G.; Gao, J.; Xia, M.; Cheng, Y.; Wang, M.; Hong, W.; Yang, Y.; Zheng, J. Strengthening the interfacial stability of the silicon-based electrode via an electrolyte additive—Allyl phenyl sulfone. *ACS Appl. Mater. Interfaces* **2022**, *14*, 38281. [[CrossRef](#)] [[PubMed](#)]
830. Jiao, T.; Liu, G.; Zou, Y.; Yang, X.; Zhang, X.; Fu, A.; Zheng, J.; Yang, Y. A novel trimethylsilyl 2-(fluorosulfonyl)difluoroacetate additive for stabilizing the Ni-rich $\text{LiNi}_{0.9}\text{Co}_{0.05}\text{Mn}_{0.05}\text{O}_2$ /electrolyte interface. *J. Power Sources* **2021**, *515*, 230618. [[CrossRef](#)]
831. Jiao, T.; Liu, G.; Huang, L.; Zou, Y.; Zhang, X.; Zheng, J.; Yang, Y. Tuning interface stability of nickel-rich $\text{LiNi}_{0.9}\text{Co}_{0.05}\text{Mn}_{0.05}\text{O}_2$ cathode via a novel bis(vinylsulphonyl)methane additive. *J. Power Sources* **2022**, *521*, 230917. [[CrossRef](#)]
832. Jiang, S.; Xu, X.; Yin, J.; Wu, H.; Zhu, X.; Guan, H.; Wei, L.; Xi, K.; Lan, Y.; Zhang, L.; et al. Regulating electrode-electrolyte interphases and eliminating hydrogen fluoride to boost electrochemical performances of Li/NMC811 batteries. *Chem. Eng. J.* **2023**, *451*, 138359. [[CrossRef](#)]
833. Choi, M.; Choi, H.; Park, S.; Seong, W.M.; Lee, Y.; Ko, W.; Cho, M.; Ahn, J.; Kong, Y.; Kim, J. Stabilized high-voltage operation of Co-free NMX cathode via CEI-controlling. *Energy Storage Mater.* **2024**, *67*, 103291. [[CrossRef](#)]

834. Jo, M.; Park, S.-H.; Lee, H. NaH_2PO_4 as an electrolyte additive for enhanced thermal stability of $\text{LiNi}_{0.8}\text{Co}_{0.1}\text{Mn}_{0.1}\text{O}_2$ /graphite batteries. *J. Electrochem. Soc.* **2020**, *167*, 130502. [[CrossRef](#)]
835. Zhao, H.; Qian, Y.; Luo, G.; Chang, J.; Wang, C.; Wang, J.; Shao, H.; Deng, Y. Cathode-anode reaction products interplay enabling high performance of $\text{LiNi}_{0.8}\text{Co}_{0.1}\text{Mn}_{0.1}\text{O}_2$ /artificial graphite pouch batteries at elevated temperature. *J. Power Sources* **2021**, *514*, 230583. [[CrossRef](#)]
836. Song, W.; Gauthier, R.; Taskovic, T.; Ouyang, D.; Ingham, H.A.; Eldesoky, A.; Azam, S.M.; Zsoldos, E.S.; Deng, Z.; Heino, D.H.; et al. Lithium difluoro(dioxalato) phosphate as an electrolyte additive for NMC811/graphite Li-ion pouch cells. *J. Electrochem. Soc.* **2022**, *169*, 110513. [[CrossRef](#)]
837. Jiang, S.; Xu, X.; Yin, J.; Lei, Y.; Wu, X.; Gao, Y. Interfacial regulation and hydrogen fluoride capture enabled by allyltrimethylsilane as multifunctional electrolyte additive for $\text{Li}/\text{LiNi}_{0.8}\text{Co}_{0.1}\text{Mn}_{0.1}\text{O}_2$ batteries. *ACS Appl. Energy Mater.* **2022**, *5*, 13501–13510. [[CrossRef](#)]
838. Lin, J.; Yang, Y.; Lin, X.; Li, G.; Zhang, W.; Li, W. Insight into the improved performances of Ni-rich/graphite cells by 1,3,5-Trimethyl-1,3,5-tris(3,3,3-trifluoropropyl) cyclotrisiloxane as an electrolyte additive. *ACS Appl. Energy Mater.* **2022**, *5*, 11684–11693. [[CrossRef](#)]
839. Chen, Y.; He, Q.; Mo, Y.; Zhou, W.; Hao, Y.; Piao, N.; Liu, C.; Xiao, P.; Liu, H.; Li, B.; et al. Engineering an insoluble cathode electrolyte interphase enabling high performance NMC811//graphite pouch cell at 60 °C. *Adv. Energy Mater.* **2022**, *12*, 2201631. [[CrossRef](#)]
840. Ren, Z.; Qiu, H.; Fan, C.; Zhang, S.; Zhang, Q.; Ma, Y.; Qiao, L.; Wang, S.; Xu, G.; Cui, Z.; et al. Delicately designed cyano-siloxane as multifunctional additive enabling high voltage $\text{LiNi}_{0.9}\text{Co}_{0.05}\text{Mn}_{0.05}\text{O}_2$ /graphite full cell with long cycle life at 50 °C. *Adv. Funct. Mater.* **2023**, *33*, 302411. [[CrossRef](#)]
841. Zhang, D.; Liu, M.; Ma, J.; Yang, K.; Chen, Z.; Li, K.; Zhang, C.; Wei, Y.; Zhou, M.; Wang, P.; et al. Lithium hexamethyldisilazide as electrolyte additive for efficient cycling of high-voltage non-aqueous lithium metal batteries. *Nat Commun.* **2022**, *13*, 6966. [[CrossRef](#)]
842. Xu, N.; Shi, J.; Liu, G.; Yang, X.; Zheng, J.; Zhang, Z.; Yang, Y. Research progress of fluorine-containing electrolyte additives for lithium ion batteries. *J. Power Sources Adv.* **2021**, *7*, 100043. [[CrossRef](#)]
843. Dong, Q.; Guo, F.; Cheng, Z.; Mao, Y.; Huang, R.; Li, F.; Dong, H.; Zhang, Q.; Li, W.; Chen, H.; et al. Insights into the dual role of lithium difluoro(oxalato)borate additive in Improving the electrochemical performance of NMC811//graphite cells. *ACS Appl. Energy Mater.* **2020**, *3*, 695–704. [[CrossRef](#)]
844. Zhao, Q.; Wu, Y.; Yang, Z.; Song, D.; Sun, X.; Wang, C.; Yang, L.; Zhang, Y.; Gao, J.; Ohsaka, T.; et al. A fluorinated electrolyte stabilizing high-voltage graphite/NMC811 batteries with an inorganic-rich electrode-electrolyte interface. *Chem. Eng. J.* **2022**, *440*, 135939. [[CrossRef](#)]
845. Ahn, J.; Im, J.; Seo, H.; Yoon, S.; Cho, K.Y. Enhancing the cycling stability of Ni-rich $\text{LiNi}_{0.83}\text{Co}_{0.11}\text{Mn}_{0.06}\text{O}_2$ cathode at 4.5 V via 2,4-difluorobiphenyl additive. *J. Power Sources* **2021**, *512*, 230513. [[CrossRef](#)]
846. Cheng, F.; Zhang, X.; Wei, P.; Sun, S.; Xu, Y.; Li, Q.; Fang, C.; Han, J.; Huang, Y. Tailoring electrolyte enables high-voltage Ni-rich NCM cathode against aggressive cathode chemistries for Li-ion batteries. *Sci. Bull.* **2022**, *67*, 2225–2234. [[CrossRef](#)]
847. Pham, H.Q.; Nguyen, M.T.; Tarik, M.; El Kazzi, M.; Trabesinger, S. Cross-talk-suppressing electrolyte additive enabling high voltage performance of Ni-rich layered oxides in Li-ion batteries. *ChemSusChem* **2021**, *14*, 2461–2474. [[CrossRef](#)]
848. Tan, S.; Shadike, Z.; Li, J.; Wang, X.; Yang, Y.; Lin, R.; Cresce, A.; Hu, J.; Hunt, A.; Waluyo, I.; et al. Additive engineering for robust interphases to stabilize high-Ni layered structures at ultra-high voltage of 4.8 V. *Nat. Energy* **2022**, *7*, 484–494. [[CrossRef](#)]
849. Xue, W.; Huang, M.; Li, Y.; Zhu, Y.G.; Gao, R.; Xiao, X.; Zhang, W.; Li, S.; Xu, G.; Yu, Y.; et al. Ultra-high-voltage Ni-rich layered cathodes in practical Li metal batteries enabled by a sulfonamide-based electrolyte. *Nat. Energy* **2021**, *6*, 495–505.
850. Oh, M.G.; Kwak, S.; An, K.; Tran, Y.H.T.; Kang, D.G.; Park, S.J.; Lim, G.; Kim, K.; Lee, Y.S.; Song, S.W. Perfluoro macrocyclic ether as an ambifunctional additive for high-performance SiO and nickel 88%-based high-energy Li-ion battery. *Adv. Funct. Mater.* **2023**, *33*, 2212890. [[CrossRef](#)]
851. Peng, X.; Shen, H.; Su, K.; Wang, W.; Weng, S.; Tang, C.; Xue, Z.; Xiang, Y. Stable and fast ion transport electrolyte interfaces modified with novel fluorine- and nitrogen-containing solvents for Ni-rich cathode materials. *ACS Appl. Mater. Interfaces* **2024**, *16*, 34281–34293. [[CrossRef](#)] [[PubMed](#)]
852. Lei, Y.; Xu, X.; Yin, J.; Jiang, S.; Xi, K.; Gao, Y. LiF-rich interfaces and HF elimination achieved by a multifunctional additive enable high-performance $\text{Li}/\text{LiNi}_{0.8}\text{Co}_{0.1}\text{Mn}_{0.1}\text{O}_2$ batteries. *ACS Appl. Mater. Interfaces* **2023**, *15*, 11777–11786. [[CrossRef](#)]
853. Liu, G.; Xu, N.; Zou, Y.; Zhou, K.; Yang, X.; Jiao, T.; Yang, W.; Yang, Y.; Zheng, J. Stabilizing Ni-rich $\text{LiNi}_{0.83}\text{Co}_{0.12}\text{Mn}_{0.05}\text{O}_2$ with cyclopentyl isocyanate as a novel electrolyte additive. *ACS Appl. Mater. Interfaces* **2021**, *13*, 12069–12078. [[CrossRef](#)]
854. Tan, C.; Yang, J.; Pan, Q.; Li, Y.; Li, Y.; Cui, L.; Fan, X.; Zheng, F.; Wang, H.; Li, Q. Optimizing interphase structure to enhance electrochemical performance of high voltage $\text{LiNi}_{0.5}\text{Mn}_{1.5}\text{O}_4$ cathode via anhydride additives. *Chem. Eng. J.* **2021**, *410*, 128422. [[CrossRef](#)]

855. Han, F.; Cang, Z.; Wang, R.; Yun, F.; Wang, J.; Ma, C.; Zhang, Y.; Tang, L.; Ding, H.; Lu, S. Isocyanate additives improve the low-temperature performance of $\text{LiNi}_{0.8}\text{Mn}_{0.1}\text{Co}_{0.1}\text{O}_2 \parallel \text{SiO}_x$ @graphite lithium-ion batteries. *ACS Appl. Mater. Interfaces* **2023**, *15*, 20966–20976. [[CrossRef](#)]
856. Zheng, J.; Qiu, Y.; Liao, S.; Yue, Z.; Fang, S.; Zhou, N.; Li, Y.; Jiang, Y. A novel 4-fluorophenyl isocyanate additive constructing solid cathodes-electrolyte interface for high-performance lithium-ion batteries. *Small* **2024**, *20*, 2405853. [[CrossRef](#)]
857. Zou, Y.; Zhou, K.; Liu, G.; Xu, N.; Zhang, X.; Yang, Y.; Zhang, J.; Zheng, J. Enhanced cycle life and rate capability of single-crystal, Ni-rich $\text{LiNi}_{0.9}\text{Co}_{0.05}\text{Mn}_{0.05}\text{O}_2$ enabled by 1,2,4-1H-triazole additive. *ACS Appl. Mater. Interfaces* **2021**, *13*, 16427–16436. [[CrossRef](#)]
858. Lu, J.; Li, S.; Jiang, L.; Yang, T.; Fan, W.; Wang, W.; Zhao, X.; Zuo, X.; Nan, J. Isocyanooethyl methacrylate (IMA) as a bifunctional electrolyte additive for $\text{LiNi}_{0.8}\text{Co}_{0.1}\text{Mn}_{0.1}\text{O}_2$ /graphite batteries with enhanced performance. *ChemElectroChem* **2021**, *8*, 3716–3725. [[CrossRef](#)]
859. Pham, H.Q.; Mirolo, M.; Tarik, M.; El-Kazzi, M.; Trabesinger, S. Multifunctional electrolyte additive for improved interfacial stability in Ni-rich layered oxide full-cells. *Energy Storage Mater.* **2020**, *33*, 216–229. [[CrossRef](#)]
860. Li, Y.; Qu, Q.; Lv, L.; Shao, J.; Zheng, H. A multifunctional additive capable of electrolyte stabilization and structure/interphases regulation of high-energy Li-ion batteries. *Adv. Funct. Mater.* **2024**, *34*, 2314100. [[CrossRef](#)]
861. Cheng, F.; Zhang, X.; Qiu, Y.; Zhang, J.; Liu, Y.; Wei, P.; Ou, M.; Sun, S.; Xu, Y.; Li, Q.; et al. Tailoring electrolyte to enable high-rate and super-stable Ni-rich NCM cathode materials for Li-ion batteries. *Nano Energy* **2021**, *88*, 106301. [[CrossRef](#)]
862. Guan, P.; Min, J.; Zhang, S.; Lu, Y.; Liang, T.; Meng, L.; Yuan, Y.; Zhou, Y.; Chen, F.; Zhou, L.; et al. Stabilizing high-voltage performance of nickel-rich cathodes via facile solvothermally synthesized niobium-doped strontium titanate. *ACS Appl. Mater. Interfaces* **2024**, *16*, 26167–26181. [[CrossRef](#)] [[PubMed](#)]
863. Zhang, X.; Liu, G.; Jiao, T.; Cheng, Y.; Zou, Y.; Wang, M.-S.; Yang, Y.; Zheng, J. Electrolyte additive cis-1,2,3,6-tetrahydrophthalic anhydride enhanced the cycle life of nickel-rich $\text{LiNi}_{0.9}\text{Co}_{0.05}\text{Mn}_{0.05}\text{O}_2$. *ACS Appl. Energy Mater.* **2021**, *4*, 12275–12284. [[CrossRef](#)]
864. Zou, Y.; Liu, G.; Zhou, K.; Zhang, J.; Jiao, T.; Zhang, X.; Yang, Y.; Zheng, J. Enhanced interfacial stability of a $\text{LiNi}_{0.9}\text{Co}_{0.05}\text{Mn}_{0.05}\text{O}_2$ cathode by a diboron additive. *ACS Appl. Energy Mater.* **2021**, *4*, 11051–11061. [[CrossRef](#)]
865. Zeng, X.; Gao, X.; Zhou, P.; Li, H.; He, X.; Fan, W.; Fan, C.; Yang, T.; Ma, Z.; Zhao, X.; et al. Eliminating $\text{H}_2\text{O}/\text{HF}$ and regulating interphase with bifunctional tolylene-2, 4-diisocyanate (TDI) additive for long life Li-ion battery. *J. Energy Chem.* **2024**, *95*, 519–528. [[CrossRef](#)]
866. Lim, D.-A.; Shin, Y.-K.; Seok, J.-H.; Hong, D.; Ahn, K.H.; Lee, C.H.; Kim, D.-W. Cathode electrolyte interphase-forming additive for improving cycling performance and thermal stability of Ni-rich $\text{LiNi}_x\text{Co}_y\text{Mn}_{1-x-y}\text{O}_2$ cathode materials. *ACS Appl. Mater. Interfaces* **2022**, *14*, 54688–54697. [[CrossRef](#)]
867. Li, S.; Zhao, D.; Wang, P.; Cui, X.; Tang, F. Electrochemical effect and mechanism of adiponitrile additive for high-voltage electrolyte. *Electrochim. Acta* **2016**, *222*, 668–677. [[CrossRef](#)]
868. Lee, S.H.; Hwang, J.Y.; Park, S.J.; Park, G.T.; Sun, Y.K. Adiponitrile ($\text{C}_6\text{H}_8\text{N}_2$): A new Bi functional additive for high performance Li metal batteries. *Adv. Funct. Mater.* **2019**, *29*, 1902496. [[CrossRef](#)]
869. Li, X.; Han, X.; Li, G.; Du, J.; Cao, Y.; Gong, H.; Wang, H.; Zhang, Y.; Liu, S.; Zhang, B.; et al. Nonsacrificial nitrile additive for armoring high-voltage $\text{LiNi}_{0.83}\text{Co}_{0.07}\text{Mn}_{0.1}\text{O}_2$ cathode with reliable electrode-electrolyte interface toward durable battery. *Small* **2022**, *18*, 2202989. [[CrossRef](#)] [[PubMed](#)]
870. Qiu, C.; Li, Z.; Pan, J.; Hong, Y.; Li, J.; Lin, Y.; Shi, K.; Liu, Q. Designing stable electrode interfaces from a pyrrolidine-based electrolyte for improving $\text{LiNi}_{0.8}\text{Co}_{0.1}\text{Mn}_{0.1}\text{O}_2$ batteries. *Ind. Eng. Chem. Res.* **2022**, *61*, 14173–14180. [[CrossRef](#)]
871. Park, S.; Jeong, S.Y.; Lee, T.K.; Park, M.W.; Lim, H.Y.; Sung, J.; Cho, J.; Kwak, S.K.; Hong, S.Y.; Choi, N.-S. Replacing conventional battery electrolyte additives with dioxolone derivatives for high-energy-density lithium-ion batteries. *Nat. Commun.* **2021**, *12*, 838. [[CrossRef](#)]
872. Zhuang, X.; Zhang, S.; Cui, Z.; Cui, Z.; Xie, B.; Gong, T.; Zhang, X.; Li, J.; Wu, R.; Wang, S.; et al. Interphase regulation by multifunctional additive empowering high energy lithium-ion batteries with enhanced cycle life and thermal safety. *Angew. Chem. Int. Ed.* **2024**, *63*, e202315710. [[CrossRef](#)] [[PubMed](#)]
873. Song, W.; Harlow, J.; Logan, E.; Hebecker, H.; Coon, M.; Molino, L.; Johnson, M.; Dahn, J.; Metzger, M. A systematic study of electrolyte additives in single crystal and bimodal $\text{LiNi}_{0.8}\text{Mn}_{0.1}\text{Co}_{0.1}\text{O}_2$ /graphite pouch cells. *J. Electrochem. Soc.* **2021**, *168*, 090503. [[CrossRef](#)]
874. Lu, D.; Li, R.; Rahman, M.M.; Yu, P.; Lv, L.; Yang, S.; Huang, Y.; Sun, C.; Zhang, S.; Zhang, H.; et al. Ligand-channel-enabled ultrafast Li-ion conduction. *Nature* **2024**, *627*, 101–107. [[CrossRef](#)]
875. Li, G.-X.; Koverga, V.; Nguyen, A.; Kou, R.; Ncube, M.; Jiang, H.; Wang, K.; Liao, M.; Guo, H.; Chen, J.; et al. Enhancing lithium-metal battery longevity through minimized coordinating diluent. *Nat. Energy* **2024**, *9*, 817–827. [[CrossRef](#)]
876. Liu, X.; Mariani, A.; Diemant, T.; Pietro, M.E.D.; Dong, X.; Kuenzel, M.; Mele, A.; Passerini, S. Difluorobenzene-based locally concentrated ionic liquid electrolyte enabling stable cycling of lithium metal batteries with nickel-rich cathode. *Adv. Energy Mater.* **2022**, *12*, 2200862. [[CrossRef](#)]

877. Fan, X.; Ji, X.; Chen, L.; Chen, J.; Deng, T.; Han, F.; Yue, J.; Piao, N.; Wang, R.; Zhou, X.; et al. All-temperature batteries enabled by fluorinated electrolytes with non-polar solvents. *Nat. Energy* **2019**, *4*, 882–890. [[CrossRef](#)]
878. Zhang, W.; Yang, T.; Liao, X.; Song, Y.; Zhao, Y. All-fluorinated electrolyte directly tuned Li⁺ solvation sheath enabling high-quality passivated interfaces for robust Li metal battery under high voltage operation. *Energy Storage Mater.* **2023**, *57*, 249–259. [[CrossRef](#)]
879. Su, C.-C.; He, M.; Shi, J.; Amine, R.; Yu, Z.; Cheng, L.; Guo, J.; Amine, K. Principle in developing novel fluorinated sulfone electrolyte for high voltage lithium-ion batteries. *Energy Environ. Sci.* **2021**, *14*, 3029–3034. [[CrossRef](#)]
880. Chen, Y.; Zhao, Y.; Wang, A.; Zhang, D.; Li, B.; He, X.; Fan, X.; Liu, J. Cosolvent occupied solvation tuned anti-oxidation therapy toward highly safe 4.7 V-class NMC811 batteries. *Energy Environ. Sci.* **2024**, *17*, 6113–6126. [[CrossRef](#)]
881. Chen, Y.; He, Q.; Zhao, Y.; Zhou, W.; Xiao, P.; Gao, P.; Tavajohi, N.; Tu, J.; Li, B.; He, X.; et al. Breaking solvation dominance of ethylene carbonate via molecular charge engineering enables lower temperature battery. *Nat. Commun.* **2023**, *14*, 8326. [[CrossRef](#)]
882. Xiao, Y.; Zhang, W.; Dong, W.; Yang, K.; Chao, Y.; Xi, C.; Li, M.; Zhang, Q.; Liu, Z.; Du, P.; et al. Enhancing the cathode/electrolyte interface in Ni-rich lithium-ion batteries through homogeneous oxynitridation enabled by NO₃⁻ dominated clusters. *Chem. Eng. J.* **2024**, *494*, 153001. [[CrossRef](#)]
883. Wang, K.; Wang, X.; Ahmad, W.; Zhao, J.; Li, H.; Wang, L.; Wan, Z.; Jiang, W.; Li, S.; Yang, F.; et al. Synergistic dual-additive regulated carbonate electrolyte stabilizes bidirectional interface for aggressive Ni-rich Li-metal full batteries. *Nano Energy* **2024**, *128*, 109862. [[CrossRef](#)]
884. An, K.; Tran, Y.H.T.; Kwak, S.; Han, J.; Song, S.-W. Design of fire-resistant liquid electrolyte formulation for safe and long-cycled lithium-ion batteries. *Adv. Funct. Mater.* **2021**, *31*, 2106102. [[CrossRef](#)]
885. Huang, X.; Li, R.; Sun, C.; Zhang, H.; Zhang, S.; Lv, L.; Huang, Y.; Fan, L.; Chen, L.; Noked, M.; et al. Solvent-assisted hopping mechanism enables ultrafast charging of lithium-ion batteries. *ACS Energy Lett.* **2022**, *7*, 3947–3957. [[CrossRef](#)]
886. Li, Z.; Yao, N.; Yu, L.; Yao, Y.-X.; Jin, C.-B.; Yang, Y.; Xiao, Y.; Yue, X.-Y.; Cai, W.-L.; Xu, L.; et al. Inhibiting gas generation to achieve ultralong-lifespan lithium-ion batteries at low temperatures. *Matter* **2023**, *6*, 2274–2292. [[CrossRef](#)]
887. Zou, Y.; Ma, Z.; Liu, G.; Li, Q.; Yin, D.; Shi, X.; Cao, Z.; Tian, Z.; Kim, H.; Guo, Y.; et al. Non-flammable electrolyte enables high-voltage and wide-temperature lithium-ion batteries with fast charging. *Angew. Chem. Int. Ed.* **2023**, *62*, e202216189. [[CrossRef](#)]
888. Wu, C.; Wu, Y.; Yang, X.; Xin, T.; Chen, S.; Yang, M.; Peng, Y.; Xu, H.; Yin, Y.; Deng, T.; et al. Thermal runaway suppression of high-energy lithium-ion batteries by designing the stable interphase. *J. Electrochem. Soc.* **2021**, *168*, 090563. [[CrossRef](#)]
889. Wu, Y.; Feng, X.; Liu, X.; Wang, X.; Ren, D.; Wang, L.; Yang, M.; Wang, Y.; Zhang, W.; Li, Y.; et al. In-built ultraconformal interphases enable high-safety practical lithium batteries. *Energy Storage Mater.* **2021**, *43*, 248–257. [[CrossRef](#)]
890. Pan, R.; Cui, Z.; Yi, M.; Xie, Q.; Manthiram, A. Ethylene carbonate-free electrolytes for stable, safer high-nickel lithium-ion batteries. *Adv. Energy Mater.* **2022**, *12*, 2103806. [[CrossRef](#)]
891. Wu, Y.; Ren, D.; Liu, X.; Xu, G.-L.; Feng, X.; Zheng, Y.; Li, Y.; Yang, M.; Peng, Y.; Han, X.; et al. High-voltage and high-safety practical lithium batteries with ethylene carbonate-free electrolyte. *Adv. Energy Mater.* **2021**, *11*, 2102299. [[CrossRef](#)]
892. Li, W.; Dolocan, A.; Li, J.; Xie, Q.; Manthiram, A. Ethylene carbonate-free electrolytes for high-nickel layered oxide cathodes in lithium-ion batteries. *Adv. Energy Mater.* **2019**, *9*, 1901152. [[CrossRef](#)]
893. Klein, S.; van Wickeren, S.; Röser, S.; Bärmann, P.; Borzeutzki, K.; Heidrich, B.; Börner, M.; Winter, M.; Placke, T.; Kasnatscheew, J. Understanding the outstanding high-voltage performance of NCM523||graphite lithium ion cells after elimination of ethylene carbonate solvent from conventional electrolyte. *Adv. Energy Mater.* **2021**, *11*, 2003738. [[CrossRef](#)]
894. Xu, C.; Liang, Y.; Zhang, R.; Cheng, J.; Yun, H. Ethylene carbonate-free electrolytes for high voltage lithium-ion batteries: Progress and perspectives. *Energy Fuels* **2024**, *38*, 18208–18226. [[CrossRef](#)]
895. Lv, L.; Zhang, H.; Lu, D.; Yu, Y.; Qi, J.; Zhang, J.; Zhang, S.; Li, R.; Deng, T.; Chen, L.; et al. A low-concentration sulfone electrolyte enables high-voltage chemistry of lithium-ion batteries. *Energy Mater.* **2022**, *2*, 200030. [[CrossRef](#)]
896. Lu, D.; Lei, X.; Weng, S.; Li, R.; Li, J.; Lv, L.; Zhang, H.; Huang, Y.; Zhang, J.; Zhang, S.; et al. A self-purifying electrolyte enables high energy Li ion batteries. *Energy Environ. Sci.* **2022**, *15*, 3331–3342. [[CrossRef](#)]
897. Xu, J.; Zhang, J.; Pollard, T.P.; Li, Q.; Tan, S.; Hou, S.; Wan, H.; Chen, F.; He, H.; Hu, E.; et al. Electrolyte design for Li-ion batteries under extreme operating conditions. *Nature* **2023**, *614*, 694. [[CrossRef](#)]
898. Su, H.; Chen, Z.; Li, M.; Bai, P.; Li, Y.; Ji, X.; Liu, Z.; Sun, J.; Ding, J.; Yang, M.; et al. Achieving practical high-energy-density lithium-metal batteries by a dual-anion regulated electrolyte. *Adv. Mater.* **2023**, *35*, 2301171. [[CrossRef](#)]
899. Chen, P.-P.; Zhang, B.-H.; Li, Z.-A.; Lei, J.-T.; Chen, J.-Z.; Hou, Y.-L.; Zhao, D.-L. Regulate the solvation structure and interface by nitrate in phosphate-based electrolytes for 4.5 V-class Ni-rich batteries. *Small* **2024**, *20*, 2403079. [[CrossRef](#)] [[PubMed](#)]
900. Yang, Q.; Li, Q.; Tan, G.; Li, L.; Chen, R.; Wu, F. Double-salts super concentrated carbonate electrolyte boosting electrochemical performance of Ni-rich LiNi_{0.90}Co_{0.05}Mn_{0.05}O₂ lithium metal batteries. *Small* **2024**, *20*, 2311650. [[CrossRef](#)]
901. Zhang, J.; Zhang, H.; Weng, S.; Li, R.; Lu, D.; Deng, T.; Zhang, S.; Lv, L.; Qi, J.; Xiao, X.; et al. Multifunctional solvent molecule design enables high-voltage Li-ion batteries. *Nat. Commun.* **2023**, *14*, 2211. [[CrossRef](#)]

902. Zhang, X.; Zou, L.; Cui, Z.; Jia, H.; Engelhard, M.H.; Matthews, B.E.; Cao, X.; Xie, Q.; Wang, C.; Manthiram, A.; et al. Stabilizing ultrahigh-nickel layered oxide cathodes for high-voltage lithium metal batteries. *Mater. Today* **2021**, *44*, 15–24. [CrossRef]
903. Zhang, S.S. Unveiling the mystery of lithium bis(fluorosulfonyl)imide as a single salt in low-to-moderate concentration electrolytes of lithium metal and lithium-ion batteries. *J. Electrochem. Soc.* **2022**, *169*, 110515. [CrossRef]
904. Huang, H.; Zheng, J.; Li, H.; Guan, S.; Zhao, H.; Han, W.; Zhang, H.; Jiang, G.; Li, L.; An, B.; et al. Self-induced corrosion of Ni-rich cathode materials by fluor-lithium salts. *Energy Storage Mater.* **2025**, *74*, 103953. [CrossRef]
905. Qiao, L.; Oteo, U.; Martínez-Ibáñez, M.; Santiago, A.; Cid, R.; Sanchez-Diez, E.; Lobato, E.; Meabe, L.; Armand, M.; Zhang, H. Stable non-corrosive sulfonimide salt for 4-V-class lithium metal batteries. *Nat. Mater.* **2022**, *21*, 455–462. [CrossRef] [PubMed]
906. Xia, Y.; Zhou, P.; Kong, X.; Tian, J.; Zhang, W.; Yan, S.; Hou, W.-H.; Zhou, H.-Y.; Dong, H.; Chen, X.; et al. Designing an asymmetric ether-like lithium salt to enable fast-cycling high-energy lithium metal batteries. *Nat. Energy* **2023**, *8*, 934–945. [CrossRef]
907. Li, L.; Xu, G.; Zhang, S.; Dong, S.; Wang, S.; Cui, Z.; Du, X.; Wang, C.; Xie, B.; Du, J.; et al. Highly fluorinated Al-centered lithium salt boosting the interfacial compatibility of Li-metal batteries. *ACS Energy Lett.* **2022**, *7*, 591–598. [CrossRef]
908. Wu, F.; Fang, S.; Kuenzel, M.; Mullaliu, A.; Kim, J.-K.; Gao, X.; Diemant, T.; Kim, G.-T.; Passerini, S. Dual-anion ionic liquid electrolyte enables stable Ni-rich cathodes in lithium-metal batteries. *Joule* **2021**, *5*, P2177–P2194. [CrossRef]
909. Kato, Y.; Nagahara, A.; Gerile, N.; Fujinaka, S.; Hamamoto, N.; Nishimura, H.; Nakai, H. Investigation of water-washing effect on electrochemical properties of Ni-Rich NCA cathode material for lithium-ion batteries. *J. Electrochem. Soc.* **2022**, *169*, 060543. [CrossRef]
910. Hartmann, L.; Pritzl, D.; Beyer, H.; Gasteiger, H.A. Evidence for Li^+/H^+ exchange during ambient storage of Ni-rich cathode active materials. *J. Electrochem. Soc.* **2021**, *168*, 070507. [CrossRef]
911. Wang, X.; He, W.; Xue, H.; Zhang, D.; Wang, J.; Wang, L.; Li, J. A nonflammable phosphate-based localized high-concentration electrolyte for safe and high-voltage lithium metal batteries. *Sustain. Energy Fuels* **2022**, *6*, 1281–1288. [CrossRef]
912. Wang, J.; Zhang, S.; Li, R.; Chen, L.; Zhang, H.; Ma, B.; Jiang, S.; Zhou, T.; Huang, J.; Zhu, H.; et al. Surface chemical coordination stabilizes Ni-rich cathodes for high-energy Li-metal batteries. *J. Am. Chem. Soc.* **2025**, *147*, 9396–9406. [CrossRef] [PubMed]
913. Pillot, C. Lithium-Ion Battery Raw Material Supply and Demand 2016–2025. Available online: http://cii-resource.com/cet/AABE-03-17/Presentations/BRMT/Pillot_Christophe.pdf (accessed on 1 February 2024).
914. Greim, P.; Solomon, A.A.; Breyer, C. Assessment of lithium criticality in the global energy transition and addressing policy gaps in transportation. *Nat. Commun.* **2020**, *11*, 4570. [CrossRef]
915. Shi, Y.; Zhang, M.; Meng, Y.S.; Chen, Z. Ambient-pressure relithiation of degraded $\text{Li}_x\text{Ni}_{0.5}\text{Co}_{0.2}\text{Mn}_{0.3}\text{O}_2$ ($0 < x < 1$) via eutectic solutions for direct regeneration of lithium-ion battery cathodes. *Adv. Energy Mater.* **2019**, *9*, 1900454.
916. Wang, T.; Luo, H.M.; Bai, Y.C.; Li, J.L.; Belharouak, I.; Dai, S. Direct recycling of spent NCM cathodes through ionothermal lithiation. *Adv. Energy Mater.* **2020**, *10*, 2001204. [CrossRef]
917. Harper, G.; Sommerville, R.; Kendrick, E.; Driscoll, L.; Slater, P.; Stolkin, R.; Walton, A.; Christensen, P.; Heidrich, O.; Lambert, S.; et al. Recycling lithium-ion batteries from electric vehicles. *Nature* **2019**, *575*, 75. [CrossRef]
918. Cao, Y.; Li, J.; Ji, H.; Wei, X.; Zhou, G.; Cheng, H.-M. A review of direct recycling methods for spent lithium-ion batteries. *Energy Storage Mater.* **2024**, *70*, 103475. [CrossRef]
919. Zhang, X.; Li, L.; Fan, E.; Xue, Q.; Bian, Y.; Wu, F.; Chen, R. Toward sustainable and systematic recycling of spent rechargeable batteries. *Chem. Soc. Rev.* **2018**, *47*, 7239–7302. [CrossRef]
920. Mao, J.; Ye, C.; Zhang, S.; Xie, F.; Zeng, R.; Davey, K.; Guo, Z.; Qiao, S. Toward practical lithium-ion battery recycling: Adding value, tackling circularity and recycling-oriented design. *Energy Environ. Sci.* **2022**, *15*, 2732–2752. [CrossRef]
921. Wang, D.; Zhang, X.; Chen, H.; Sun, J. Separation of Li and Co from the active mass of spent Li-ion batteries by selective sulfating roasting with sodium bisulfate and water leaching. *Miner. Eng.* **2018**, *126*, 28–35. [CrossRef]
922. Yang, Y.; Qu, X.; Zhang, B.; Zhao, Y.; Xie, H.; Zhao, J.; Ning, Z.; Xing, P.; Yin, H. Recycling of spent lithium nickel cobalt manganese oxides via a low-temperature ammonium sulfation roasting approach. *J. Clean. Prod.* **2021**, *279*, 123633.
923. Lander, L.; Rousse, G.; Batuk, D.; Colin, C.V.; Corte, D.A.D.; Tarascon, J.-M. Synthesis, structure, and electrochemical properties of K-based sulfates $\text{K}_2\text{M}_2(\text{SO}_4)_3$ with M = Fe and Cu. *Inorg. Chem.* **2017**, *56*, 2013–2021. [CrossRef]
924. Wang, X.; Zhang, X.; Zhang, C.; Zhang, L.; Wen, J.; Wang, C.; Huang, G. Synthesis of high-nickel and high-performance ternary cathode materials through spent lithium-ion batteries recycling system. *Sustain. Chem. Pharm.* **2023**, *31*, 100959. [CrossRef]
925. Hamitouche, L.; Robert, C.; Rollet, A.-L.; Briois, V.; Selmane, M.; Gutierrez, A.G.P.; Leclerc, S.; Krulic, D.; Fatouros, N.; Sirieix-Plénet, J.; et al. Elucidating salt conversion mechanisms of lithiated transition metal oxides for lithium-ion battery recycling. *Chem. Mater.* **2024**, *36*, 2544–2553. [CrossRef]
926. Ji, H.; Wang, J.; Qu, H.; Li, J.; Ji, W.; Qiu, X.; Zhu, Y.; Ren, H.; Shi, R.; Li, G.; et al. Closed-loop direct upcycling of spent Ni-rich layered cathodes into high-voltage cathode materials. *Adv. Mater.* **2024**, *36*, 2407029. [CrossRef] [PubMed]
927. Ji, G.; Wang, J.; Liang, Z.; Jia, K.; Ma, J.; Zhuang, Z.; Zhou, G.; Cheng, H.-M. Direct regeneration of degraded lithium-ion battery cathodes with a multifunctional organic lithium salt. *Nat. Commun.* **2023**, *14*, 584. [CrossRef]

928. Xu, M.L.; Wu, C.; Zhang, F.X.; Zhang, Y.H.; Ren, J.X.; Zhang, C.Y.; Wang, X.Z.; Xiao, L.; Fontaine, O.; Qian, J.F. Potential regulation strategy enables ferrocene as p-type redox mediator for direct regeneration of spent LiFePO₄ cathode. *Energy Storage Mater.* **2024**, *71*, 103611. [[CrossRef](#)]
929. Liu, Z.Z.; Zhang, C.; Ye, M.X.; Li, H.M.; Fu, Z.; Zhang, H.M.; Wang, G.Z.; Zhang, Y.X. Closed-loop regeneration of a spent LiFePO₄ cathode by integrating oxidative leaching and electrochemical relithiation. *ACS Appl. Energy. Mater.* **2022**, *5*, 14323–14334. [[CrossRef](#)]
930. Wu, C.; Hu, J.M.; Ye, L.; Su, Z.P.; Fang, X.L.; Zhu, X.L.; Zhuang, L.; Ai, X.P.; Yang, H.X.; Qian, J.F. Direct regeneration of spent Li-ion battery cathodes via chemical relithiation reaction. *ACS Sustain. Chem. Eng.* **2021**, *9*, 16384–16393. [[CrossRef](#)]
931. Wu, C.; Xu, M.L.; Zhang, C.Y.; Ye, L.; Zhang, K.L.; Cong, H.J.; Zhuang, L.; Ai, X.P.; Yang, H.X.; Qian, J.F. Cost-effective recycling of spent LiMn₂O₄ cathode via a chemical lithiation strategy. *Energy Storage Mater.* **2023**, *55*, 154–165. [[CrossRef](#)]
932. Park, K.; Yu, J.L.; Coyle, J.; Dai, Q.; Frisco, S.; Zhou, M.; Burrell, A. Direct cathode recycling of end-of-life Li-ion batteries enabled by redox mediation. *ACS Sustain. Chem. Eng.* **2021**, *9*, 8214–8221. [[CrossRef](#)]
933. Ko, S.; Choi, J.; Hong, J.; Kim, C.; Hwang, U.; Kwon, M.; Lim, G.; Sohn, S.S.; Jang, J.; Lee, U.; et al. Thermodynamically controlled chemical regeneration of spent battery cathodes using recyclable electron donors under ambient conditions. *Energy Environ. Sci.* **2024**, *17*, 4064. [[CrossRef](#)]
934. Kim, S.; Shin, U.; Yoon, H.J.; Song, J.; Ma, J.; Woo, J.-J.; Nam, K.-W.; Seo, D.-H.; Ryu, W.-H. Unraveling redox mediator-assisted chemical relithiation mechanism for direct recycling of spent Ni-rich layered cathode materials. *Adv. Sci.* **2025**, *12*, 2417094. [[CrossRef](#)]
935. Zheng, Y.; Pu, J.; Yang, Q.; You, L.; Wang, W.; Liu, J. Efficient selective leaching and direct regeneration of spent Ni-rich cathodes via advanced oxidation. *Sep. Purif. Technol.* **2025**, *361*, 131366. [[CrossRef](#)]
936. Xu, G.; Huang, L.; Lu, C.; Zhou, X.; Cui, G. Revealing the multilevel thermal safety of lithium batteries. *Energy Storage Mater.* **2020**, *31*, 72–86. [[CrossRef](#)]
937. Wang, Y.; Feng, X.; Huang, W.; He, X.; Wang, L.; Ouyang, M. Challenges and opportunities to mitigate the catastrophic thermal runaway of high-energy batteries. *Adv. Energy Mater.* **2023**, *13*, 2203841. [[CrossRef](#)]
938. Cui, Z.; Manthiram, A. Thermal stability and outgassing behaviors of high-nickel cathodes in lithium-ion batteries. *Angew. Chem. Int. Ed.* **2023**, *62*, e202307243. [[CrossRef](#)]
939. Liu, X.; Ren, D.; Hsu, H.; Feng, X.; Xu, G.-L.; Zhuang, M.; Gao, H.; Lu, L.; Han, X.; Chu, Z.; et al. Thermal runaway of lithium-ion batteries without internal short circuit. *Joule* **2018**, *2*, 2047–2064. [[CrossRef](#)]
940. Hou, J.; Feng, X.; Wang, L.; Liu, X.; Ohma, A.; Lu, L.; Ren, D.; Huang, W.; Li, Y.; Yi, M.; et al. Unlocking the self-supported thermal runaway of high-energy lithium-ion batteries. *Energy Storage Mater.* **2021**, *39*, 395–402. [[CrossRef](#)]
941. Li, Y.; Liu, X.; Wang, L.; Feng, X.; Ren, D.; Wu, Y.; Xu, G.; Lu, L.; Hou, J.; Zhang, W.; et al. Thermal runaway mechanism of lithium-ion battery with LiNi_{0.8}Mn_{0.1}Co_{0.1}O₂ cathode materials. *Nano Energy* **2021**, *85*, 105878. [[CrossRef](#)]
942. Galushkin, N.E.; Yazvinskaya, N.N.; Galushkin, D.N. Mechanism of thermal runaway in lithium-ion cells. *J. Electrochem. Soc.* **2018**, *165*, A1303–A1308. [[CrossRef](#)]
943. Huang, L.; Xu, G.; Du, X.; Li, J.; Xie, B.; Liu, H.; Han, P.; Dong, S.; Cui, G.; Chen, L. Uncovering LiH triggered thermal runaway mechanism of a high-energy LiNi_{0.5}Co_{0.2}Mn_{0.3}O₂/graphite pouch cell. *Adv. Sci.* **2021**, *8*, 2100676. [[CrossRef](#)]
944. Liu, X.; Yin, L.; Ren, D.; Wang, L.; Ren, Y.; Xu, W.; Lapidus, S.; Wang, H.; He, X.; Chen, Z.; et al. In situ observation of thermal-driven degradation and safety concerns of lithiated graphite anode. *Nat. Commun.* **2021**, *12*, 4235. [[CrossRef](#)]
945. Xu, G.; Li, J.; Wang, C.; Du, X.; Lu, D.; Xie, B.; Wang, X.; Lu, C.; Liu, H.; Dong, S.; et al. The formation/decomposition equilibrium of LiH and its contribution on anode failure in practical lithium metal batteries. *Angew. Chem. Int. Ed.* **2021**, *60*, 7770–7776. [[CrossRef](#)]
946. Xu, G.; Du, X.; Zhang, S.; Li, J.; Dong, S.; Hu, Z.; Cui, G. Revealing the importance of suppressing formation of lithium hydride and hydrogen in Li anode protection. *Interdiscip. Mater.* **2023**, *2*, 337–347. [[CrossRef](#)]
947. Soto, F.A.; Ma, Y.; Martinez De La Hoz, J.M.; Seminario, J.M.; Balbuena, P.B. Formation and growth mechanisms of solid-electrolyte interphase layers in rechargeable batteries. *Chem. Mater.* **2015**, *27*, 7990–8000. [[CrossRef](#)]
948. Li, M.; Yang, X.; Wei, X.; Zhu, Y.; Sun, X.; Gu, M.D. Cathode–electrolyte interphase of Ni-rich layered oxides: Evolving structure and implication on stability. *Nano Lett.* **2025**, *25*, 2769–2776. [[CrossRef](#)]
949. Park, N.-Y.; Lee, H.-H.; Kim, H.; Park, S.-M.; Jung, H.-G.; Jung, Y.-C.; Sun, Y.-K. High-energy, long-life Ni-rich cathode materials with columnar structures for all-solid-state batteries. *Nature Energy* **2025**, *10*, 479–489. [[CrossRef](#)]
950. Zhang, S.; Ma, J.; Hu, Z.; Cui, G.; Chen, L. Identifying and addressing critical challenges of high-voltage layered ternary oxide cathode materials. *Chem. Mater.* **2019**, *31*, 6033–6065. [[CrossRef](#)]
951. Kim, U.-H.; Park, G.-T.; Conlin, P.; Ashburn, N.; Cho, K.; Yu, Y.-S.; Shapiro, D.A.; Maglia, F.; Kim, S.J.; Lamp, P.; et al. Cation ordered Ni-rich layered cathode for ultra-long battery life. F1-GC80: Fluorine doped compositionally graded cathode, with an average concentration of Li[Ni_{0.80}Co_{0.05}Mn_{0.15}]O₂. *Energy Environ. Sci.* **2021**, *14*, 1573–1583. [[CrossRef](#)]

952. Wang, S.; Dai, A.; Cao, Y.; Yang, H.; Khalil, A.; Lu, J.; Li, H.; Ai, X. Enabling stable and high-rate cycling of a Ni-rich layered oxide cathode for lithium-ion batteries by modification with an artificial Li^+ -conducting cathode-electrolyte interphase. NMC811 with artificial Li^+ -conducting cathode-electrolyte interphase (ALCEI). *J. Mater. Chem. A* **2021**, *9*, 11623–11631.
953. Ma, J.; Sun, Y.; Wu, D.; Wang, C.; Yu, R.; Duan, H.; Zheng, M.; Li, R.; Gu, D.; Zhao, Y.; et al. Highly stabilized Ni-rich cathodes enabled by artificially reversing naturally-formed interface. *Adv. Energy Mater.* **2025**, *15*, 2403150. [[CrossRef](#)]

Disclaimer/Publisher’s Note: The statements, opinions and data contained in all publications are solely those of the individual author(s) and contributor(s) and not of MDPI and/or the editor(s). MDPI and/or the editor(s) disclaim responsibility for any injury to people or property resulting from any ideas, methods, instructions or products referred to in the content.